Overcoming Energy Losses for Efficient Organic Solar Cells

A Dissertation
SUBMITTED TO THE FACULTY OF
UNIVERSITY OF MINNESOTA
BY

Tao Zhang

IN PARTIAL FULFILLMENT OF THE REQUIREMENTS
FOR THE DEGREE OF
DOCTOR OF PHILOSOPHY

Russell J. Holmes, Advisor

September 2019

Acknowledgements

First of all, I have to pay my deepest appreciation to my advisor Professor Russell Holmes for his guidance and support through my entire Ph.D. study at the University of Minnesota. His passion for science, enthusiasm on discovery, and the highest standards for research works keep inspiring me and would definitely impact my future career.

I would like to thank all my colleagues in Holmes research group, Matt, Yunlong, Tyler, Nathan, Tom, Ian, Gang, Kyle, Abbey, Caroline, Deepesh, Catherine, John, Kaicheng, Nolan, and Robert, for their consistent help and friendship. I am very fortunate to work with these talented scholars. I am especially indebted to Ian who not only provides me guidance in research work but also helps me to start the next stage of my career. Besides, my special appreciation goes to Deepesh who provides support and thoughtful discussion especially during late night and weekend.

I would like to thank my all collaborators, Prof. Ken-Tsung Wong at National Taiwan University, Dr. Dana Dement and Prof. Vivian Ferry at the University of Minnesota. It would be impossible to carry on my research without their high-quality nanomaterials. I would also like to acknowledge Professor Eray Aydil for his insightful discussions.

I also would like to thank all my friends for their friendship in the last five years. I especially want to thank Dr. Hao Xu and Dr. Zhuoran Zhang, who keep me company in the gym, on the court, and in other after-hours activities.

Last but not least, I am indebted to my parents for their unconditional love, support, and encouragement throughout my life. I would like to thank my significant other, Feng, who shares her life journey with me.

Dedication

I dedicate this dissertation to my family, Liqiong Wei, Yunquan Zhang, and Feng Xue.

Abstract

Organic photovoltaic cells (OPVs) are promising for low-cost solar energy harvesting as they are light-weight, mechanically flexible and compatible with large area fabrication methods. The power conversion efficiency of OPVs, however, still lags behind inorganic counterparts, which limits their widespread commercial application. This dissertation is focused on understanding the various energy loss mechanisms in OPVs and devising general design rules for minimizing these losses.

Among all parasitic energy loss pathways in OPVs, charge recombination is a major source of inefficiency in state-of-the-art systems. It can take place at the donor-acceptor interface when charges are bound by electrostatic forces as charge-transfer (CT) states, or in bulk active layers when free charge carriers are in transit to electrodes. To develop a detailed understanding of recombination loss mechanisms, a novel technique based on transient photovoltage has been developed, which allows quantitative elucidation of the dominant recombination mechanisms (CT state vs. free charge carrier losses) in OPVs.

Using the information obtained from photovoltage measurement, strategies have been developed to suppress charge recombination losses in various OPV systems, including optimizing thin film morphology that facilitates charge transport for dipolar donor materials system and devising advanced device architectures that can stabilize CT states and maximize charge collection for metal phthalocyanine-fullerene materials system. Efforts have also been devoted to understanding and engineering the transport of CT states, a potential strategy that reduces recombination losses in OPVs.

Based on the detailed understanding of charge recombination losses, a device-based methodology has been developed to probe exciton losses in OPVs. It is the first method capable of probing the intrinsic active material exciton diffusion length, equally applicable to both luminescent and dark materials. With this novel technique, exciton transport has been investigated in various excitonic semiconductor systems, including dark small molecules, polymers, inorganic semiconductor quantum dots.

Moving forward, topics like exploring long-range CT state migration and understanding singlet fission mechanisms are pathways towards enhanced device efficiency.

Table of Contents

List of Tables

List of Figures

List of Abbreviations

BHJ ..... Bulk Heterojunction
CT state ..... Charge Transfer State
CRZ ..... Charge Recombination Zone
D-A ..... Donor-Acceptor
FF ..... Fill Factor
GR ..... Geminate Recombination
HOMO ..... Highest Occupied Molecular Orbital
ITO ..... Indium Tin Oxide
J_{Dark} ..... Dark Current Density
J_{Photo} ..... Photo Current Density
J_{SC} ..... Short-Circuit Current Density
L_D ..... Exciton Diffusion Length
LUMO ..... Lowest Unoccupied Molecular Orbital
NGR ..... Non- Geminate Recombination
η_A ..... Absorption Efficiency
η_{CS} ..... Charge Separation Efficiency
η_D ..... Exciton Diffusion Efficiency
η_{EQE} ..... External Quantum Efficiency
η_{FC} ..... Free Carrier Collection Efficiency
η_P ..... Power Conversion Efficiency
OPV ..... Organic Photovoltaic Cell
PHJ ..... Planar Heterojunction
PL ..... Photoluminescence
PMHJ ..... Planar Mixed Heterojunction
S_0 ..... Singlet ground state
S_1 ..... First excited singlet state
T_1 ..... First triplet excited state
V_{OC} ..... Open-Circuit Voltage

1. Introduction to Photovoltaics

1.1 Photovoltaic Cells

The realization of clean and renewable energy sources remains a critical challenge for modern society due to dwindling fossil fuel reserves and an ever-growing demand for energy.[1-2] To address this challenge, tremendous efforts have been paid to developing renewable energy technologies in past decades, such as wind power, hydroelectricity, biomass combustion, and photovoltaics. Interestingly, most of these commonly utilized renewable energy technologies harvest solar energy either directly or indirectly.[3]

As the most direct means to harvest solar energy, photovoltaic cells (PVs) can convert optical radiation into useable electricity. Due to the large scale of the ubiquitous solar resource, PV technology has shown the potential to play an important role in future energy systems. The global installed PV capacity has exceeded 500 gigawatts in 2018 and will exceed a terawatt in the near future.[4] The most widely deployed first-generation solar technology is based on crystalline silicon, which can achieve an optical-to-electrical power conversion efficiency (η_P) of 26.7% (record).[5] For typical modules, the η_P is ~20%.[6] To further improve η_P, there has been a continuous effort to develop multi-junction photovoltaic cells and solar concentrators. Under typical sunlight conditions (AM1.5 spectrum, one sun irradiance), a single-junction photovoltaic cell has a maximum theoretical η_P of 33.7% according to the Schockley-Quessier limit.[7-8] Multi-junction cells can outperform this limit and raise the theoretical η_P up to 86.8% in extreme conditions (infinite sub-cells under concentrated sunlight).[7] To date, the record efficiency of multi-

junction photovoltaic cells has exceeded 45%.[9] However, the application of these highly efficient photovoltaic cells is limited to aerospace applications due to significantly higher cost than conventional crystalline silicon cells.

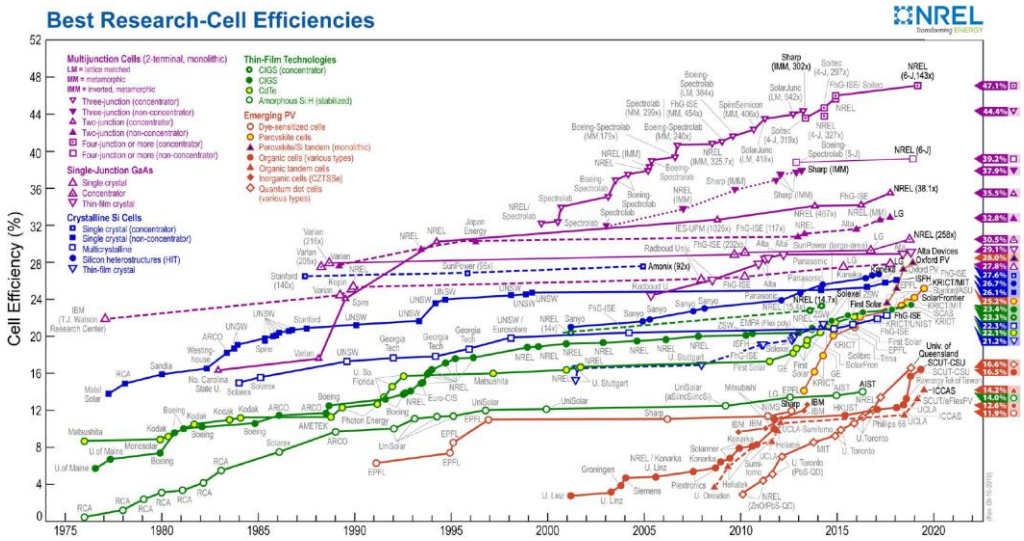

Figure 1.1 Chart of best research-cell efficiencies summarized by the national renewable energy laboratory (NREL).[10]

While mature, first-generation solar technology continues to be limited by the high cost of manufacturing and deployment.[11] To reduce the cost, second-generation thin-film photovoltaics utilizing amorphous silicon, cadmium telluride (CdTe) and copper indium gallium diselenide (CIGS) have also been investigated.[12-14] The thickness of these cells can vary from tens of nanometers to a few micrometers, much thinner than the first-generation photovoltaic cells. This leads to a significant reduction in the materials cost. Despite operating at reduced efficiency, thin-film photovoltaic cells can achieve a lower price per unit Watt of power produced.[9-10] In addition to lowered material cost, thin-film photovoltaic cells can be flexible, low-weight and semi-transparent. These properties allow the thin-film

photovoltaic cells to be used as building-integrated photovoltaics (BIPV), one of the fastest-growing segments of the photovoltaic industry.[15]

As the market share of second-generation photovoltaic cells is still limited by toxicity, stability, and usage of rare elements, third-generation cells based on copper zinc tin sulfide (CZTS), inorganic semiconductors quantum dots, organic semiconductors, and organic-inorganic hybrid metal-halide perovskite materials have been heavily investigated by both industry and academia in recent years.[11, 16-18] Among the third-generation photovoltaic technologies, organic photovoltaic cells (OPVs) based on organic semiconductors (conjugated small molecules and polymers) are attractive due to their compatibility with low-temperature, large area, high-throughput processing, potentially enabling low cost.[19] Unlike their inorganic counterparts which are opaque, brittle, and inflexible, organic semiconductors can be made transparent are mechanically flexible as they create solids as a result of weak van der Waals interactions. These make OPVs promising for various applications, such as transparent windows for BIPV and internet of things (IoT) devices.

Figure 1.2 Roll-to-roll manufacturing and building-integrated OPVs of Heliatek.

The harvesting of solar energy with OPVs has been a topic of study for more than 60 years.[20-21] These prototype OPVs developed in the 1950s had a simple metal-semiconductor-metal Schottky device configuration and can only show $\eta_P < 1$ %. Currently, the most efficient OPVs are based on donor-acceptor (D-A) heterojunction device architecture. The record efficiency has exceeded 14% for single-junction OPVs.[22] Recently, researchers reported a 17.3 % power conversion efficiency for two-junction tandem cells, further approaching commercially-viable levels of power generation performance.[23]

1.2 Overview of This Thesis

The primary focus of this dissertation is to elucidate the dominant energy loss mechanisms as a function of active material selection and solar cell architecture using a novel technique. Of particular interest are the properties of charge-transfer (CT) states, and how their behavior impacts corresponding loss mechanisms. This deeper understanding of CT states can guide efforts to engineer solar cells that mitigate energy losses and maximize efficiency.

After introducing the fundamentals of organic semiconductors and OPV operation and characterization, this thesis focuses on characterization and suppression of electron-hole recombination losses, the major source of inefficiency for OPVs. Equipped with a deeper understanding of charge recombination losses, the focus of this thesis moves to address a long-standing challenge, measuring intrinsic energy (exciton) transport electrically using a PV. This measurement is previously limited by unknown charge recombination losses.

2. Fundamentals of Organic Semiconductors

In Chapter 1, OPV has been introduced as a promising third-generation thin-film PV technology and may play a central role in the future renewable energy system. This chapter will cover the fundamental physics of organic semiconductors, which are critical for photoconversion in OPVs.

2.1 Energetics of Organic Semiconductors

Organic semiconductors, the building blocks for OPVs are conjugated small molecules (monomers and oligomers) or polymers consisting mainly of carbon. They have also demonstrated the successful application in organic field-effect transistors (OFETs) as well as organic light-emitting devices (OLEDs), a widely commercialized technology in the last few years.[24-25]

As these organic molecules have a full valence shell, they form solid-state via relatively weak intermolecular van der Waals interactions. Due to the weak intermolecular bonding, organic semiconductors often form amorphous films, which are “softer” than thin films of their inorganic counterpart. For instance, Young's modulus for small molecule tris-(8-hydroxyquinoline)aluminum (Alq3) is ~1 GPa, much lower than amorphous silicon (~80 GPa) and crystalline silicon (~180 GPa).[26-28] As a result, organic semiconductor thin films can be compatible with flexible and stretchable substrates suitable for high throughput, roll-to-roll processing.

The weak intermolecular interaction of organic semiconductors also results in different electronic properties compared to inorganic semiconductors. Their electrons tend to be

highly localized on a single molecule. Within the conjugated organic molecules, atoms are connected with covalent bonds. Electrons occupy molecular orbitals, which reflect a superposition of all atomic orbitals. The carbon atom has an electronic configuration of $1s^2 2s^2 2p^2$ at the ground state and therefore with two paired s electrons and 2 unpaired p electrons in its valence shell. When bonded with other atoms, 2s and 2p orbitals of carbon atom can hybridize and form degenerate orbitals. For example, carbon in methane has four degenerate sp^3 orbitals while benzene is a result of carbon sp^2 hybridization which forms three degenerate orbitals for each carbon atom. As shown in Figure 2.1, the sp^2 orbital hybridization between carbon atoms leads to π-bonds formed from the remaining p_z orbitals. The delocalized π-orbitals define the highest occupied (HOMO) and lowest unoccupied (LUMO) molecular orbitals. In some respects, they are analogous to the valence and conduction bands of inorganic semiconductors, respectively.

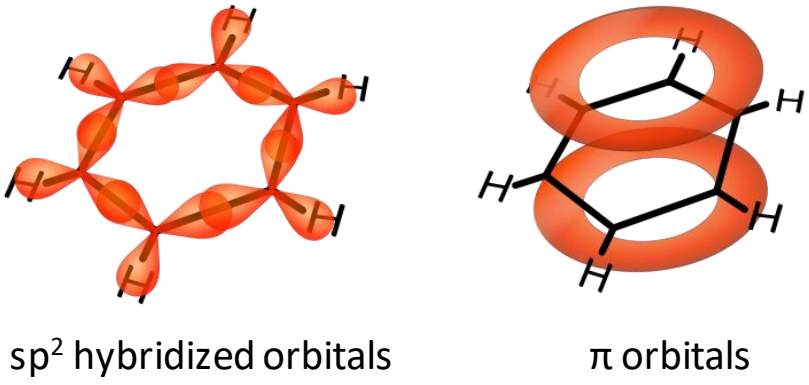

Figure 2.1 Orbital hybridization for the benzene molecule. The sp^2 orbital hybridization between carbon atoms leads to π-bonds formed from the remaining p_z orbitals.

Organic semiconductors typically have electronic energy gaps of 1-3 eV between the

HOMO and LUMO levels.[29] After absorbing an incident photon, an electron in HOMO is excited into the LUMO, leaving a hole behind in the HOMO. The resulting electron-hole pair is Coulombically-bound, forming as an exciton. The electrostatic Coulomb force leads to binding energy for exciton:[30]

$$E_b = \frac{q^2}{4\pi\varepsilon_0\varepsilon_r r} \qquad (2.1)$$

Where q is elementary charge, ε_0 is the permittivity of vacuum, ε_r is the relative permittivity of the organic material and r is the separation distance of the electron and hole that form an exciton. For excitons localized on a single molecule, this equation is typically not straightforward to apply due to the delocalization of electron and hole within the molecule. Due to the exciton binding energy, the energy of the molecular excited state, often called optical gap, is lower than the charge transport energy gap (HOMO-LUMO difference). For organics, the relative permittivity, also called dielectric constant, is typical ~3, much lower than inorganic materials (~10).[31-32] This results in large exciton binding energy typically ~0.5 eV, a bond can be hardly overcome with thermal energy at room temperature (k_BT= 25.9 meV).[31] As such, dissociation of excitons is critical to generate electricity using OPVs. Organic semiconductors tend to have strong interactions with visible light and near-infrared light, with relatively high absorption coefficients on the order of 10^5 cm^{-1}.[33] Therefore, a ~100 nm thick organic layer can absorb most incident sunlight, leading to low material cost for photovoltaic application.[34-35] In next section, molecular excited states and optical properties of organic semiconductors will be discussed in more details.

2.2 Excitons and Optical Properties

Excitons are Coulombically-bound electron-hole pairs that serve as energetic intermediates. There are three types of excitons depending on their spatial extent: Wannier-Mott excitons, charge transfer (CT) excitons and Frenkel excitons. For conventional inorganic semiconductors, such as Si and GaAs, the dielectric constant is generally large. As a result, screening tends to attenuate the Coulombic interaction between charges leading to large exciton radii. This type of exciton is Wannier-Mott exciton which has a radius greater than the crystal lattice spacing.

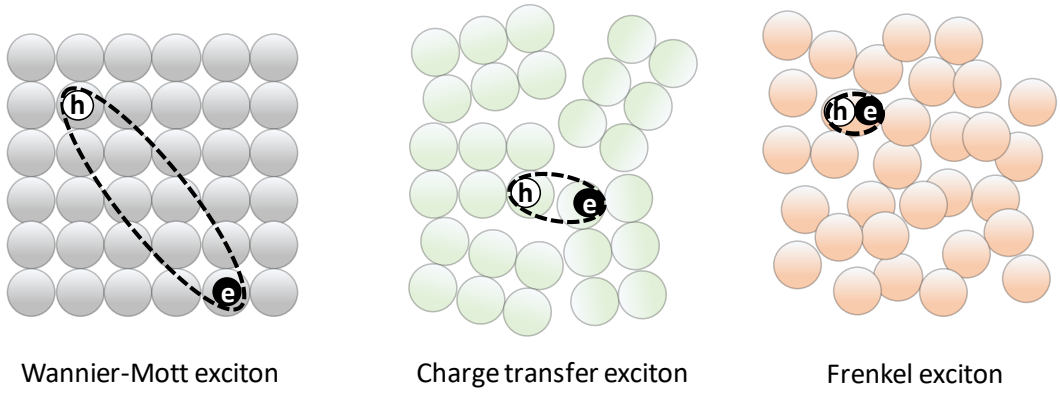

Figure 2.2 Spatial extents of Wannier-Mott, charge transfer and Frenkel excitons. The charge transfer exciton is typically called charge transfer state.

The most common excitons in organic semiconductors are the Frenkel type. The excitons are highly localized in a single molecule due to the low dielectric constant and large effective mass of electrons (poor intermolecular coupling).[30] A CT state (or CT exciton) is an intermediate type between Frenkel and Wannier-Mott excitons. In OPVs, CT states typically form at heterojunctions between two organic semiconductors. In several cases, CT states can exist in the bulk of organic semiconductors.[36-37]

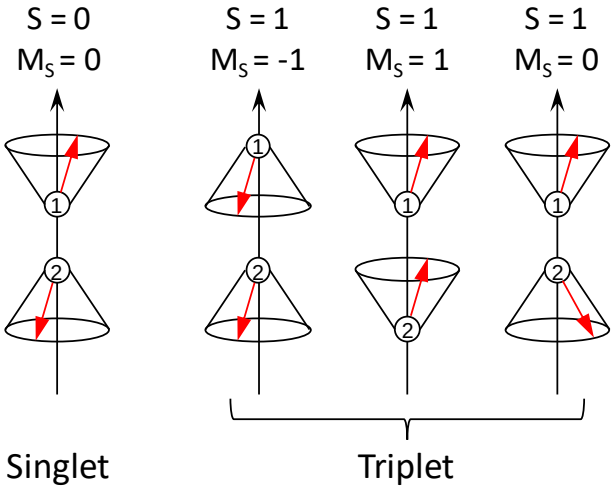

Figure 2.3 Singlet and triplet spin states for molecular excitons.

Spin is an important property of the exciton. According to the principles of quantum mechanics, excitons can be categorized as singlets and triplets depending on the spin of the component electrons. As Fermions, electrons have a spin of $\frac{1}{2}$ with a projection up or down the z-axis. The wavefunction of an exciton $\Psi(r_1, r_2)$ can be broken into spatial (ψ) and spin (σ) components. This wavefunction has to be anti-symmetric since electrons cannot simultaneously occupy the same quantum state (Pauli exclusion principles). As such, one of ψ and σ needs to be antisymmetric so that $\Psi(r_1, r_2) = -\Psi(r_2, r_1)$. Only one of the allowed spin states has a total spin (S) of 0:[38]

$$\Psi(r_1, r_2) = \psi_{sym} \times \frac{1}{\sqrt{2}}[\sigma_\uparrow(1)\sigma_\downarrow(2) - \sigma_\uparrow(2)\sigma_\downarrow(1)] \quad (2.2)$$

This state with the degeneracy of one is called singlet. The spin of the unpaired electron is out of phase and leads to the spin projection quantum number Ms = 0 (Figure 2.3). There are three states with S =1:[38]

$$\Psi(r_1, r_2) = \psi_{anti-sym} \times \sigma_{\uparrow}(1)\sigma_{\downarrow}(2)$$

$$\Psi(r_1, r_2) = \psi_{anti-sym} \times \sigma_{\uparrow}(2)\sigma_{\downarrow}(1)$$

$$\Psi(r_1, r_2) = \psi_{anti-sym} \times \frac{1}{\sqrt{2}}[\sigma_{\uparrow}(1)\sigma_{\downarrow}(2) + \sigma_{\uparrow}(2)\sigma_{\downarrow}(1)] \qquad (2.3)$$

These states with a degeneracy of three are called triplets. As shown in Figure 2.3, the spin quantum number M_s can take three possible values: -1,0 or 1.

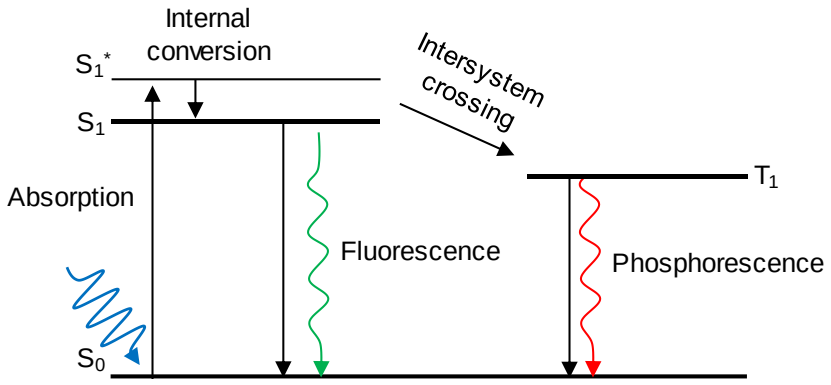

Figure 2.4 Excitonic state transition between the ground state and a high energy vibronic state.

The ground molecular state is generally singlet (denoted S_0) as the two highest energy electrons have to pair when sharing the HOMO. In theory, only singlet excitons are populated directly upon photoexcitation since the photon carries negligible spin angular momentum to the system. The optical transition between ground state and triplet states is therefore forbidden. Practically, it is possible to couple triplet and ground states radiatively in the presence of spin-orbit coupling. The conservation of total angular momentum can be realized with the help of orbital angular momentum, especially for molecules containing a high Z coordinating atom. The high Z atoms have bigger nuclear charges and can lead to

stronger spin-orbit interaction, frequently as large as or larger than spin-spin interactions or orbit-orbit interactions.[39] Typically, triplet excitons are generated from photoexcited singlet excitons through intersystem crossing. Figure 2.4 shows a diagram of excitonic state transition. A higher energy vibronic state of S_1 (S_1^*) is generated by absorbing a photon and then rapidly relaxes to the lowest singlet state by internal conversation. The resulting singlet state can either become a triplet (T_1) or recombine (radiatively/non-radiatively) back to ground state. Besides photoexcitation, electrical excitation can also generate excitons. However, both singlet and triplet excitons can be populated directly as these states are formed from mobile charge carriers. Because of the state degeneracy, the probability is 25% and 75% to generate singlet and triplet excitons from the random charge carriers, respectively.[40-41]

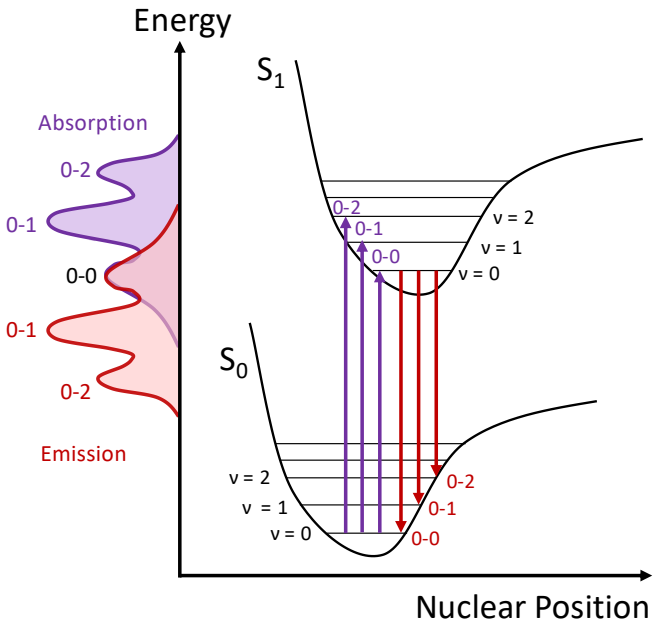

Figure 2.5 Molecular energy diagram for absorption and emission transition between vibration modes of S_0 and S_1.

To understand the absorption and emission spectra of organic semiconductors, the role of molecule vibration needs to be considered. For each singlet and triplet manifolds, there are energetically discrete states originated from molecular vibration called vibration modes. As the internal conversion (relaxation) is much faster than other processes, electronic transitions mostly start from the $\upsilon = 0$ level of S_1 (Kasha's rule).[39] As shown in Figure 2.5, the transitions into higher energy vibration modes can be stronger than the 0-0 transition, resulting in multiple peaks in absorption and emission spectra. Besides, the electronic transition is much faster than the reconfiguration of the nuclear (Frank-Condon principle). The transition is thus vertical in Figure 2.5 and can only take place when initial molecular configuration also supports the final state configuration.

2.3 Energy Transfer and Exciton Diffusion

As organic semiconductors are excitonic, the migration of excitons is critical for the device performance of various optoelectronic devices. For OPVs, long-range transport of these charge-neutral quasi-particles can maximize charge generation at the heterojunction interface. There are several energy transfer mechanisms for organic molecules, including cascade energy transfer, Förster energy transfer, and Dexter transfer.[42-44]

Cascade energy transfer, also called trivial transfer, is a radiative process that the energy accepting molecules re-absorb the photons emitted by the energy donating molecules. Therefore, this process requires an overlap between the ground-state absorption and excited state emission spectra. As the absorption length of organic semiconductors is

typically 50-100 nm, cascade energy transfer is a long-range process.[44]

Förster energy transfer is a dipole-dipole coupling energy transfer process that also requires overlap between absorption and emission spectra and a high photoluminescence efficiency.[31, 44] However, this process does not require a real photon to be emitted and is a non-radiative process. The electric field generated by oscillating dipoles in donor molecules can excite the acceptor molecules directly before the transfer of the energy to a photon (electromagnetic wave). The rate of Förster energy transfer can be expressed as below:[45]

$$k_F(d) = \frac{1}{\tau}\left(\frac{R_0}{d}\right)^6 \qquad (2.4)$$

Here, k_F is the rate of Förster transfer, d is the distance between the energy donating molecule and the energy accepting molecule, τ is the lifetime of exciton and R_0 is a characteristic Förster radius which can be expressed as:[46]

$${R_0}^6 = \frac{9\eta_{PL}\kappa^2}{128\pi^5 n^4}\int \lambda^4 F_D(\lambda)\sigma_A(\lambda)d\lambda \qquad (2.5)$$

Where η_{PL} is the photoluminescence efficiency, κ is the dipole orientation factor, n is the refractive index of the medium, λ is the wavelength, F_D is the normalized fluorescence spectrum of the donor molecule and σ_A is the absorption cross-section of the acceptor molecule at the ground state.[47] Förster energy transfer is therefore maximized when there is a strong spectral overlap between absorption and emission, indicating resonance. Although it is a non-radiative process, dipole-dipole energy transfer still depends on η_{PL} to compete with non-radiative exciton recombination. Typically, Förster energy transfer is in

the near field range ~10 nm, much shorter than the cascade energy transfer.

Energy can also be transferred to the neighboring molecules through a simultaneous electron exchange process, namely Dexter transfer. In contrast to cascade and Förster transfer, this process requires the physical transfer of electrons. The electron and hole of the donor molecule are simultaneously transferred to the acceptor molecule. The transfer rate of this process depends on the coupling strength between initial and final states:[42]

$$k_D = \frac{4\pi^2}{h}|\beta_{DA}|^2 \int E_D(E)E_A(E)dE \qquad (2.6)$$

Here, k_D is the rate of Dexter energy transfer, h is the Planck's constant, E_D is the normalized donor photoluminescence spectra and E_A is the normalized acceptor absorption spectra. β_{DA} is the matrix element for the donor-acceptor molecule interaction, which is related to the electronic orbital overlap between two molecules. As β_{DA} falls exponentially with transfer distance d, the k_D is often expressed as:[44]

$$k_D = \frac{4\pi^2}{h}Ke^{\frac{2d}{L}} \int E_D(E)E_A(E)dE \qquad (2.7)$$

where K is a prefactor determined by specific donor-acceptor molecular orbital interaction, and L is the van der Waals radius of the molecules. Dexter energy transfer is the most prevalent transport mechanism for triplet excitons as it does not require a radiative transition. It takes place mostly between nearest-neighbor molecules as the orbital overlap decreases exponentially with d.

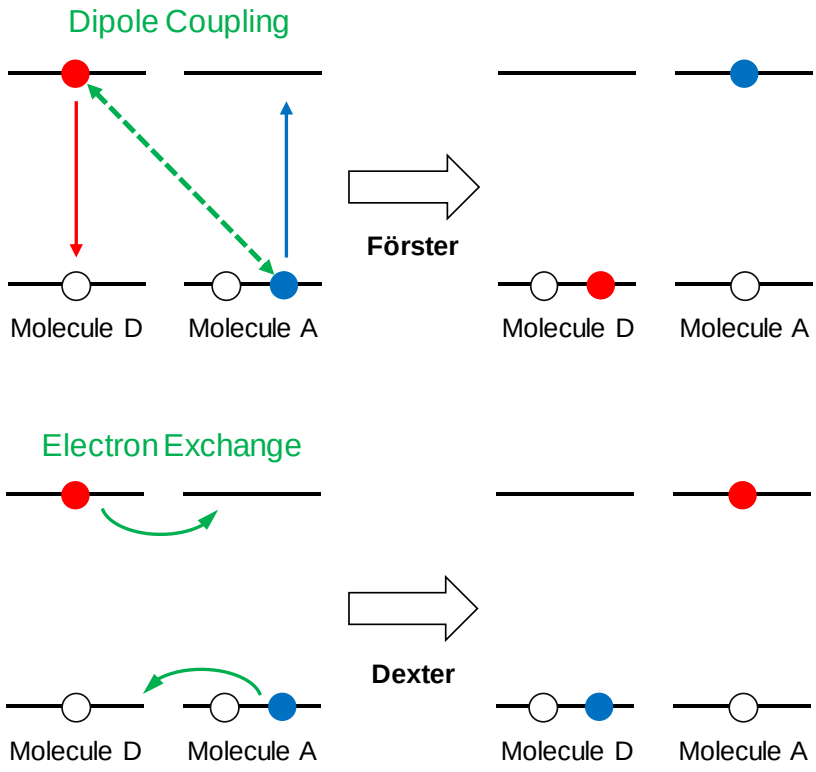

Figure 2.6 Förster and Dexter energy transfer between the energy donating molecule (D) and energy accepting molecule (A).The Dexter energy transfer requires physical exchange of electrons.

To connect energy transfer to exciton transport, exciton diffusion can be simulated as an ensemble of self-energy transfer events on a cubic lattice. Thus, a generalized diffusion coefficient D can be expressed as:[44]

$$D = \frac{A}{6}\sum_{N} d^2 k_{ET}(d) \qquad (2.8)$$

where A is a factor related to the thin-film disorder, and k_{ET} is the energy transfer rate to a specified lattice point of set N. In the absence of second-order processes, the exciton diffusion can be modeled as a function of position (r) and time (t):[48]

$$\frac{\partial n(r,t)}{\partial t} = D\nabla^2 n(r,t) - \frac{n(r,t)}{\tau} + G(r,t) \quad (2.9)$$

Here, n is the exciton density, and G is the exciton generation rate. The product of D and τ yields the exciton diffusion length L_D:[44]

$$L_D = \sqrt{D\tau} \quad (2.10)$$

From the perspective of OPV device performance, a long L_D is beneficial for both efficiency and long term stability (in terms of phase separation issues). More details about exciton diffusion will be discussed in Chapter 3, 7, 8 and 9.

2.4 Charge Transport in Organic Semiconductors

The motion of charge carriers in organic semiconductors is of great importance for organic electronic devices. In OPVs, fast charge carrier transport to electrodes can minimize the energy losses to charge recombination. There are two types of charge transport mechanisms: band-like and hopping transport.[24] Band-like transport is most common in conventional inorganic semiconductor materials.[49] These crystalline materials are highly ordered and provide periodic electric potential well for electrons. This leads to the formation of broad electronic bands and small effective mass for electrons. Electrons are highly delocalized in this case and have very high mobility when traveling within thin the bands. Few organic semiconductors can show band-like transport. Among them, rubrene single-crystal holds the record for the highest field-effect mobility of organic semiconductors (15-40 $cm^2/V{\cdot}s$).[50] It is much higher than the carrier mobility of typical amorphous organic semiconductor films (~10^{-5} $cm^2/V{\cdot}s$).[51-53]

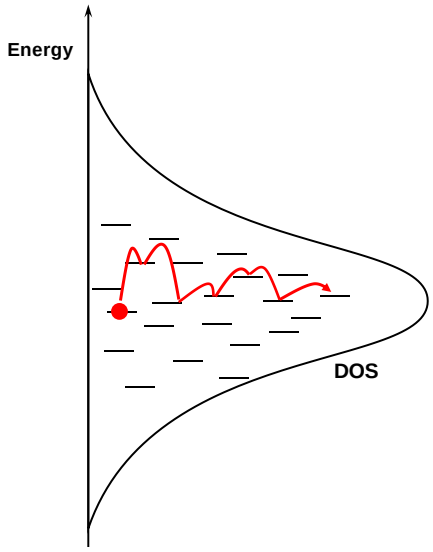

Figure 2.7 Electron hopping in disordered organic semiconductors via discrete energetic states.

As described before, most organic semiconductor thin films have weak van der Waals intermolecular interaction and are amorphous or polycrystalline in the solid phase.[54] Thus, their electrons can hardly move with band-like transport. Instead, electrons through hopping mechanism in disordered systems and result in relatively low charge carrier mobility. In this scenario, electron motion is slow compared to inter and intramolecular vibrations. The surrounding lattice has time to relax the Coulombic potential of the charges. This process reduces the overall energy of the states and makes the charge self-trapped. The charge and the polarized surrounding is called polaron. In organic semiconductors, hole and electron polarons travel in HOMO and LUMO, respectively. The rate of polaron hopping can be expressed as:[55]

$$k_h = \nu \exp(-2\gamma d)\begin{cases} exp(-\frac{-\Delta E}{k_B T}), & if\ \Delta E > 0 \\ 1, & if\ \Delta E < 0 \end{cases} \quad (2.11)$$

Here, ν is the attempt frequency, γ is the overlap factor, *d* is the distance between molecules and ΔE is the difference between polaron energies. The mobility μ of organic semiconductors depends on temperature and strength of the electric field. A variety of models have been proposed to describe this dependence. The thermally activated mobility can be expressed as:[56]

$$\mu(T) = \mu_\infty exp(-\frac{\Delta E_\mu}{k_B T}) \quad (2.12)$$

where μ_∞ is the infinite temperature mobility and ΔE_μ is the activation energy. For the field dependence, W. D. Gill describe mobility as:[57]

$$\mu(F,T) = \mu_\infty \exp\left(-\frac{E_0 - \beta\sqrt{F}}{k_B T_{eff}}\right)$$

$$\text{with } \frac{1}{T_{eff}} = \frac{1}{T} - \frac{1}{T_0} \quad (2.13)$$

where E_0 is the zero-field activation energy, β is prefactor related to the field-dependence, and T_0 is known as Gill temperature. For OPVs, charge transport properties of photoactive materials are very important which determine both charge recombination losses at heterojunction interfaces as well as in the bulk of films. More details about the role of charge transport in recombination will be introduced in Chapter 3 and 5.

3. Operation of Organic Photovoltaic Cells

3.1 Device Architectures and Operation

Early studies in organic photovoltaics can be traced back to 1950s.[20-21] These OPVs employed a sandwich structure where the organic light absorber is placed between two metal electrodes.[21, 58] Devices with this architecture are known as Schottky cells. As introduced in Chapter 2, OPVs are excitonic and can only generate charge carriers through dissociation of excitons. In Schottky cells, the device built-in electric field can hardly dissociate tightly bound excitons, leading to very low photocurrent and η_P <1 %.[59-62]

To achieve more efficient exciton dissociation, Tang reported the first organic donor-acceptor planar heterojunction (PHJ) device architecture, the foundation of modern efficient OPVs.[63] The PHJ architecture contains an electron donor layer and an electron acceptor layer between two conductive electrodes. The energy level offset at donor-acceptor (D-A) interface provides the driving force to separate excitons. At the D-A interface, excitons are dissociated into a more delocalized state called charge transfer (CT) states. CT state, also called CT exciton, exciplex and geminate pair, has a hole in the donor molecule and an electron on the acceptor molecule.[30] Despite the CT state being Coulombically bound, it is much easier to dissociate into free charge carriers with built-in electric fields compared to Frenkel excitons. Therefore, the PHJ structure is much more efficient in charge generation than single organic layer structures found in early OPVs.

Photoconversion in a PHJ OPV can be divided into four key steps, each with its own efficiency. As shown in Figure 3.1, the four component steps are photon absorption and

exciton generation (η_A), exciton diffusion (η_{Diff}), CT state separation (η_{CS}) and free charge carrier collection (η_{FC}). As described before, the incident photons first excite electrons from HOMO to LUMO and form excitons. Excitons diffuse within the organic photoactive layer. The excitons that reach the D-A interface can be dissociated into more delocalized CT states. Assisted with electric field and thermal energy, CT states can be separated and form mobile free polarons. The collection of these polarons at the metal electrodes generate electricity. The overall external quantum efficiency (η_{EQE}) is the product of four efficiencies mentioned above. It is defined as the ratio of collected electrons to incident photons. The device short-circuit current density (J_{SC}) can be derived as the integration of the η_{EQE} across the solar spectrum. Combined with two other critical device parameters, the fill factor (FF) and open-circuit voltage (V_{OC}), the power conversion efficiency (η_P) can be determined.

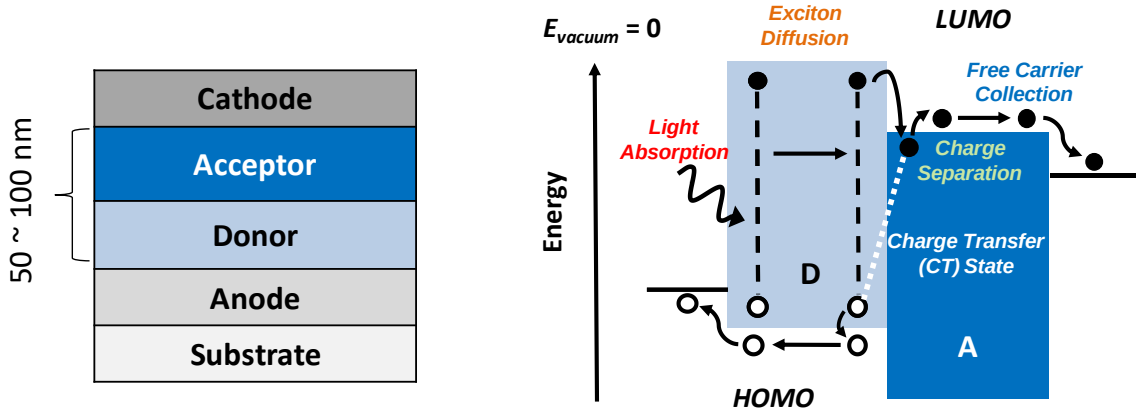

Figure 3.1 Device architecture photoconversion processes of a planar heterojunction (PHJ) OPV.

In the PHJ architecture, the exciton diffusion length (L_D ~10 nm) is much shorter than the typical optical absorption length (L_A ~50 nm), the distance where the intensity of

the beam has dropped to 1/e).[44] Only excitons generated within a distance ~L_D from D-A interface, where exciton dissociation takes place, can contribute to the photocurrent. Therefore, there is a trade-off between exciton harvesting and optical absorption, referred as the diffusion bottleneck, that limits the absorption-diffusion efficiency product thus limiting η_{EQE} and J_{SC}.[30] To address this challenge, several device architectures based on PHJ have been designed to improve exciton harvesting, including charge cascade cells, energy cascade cells and planar cells with exciton gates.[64-68]

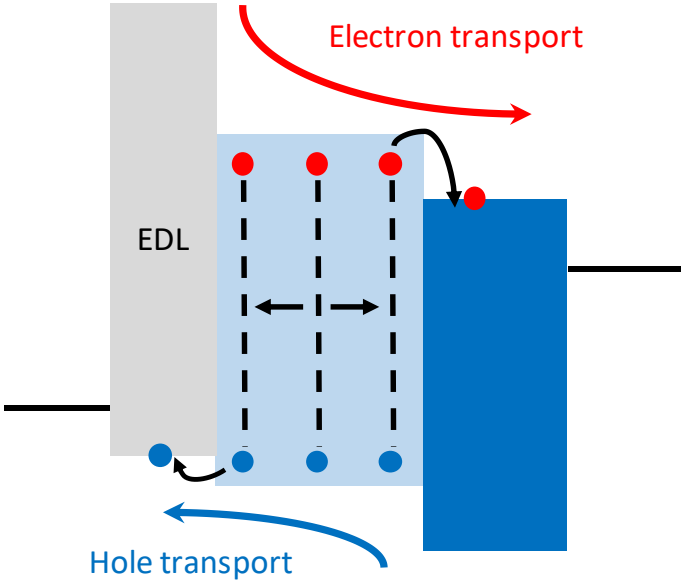

Figure 3.2 Schematic energy level diagram for a charge cascade OPV. The excitons generated in the middle layer can be efficiently dissociated at both the D-A interface and EDL-donor interface. Electrons (holes) can migrate toward anode (cathode) through LUMO (HOMO) with decreasing energy.

In a typical charge cascade cell, an exciton dissociation layer (EDL) is introduced between donor and anode. The EDL has a shallower HOMO level than the donor material, forming an exciton dissociating interface between EBL and donor layers. Therefore, donor

excitons generated near anode can be more efficient harvested. Previously, Barito et. al. demonstrated an improvement of 46% in device power conversion efficiency by using a transparent EDL TAPC in SubNc-C_{60} planar system.[65] As the donor material also serves as the electron acceptor for EDL, both electron and hole are traveling in the same layer. To avoid significant charge recombination loss and low FF, it is critical to use ambipolar middle layers with good charge transport properties for both electrons and holes.

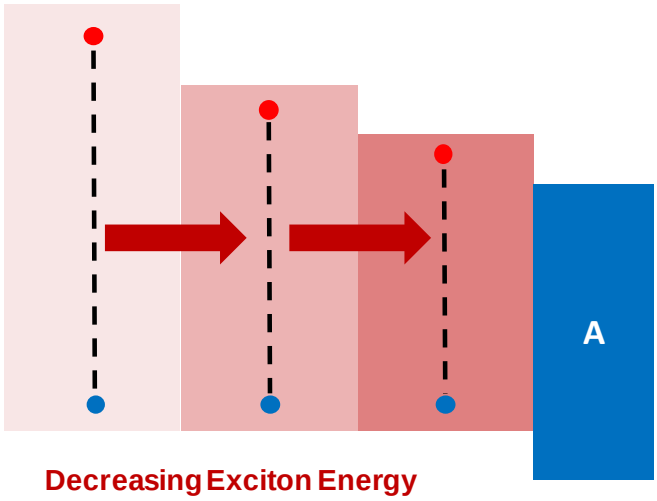

Figure 3.3 Schematic energy level diagram for an energy cascade OPV. The difference in excitonic energy drives efficient exciton transport towards dissociating interface.

Energy cascade cells and exciton gates are both designed to enhance exciton transport toward the D-A interface. Unlike charge cascade cells, these devices still have only one exciton dissociating interfaces. Energy cascade cells employ a multilayer donor design. As shown in Figure 3.3, these layers of the donor region are arranged in decreasing exciton energy order from the anode to the acceptor. The asymmetry in excitonic energy at interfaces driving exciton transfer from the anode side to the D-A interface while allowing

a broader light absorption. This design has demonstrated the record efficiency of 8.4% for planar OPVs. Similarly, exciton gating OPVs also utilize asymmetric energy transfer. Instead of using multiple photoactive materials in the donor region, exciton gating OPVs only have one donor material. Multiple donor layers with different concentration are stacked in donor region to create concentration asymmetry at their interface.[68-70] At their interfaces, there are more available exciton accepting sites in high concentration layer than the low concentration layer (Figure 3.4). This symmetry-breaking design drives excitons to move toward the higher concentration sides and realize a more efficient exciton harvesting in OPVs.

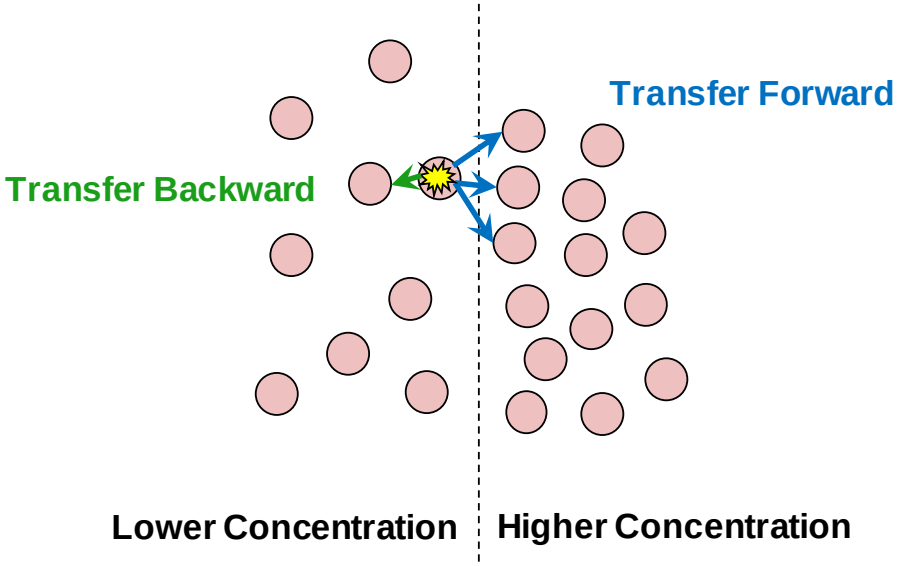

Figure 3.4 Asymmetry in available sites drives excitons to move towards the higher concentration side.

In most high-efficiency OPVs, the problem of the diffusion bottleneck is addressed by introducing another OPV architecture termed a bulk heterojunction (BHJ). In a BHJ, the donor and acceptor materials are blended to increase the interface area for exciton

dissociation.[71-73] As the excitons with limited L_D can be efficiently dissociated by the nearby D-A interface (Figure 3.5), the thickness of the mixed active layer can be much greater than L_D to achieve high absorption efficiency.

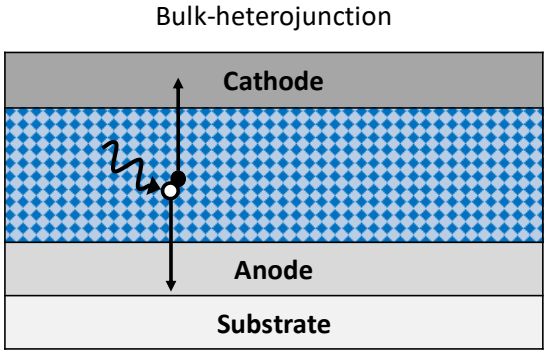

Figure 3.5 Device architecture of a bulk heterojunction (BHJ) OPV. The photogenerated excitons can be dissociated efficiently by the nearby D-A interface.

The BHJ OPVs often suffer from poor charge collection when the morphology of D-A mixture is not optimized. Electrons (or holes) can be trapped if they are generated in acceptor (or donor) islands. Thus, significant efforts have been paid to optimize film morphology of BHJ OPVs. A phase-separated BHJ is more desirable as it provides large D-A interface area and continuous charge transport pathways simultaneously. In addition, BHJ OPVs typically show a higher leakage current than PHJ OPVs. Charge carriers can leak from an electrode to the other through continuous donor or acceptor materials within the mixed films. To realize a better current rectification of the junction, a planar-mixed heterojunction (PMHJ) device architecture has been developed, in which a neat donor (acceptor) layer is inserted between D-A mixture and anode (cathode). As a result, holes and electrons are only collected at anode and cathode, respectively.

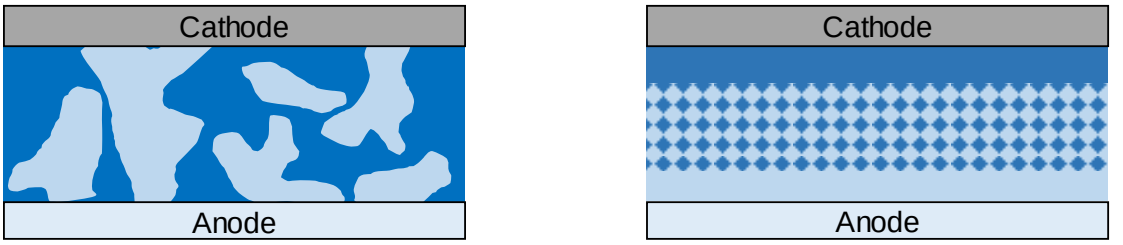

Figure 3.6 Device architecture of a phase-separated BHJ and PMHJ.

For OPVs showing record efficiency, they often adopted a tandem device architecture. Tandem OPVs consist of two or more sub-cells stacked together for complementary absorption. The most common tandem cell structure is based on a two-terminal monolithic geometry (Figure 3.7), in which sub-cells are connected together by a charge recombination zone (CRZ).[74] The electrons from one side sub-cell and holes from the opposite side sub-cell can recombine in the CRZ, hence the current is continuous throughout all sub-cells and the voltage is the sum of all sub-cells voltages.[74] Consequently, tandem OPVs can achieve high V_{OC}. Different from inorganic tandem cells, tandem OPVs have donor and acceptor materials in each heterojunction sub-cell. Therefore, tandem OPVs may consist of at least four active materials for improved spectral coverage, which can largely reduce the spectrum loss from sub-band photons and excess energy compared to the band gap of active materials.[74]

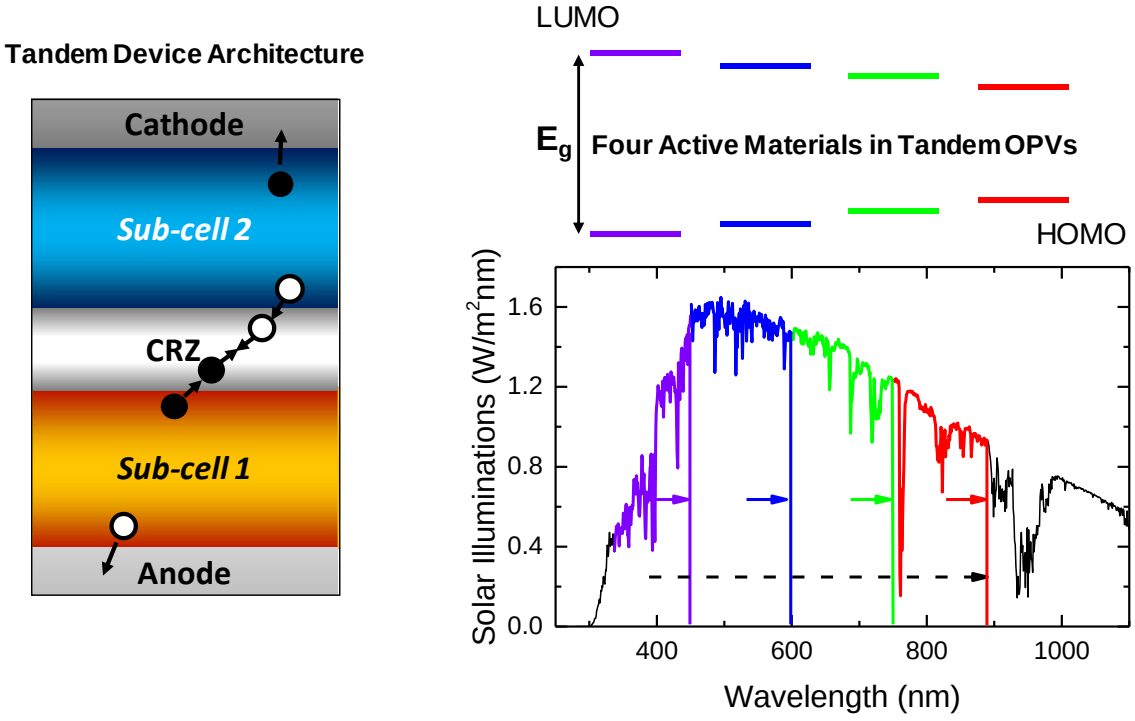

Figure 3.7 Device architecture of a two-junction tandem cell. The subcells are connected with a charge recombination zone (CRZ). The four active materials with different energy gap E_g can significantly reduce thermalization energy loss for hot electron excited upon light absorption.

3.2 Energy Loss Pathways

Despite the high efficiencies >15% reported recently, most efficient lab-scale OPVs still show power conversion efficiency ~10%, hindering widely commercialization of this technology.[75-77] Unlike inorganic PVs which can directly generate mobile charge carriers upon photoexcitation, excitonic OPVs require a photon-exciton-polaron multistep conversion in order to generate electricity.[30] Due to this multistep nature of photoconversion in OPVs, there are more opportunities for parasitic energy loss compared

to the inorganic counterparts.[78-80]

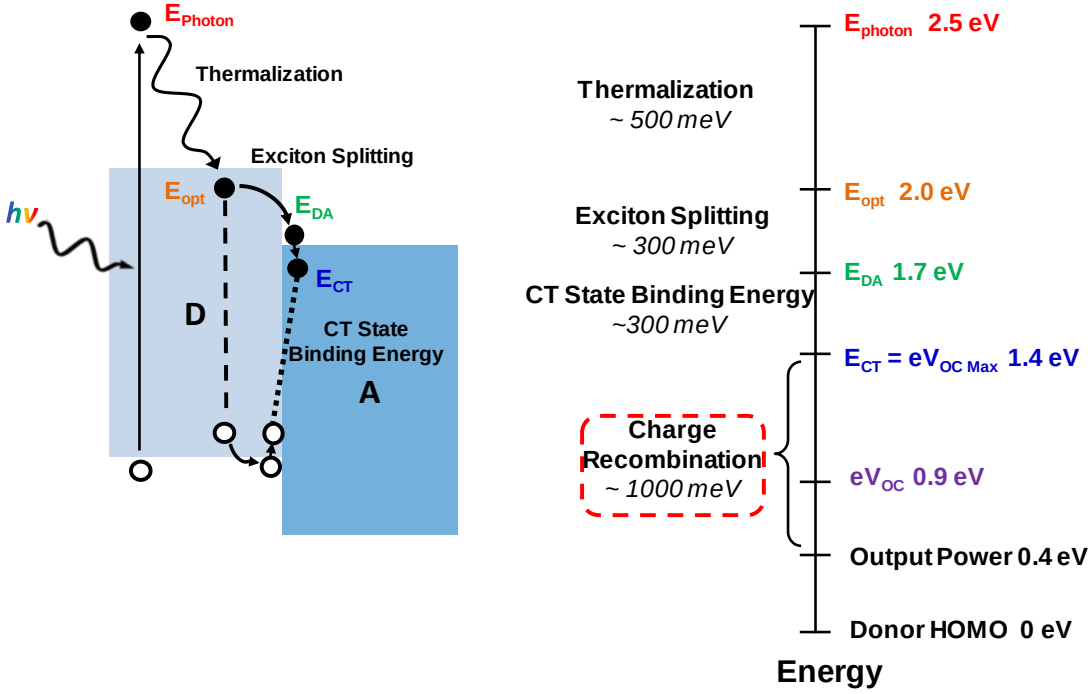

Figure 3.8 The pathways of energy losses in OPVs and various energy levels in the device to which they correspond.[78] Charge recombination serves as the major source of inefficiency for the current state-of-the-art device.

As an example shown in Figure 3.8, a photon with an energy of 2.5 eV is absorbed by the donor and excite an electron from the HOMO to a high energy molecular level. The resulting hot electron rapidly relaxes to the LUMO and form an exciton, keeping the energy of the optical gap. Thus, there is energy loss to the thermalization process. Excited states only keep optical gap energy regardless of the excitation photon energy. This type of loss also takes place in inorganic PVs and cast theoretical efficiency limit to single-junction solar cells (Shockley-Queisser limit).[74] At D-A interfaces, energy loss takes place for dissociation of excitons and overcoming the Coulombic binding energy of CT states. The

loss is typical ~300 meV for each of these two processes. CT state is the lowest energy state in the photoconversion process.[78] Its energy, the CT state energy (E_{CT}), defines the theoretical upper limit for device open-circuit voltage V_{OC} (maximum energy for each collected electron). At room temperature, V_{OC} is limited by rapid electron-hole recombination can cause energy losses during CT state separation (geminate) and free charge carrier collection (non-geminate) processes.[79, 81-86] Geminate and non-geminate charge recombination can both convert solar radiation into heat rather than usable electricity. They limit both output current and voltage and thus limiting the output power conversion efficiency.

For current state-of-the-art OPVs, charge recombination is the major source of inefficiency.[87] Therefore, suppression of both geminate and non-geminate recombination loss is critical to further increase device efficiency. Geminate recombination (CT state loss) is a first-order recombination process.[88-89] This means the number of CT states (often called geminate pairs) recombined scales linearly with the number of photons absorbed. Thus the fraction of CT state loss is the same under very weak illumination as under one sun condition. However, at very high light intensity, other recombination processes like exciton-exciton and exciton-polaron quenching can be significant.[86] During the CT State separation process at the D-A interface, CT states may decay to ground state or transfer to available triplet states of donor or acceptor materials. The separation of CT states has been observed to be electric field dependent. The CT state separation rate is typically described using the Onsager-Braun formulism:[90-92]

$$k_{CS} = \frac{3e\langle\mu\rangle}{4\pi r^3\langle\varepsilon\rangle\varepsilon_0} \times exp\left(\frac{-E_B}{k_B T}\right) \times \frac{J_1\left(2\sqrt{-2b}\right)}{\sqrt{-2b}} \qquad (3.1)$$

$$with\ E_B = \frac{e^2}{4\pi\langle\varepsilon\rangle\varepsilon_0 r}\ , b = \frac{e^3 E}{8\pi\langle\varepsilon\rangle\varepsilon_0 (k_B T)^2}$$

where k_{CS} is the separation rate, $\langle\mu\rangle$ and $\langle\varepsilon\rangle$ are the effective charge carrier mobility and dielectric constant across the D-A interface, respectively, E_B is the binding energy of CT states, J_1 is the first-order Bessel function, E is the electric field, r is the size of the CT states. To minimize geminate recombination losses, k_{CS} must be much greater than other decay rates of CT states.

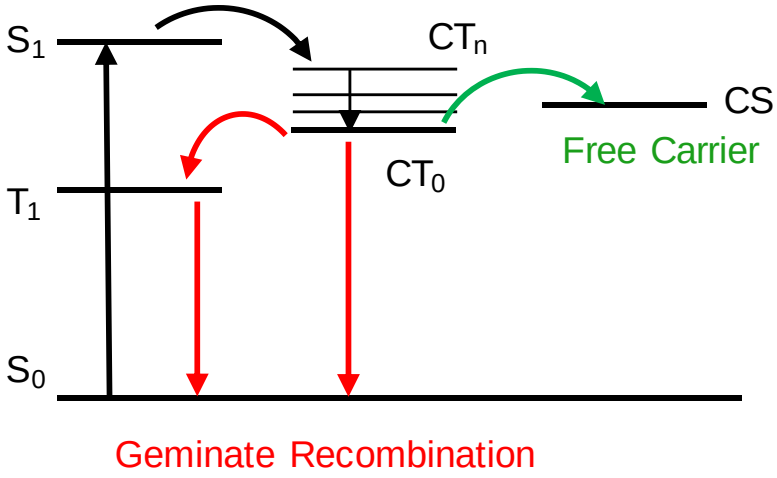

Figure 3.9 Energy diagram for the charge separation process. The singlet exciton (S_1) is dissociated into a CT state, which will rapidly thermalize to the relaxed CT state (CT_0). If failed to separate, the CT_0 may recombine or transfer to a local triplet state (T_1). The local triplet state serves as an energetic trap and will eventually recombine to ground state.

Once CT states are separated, generated free charge carriers need to drift to electrodes before non-geminate recombination takes place. There are several non-geminate recombination mechanisms, including bimolecular recombination, trap-assisted

recombination, and Auger recombination.

Bimolecular recombination is the most common carrier recombination mechanism in OPVs. In the disordered organic semiconductor systems, charges are highly localized.[49] Bimolecular recombination is limited by the rate at which carriers find each other.[81-82] Thus, the faster charge carriers move, the faster they catch each other and recombine. The bimolecular recombination rate is often described by the Langevin expression:[86]

$$R_L = \frac{q}{\varepsilon\varepsilon_0}(\mu_n + \mu_p)(np - {n_i}^2) \quad (3.2)$$

where μ_n and μ_p are mobilities of electrons and holes respectively, n_i is the intrinsic charge carrier concentration. Despite being applied to several organic semiconductors, Langevin recombination often overestimates the recombination rate in OPVs. As such, another prefactor is typically added to the above equation in order to describe the reduced Langevin type recombination.

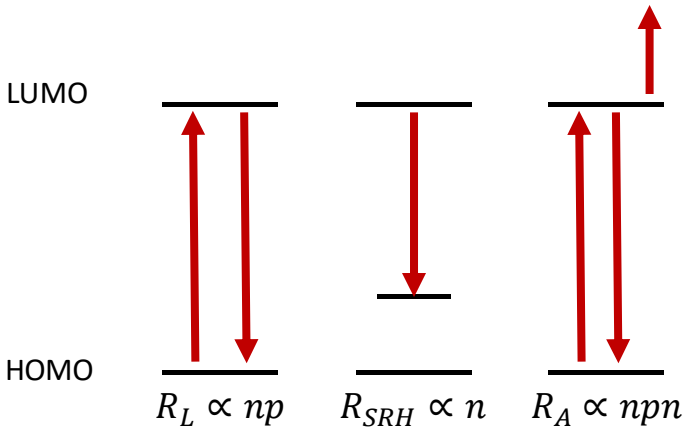

Figure 3.10 Three nongeminate recombination mechanisms including bimolecular Langevin recombination, trap-assisted Shockley–Read–Hall recombination and Auger recombination.

Trap-assisted recombination is a process in which one electron and one hole recombine with the assist of localized energetic traps. One of the charge carriers is trapped first and recombines with the opposing charge carrier when they meet. As a result, the rate of trap-assisted recombination is determined by trap concentration and how fast the charge carriers move. It is also known as Shockley–Read–Hall (SRH) recombination with recombination rate:[93-94]

$$R_{SRH} = \frac{C_n C_p N_{tr}(np - {n_i}^2)}{\left[C_n(n + n_1)C_p(p - p_1)\right]} \qquad (3.3)$$

Here, C_n and C_p denote the probability per unit time that an electron in the LUMO and a hole in the HOMO will be captured by empty traps, N_{tr} is the trap density, n_1 and p_1 are the electron and hole densities when the quasi-Fermi level matches the trapped energy. Auger recombination is a three-particle process. The energy from recombination of an electron in the LUMO and a hole in the HOMO is transferred to the third electron and excites it to a higher energy state. This mechanism requires high charge carrier density, thus barely observed in OPV systems.[95-96] For the state-of-the-art OPV systems, bimolecular recombination is the primary mechanism for non-geminate recombination. Therefore, non-geminate recombination is often a second-order process and cause significant energy losses in OPVs under forward bias.

3.3 Device Fabrication and Characterization

High-performance OPVs require pinhole-free thin films and well-defined film interfaces. There are two common fabrication methods for OPVs, solution processing and

vapor deposition. They are suitable for different types of organic materials. Organic molecules with relatively high molecular weight, such as polymer materials, solution processing are a better option as they are too heavy to sublime in vacuum chamber. To realize high-throughput roll-to-roll manufacturing, continuous efforts have been paid to developing various printing technology, such as blade coating and inkjet printing. Currently, spin-coating is still the most common solution processing technique for lab-scale fabrication. As compared to other printing technologies, spin-coating only required very small amount of active materials for depositing uniform thin films across the substrates. During the spin-coating process, the solution of organic materials is first dropped on the substrates. Then the substrate is spun at 500-5000 rpm until the films are fully dried and solidified. Typically, polymer materials are designed to have long alky side chains in order to optimize solution viscosity for better film deposition.[97-98]

Vapor deposition is another commonly used processing technique for OPVs. This technique is suitable for organic small molecules. During this process, organic powders are heated (to several hundred degrees Celsius) in a high vacuum chamber with a pressure < 10^{-6} Torr. The heated small molecules will have a phase transition from solid to vapor. As they are under high vacuum condition, the sublimed small molecules have very long mean free paths as compared to the distance between source boat and substrates. Therefore, they move ballistically as they have a very low probability of colliding with other molecules before reaching the substrates or chamber walls. In this dissertation, most studied OPV systems are based on small molecules. As a result, vacuum vapor deposition is chosen as the major fabrication technique. The vacuum chamber is shown in Figure 3.11. A liquid

helium based cryogenic pump is used to maintain high vacuum. The deposition rate is monitored with quartz crystal microbalances (QCM) located near the source boat. The substrate holder is rotating for better film uniformity during the deposition.

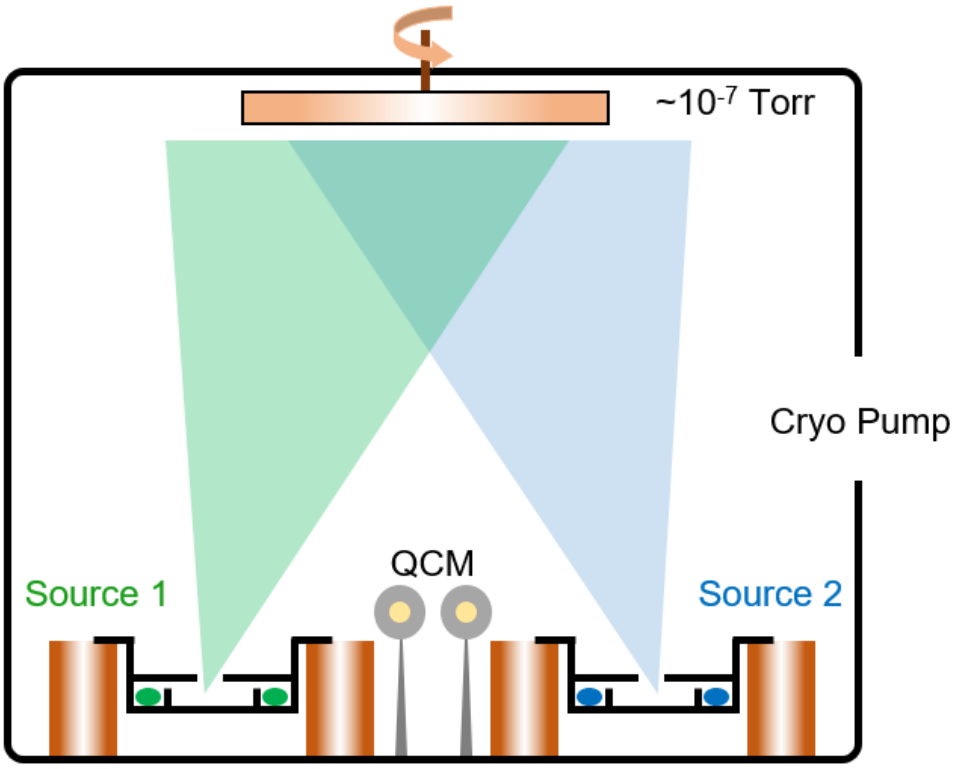

Figure 3.11 Vacuum vapor deposition system with two sources depositing at the same time. The deposition rate is monitored with quartz crystal microbalances (QCM) located near the source boat.

Once the organic devices are fabricated with techniques described above, optical and electrical characterizations are needed to evaluate their performance. For OPVs, the most important characterization is current density-voltage (J-V) characteristics as it yields the power conversion efficiency η_P. Figure 3.12 shows typical J-V characteristics of an OPV tested under AM 1.5G simulated solar illumination (100 mW/cm^2) at 25 ºC. The short-

circuit current (J_{SC}), open-circuit voltage (V_{OC}) and fill factor (FF) determined the η_P:

$$\eta_P = \frac{J_{SC}V_{OC}FF}{P_{optical}} \quad with\ FF = \frac{(JV)_{max}}{J_{SC}V_{OC}} \qquad (3.4)$$

The FF is determined as the ratio of the maximum output power from the cell to the product of J_{SC} and V_{OC}. As discussed previously, the V_{OC} is determined by energy losses during photoconversion for each collected charge carriers and J_{SC} is determined by external quantum efficiency under the same illumination.

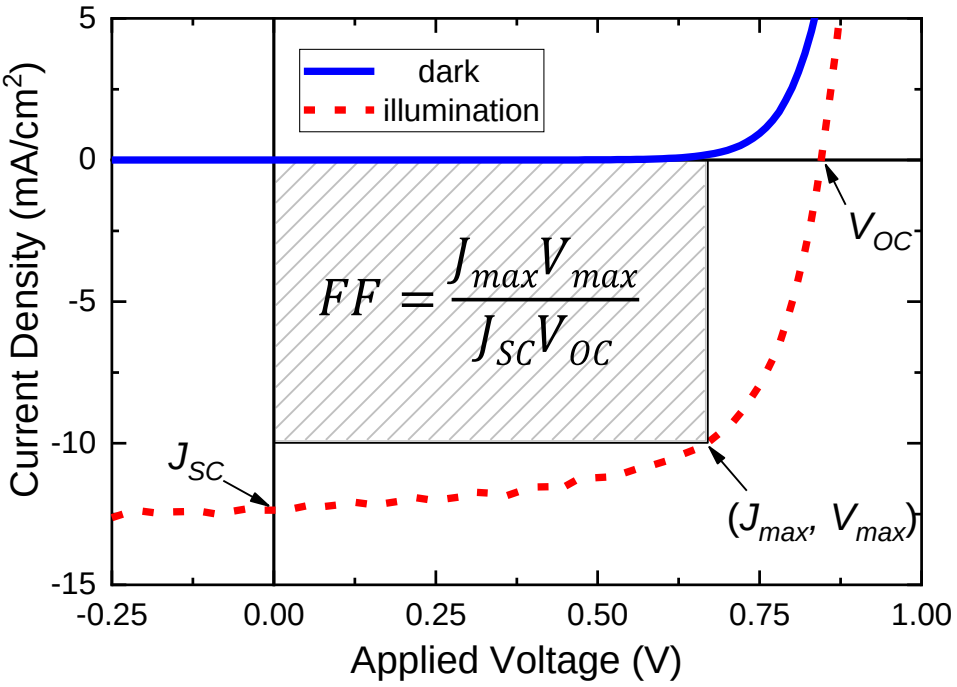

Figure 3.12 Current density-voltage (J-V) characteristics of an OPV in the dark (blue) and under illumination (red dash).

The η_{EQE} is defined as the percentage of incident photons that are converted into charge carriers reaching the electrodes. Experimentally, the OPV is illuminated with

monochromatic light. A chopper wheel is often utilized for incident light and the photocurrent is measured using a lock-in technique which isolates photocurrent signals at chopper wheel frequency. The J_{SC} can be calculated with the solar spectrum and η_{EQE}:

$$J_{SC} = \frac{q}{hc}\int \lambda \eta_{EQE} S_\lambda d\lambda \qquad (3.5)$$

where h is Planck's constant and S_λ is the solar spectrum (e.g. AM 1.5G).

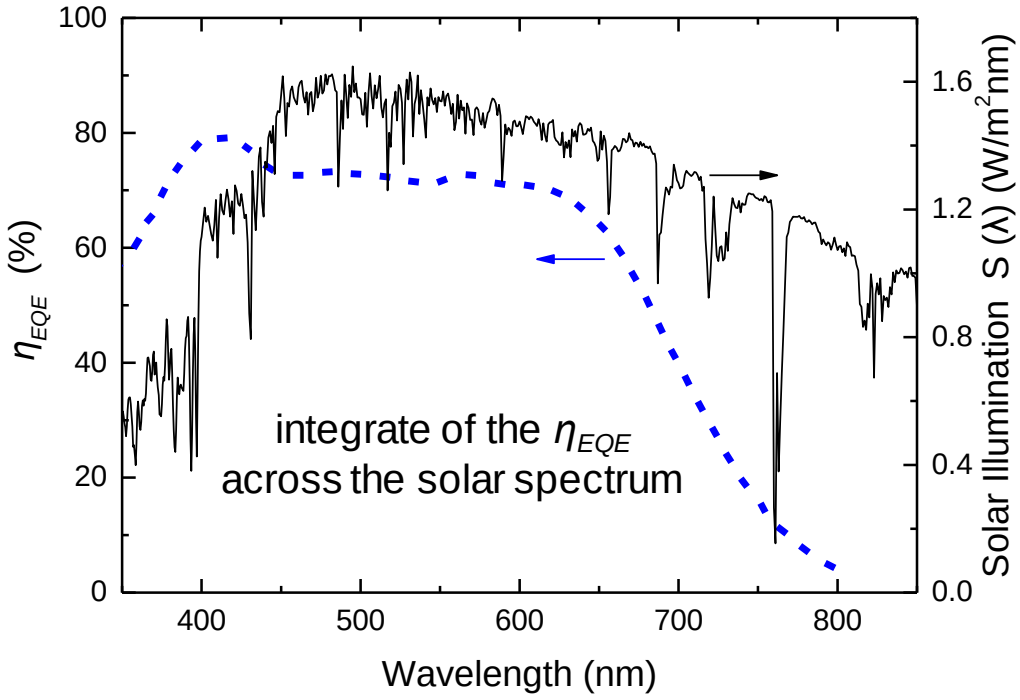

Figure 3.13 Plot of the AM 1.5G solar spectrum and a reprehensive η_{EQE} spectrum.

Although this measurement typically performed at short-circuit, it is worth noting that η_{EQE} measured under reverse bias provide useful information of charge recombination losses in BHJ OPVs. The η_{EQE} is the product of four component efficiencies for light

absorption, exciton diffusion, CT state separation, and free carrier collections:

$$\eta_{EQE} = \eta_A \eta_D \eta_{CS} \eta_{FC} = \eta_A \eta_D \eta_{CC} \quad (3.6)$$

where η_{CC} is overall charge collection efficiency for both interfacial and bulk charges. For BHJ OPVs, the η_D can be approximated as unity, thus η_{CC} can be approximated as:[99-100]

$$\eta_{CC} = \eta_{CS} \eta_{FC} \approx \frac{\eta_{EQE}}{\eta_A} \quad (3.7)$$

The charge recombination losses are strongly dependent on the bias. When the device is held at a large reverse-bias voltage, CT states will be quickly separated into mobile polarons and extracted out of the organic active layer before geminate and non-geminate recombination. As a result, the η_{CC} will approach unity, leading to a saturation of η_{EQE} at reverse bias. This saturation value can be approximated as the η_A, which allows the η_{CC} to be derived.

3.4 Device Modeling

Unlike conventional silicon-based solar cells with thickness greater than the visible light wavelength, OPVs are based on much thinner films and have overall thickness ~100 nm between the transparent anode and the reflective metal cathode. In this case, the optical energy dissipation within OPVs cannot be described by Beer's law due to the interference of incident light and reflected light.

The most commonly used method to simulate the optical field in an OPV is the transfer matrix model developed by Pettersson et al.[48] For isotropic and homogeneous thin films with sharp parallel interfaces, this model uses 2×1 matrices to describe the steady-

state incident and reflected optical field as a function of position in the device. A series of 2×2 matrices are utilized to describe the propagation of the optical field at interfaces or bulk of thin films. These 2×2 matrices are built upon the optical constants (refractive index and extinction coefficient) of each layer. The total system transfer matrix S, which relates the optical field at the two boundaries by:

$$\begin{bmatrix} E_0^+ \\ E_0^- \end{bmatrix} = S \begin{bmatrix} E_{m+1}^+ \\ E_{m+1}^- \end{bmatrix} \quad (3.8)$$

where m is the total number of layers between two semi-infinite medium. The superscript and subscript denote the direction of light propagation and the index of the layer, respectively.

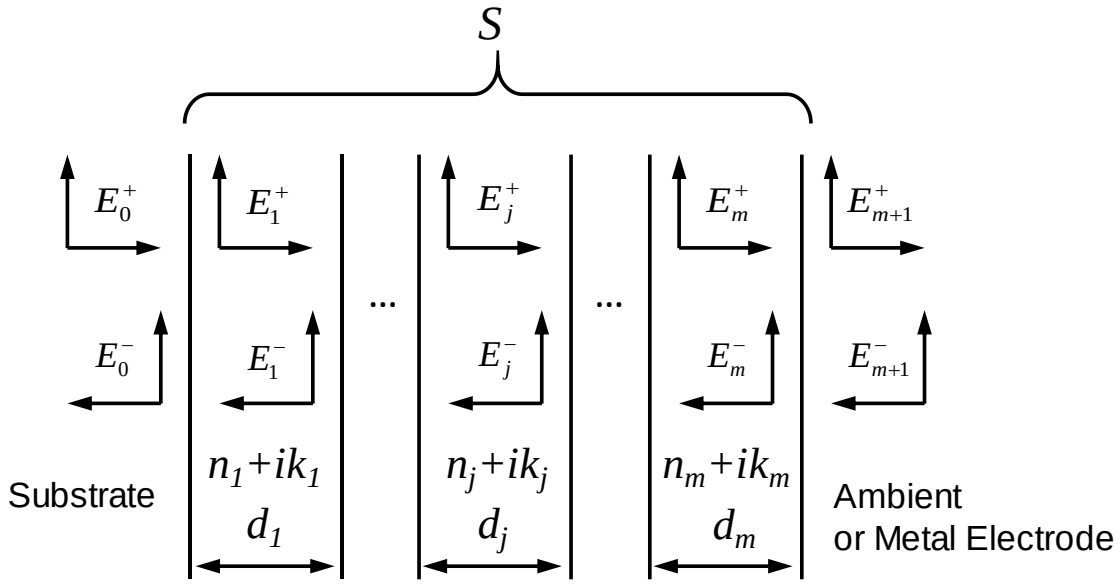

Figure 3.14 A multi-layer structure with m layers between semi-infinite medium.

With the optical field profile, the energy dissipation rate Q in layer j due to light absorption can be determined as:

$$Q(x) = \frac{1}{2} c\varepsilon_0 \alpha_j n_j \left| E_j^+(x) + E_j^-(x) \right|^2 \quad (3.9)$$

Here, α_j is the absorption coefficient of layer j. This energy dissipation within photoactive layers results in the generation of molecular excitons, which can only generate charges if they are close enough to D-A interface (within distance ~L_D). Therefore, the transfer matrix model is a useful tool to optimize device architecture for maximizing η_A and J_{SC}.

In addition to optical modeling, electrical modeling is also of great importance for OPVs, especially for charge recombination and V_{OC}. The Shockley model, initially developed for inorganic systems, is one of the most widely adopted approaches to simulate the electrical operation of OPVs. The current density and voltage of an OPV can be correlated with the Shockley equation:[101]

$$J = \frac{R_{Sh}}{R_{Sh} + R_S} \left\{ J_S \left[exp\left(\frac{q(V - JR_S)}{nk_BT} \right) - 1 \right] + \frac{V}{R_S} - J_{Photo} \right\} \quad (3.10)$$

Here, R_{Sh} and R_S are shunt and series resistance respectively, n is the ideality factor, J is the total current density, J_S is the reverse saturation current density, and J_{Photo} is the photocurrent density (the flux of generated free carriers at the D-A interface). For a good device with low R_S and large R_{Sh}, the V_{OC} can be expressed as:

$$V_{OC} \approx \frac{nk_BT}{q} \ln\left(\frac{J_{Photo}(V_{OC})}{J_S} \right) \quad with\, J_S = J_0 \ln\left(\frac{-E_{eff}}{nk_BT} \right) \quad (3.10)$$

The reverse saturation current density J_0 is thermally activated and related the effective energy gap E_{eff} at the D-A interface. Thus, the V_{OC} can be rewritten as:[102]

$$qV_{OC} \approx E_{eff} - nk_BT \ln\left(\frac{J_0}{J_{Photo}(V_{OC})} \right) \quad (3.11)$$

It is obvious that the E_{eff} serves as the upper limit for V_{OC}. For OPVs, this effective energy gap can be approximated as the CT state energy. As such, controlling the physical properties of CT states is critical to reducing voltage and energy losses in OPVs.

4. Quantify Charge Recombination Losses using Photovoltage

4.1 Background

As introduced in Chapter 3, during photoconversion, intermolecular charge transfer (CT) states form when excitons are dissociated at a donor-acceptor (D-A) interface. These CT states may either dissociate into free charge carriers (mobile polarons) or, recombine (geminate recombination). If the CT state is dissociated, the generated charge carriers must be collected at the electrodes prior to recombination with another free carrier (non-geminate recombination).[86] Previous work has shown that both geminate and non-geminate recombination are voltage dependent and can limit the illuminated current under forward bias, thereby limiting the short-circuit current (I_{SC}), open-circuit voltage (V_{OC}) and fill factor (FF).[81-82, 85, 103] It is therefore critical to develop a deeper and quantitative understanding of how various recombination mechanisms dominate device performance in order to better guide activities in materials and device engineering.[86]

Figure 4.1a shows the component processes of photoconversion in OPV. These processes can be quantified as current using:

$$I_{Max} - I_{GR} - I_{NGR} = I_{Gen} - I_{NGR} = I_{Illum} \quad (4.1)$$

In Equation 4.1, I_{Max} is the maximum achievable current in the absence of all charge recombination, determined by the generation rate and the efficiency of exciton dissociation at the D-A interface. I_{GR} and I_{NGR} are current losses due to geminate and non-geminate recombination, respectively. On the right of Equation 4.1, I_{Illum} is the final collected current at electrodes, experimentally measured from device current-voltage (I-V) characteristics

under illumination. Charge collection can thus be separated into two component processes, the separation of CT states and the collection of free charges, with an efficiency:

$$\eta_{CC} = \eta_{CS}\eta_{FC} = \left(\frac{I_{Gen}}{I_{Max}}\right)\left(\frac{I_{Illum}}{I_{Gen}}\right) = \left(\frac{I_{Illum}}{I_{Max}}\right) \quad (4.2)$$

In Equation 4.2, η_{CC} is overall charge collection efficiency, the ratio of collected free charges to generated CT states. The component efficiencies, charge separation efficiency (η_{CS}) and free charge collection efficiency (η_{FC}), are the ratio of I_{Gen} to I_{Max} and I_{Illum} to I_{Gen}, respectively (Figure 4.1b). Thus, geminate and non-geminate losses can be quantitatively examined with knowledge of η_{CS} and η_{FC}.

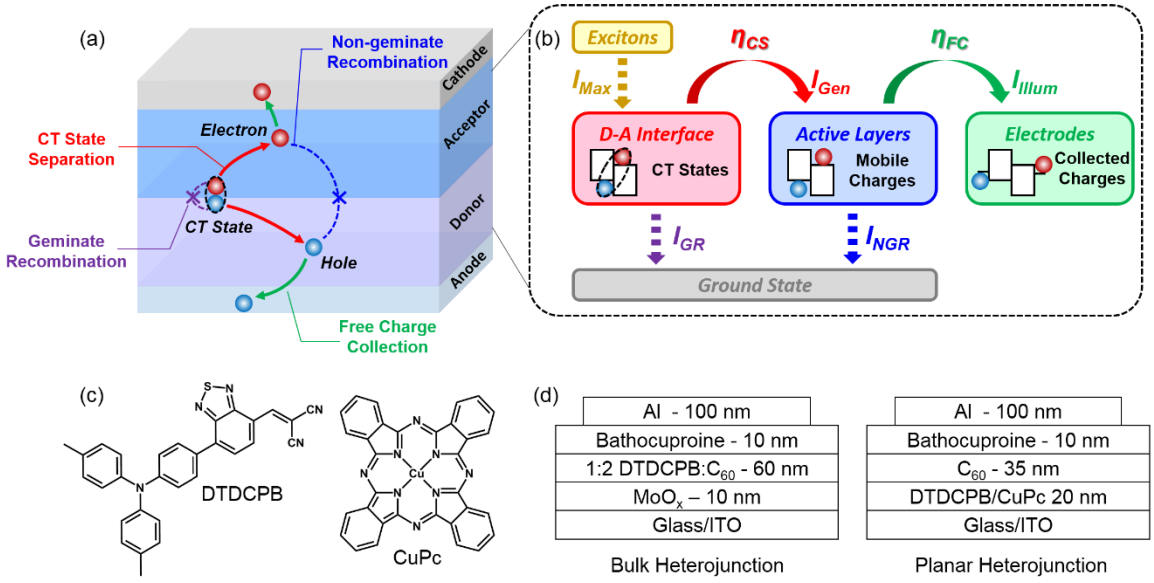

Figure 4.1 (a) Geminate recombination (GR),charge transfer (CT) state separation (free charge generation), non-geminate recombination (NGR) and free charge collection processes in a donor-acceptor OPV during photoconversion. (b) The currents that represent the component processes of photoconversion discussed in the text. (c) Molecular structures of DTDCPB and CuPc. (d) Device architectures of interest in this work.

Previously, a variety of approaches have been used to measure I_{Max} in order to deduce

the overall charge carrier recombination loss from the difference between I_{Max} and I_{Illum} (I-V characteristics).[44, 48, 100, 104] Nonetheless, experimentally determining the efficiency of CT state dissociation remains an area of active research as it is crucial for decoupling geminate and non-geminate recombination.[85, 105-106] The I_{Gen} in an OPV is typically extracted as the 'photocurrent', which is the difference between the illuminated current and the dark current. This simple calculation assumes that the current to non-geminate recombination under illumination is the same as it is in the dark.[84, 107] This assumption is however not necessarily true as previous work has shown that non-geminate recombination can be light intensity dependent.[108] Other techniques have sought to measure the voltage dependent I_{Gen}, including transient absorption spectroscopy (TAS) and time delayed collection field (TDCF) measurements.[85, 105-106] However, these techniques require the use of a high power laser rather than a solar simulated light source. It therefore can be challenging to translate results into a value of the current comparable to solar simulated I-V characteristics.[83, 85, 105, 109] This complicates the extraction of I_{Gen}, a decoupling that is essential for deeper examinations of charge carrier recombination in OPVs.

In this chapter, a photovoltage-based technique is used to directly measure I_{Gen}. In this measurement, an OPV is held at open-circuit so that non-geminate recombination within the device is the only pathway for consuming free charge carriers. In the most general version of this technique, the OPV is initially under steady-state illumination leading to a corresponding open-circuit voltage (V_0). At a later time t_0, the light intensity is increased and the resulting transient photovoltage (TPV) rise is recorded (a typical TPV trace is shown in Figure 4.2a). The TPV rise can be quantitatively translated into an increase in the

number of charge carriers (n) in the device when a general relationship between the open-circuit voltage and carrier number is separately known. Here, charge extraction (CE) methods are used to experimentally determine this relationship. With knowledge of the number of charge carriers stored in the device as a function of time, the charge accumulation rate can be estimated from the slope of carrier number rise. For the region very close to t_0, free carrier recombination losses are negligible when the timescale is much shorter than the free carrier lifetime (τ).[110] Thus a linear increase in charge carrier number will be observed and the I_{Gen} at V_0 can be readily extracted from the accumulation rate of charge carriers. The background illumination can be varied in order to vary V_0 and extract I_{Gen} as a function of open-circuit voltage. As open-circuit and actual operating condition can correspond to a different number of carriers in the device at a given voltage, a second CE measurement is carried out to determine the relationship between operating voltage (V_{OP}) and n, which allows V_0 to be converted to V_{OP}.[111] Comparing the extracted I_{Gen} (V_{OP}) with commonly measured current-voltage (I-V) characteristics, the illuminated current losses to both geminate and non-geminate recombination are able to be quantified as a function of voltage. As TPV is often used to determine charge carrier lifetimes and voltage dependence of non-geminate recombination, the I_{NGR} is also able to be measured directly to check the validity of this technique.

4.2 Charge Recombination Losses in DTDCPB-C_{60} BHJ OPVs

4.2.1 Transient Photovoltage and Charge Extraction

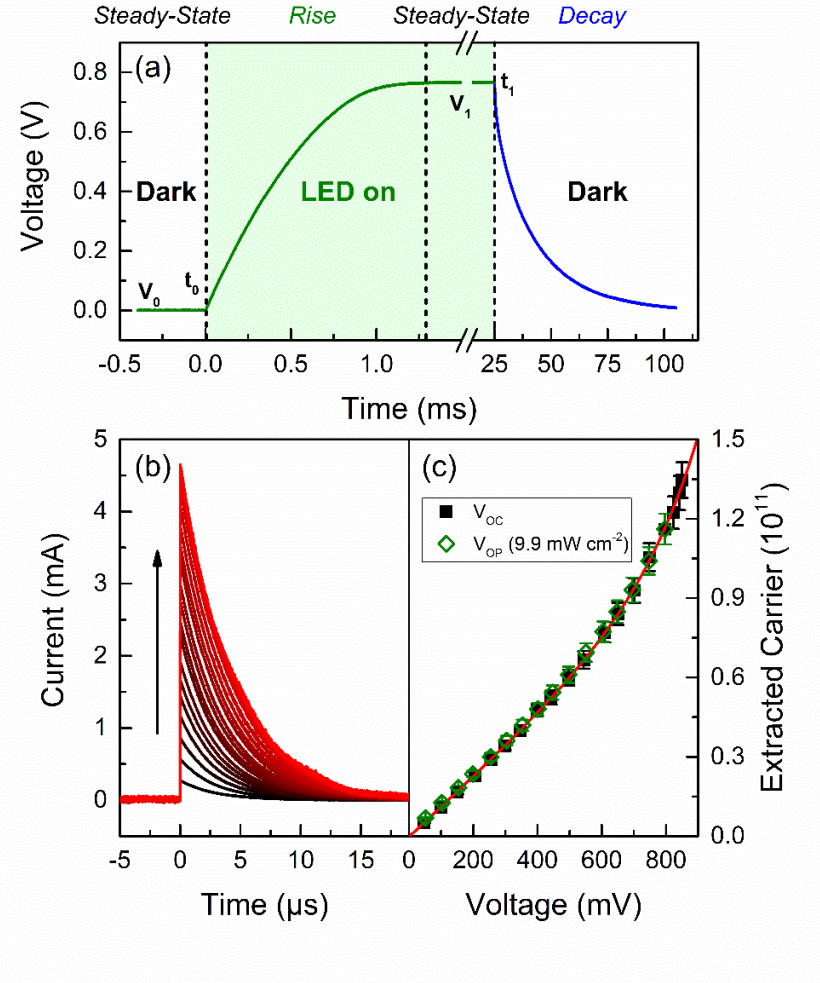

Figure 4.2 (a) The photovoltage rise and decay of DTDCPB-C_{60} BHJ in Figure 4.1d caused by the green LED illumination (9.9 mW cm^{-2}) turned on from t = 0 ms to 25 ms in the absence of background illumination. (b) Current transients obtained by switching the device in (a) from steady state open-circuit to short-circuit. The steady state voltage is varied from 47.0 mV to 851.0 mV. (c) The number of extracted carriers as a function of open-circuit voltage (V_{OC}) and operating voltage (V_{OP}) derived by integrating current transients with respect to time. The solid red line is the sum of linear fit for data up to 300 mV and an exponential fit.

To demonstrate the photovoltage-based technique, the illuminated current losses from

geminate and non-geminate recombination are first quantified for a small molecule BHJ OPV based on the high efficiency D-A pairing of 2-((7-(4-N,N-ditolylaminophenylen-1-yl)benzo[c][1,2,5] thiadiazol-4-yl)methylene)malononitrile (DTDCPB)-C_{60}.[112-114] Two planar heterojunction (PHJ) OPVs based on the D-A pairings of DTDCPB-C_{60} and copper phthalocyanine (CuPc)-C_{60} are also examined. Figure 4.1c,d shows the electron donors and device architectures of interest for this study.

Figure 4.2a shows a representative TPV response of DTDCPB-C_{60} BHJ OPVs under illumination by a green light-emitting diode (LED) (λ_{peak} = 530 nm, intensity: 9.9 mW cm^{-2}) turned on at $t = t_0$ (0 μs) and turned off at $t = t_1$ (25 ms). Prior to t_0, the voltage (V_0) is constant as steady-state is reached with no background illumination. Under illumination, the photovoltage increases with a decreasing slope until a new steady-state voltage (V_1) is reached. Only the first few microseconds of the TPV rise are used for the extraction of I_{Gen} in order to avoid potential non-geminate losses, consistent with previous work.[110]

To translate photovoltage transients into a measure of charge carrier accumulation, CE methods are used to connect photovoltage and the number of charge carriers stored within the device. In the CE measurement, OPVs are first illuminated at open-circuit to reach steady-state. This is followed by rapid switching of the device to short-circuit, with the resulting current transient recorded. Figure 4.2b shows the current transients (from starting voltages ranging from 47.0 mV to 851.0 mV) recorded for the DTDCPB-C_{60} BHJ in Figure 4.1d. The number of stored charge carriers is the integral of each current transient, and plotted versus the initial steady-state V_{OC} (Figure 4.2c). Although non-geminate recombination may take place during the CE experiment and lead to an underestimate in

the number of carriers present in the device, the much shorter time required to complete the CE versus the photovoltage decay at open-circuit suggests that only a negligible fraction of carriers recombine within the device rather than through the outside circuit.

4.2.2 Free Carrier Generation and Recombination Rates

By translating TPV into charge carriers, carrier number as a function of time can be plotted. Figure 4.3a shows four representative plots of carrier number versus time for the DTDCPB-C_{60} BHJ in Figure 4.1d. A second blue LED (λ_{peak} = 455 nm) provides background illumination and is used to vary the steady-state carrier number n_0. As the green LED illumination is mostly absorbed by DTDCPB, a blue LED (mostly absorbed by C_{60}) is chosen to avoid a significant change in exciton generation for the donor. The value of initial steady-state carrier number (n_0) is taken as the average value before t = 0 μs (n_0 = $5.32\cdot10^9$, $1.14\cdot10^{10}$, $1.60\cdot10^{10}$, $2.26\cdot10^{10}$ in Figure 4.3a). For a very short time after t_0, the increase in n is not significant, it is therefore assumed that the changes in carrier generation rates and carrier lifetime are not significant. The accumulation rate ($\frac{dn}{dt}$) after t_0 is then given as:

$$\frac{dn}{dt} = (G_{BG} + G) - \left(R + \frac{n - n_0}{\tau}\right) = G - \frac{n - n_0}{\tau} \qquad \text{with } R = \frac{n_0}{\tau} \quad (4.3)$$

In Equation 4.3, G_{BG} and R are carrier generation rate (background light) and recombination rate before t_0, respectively. G_{BG} and R are equal due to the steady-state condition for $t < t_0$. G is the carrier generation rate corresponding to the light turned on at t_0. As accumulation rate is less than G, the difference between them $\frac{n-n_0}{\tau} < \frac{Gt}{\tau}$

(corresponding to recombination loss). It means that the accumulation rate is constant and equals G when $t << \tau$. Accordingly, the observed linear charge carrier rise within the first 10 μs suggests that the free carrier loss due to recombination is not significant, consistent with the observed long τ for non-geminate recombination. As such, the carrier generation rate G as a function of n_0 can be estimated from the slope of the rise near t = 0 μs. In order to convert n_0 into V_{OP}, a second CE measurement is carried out.[111] The only difference between this and previously described CE is that the device is held at V_{OP} using a rheostat before switching to short-circuit (illuminated by a green LED, 9.9 mW cm^{-2}). Figure 4.2c shows the total extracted carriers as a function of initial steady-state V_{OP}. The result suggests that there is not a significant carrier reorganization between open-circuit and operating condition as V_{OP} and V_{OC} correspond to around the same number of carriers in the device ($V_{OP} \approx V_{OC}$). This is consistent with recent observation in DTDCPB-C_{60} BHJ.[85] However, this is not always true according to previous work on other OPV systems, especially for high intensity illumination (beyond 1 Sun).[85, 108] With the relationship between n_0 and V_{OP} (V_{OP} = 48.4 mV, 102.7 mV, 142.7 mV and 200.0 mV in Figure 4.3a), the I_{Gen} can then be derived as a function of operating voltage as:

$$I_{Gen}(V_{OP}(n_0)) = e \cdot G(n_0) \quad (4.4)$$

To measure I_{NGR} as a function of V_{OP}, a similar approach is employed. The steady-state illumination is turned off at t_0 so that the non-geminate recombination is left to be the only process.

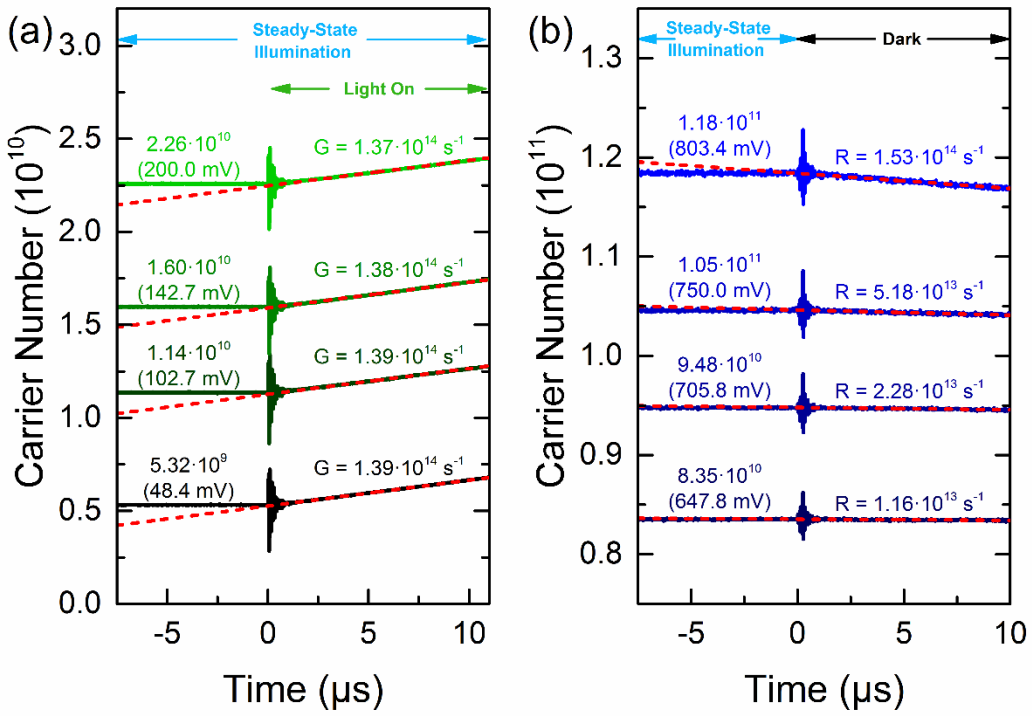

Figure 4.3 (a) Representative plots of charge carriers stored within the device in Figure 4.1d versus time for measurement of carrier generation rate (G). (b) Representative plots of carrier decay for measurement of carrier recombination rate (R). The rates are approximated as the slope of linear rise/decay region. A variable background blue LED illumination is used to set the target steady-state carrier number and corresponding V_{OP} (in the brackets) for measurement.

Figure 4.3b shows four representative plots of carrier number decay for the DTDCPB-C_{60} BHJ (n_0 = $8.35\cdot10^{10}$, $9.48\cdot10^{10}$, $1.05\cdot10^{11}$, $1.18\cdot10^{11}$). Instead of measuring carrier lifetime with a perturbing laser pulse and calculating R as $\frac{n}{\tau}$, which has been done previously, R is measured directly from the slope of initial TPV decay.[85] When a decrease in n is not significant, the lifetime can be treated as constant. Therefore, the carrier changing rate $\frac{dn}{dt}$ ($t > t_0$) can be expressed as:

$$\frac{dn}{dt} = -\frac{n}{\tau} = -(R - \frac{n_0 - n}{\tau}) \quad (4.5)$$

The term $\frac{n_0 - n}{\tau}$ is less than $\frac{Rt}{\tau}$ due to the decreasing carrier number during the decay. Thus R can be extracted from the slope of the initial linear decay region ($t << \tau$). The I_{NGR} can then be derived as a function of operating voltage as:

$$I_{NGR}(V_{OP}(n_0)) = e \cdot R(n_0) \quad (4.6)$$

The τ as a function of n is also extracted as $\frac{n}{R}$. It needs to be noted that the carrier lifetime mentioned above is an effective lifetime for all charge carriers stored within the device. The shortest τ extracted here ($n = 1.31 \cdot 10^{11}$) is ~350 μs, corresponding to V_{OC} = 845.5 mV, which is much longer than the timescale for the measurement of G and R.

4.2.3 Quantification of Geminate and Non-Geminate Losses

With I_{Gen} extracted directly from the TPV measurement, the current loss from non-geminate recombination is the difference between I_{Gen} and the value of I_{Illum} collected from steady-state I-V characteristics. Figure 4.3 shows I_{Gen} and I_{Illum} for a DTDCPB-C_{60} BHJ OPV illuminated by a green LED (9.9 mW cm^{-2}) as a function of voltage. While the measured I_{Gen} and I_{Illum} are well matched at low forward bias, the two curves begin to diverge at 0.4 V due to non-geminate recombination. This result suggests that CT state dissociation is the only current-limiting process at short-circuit, while inefficient collection of free carriers causes a roll-off in I_{Illum} near V_{OC}, consistent with previous observations in solution-processed BHJ systems.[79, 81-82] To further verify that I_{Illum} at short-circuit is limited primarily by geminate recombination, the I_{SC} was measured as a function of light intensity

(simulated AM1.5G). A linear dependence of I_{SC} on light intensity is observed, indicating the presence of a first order recombination process at short-circuit, consistent with geminate recombination.[80]

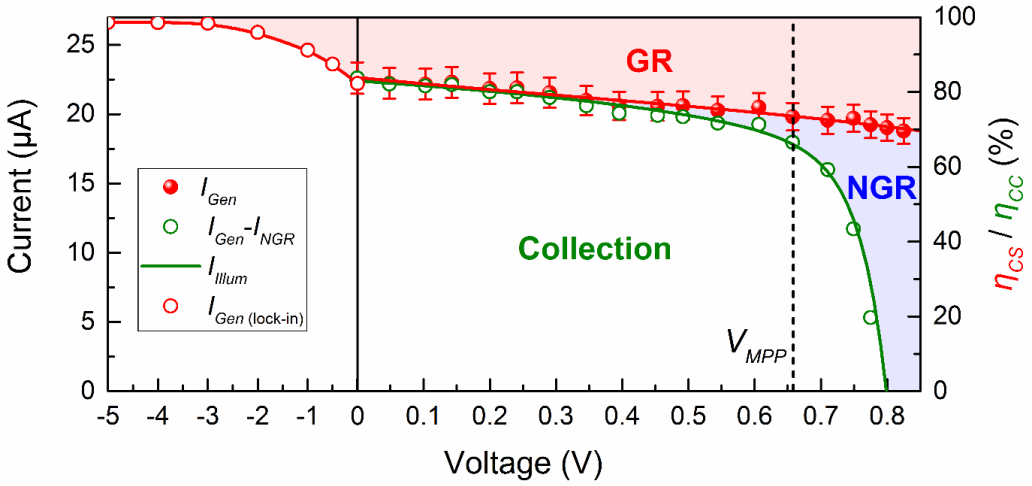

Figure 4.4: Current from generated free carriers (I_{Gen}) and collected free carriers (I_{Illum}) (charge separation efficiency and charge collection efficiency for the right axis) as a function of voltage in DTDCPB-C_{60} BHJ OPV in Figure 4.1d under green LED illumination (9.9 mW cm^{-2}). The I_{Illum} recreated as I_{Gen}-I_{NGR} from TPV measurement (green hollow circle) is plotted in comparison with I_{Illum} from I-V characteristics (green solid line). The red and blue areas represent illuminated current loss due to geminate recombination and non-geminate recombination, respectively. Under reverse bias, photocurrent is determined by a lock-in measurement. The photocurrent at -5 V is approximated to be the maximum achievable current when charge recombination is fully eliminated.

While a free carrier collection efficiency of 100% at short-circuit seems counter-intuitive for a BHJ, the linear relationship between collected carriers and voltage near short-circuit suggests that the active layer capacitance is much lower than the electrode capacitance (Figure 4.2c), leading to efficient carrier extraction and low non-geminate recombination loss within the mixed active layer.[85, 115] To further check the reliability of this technique, the I_{Illum} recreated from I_{Gen} and I_{NGR} measured directly from TPV is also

plotted in Figure 4.3. The recreated I_{Illum} is in excellent agreement with the measured I-V characteristics. The I_{Illum} can also be well recreated as a function of light intensity.[116]

To extract the absolute values of the η_{CS} and η_{CC} in Equation 4.2 as a function of voltage, the maximum possible current I_{Max} must also be known. Due to the near unity exciton diffusion efficiency (η_{Diff}) of an optimized BHJ, I_{Max} can be approximated as I_{Illum} at high reverse bias (-5 V), with both geminate and non-geminate recombination losses overcome by the large applied field.[90-91, 100, 109] For the DTDCPB-C_{60} BHJ device, $I_{Illum} \sim I_{Gen}$ (*i.e.* $I_{NGR}=0$) under reverse bias, since the collection of free carriers is already efficient ($\eta_{FC} \approx 100\%$) at short-circuit. At short-circuit, I_{Gen} from the lock-in measurement (22.2 μA) is well matched with previously measured I_{Gen} (22.6 μA) from TPV. The I_{Gen} (lock-in) is plotted as a function of reverse bias in Figure 4.4. A value of η_{CS} = 85.0% is measured at short-circuit, consistent with the value extracted from reverse bias external quantum efficiency measurements.[100] At the maximum power point (660 mV), values of η_{CS} = 74.4% and η_{FC} = 88.9% are extracted, leading to an overall η_{CC} = 66.1%. In this case, both geminate and non-geminate recombination limit the power output at the maximum power point voltage (V_{MPP}), and CT state separation serves as the major limiting step to complete exciton-to-carrier conversion despite efficient exciton harvesting in the mixed active layer. Thus, there is still room for further improvement in η_{CS} in the DTDCPB-fullerene system, which has already been used to demonstrate high power conversion efficiency (8~10%).[113-114]

4.3 DTDCPB-C_{60} and CuPc-C_{60} PHJ OPVs

While the discussion to this point is focused on BHJ OPVs, the photovoltage approach to measure I_{Gen} is widely applicable to OPVs with a variety of architectures. The recombination losses are further identified in DTDCPB-C_{60} and CuPc-C_{60} planar heterojunction (PHJ) OPVs to understand what processes limit the *FF* in these devices.

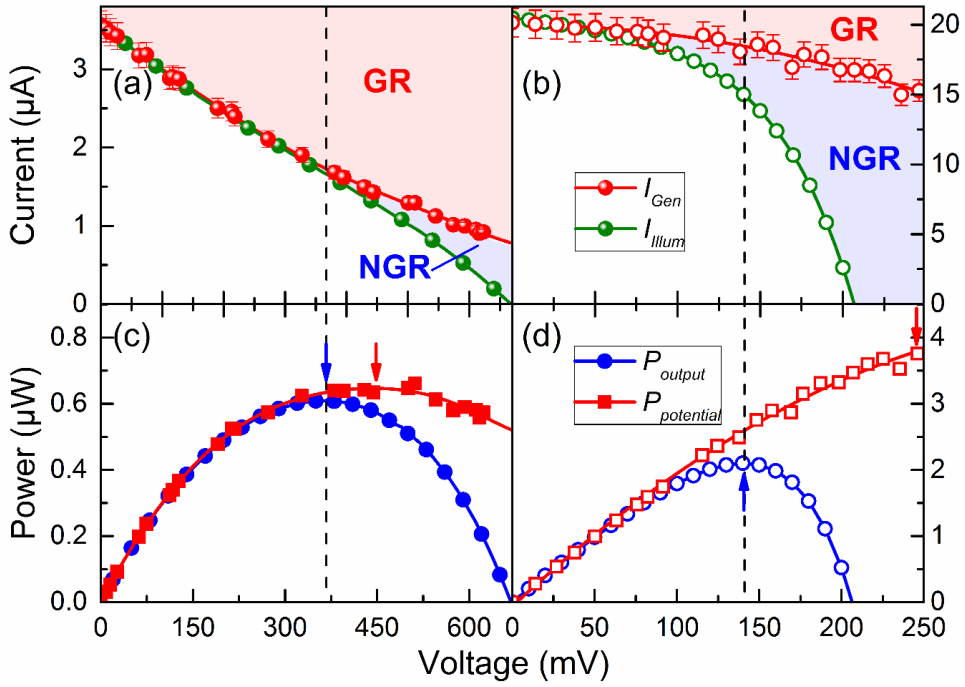

Figure 4.5 (a-b) Current from generated free carriers and collected free carriers, (c-d) actual/potential power output as a function of voltage for DTDCPB-C_{60} (solid sphere) and CuPc-C_{60} (hollow circle) planar OPVs in Figure 4.1d under green LED illumination (33.2 mW cm^{-2}). The broken vertical line represents the voltage of maximum power point. The blue and red arrows show the maximum point of actual and potential power output, respectively.

As η_{Diff} is no longer unity in a PHJ, I_{Max} cannot be approximated as the reverse bias I_{Gen} as reverse bias may also improve η_{Diff} via bulk exciton ionization, leading to an

overestimate of I_{Max}.[117] Therefore, optical modeling and a standard diffusion equation are generally used to estimate I_{Max} of a PHJ. This approach requires an accurate estimate of the exciton diffusion length of the non-luminescent active materials like CuPc, nontrivial to determine experimentally.[44, 48]

Figure 4.5a and b show the I_{Gen} and I_{Illum} of DTDCPB and CuPc planar devices under green LED illumination (33.2 mW cm^{-2}), respectively. The illuminated current losses of these devices due to geminate and non-geminate recombination are identified as a function of forward bias. Unlike the high FF (0.65) observed in BHJ devices, the DTDCPB-C_{60} PHJ shows a low FF of 0.26. This low FF comes from rapidly increased geminate recombination loss under forward bias. To better understand the origin of severe geminate recombination in DTDCPB-C_{60} PHJ under forward bias, the impact of neat DTDCPB layer on CT state separation in planar mixed heterojunction devices is examined.[116] The results indicate that neat DTDCPB layer leads to a lower electric field at D-A interface, which is critical for dissociation of CT states. At V_{MPP} (370 mV), over 99.7% of I_{Illum} loss relative to short-circuit is from geminate recombination. Thus, for the DTDCPB-C_{60} PHJ, the I_{Illum} at V_{MPP} can be improved only slightly if non-geminate losses are reduced. It is essential to suppress geminate recombination to effectively improve device efficiency. This contrasts with the previously discussed DTDCPB-C_{60} BHJ which will benefit from a reduction in either geminate or non-geminate recombination losses. As in DTDCPB PHJs, devices based on CuPc-C_{60} are also limited by a low *FF* (~0.49). The efficiency of a CuPc PHJ device is limited by both geminate and non-geminate recombination, in contrast to the DTDCPB PHJ device. A η_{FC} of only 81.0% is observed at the maximum power point in the CuPc

device while the η_{FC} is near unity for the DTDCPB case. As such, the limiting recombination mechanism within the power generating quadrant can vary with both device architecture and D-A materials choice.

While significant efforts have been made to suppress non-geminate recombination and improve V_{OC} in OPVs, these efforts are only fruitful if the device is limited by non-geminate recombination.[102, 118-120] Accordingly, understanding the potential power output ($P_{potential}$) in the absence of free carrier loss is essential before attempting to reduce non-geminate recombination for improved V_{OC}. Figure 4.5c,d show the actual output power (P_{output}) and $P_{potential}$ of DTDCPB and CuPc PHJ devices. For the DTDCPB planar device, both P_{output} and $P_{potential}$ increase with forward bias up to the maximum power point (0.37 V) then start to roll off. This suggests that the efficiency can be improved only slightly by further suppression of non-geminate recombination. To effectively improve its η_P, more efficient dissociation of CT states is required. In contrast, $P_{potential}$ for the CuPc planar device increases with forward bias up to 250 mV, with the maximum voltage limited only by the background light source. If non-geminate recombination could be completely avoided (before 250 mV), an increase of 25% in V_{OC} and 80% in η_P could be achieved. As such, the CuPc planar device can benefit from reduction of either geminate or non-geminate recombination.

4.4 Conclusions

In this chapter, a photovoltage-based technique is developed to directly probe free

carrier generation in an OPV at any operating voltage. For D-A systems studied here, this technique is applied to quantitatively decouple their geminate and non-geminate recombination losses within the power generating quadrant. Geminate recombination is found to be a significant factor limiting the device efficiency while the role of non-geminate recombination can vary with choice of active materials and device architecture. This deeper understanding of recombination will help to guide materials selection and device design in efforts for high efficiency. In next two chapters, strategies are developed to suppress recombination losses according to the primary loss mechanisms identified in this chapter.

4.5 Experimental Methods

Organic photovoltaic cells were fabricated using pre-patterned indium-tin-oxide (ITO)-coated glass substrates with a sheet resistance of 15 Ω/□. Substrates were cleaned in tergitol solution and in organic solvents and treated in UV-Ozone ambient for 10 minutes prior to thin film deposition. All layers were deposited at room temperature by high vacuum thermal evaporation at a pressure of $<8x10^{-7}$ Torr. In BHJ devices, a 10-nm-thick layer of MoO_x was deposited at 0.05 nm s^{-1} on ITO as an anode buffer layer. Mixed organic layers were prepared via co-deposition from two sources at a total rate of 0.2 nm s^{-1}. All devices are capped with a 10-nm-thick exciton blocking layer (EBL) of bathocuproine (BCP) and a 100-nm-thick Al cathode. The active area of the obtained device is 0.25 cm^2. For this study, DTDCPB (≈97%) was obtained from Sigma-Aldrich,[112] C_{60} (≈99%) was obtained from MER Corporation, MoO_3 (99.5%) and BCP (98%) were obtained from Alfa Aesar.

Chapter 4 – Quantify Charge Recombination Losses using Photovoltage

All materials were used as received without further purification. Transient photovoltage and charge extraction measurements were conducted according to previously published methods (illumination area: 0.0176 cm^2).[110-111] Current density-voltage characteristics were measured in air ambient with an Agilent 4155C parameter analyzer. Photocurrent under bias was measured using a Stanford Research Systems SR810 lock-in amplifier and a SR570 current preamplifier. External quantum efficiency measurements were performed under illumination from a 300W Xe lamp coupled to a monochromator and chopped with a SR540 optical shopper. All film thicknesses and optical constants were measured with a J. A. Woollam spectroscopic ellipsometer (fit by a Cauchy model).

5. Engineering Film Morphology for Efficient Charge Separation

In this Chapter, the impact of thermal annealing on film morphology and charge separation is investigated for a promising set of donor-acceptor-acceptor (D-A-A) electron donor materials are based on coplanar thieno[3,2-b]/[2,3-b]indole, benzo[c][1,2,5]thiadiazole and dicyanovinylene, which are found to show broadband absorption with high extinction coefficients. The material synthesis, single crystal analysis and Density functional theory (DFT) calculations were completed by the research group of Prof. Ken-Tsung Wong at National Taiwan University.

5.1 Background

In Chapter 4, a photovoltage technique is developed to identify the dominant recombination loss mechanism for various OPV systems. Despite the dipolar molecule DTDCPB system has demonstrated high efficiency in BHJ, its PHJ OPVs is severely limited by geminate recombination loss, suggesting a poor morphology of the vacuum deposited neat film that can frustrate charge separation at D-A interface.[114, 121] It is therefore important to explore methods to improve film morphology for materials like DTDCPB in order to avoid significant geminate recombination losses and realize their full potential in OPVs.

DTDCPB is a donor-acceptor-acceptor (D-A-A) type molecules. Their molecular architecture is composed of an electron-donating moiety and two electron-accepting moieties.[122] have an In recent years, organic small molecules with this D-A-A molecular configuration have been demonstrated with easily tunable molecular orbital energy levels

and optoelectronic properties.[112] Having both a narrow optical gap and a deep-lying highest occupied molecular orbital (HOMO) energy level, these systems have the potential to simultaneously show high short-circuit current density (J_{SC}) and open-circuit voltage (V_{OC}) when utilized as the electron donor in an OPV. Previously reported vacuum-deposited single-junction OPVs based on the D–A pairing of the DTDCPB and C_{70} have demonstrated high power conversion efficiencies of η_P = 8~10%.[113-114] This molecular design can result in a high ground state dipole moment. Thus, optimizing molecular packing within the thin films is critical to reduce recombination losses for these D-A-A systems.

In order to further improve the efficiency of OPVs based on D-A-A type donors, new molecules with larger extinction coefficients and deeper HOMO levels are needed. Here, two new D-A-A donors are demonstrated; 2-((7-(4-ethyl-4H-thieno[3,2-b]indol-2-yl) benzo[c][1,2,5]thiadiazol-4-yl)methylene)malononitrile (NTU-1) and 2-((7-(8-ethyl-8H-thieno[2,3-b]indol-2-yl)benzo[c][1,2,5]thiadiazol-4-yl)methylene)malononitrile (NTU-2). The electron donating moieties in these systems are coplanar and more electron donating than the previously reported DTDCPB, leading to a red-shift in the absorption spectrum.[9] The molecular structures of NTU-1 and NTU-2 are shown in Figure 5.1a. The electron-donating moieties thieno[3,2-b]indole and thieno[2,3-b]indole, have recently been used as building blocks for light sensitizers in efficient dye-sensitized solar cells.[123-124] These electron-donating moieties and the electron-withdrawing dicyanovinylene are connected by an electron-withdrawing benzo[c][1,2,5]thiadiazol (BTD) block to form the D-A-A configuration. Here, the regioisomeric effects of the thienoindole moieties on the physical

and structural characteristics of NTU-1 and NTU-2 are examined. These materials are further characterized as electron donors in both bulk and planar heterojunction OPVs. Optimized bulk heterojunction (BHJ) OPVs based on the donor-acceptor pairings of NTU-1-C_{70} and NTU-2-C_{70} show promising efficiencies limited by a low fill factor (FF). Planar heterojunction devices are examined as in order to directly study donor layer charge transport, and isolate the role played by donor layer morphology.

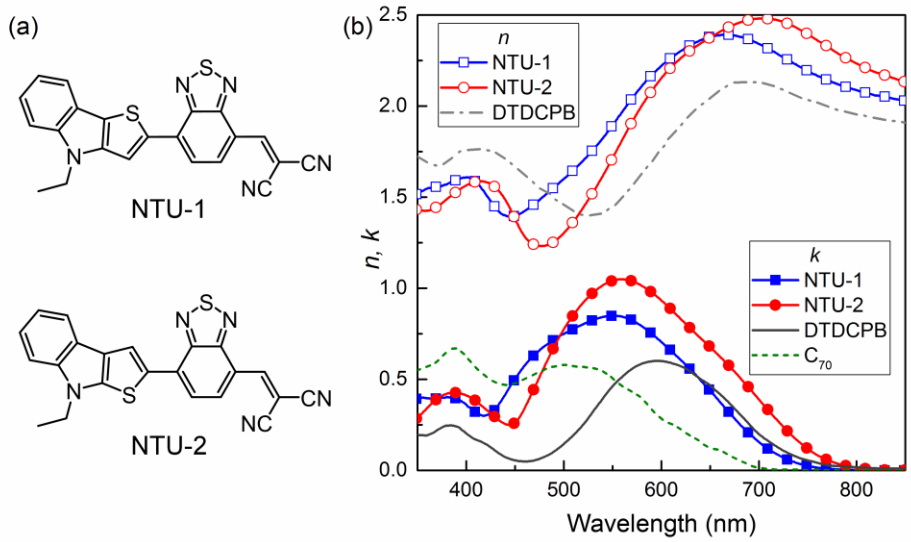

Figure 5.1 (a) Molecular structures of NTU-1 and NTU-2. (b) Optical constants for 30-nm-thick films of the compounds in (a) on glass substrates and extinction coefficient of C_{70} measured by spectroscopic ellipsometry.

5.2 Physical Properties of D-A-A donors NTU-1 and NTU-2

Figure 5.1b shows the optical constants (refractive index, *n*, and extinction coefficient, *k*) for 30-nm-thick films of NTU-1 and NTU-2. Both D-A-A donors show broadband absorption with large extinction coefficients, the k_{max} of NTU-1 (k_{max} = 0.85 at λ_{max} = 550 nm) and NTU-2 (k_{max} = 1.05 at λ_{max} = 560 nm) are significantly larger than the value of

k_{max} (0.67 at λ_{max} = 590 nm) for DTDCPB. A similar trend is observed for measurements in dichloromethane solution.

Density functional theory (DFT) calculations also suggest that NTU-2 should show a bathochromic shift in absorption position and a larger absorption coefficient compared to NTU-1, consistent with experimental observation. This is due to increased intramolecular charge transfer (ICT) character in NTU-2 relative to NTU-1 resulting from the stronger electron-donating ability and higher quinoidal character of N-ethylthieno[2,3-b]indole as indicated by separate calculations of a lower oxidation potential and increased oscillator strength, as well as bond length alternation calculations. The photophysical behavior of both compounds in thin film and dichloromethane solution is summarized in Table 5.1.

Table 5.1. Physical properties of NTU-1 and NTU-2.

	λ_{max} [nm][a]	$\varepsilon \times 10^4$ [M^{-1} cm^{-1}][a]	λ_{max}^{film} [nm][b]	E_g^{opt} [eV][c]	E_{ox}^{onset} [V][d]	E_{red}^{onset} [V][e]	HOMO [eV][f]	LUMO [eV][g]	E_g [eV][h]	T_d [°C][i]
NTU-1	569	4.49	552	1.69	0.74	-0.92	-5.54	-3.88	1.66	298
NTU-2	602	5.59	560	1.60	0.58	-0.96	-5.38	-3.84	1.54	314

[a]Measured in 10^{-5} M CH_2Cl_2 solution; [b]Estimated from the maximum thin film extinction coefficient; [c]Estimated from the onset of the thin film extinction coefficient; [d]In CH_2Cl_2 with 0.1 M $TBAPF_6$ as supporting electrolyte, Fc/Fc^+ as 0 eV; [e]In THF with 0.1 M TBAP as supporting electrolyte, Fc/Fc^+ as 0 eV; [f]HOMO = -4.8-($E_{ox,\ onset}$-$E_{Fc,\ onset}$); [g]LUMO = -4.8-($E_{red,\ onset}$-$E_{Fc,\ onset}$); [h]Difference between HOMO and LUMO; [i]Corresponding to 5% weight loss from TGA analysis under N_2 at the heating rate of 10 °C min^{-1}.

The electrochemical properties of NTU-1 and NTU-2 were probed by cyclic voltammetry (CV). An irreversible oxidation peak with an onset at 0.74 V (vs. Fc/Fc^+) for NTU-1 was observed. In contrast, a quasi-reversible oxidation (onset at 0.58 V) was

observed in NTU-2, where the *syn*-positioned nitrogen (vs. S atom) lone-pair electrons can be effectively delocalized with BTD ring, leading to increased conjugation and a lower oxidation potential. For reduction, both NTU-1 and NTU-2 exhibit a quasi-reversible reduction, referring to the BTD-stabilized radical anion. The stronger electron-donating ability of thieno[3,2-b]indole leads to a slightly higher reduction potential of NTU-2 (-0.96 V) compared to NTU-1 (-0.92 V). Based on the CV data, the calculated HOMO (LUMO) energy levels for NTU-1 and NTU-2 are -5.54 eV (-3.88 eV) and -5.38 eV (-3.84 eV), respectively. The fairly shallow LUMOs suggest a favorable offset for exciton dissociation by charge transfer with common fullerene acceptors.[29, 125-126]

In order to facilitate the interpretation of thin film crystallinity for NTU-1 and NTU-2, the relationship between molecular structure, intermolecular structure and crystal lattice was first examined in single crystals. Single crystals of NTU-1 (NTU-2) were obtained by the slow diffusion of a dichloromethane (methanol) and a toluene (hexane) solution. In single crystal, neighboring molecules of NTU-1 couple to form centrosymmetrical antiparallel slipped dimers with an interplanar distance of 3.41 Å. DFT calculations are also performed on XRD-derived crystal structures. Despite the different packing manners in one antiparallel dimeric pair of NTU-1 and E-, Z-configured NTU-2, all feature evident reduction of molecular dipole, which is crucial for preventing energetic disorder and facilitating charge carrier hopping.[127-130] As such, both molecules may be expected to show effective charge transport in crystalline thin films.

5.3 Performance of BHJ and PHJ OPVs

In order to investigate the performance of NTU-1 and NTU-2 as donors in BHJ OPVs, a composition and thickness optimization of the mixed active layer was carried out. Figure 5.2a-d show the operating parameters for an NTU-x-C_{70} BHJ with a 55-nm-thick active layer as a function of film composition. For both donors, the short-circuit current density (J_{SC}) and FF peak at a donor concentration of 20 vol%, possibly indicating optimal morphology at this composition. In particular, NTU-1-C_{70} BHJ devices show a high V_{OC} of 1.08 V at this composition. Both sets of devices show an improvement in V_{OC} over devices based on DTDCPB-C_{70} (V_{OC} = 0.94 V), consistent with the measured HOMO levels in Table 5.1.[113]

Device performance at this optimum composition (D:A = 1:4 vol.) is plotted as a function of active layer thickness in Figure 5.2e-h. Both sets of devices show a drastic decrease in FF with increasing active layer thickness, indicating that the efficient charge collection observed in the DTDCPB-C_{70} mixtures likely does not exist in the NTU-x-C_{70} mixtures.[113-114] The optimized active layer thicknesses are 40 nm and 55 nm for devices based on NTU-1 and NTU-2, respectively. A representative external quantum efficiency (η_{EQE}) spectrum is shown in Figure 5.2i, with both devices showing a broad spectral response. The η_{EQE} for the device containing NTU-2 extends further into the near-IR region compared to NTU-1 devices, consistent with the extinction coefficients of Figure 5.1b. The optimized NTU-1-C_{70} and NTU-2-C_{70} BHJs show average power conversion efficiencies of (3.69 ± 0.07) % and (5.05 ± 0.18) %, respectively. These efficiencies are limited by a

low FF (< 0.45) that persists throughout the entire composition range for both sets of devices.

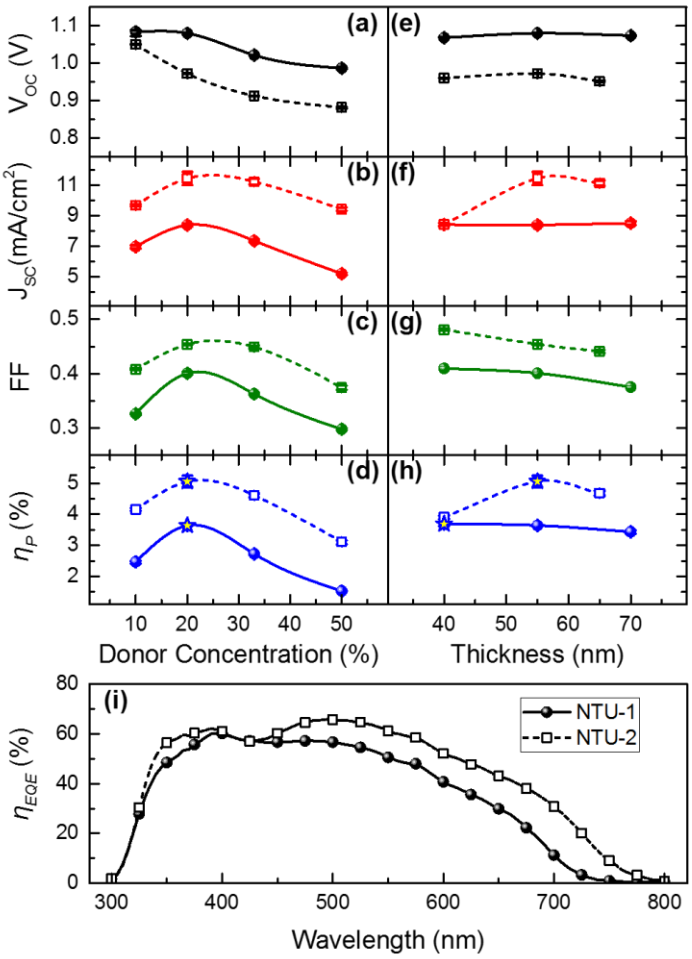

Figure 5.2 (a-d) Short-circuit current density (J_{SC}), open-circuit voltage (V_{OC}), fill factor (FF) and power conversion efficiency (η_P) as a function of donor concentration for NTU-1-C_{70} (closed symbols) and NTU-2-C_{70} (open symbols) BHJ devices with a 55-nm-thick active layer. (e–h) Device operating parameters as a function of active layer thickness for a NTU-x-C_{70} BHJ with a donor–acceptor ratio of 1 : 4. (i) External quantum efficiency for devices with the following structure:10 nm MoO_x/40 nm NTU-1-C_{70} (1 : 4) or 55 nm NTU-2-C_{70} (1 : 4) /10 nm BCP/100 nm Al. The BHJ results in this figure were from Dr. Yunlong Zou.

2.4.2. Performance of Planar Heterojunction OPVs

Although NTU-1 and NTU-2 show desirable optical properties and realize high V_{OC}, poor device FF remains the bottleneck to further increases in power conversion efficiency (η_P). To better understand the challenges associated with FF and the underlying film morphology, planar heterojunction (PHJ) devices were examined based on neat NTU-x layers to isolate the charge transport ability of each donor.

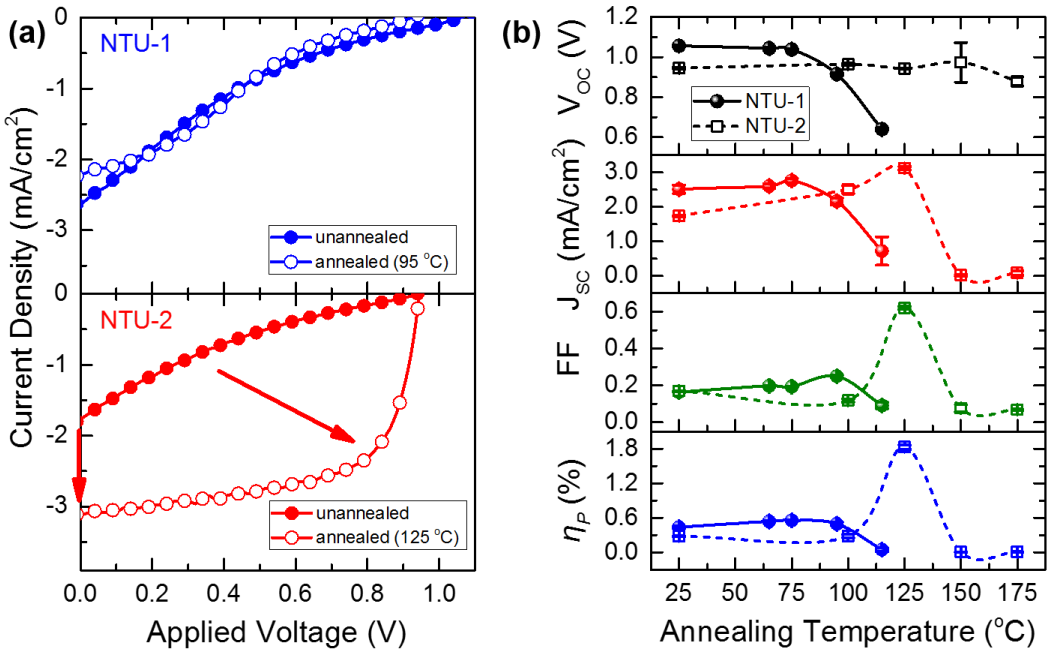

Figure 5.3 (a) Current density–voltage characteristics for unannealed and optimally annealed PHJs with the following device structure: 10 nm MoO_x/20 nm NTU-x/35 nm C_{60}/10 nm BCP/100 nm Al under simulated AM1.5G solar illumination at 100 mW cm^{-2}. (b) Operating parameters as a function of donor layer annealing temperature (annealing time: 60 s) for the PHJs in (a).

Figure 5.3a shows current density-voltage characteristics of the devices obtained

under simulated AM1.5G (100 mW/cm^2) illumination. Both sets of devices show S-shaped current density-voltage characteristics in the fourth quadrant and low FF (~0.16), potentially indicating an imbalance of charge carrier mobility between electrons and holes.[131] This low FF case is very similar to DTDCPB-C_{60} PHJ case in Chapter 4, which can be commonly observed in D-A-A systems. This imbalance has been previously identified as a source of charge carrier accumulation that can increase the rate of recombination at the D-A interface, especially at forward bias.[121] As C_{60} has been widely used in PHJ OPVs as an effective electron transport material, the charge carrier transport bottleneck likely originates within the donor layer.[70, 99]

5.4 Engineering Crystallinity via Thermal Annealing

5.4.1 Thin Film Crystallinity

According to the discussion of Section 5.2, NTU-1 and NTU-2 exhibit intermolecular interactions that should support efficient charge transport in crystalline thin films. This expectation is contradicted by the observation of poor FF in PHJ OPVs. In order to assess the role of donor layer crystallinity, as deposited thin films were examined using XRD for NTU-1 and NTU-2 (Figure 5.4a) on glass substrates. As no obvious diffraction peak is observed, both films are assumed to be amorphous. This indicates that the ideal molecular packing present in single crystals is unable to form during vacuum deposition. Indeed, recent work has suggested that high ground state dipole moment D-A-A molecules can form dimers and crystals directly without additional processing.[114] Here, an external

driving force is required to realize crystallinity in thin films of NTU-1 and NTU-2. Thin films are annealed immediately after deposition in N_2 for 60 s in order to increase film crystallinity.[132-134]

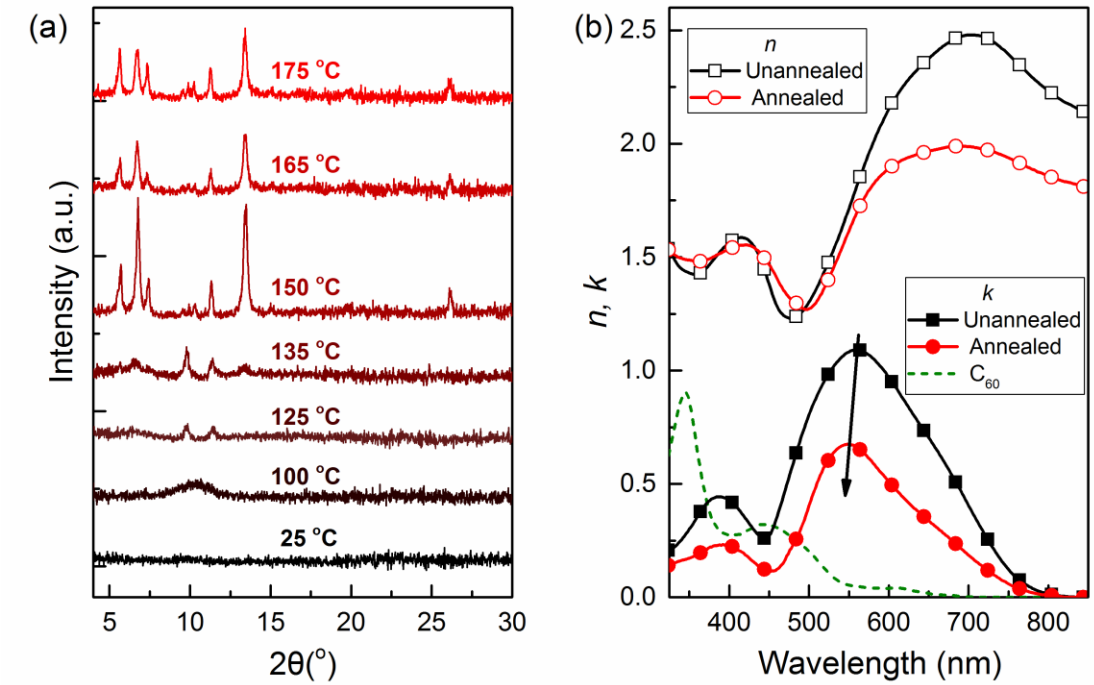

Figure 5.4 (a) X-ray diffraction pattern for a ~300-nm-thick film of NTU-2 on glass as a function of annealing temperature. A glass substrate background is subtracted for all patterns. (b) Index of refraction (n) and extinction coefficient (k) for 30-nm-thick unannealed and annealed films of NTU-2 on glass substrates. Dash line: extinction coefficient of C_{60}.

XRD patterns collected were collected from thin films of NTU-1 and NTU-2 (Figure 5.4a) deposited on glass substrates as a function of annealing temperature. For NTU-2, the film annealed at 100°C shows a broad peak at 2θ~11°. As the annealing temperature rises to 125°C, two narrower peaks at 9.8° and 11.3° emerge in the pattern. When the annealing temperature is increased above 150°C, the intensity of these peaks increases, and additional

peaks emerge, indicating increased crystallinity. Similar to NTU-2, increased crystallinity of NTU-1 thin films is also observed with increased annealing temperature. Therefore, thermal annealing can lead to an increase in thin film crystallinity and thin film morphology is sensitive to annealing temperature.

5.4.2 OPVs based on Annealed Thin Films

Figure 5.3b shows the performance of PHJ OPVs containing an annealed donor layer as a function of annealing temperature. Devices based on NTU-2-C_{60} show a significant increase in J_{SC} and FF upon annealing at 125 °C. Unannealed devices show average device operating parameters of V_{OC} = 0.94 V, J_{SC} = 1.74 mA cm^{-2}, FF = 0.17 and η_P = 0.28%. The device annealed at 125 °C shows a significant improvement in FF (0.62) and J_{SC} (3.12 mA cm^{-2}), with V_{OC} (0.94 V) almost unchanged, leading to an over 6 times improvement in η_P (1.83%). NTU-1-C_{60} devices do not show as significant an improvement in J_{SC} and FF upon annealing. The 95°C annealed device shows the highest FF (0.25) while suffering a reduction in both V_{OC} and J_{SC}. For both sets of devices, device performance is very sensitive to annealing temperature, the J_{SC}, FF and η_P drop rapidly above the optimized annealing temperature.

The observed change in the XRD pattern with annealing temperature is consistent with corresponding changes in device operating parameters. The values of *J*sc and η_P increase with annealing temperature up to 125°C before dropping once the annealing temperature exceeds 150°C. To further understand the structure-property relationships in crystallized NTU-2 thin films, 2D XRD patterns for annealed thin films of NTU-2 on Si

substrates are measured.[135] The results suggest that multiple types of crystals exist in films annealed at 125°C, with a varying degree of crystal texturing.

5.5 Analysis of Enhanced Device Performance

5.5.1 Light Absorption and Exciton Diffusion

To understand the role of crystallization in increasing the J_{SC} of NTU-2 devices, the component processes responsible for photoconversion at short circuit must be quantified as a function of annealing. Figure 5.4b shows the change in optical constants for an NTU-2 thin film after annealing at 125°C. Both n and k are reduced after annealing, with k_{max} falling from 1.05 to 0.65 and a blue shift in the peak absorption from 560 nm to 550 nm. The decreased *k* is consistent with a thin film color change from blue to purple observed during annealing. The lower absorption efficiency (η_A) of NTU-2 with annealing suggests that the observed improvement in photocurrent is not the result of enhanced optical generation.

Potential changes in the exciton diffusion length (L_D) with annealing were estimated by fitting device η_{EQE} spectra using a transfer matrix model and diffusion equation.[48, 104] When fixing the C_{60} L_D to be 35 nm,[136] the extracted L_D of unannealed NTU-2 falls from (7.1 ± 0.6) nm to (6.1 ± 0.5) nm upon annealing. Thus, the overall increase in J_{SC} is not the result of a longer L_D. As increased D-A interface area can also lead to more efficient exciton harvesting, the surface roughness of NTU-2 layers deposited on 10-nm-think MoO_x covered glass substrates was characterized by atomic-force microscopy. The root-mean-

square film roughness extracted from 5 μm× 5 μm surface height profiles increased slightly from 1.37 nm to 1.53 nm after annealing, suggesting only a negligible change in surface area and the corresponding exciton diffusion efficiency (η_D).

5.5.2 Charge Separation

Since changes in η_A and η_D are insufficient to explain the observed increase in J_{SC} with annealing, the efficiency of charge collection (η_{CC}) must increase with annealing to overcome the observed reduction in η_A. Based on the results in Chapter 4, non-geminate recombination loss is generally negligible at short-circuit. As such, the η_{CC} ($\approx \eta_{CS}$) is a universal property which is wavelength independent, the relative increase in η_{CC} can be isolated from the C_{60} component of the η_{EQE}. Here, it is assumed that the η_A-η_D products of C_{60} in both unannealed and annealed devices are same, since the simulated η_A-η_D product from transfer matrix model and diffusion equation show a difference <1% up to λ = 480 nm (L_D = 25 nm for C_{60}). This assumption is further validated by reverse bias η_{EQE} of C_{60} absorption peak (inset of Figure 5.5a).[100] The η_{EQE} spectrum of unannealed and annealed NTU-2-C_{60} PHJ devices are shown in Figure 5.5a. At λ = 355 nm (C_{60} absorption peak), an increase of 210% in η_{CC} can be estimated from the observed increase of η_{EQE}, which is also consistent with the enhancement in J_{SC} observed under broadband illumination.

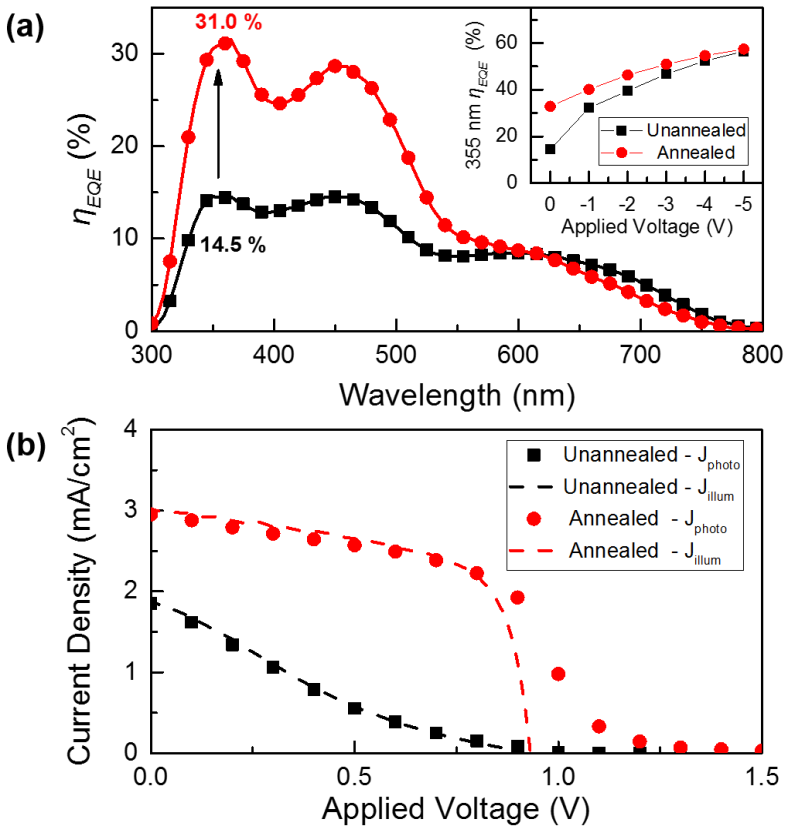

Figure 5.5 (a) External quantum efficiency spectra (η_{EQE}) for the devices in Figure 5.3a. Inset: External quantum efficiency at a wavelength of λ = 355 nm as a function of applied reverse bias. (b) Photocurrent densities under forward bias and current density–voltage characteristics for the devices in (a).

With the increase in photocurrent attributed to enhanced charge collection, the photocurrent density (J_{photo}) and dark current density (J_{dark}) under forward bias were separately measured in order to examine the change in FF with annealing. Here, J_{photo} and J_{dark} are approximated as free carrier generation flux and non-geminate recombination flus at D-A interface, respectively. They are easier to measure and agree well with J_{Gen} and J_{NGR} for D-A-A systems based on the work in Chapter 4.[116] Both unannealed and annealed

devices show a low J_{dark} (< 0.01 mA/cm^2) for applied voltages < 0.7 V, suggesting a large FF should be possible ignoring any reduction in J_{photo} under forward bias. Figure 5.5b shows J_{photo} as a function of applied bias along with the overall current density-voltage characteristics of NTU-2-C_{60} PHJ devices under simulated AM1.5G (100 mW/cm^2) illumination. For voltages less than V_{OC}, where J_{dark} is less than J_{photo}, the J_{photo} of both annealed and unannealed devices agree well with current density-voltage characteristics. The J_{photo} of the unannealed device shows a kink and falls quickly with increasing voltage, while the J_{photo} of the annealed device decreases gradually without a kink before reaching V_{OC} and shows measurable J_{photo} beyond V_{OC}. The significant enhancement in the fourth quadrant J_{photo} is consistent with improved FF and hole transport within NTU-2 upon annealing.

5.6 Conclusions

A set of D-A-A donors, NTU-1 and NTU-2, with isomeric thienoindole as the electron-donating (D) moiety coupling to benzothiadiazole-dicyanovinylene (-A-A) are synthesized and characterized. Compared to NTU-1, NTU-2 shows a red-shifted absorption maximum, a larger extinction coefficient, and a deeper HOMO energy level as the stronger electron-donating ability of thien[2,3-b]indol imparts the molecular backbone with enhanced quinoid and ICT character. Despite the different crystal packing motifs, brickwork for NTU-1 and herringbone for NTU-2, both molecules form cofacial centrosymmetric antiparallel dimers with efficient cancellation of the molecular dipoles. Bulk heterojunction

devices based on NTU-2-C_{70} show a champion η_P of 5.2% under AM1.5G solar simulated illumination. In examining thin films and planar heterojunction devices, insufficient crystallinity in the donor layer is identified to be the origin of limited FF. As thermal annealing leads to enhanced donor-layer crystallinity, crystalline OPVs based on annealed thin films show a high FF of 0.62. Compared to unannealed devices, annealed devices show an increase of over 200% in charge-collection efficiency and the corresponding power conversion efficiency. This large improvement further reinforces that dimerization is critical for the realization of effective charge transport in D−A−A molecules and fast charge separation at D-A interaface.

5.7 Experimental Methods

Organic photovoltaic cells were fabricated using indium-tin-oxide (ITO)-coated glass substrates with a sheet resistance of ~8-12 Ω/□. Substrates were cleaned in tergitol solution and in organic solvents and treated in UV-Ozone ambient for 10 minutes prior to thin film deposition. All layers were deposited at room temperature by high vacuum thermal evaporation at a pressure of $<8\text{x}10^{-7}$ Torr. In all devices, a 10-nm-thick layer of MoO_x was deposited at 0.05 nm s^{-1} on ITO as an anode buffer layer.[137] Mixed organic layers were prepared via co-deposition from two sources at a total rate of 0.2 nm s^{-1}. All devices are capped with a 10-nm-thick exciton blocking layer (EBL) of bathocuproine (BCP) and a 100-nm-thick Al cathode. The active area of the obtained device is 0.785 mm^2, defined by the cathode area. Annealing is carried out on a copper block hotplate in N_2 ambient. For

this study, C_{60} (99%) and C_{70} (99%) was obtained from MER Corporation, MoO_3 (99.5%) and BCP (98%) were obtained from Alfa Aesar. All materials were used as received without further purification. Current density-voltage characteristics were measured in air with an Agilent 4155C parameter analyzer under AM1.5G (100 mW/cm^2) solar simulated illumination from 150 W Oriel Xe lamp. External quantum efficiency measurements under bias were collected by measuring the photocurrent under monochromatic light illumination using a 300 W Oriel Xe lamp, a monochromator, an optical chopper wheel, a SR570 current preamplifier and a SR810 lock-in amplifier. X-ray diffraction patterns were measured with Bragg-Brentano geometry on Bruker-AXS D-5005 employing a Cu Kα source. All film thicknesses and optical constants were measured with a J. A. Woollam spectroscopic ellipsometer. Film thicknesses were fit using a Cauchy model.

6. Exciton Permeable Interlayer for Suppressed Recombination

6.1 Background

In Chapter 4, the CuPc-C_{60} system is identified limited by both geminate and non-geminate recombination losses at the maximum power output condition. The rapid non-geminate recombination under forward bias results in a low open-circuit voltage (V_{OC}) for this system. In this chapter, a new device architecture is exploited to slow non-geminate recombination losses while realizing efficient carrier generation at the D-A interface.

Similar to the archetypical CuPc-C_{60} system, state-of-the-art devices are also frequently limited by a low open-circuit voltage (V_{OC}) relative to the optical gap of the active materials. To maximize V_{OC}, a variety of studies have sought to better elucidate its physical origin.[102, 138-141] Previous work has demonstrated that V_{OC} in a donor-acceptor (D-A) type OPV depends not only on the energy of the relaxed charge transfer (CT) state at the D-A interface, which sets the theoretical maximum for V_{OC}, but also on the recombination of free charge carriers (non-geminate recombination).[78, 82, 142] In many systems, the current density due to non-geminate recombination (J_{NGR}) is often the primary factor limiting V_{OC} and hence must be suppressed to reduce energy losses.[82, 142]

Molecular design is frequently used to reduce J_{NGR} and improve V_{OC}, as an increased interface energy level offset (E_{DA}) between the highest occupied molecular orbital (HOMO) of the donor and the lowest unoccupied molecular orbital (LUMO) of the acceptor increases the effective energy gap via the CT state energy (E_{CT}) and reduces the dark current [Figure 6.1(a)].[112, 143-147] Despite these efforts, there remains room for further

improvement, even for energetically optimized D-A systems. E_{CT} is generally lower than E_{DA} due to the Coulombic binding energy of relaxed CT states.[148-149] Consequently, efforts have also exploited variations in device architecture to engineer E_{CT}, and reduce J_{NGR}. For example, an increase in the CT state separation has been shown to reduce the binding energy and non-geminate recombination.[102, 118, 120, 150-151] Inserting a wide energy gap interlayer (i.e. deeper HOMO than donor, shallower LUMO than acceptor) between the donor and acceptor materials can spatially separate the electron and hole that comprise the CT state, leading to an increase in the maximum achievable V_{OC}.[102, 118, 120] Unfortunately, increasing the thickness of the insulating interlayer [Figure 6.1(b)] can also lead to a drastic reduction in J_{SC} by reducing the efficiency of exciton dissociation by charge transfer.[102, 120] When the interlayer instead has a deeper LUMO than the donor and a shallower HOMO than the acceptor, two dissociating interfaces are formed leading to oppositely charged photogenerated carriers migrating within the interlayer.[64] This configuration requires an ambipolar interlayer material and carefully optimized CT states at both interfaces to prevent an increase in charge recombination loss.

To simultaneously increase the spatial extent of the CT state and maintain efficient exciton harvesting, this work demonstrates a device architecture using an interlayer with a HOMO level between those of the donor and acceptor and a LUMO level that is shallower than that of both the donor and acceptor [Figure 6.1(c)]. This architecture has one exciton dissociating interface (between the interlayer and acceptor) so that only photogenerated holes are transported within the interlayer.

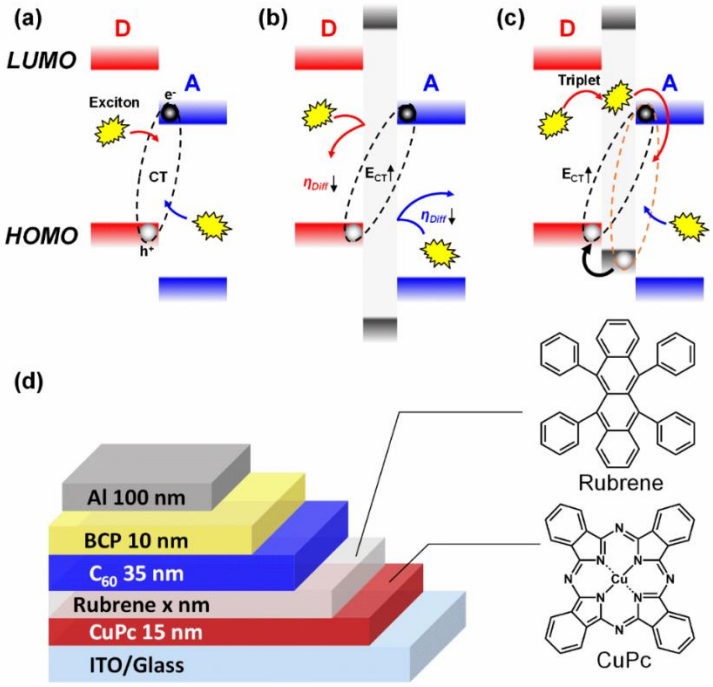

Figure 6.1 Energy diagram for donor-acceptor heterojunction OPVs with (a) an archetypical planar heterojunction, (b) a wide energy gap interlayer between the donor and acceptor materials that increases CT state energy while also frustrating exciton diffusion to the dissociating interface, (c) a triplet exciton permeable wide energy gap interlayer that allows exciton dissociation at interlayer-acceptor interface. (d) Device architecture of interest in this work. Here, rubrene serves as an interlayer between the donor of CuPc and the acceptor of C_{60}.

To avoid significant exciton loss from the donor layer, the interlayer must be permeable to donor excitons. Figure 6.1(d) shows the device architecture and molecular structures of the electron donor and interlayer used in this work. Here, triplet exciton forming metal-phthalocyanines are used as donors with a rubrene interlayer. For the archetypical donor copper phthalocyanine (CuPc), the triplet yield under optical excitation is near unity due to its rapid intersystem crossing.[152] The triplet level (T_1) of rubrene (1.14 eV) is similar to CuPc (1.16 eV), permitting exciton transport and dissociation.[153-154]

6.2 CuPc-C_{60} PHJ OPVs with Rubrene Interlayer

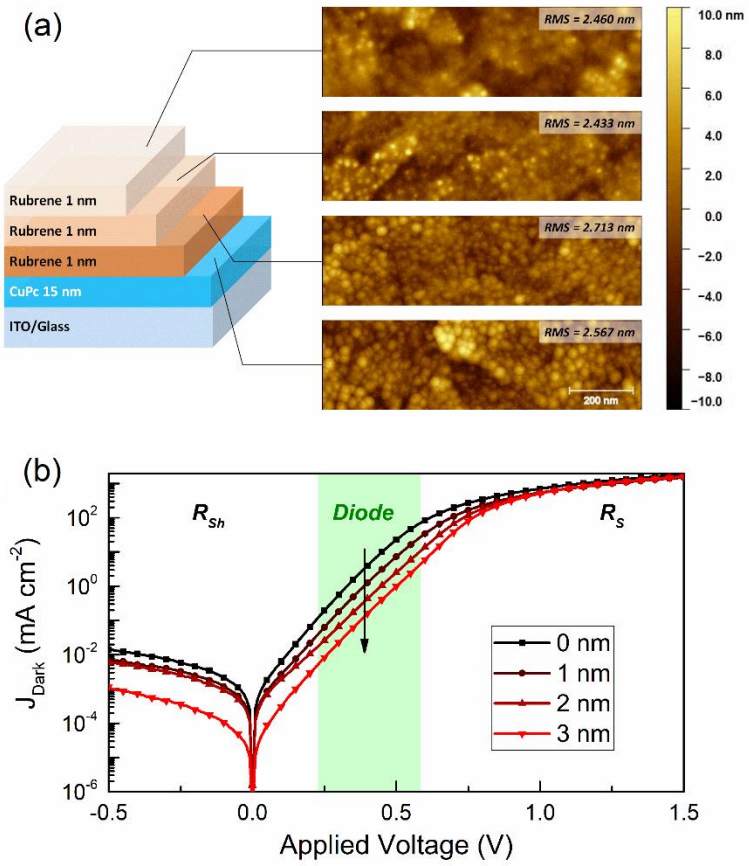

Figure 6.2 (a) Atomic force micrographs of 15 nm CuPc film on ITO substrate and 1-3 nm rubrene layer on top of CuPc. (b) Current density–voltage characteristics for the devices in Figure 6.1(d) without illumination, presented on a semilog plot and using the absolute value of current density.

The surface topography of rubrene covered CuPc measured by atomic force microscopy is shown in Figure 6.2(a). CuPc features become increasingly less prominent with increasing rubrene thickness. This suggests that the deposited rubrene is relatively uniform. The roughness of the D-A interface is barely changed by including a very thin rubrene layer. As such, the formation of a mixed or pseudo-bulk heterojunction at the

interface can be ruled out as a source for the change in exciton diffusion efficiency and photocurrent. Figure 6.2(b) shows the dark current density (J_{Dark})-voltage characteristics for CuPc-rubrene-C_{60} planar devices in Figure 6.1(d). The J_{Dark} decreases with interlayer thickness for the 'diode' dominant region and the effective interlayer coverage can be estimated to be 70% (1 nm), 89% (2 nm) and 96% (3 nm) from this region (see Supporting Information), consistent with the results of atomic force microscopy.

Figure 6.3(a) shows the operating parameters for devices in Figure 6.1(d) as a function of interlayer thickness (0-3 nm) under simulated AM1.5G (100 mW/cm^2) illumination. The V_{OC} increases with interlayer thickness while J_{SC} shows an improvement of 20% when rubrene is only 1-nm-thick and rolls off with increased thickness. This increase in V_{OC} is similar to the results of previous work which employ the wide energy gap material 1,4-bis(triphenylsilyl)benzene (UGH2) as a blocking interlayer for CuPc-C_{60} planar devices.[102] These UGH2-based devices [case in Figure 6.1(b)] showed a steep reduction in J_{SC} with no initial improvement. In contrast, J_{SC}, the fill factor (FF) and the resulting power efficiency (η_P) are maximized when including a 1-nm-thick interlayer of rubrene at the CuPc-C_{60} interface. Overall, optimized rubrene interlayer devices show a 50% enhancement in η_P.

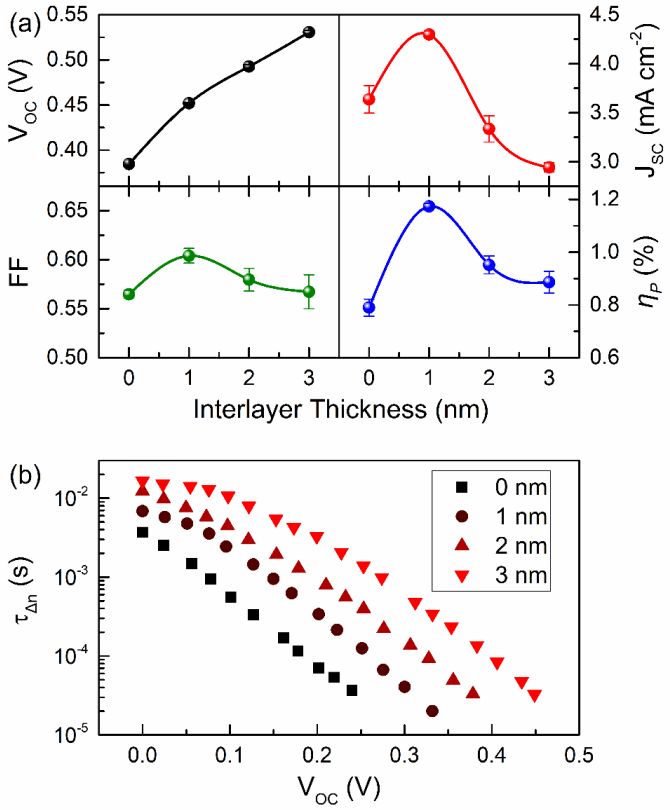

Figure 6.3 (a) Open-circuit voltage (V_{OC}), short-circuit current density (J_{SC}), fill factor (FF) and power conversion efficiency (η_P) as a function of rubrene thickness for CuPc-C_{60} planar OPVs with the device architecture in Figure 6.1(d). (b) Voltage dependence of the excess carrier lifetime ($\tau_{\Delta n}$) as a function of interlayer thickness for the CuPc-C_{60} planar OPV.

6.3 Impact on Open-Circuit Voltage

6.3.1 Non-Geminate Recombination

To identify the origin of enhanced V_{OC} in interlayer devices, the results in Figure 6.2(b) are fit with a Shockley model. [101]

$$J_{NGR} \approx J_{Dark} = J_S\left[\exp\left(\frac{q(V - J_{Dark}R_S)}{nk_BT}\right) - 1\right] + \frac{V - J_{Dark}R_S}{R_{Sh}} \qquad (6.1)$$

$$\text{with } J_S \approx J_0 \exp\left(\frac{-E_{CT}}{nk_BT}\right)$$

In Equation 6.1, q is the fundamental charge, n is the diode ideality factor, k_B is the Boltzmann constant, T is the temperature, R_S and R_{Sh} are the series and shunt resistance, respectively, and J_S is the reverse saturation current density. As E_{CT} can be considered as an effective energy gap for electron-hole pair generation across the D-A interface, J_S can be expressed using E_{CT} and a temperature independent prefactor J_0.[139, 155-156] Here, the parameters in Equation 6.1 are assumed to be intensity independent and approximate J_{NGR} as J_{Dark}. Table 6.1 shows the extracted parameters from Equation 6.1 as a function of interlayer thickness. Increasing interlayer thickness results in an increased R_{Sh} and a reduction in the saturation current density J_S. These reflect a reduction in current leakage between the electrodes and reduced non-geminate recombination at the D-A interface, respectively.[157]

Table 6.1 Parameters from Equation 6.1 as a function of interlayer thickness

Interlayer thickness	R_S [Ohm cm^{-2}]	R_{Sh} [Ohm cm^{-2}]	*n*	J_S [mA cm^{-2}]	E_{CT} [eV][a]	J_0 [mA cm^{-2}][b]
0 nm	0.40	4.0×10^{4}	2.04	1.8×10^{-3}	0.79	7.5×10^{3}
1 nm	0.46	8.3×10^{4}	2.09	6.6×10^{-4}	0.84	5.5×10^{3}
2 nm	0.40	1.0×10^{5}	2.14	2.6×10^{-4}	0.87	2.5×10^{3}
3 nm	0.42	7.0×10^{5}	2.08	8.0×10^{-5}	0.90	2.1×10^{3}

[a]Estimated from the extrapolated V_{OC} at 0 K; [b]Calculated using J_S, *n*, E_{CT} and temperature T = 294K.

To further confirm the suppression of non-geminate recombination, the recombination lifetime is probed using transient photovoltage (TPV).[116] In this

measurement, devices are held at open-circuit under constant background illumination (blue LED, λ_{peak} = 455 nm) and then excited with an additional short light pulse (20 μs, green LED, λ_{peak} = 530 nm, intensity: 16.5 mW cm^{-2}) to induce excess charge carriers.[110-111, 116] Since at open-circuit recombination within the device is the only pathway to consume charge carriers, the TPV decay back to steady-state reflects the excess charge carrier lifetime. The voltage perturbation is small enough (~5 mV) to ensure that the measurement reflects the bulk charge carrier behavior under steady-state. Figure 6.3(b) shows the small perturbation carrier lifetime ($\tau_{\Delta n}$) as a function of V_{OC} and interlayer thickness for CuPc-rubrene-C_{60} planar devices on pre-patterned indium-tin-oxide substrates. For the same V_{OC}, the measured $\tau_{\Delta n}$ increases with interlayer thickness. This observation confirms that non-geminate recombination at the D-A interface can be slowed by spatially separating oppositely charged photogenerated carriers.

6.3.2 CT State Binding Energy

To understand the impact of the rubrene interlayer on the CT state binding energy, E_{CT} must be determined as a function of interlayer thickness. Experimentally, E_{CT} is typically estimated from the temperature dependence of V_{OC}, which can be described by rearranging Equation 6.1 under open-circuit conditions (same form as Equation 3.11):

$$qV_{OC} \approx E_{CT} - nk_BT\, ln\left(\frac{J_0}{J_{Gen}(V_{OC})}\right) \quad (6.2)$$

In practice, the observed temperature-dependence of V_{OC} often deviates from a linear trend and plateaus at low temperature due to the limited quasi-Fermi level offset at finite

illumination intensity.[141, 158-160] Thus, the theoretical maximum achievable V_{OC} and E_{CT} are often approximated as the extrapolated V_{OC} at 0 K (known as V_0).[79, 158, 161] Figure 6.4(a) shows the measured V_{OC} as a function of temperature (190-294 K) for CuPc-C_{60} planar devices as a function of rubrene interlayer thickness. A linear dependence of V_{OC} on temperature is observed for all devices. The extracted value of V_0 ($\approx E_{CT}/q$) increases with rubrene interlayer thickness (from 0.79 to 0.84, 0.87, 0.90 V). As the V_0 of a standalone rubrene-C_{60} bilayer device (1.19 V) is larger than that of a CuPc-C_{60} bilayer device (0.80 V), one possible explanation for the increased value of E_{CT} is the presence of a different relaxed CT state formed at the interlayer-acceptor interface.[162] To examine this further, the measured E_{CT} is fit with a simple electrostatic model assuming the relaxed CT state continues to reside on molecules of CuPc and C_{60} with E_{CT} depending on interlayer thickness (d) as:

$$E_{CT} = E_{DA} - E_b \frac{a_0}{a_0 + d\frac{\varepsilon_i}{\varepsilon_a}} \quad \text{with } E_b = \frac{q^2}{4\pi\varepsilon_0\varepsilon_a a_0} \qquad (6.3)$$

Here, E_b and a_0 are the binding energy and the separation distance of the CT state in the absence of an interlayer, ε_0 is the permittivity of vacuum, ε_a and ε_i are the relative permittivity of the active material and interlayer, respectively.[102] To reduce fitting variables, the values of ε_a and ε_i are estimated from the near-infrared refractive indices of the D-A (1:1) mixture (ε_a = 3.8) and rubrene (ε_i = 2.9). The value of E_{DA} (1.00 eV) is taken from literature, which is measured directly from CuPc/C_{60} thin films deposited on ITO using photoelectron spectroscopy.[163]

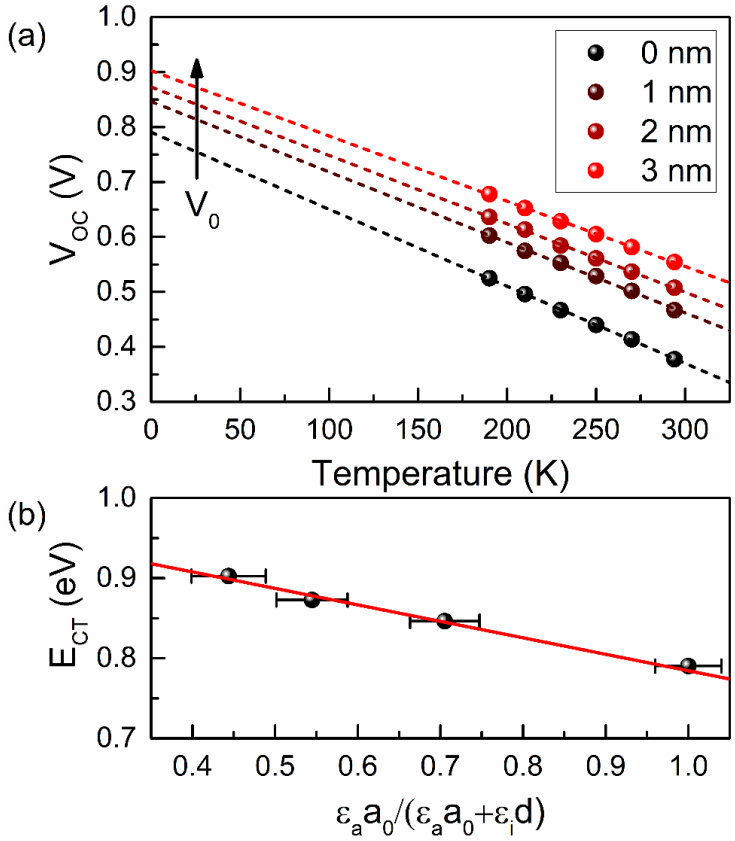

Figure 6.4 (a) Temperature dependence of V_{OC} for the devices in Figure 6.1(d) as a function of rubrene interlayer thickness. The linear extrapolations of V_{OC} to 0 K are based on data in the temperature range of 190−294 K. (b) Modeling the increased E_{CT} of a CuPc-C_{60} CT state with the incorporation of a rubrene interlayer by fitting the interlayer thickness dependence of E_{CT} extracted from (a).

The measured E_{CT} in Figure 6.4(a) can be well fit with this simple model [Figure 6.4(b)]. An initial separation distance of $a_0 = (1.9 \pm 0.3)$ nm is obtained, corresponding to a binding energy $E_b = (0.20 \pm 0.03)$ eV, similar to the previous results for CuPc-C_{60} planar devices using UGH2 interlayer (error bars are determined from the 95% confidence interval of the fit).[102] This analysis suggests that the relaxed CT state continues to reside on molecules CuPc and C_{60} up to interlayer thicknesses of 3 nm. Thus, the binding energy

of the CuPc-C_{60} CT state can be reduced by spatially separating the electron and hole, leading to an improved E_{CT} and larger V_{OC} under practical operating conditions.

6.4 Impact on Short-Circuit Current

6.4.1 Triplet Transport Through Interlayer

In order for the interlayer-based device in Figure 6.1(d) to exhibit high J_{SC}, the rubrene interlayer must be able to transport donor excitons to the dissociating interlayer-acceptor interface. To verify the transport of donor excitons via the triplet level of the interlayer, the relative change in the exciton diffusion efficiency (η_D) is investigated as a function of rubrene thickness in three metal phthalocyanine (MPc)-C_{60} systems. Devices based on donor layers of platinum phthalocyanine (PtPc) and lead phthalocyanine (PbPc), with triplet energies of 1.28 eV and 1.02 eV, respectively, are compared with those based on CuPc (1.16 eV).[154, 164-165] As the triplet excitons in these three donor materials cannot be dissociated at the MPc-rubrene interface,[162] a more exothermic exciton transfer from donor to interlayer will frustrate back transfer to the donor and improve exciton harvesting.[166-168]

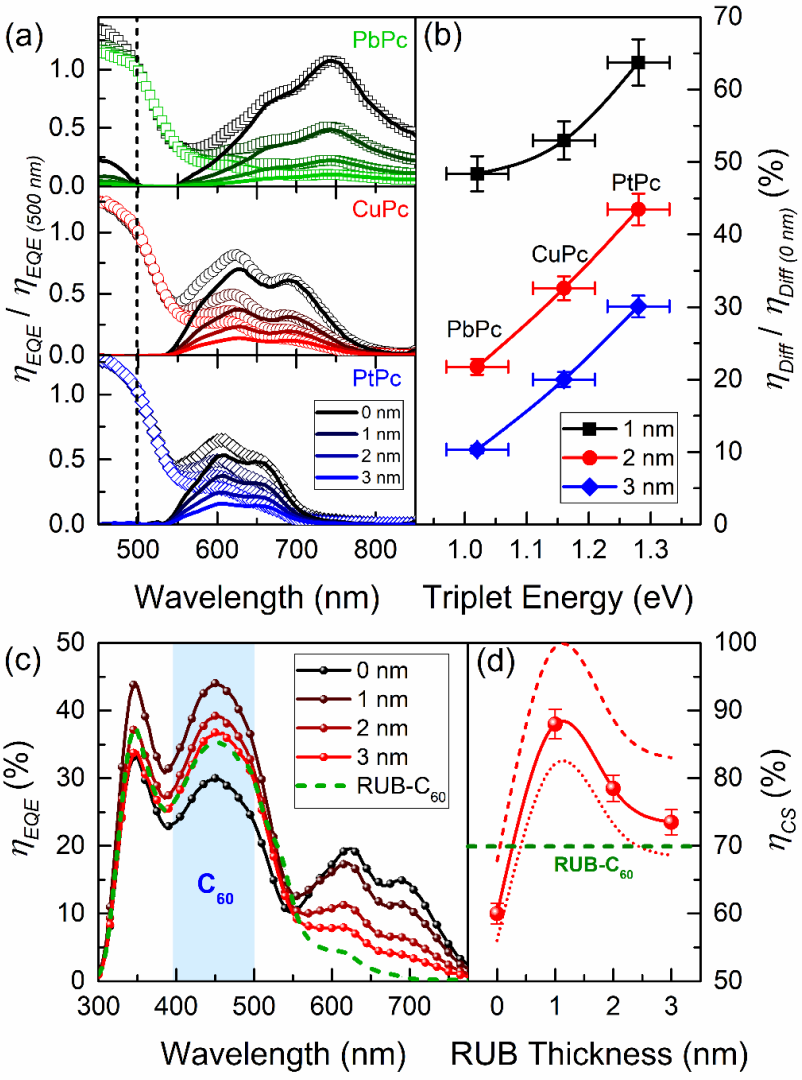

Figure 6.5 (a) Normalized external quantum efficiency (η_{EQE}) of metal phthalocyanine (PbPc, CuPc, PtPc)-C_{60} planar OPVs (structure: 15 nm donor/x nm rubrene/35 nm C_{60}/10 nm BCP/100 nm Al) as a function of interlayer thickness. The η_{EQE} is normalized to 500 nm (C_{60} absorption dominant) to isolate the impact of the interlayer on exciton harvesting. The donor component is shown as solid lines. (b) Donor diffusion efficiency (normalized to bilayer case) as a function of triplet energy and interlayer thickness of phthalocyanine donors. (c) η_{EQE} for the devices in Figure 6.1(d) and a rubrene-C_{60} bilayer OPV (structure: 15 nm rubrene/35 nm C_{60}/10 nm BCP/100 nm Al). (d) Charge separation efficiency (η_{CS}) of CuPc devices in (c) as a function of rubrene (RUB) interlayer thickness. The green dash line is the η_{CS} of the rubrene bilayer device in (c). The exciton diffusion length (L_D) of C_{60} is taken as 30 nm to extract η_{CS}. The η_{CS} of CuPc devices extracted using C_{60} L_D = 25 nm and 35 nm are also shown as red dash line and red dot line, respectively.

Figure 6.5(a) shows the external quantum efficiency (η_{EQE}) normalized to its value at a wavelength of $\lambda = 500$ nm (C_{60} absorption dominant) for MPc-rubrene-C_{60} planar devices. For all MPcs the donor contribution to the η_{EQE} falls with interlayer thickness. The η_{EQE} can be thought of as the product $\eta_{EQE} = \eta_A \eta_D \eta_{CC}$, with η_A, η_D, and η_{CC} defined as the absorption, exciton diffusion, and charge collection efficiencies, respectively. Here, the exciton dissociation efficiency at the D-A interface is taken as unity, while η_{CC}, the collection yield of CT states, is considered as a wavelength independent property.[100] As exciton diffusion in C_{60} is unaffected by the presence of the interlayer, the normalization of η_{EQE} removes any impact of the interlayer on η_{CC}. Thus, the normalized η_{EQE} is equivalent to the product η_A-η_D. Optical transfer matrix simulations of η_A show no change for either active material with the presence of the interlayer.[162] The observed reduction in normalized η_{EQE} for the donor is therefore attributed to a decrease in η_D.

To better compare the reduction in η_D induced by interlayer among MPc devices, the normalized η_D (100% for bilayer case) are plotted as a function of triplet energy and interlayer thickness for MPc absorption region [Figure 6.5(b)]. The normalized donor η_D is observed to increase with donor material triplet energy. With a 3-nm-thick rubrene layer, the normalized η_D for PtPc devices is 1.5 and 3 times higher than CuPc and PbPc, respectively, likely reflecting reduced back transfer to the MPc layer. The exciton permeable interlayer thus provides a promising strategy to improve V_{OC} while maintaining efficient exciton harvesting.

6.4.2 Geminate Recombination

Since the inclusion of the interlayer does not improve η_A and η_D, an increase in η_{CC} must be responsible for the initial increase in J_{SC}. As already noted, η_A and η_D of C_{60} are almost unchanged with rubrene thickness. Since η_{CC} is the collection yield of relaxed CT states at the D-A interface, assumed to be identical for donor and acceptor, the relative increase in wavelength independent η_{CC} can be readily isolated from the C_{60} component of the η_{EQE}.[100] Figure 6.5(c) shows the η_{EQE} spectra for the devices in Figure 6.3(a). For C_{60} absorption at $\lambda \sim 450$ nm, there is an increase of ~50 % in η_{EQE} when a 1-nm-thick layer of rubrene is inserted at the D-A interface. Relative to the 1 nm case, the η_{EQE} at this wavelength decreases with increasing interlayer thickness, while remaining larger than the case of control CuPc-C_{60} bilayer devices. This suggests that the interlayer suppresses charge recombination at short-circuit, leading to improved η_{CC}. As the dependence of J_{SC} on light intensity is linear for all of the devices studied,[162] geminate recombination (first-order) serves as the dominant recombination mechanism at short-circuit.[80, 86] Accordingly, the CT state separation efficiency (η_{CS}), the dissociation yield of relaxed CT states, can be approximated as η_{CC}.

To better understand the increased efficiency of charge separation in interlayer devices, The planar OPVs based on rubrene-C_{60} (structure: 15 nm rubrene/35 nm C_{60}/10 nm BCP/100 nm Al) are examined. By again taking the ratio of η_{EQE} spectra to η_A-η_D products (L_D = 30 nm for C_{60}), the η_{CS} ($\approx\eta_{CC}$) is extracted and plotted as a function of interlayer thickness [Figure 6.5(d)].[48, 104, 169] Due to the uncertainty of the L_D in C_{60} (especially when depositing on crystalline bottom layer), The results are also plotted using L_D = 25 nm and

35 nm for C_{60}. The η_{CS} of CuPc devices with an interlayer is in all cases larger than that of rubrene-C_{60} bilayer OPVs, reaching 100% for 1-nm-thick interlayer when taking L_D = 25 nm for C_{60}. This suggests that the observed enhancement in η_{CS} is not simply due to the formation of a more easily dissociated rubrene-C_{60} CT state. Instead, CT state separation here is likely a two-step process, with the rubrene-C_{60} CT state first relaxing to the CuPc-C_{60} CT state, followed by the dissociation of the CuPc-C_{60} CT state into free carriers. The roll-off in η_{CS} above an interlayer thicknesses of 1 nm suggest that a potential transport barrier must be overcome for the transition from the rubrene-C_{60} to CuPc-C_{60} CT state. Previously, Groves predicted a similar roll-off in η_{CS} when increasing the interlayer thickness in an energy cascade heterojunction using a Marcus model and a kinetic Monte Carlo simulation, in good agreement with our observations.[170] With increasing rubrene thickness, relaxed CT states are more likely to be rubrene-C_{60} CT states, with the resulting devices resembling a rubrene-C_{60} OPV with a CuPc hole transport layer. When the interlayer is thin, the two-step exothermic charge transfer drives excitons to form larger CT states which frustrate geminate recombination.

While the absolute device efficiency in this work is low (limited by the short L_D of CuPc and the small E_{CT} at the D-A interface.), there could be broader applications for this concept in singlet fission devices or potentially in ternary bulk heterojunctions. For singlet fission materials, OPVs require a planar device architecture as singlet fission is an intermolecular process, which is highly sensitive to packing and coupling of adjacent molecules.[171] Typically, singlet fission is combined with a small gap triplet materials for long wavelength absorption.[172-173] For instance, Jadhav et al. have used CuPc to accept and

transport the triplet excitons of tetracene to CuPc-C_{60} interface.[174] Our design will allow these systems to improve V_{OC} and thereby device efficiency. Another potential area is morphology controlled ternary bulk heterojunction (BHJ) cells.[175] Formation of the third component located at interface has been reported several times and remains as an active research area of ternary OPVs.[176-178] These interfacial third component is likely acting as a discontinuous interlayer and our design will facilitate exciton harvesting at these partially separated interfaces.

6.5 Conclusions

This chapter presents a device architecture that exploits a triplet exciton permeable interlayer at the D-A interface in an OPV to spatially separate oppositely charged carriers while maintaining efficient exciton harvesting. By comparing three MPc donors with varying triplet levels, it is found that a larger donor triplet level facilitates exciton migration through interlayer. For CuPc-C_{60} planar devices, the interlayer is found to reduce the J_S and increase the $\tau_{\Delta n}$ and E_{CT}, leading to suppressed non-geminate recombination and an increased V_{OC}. The thin interlayer also creates an energy level cascade for hole transfer that results in the formation of relaxed CT states with reduced binding energy. This suppresses the geminate recombination and leads to an increase in short-circuit current density (J_{SC}). Overall, a 50% increase in device efficiency is realized in optimized (1-nm-thick) rubrene interlayer devices. The demonstrated exciton permeable interlayer design could have further application in singlet fission devices and ternary mixture systems when the

morphology of active materials can be accurately controlled.

6.6 Experimental Methods

Organic photovoltaic cells were fabricated using indium-tin-oxide (ITO)-coated glass substrates with a sheet resistance of ~8-12 Ω/□. Substrates were cleaned in tergitol solution and in organic solvents and treated in UV-Ozone ambient for 10 minutes prior to thin film deposition. All layers were deposited at room temperature by high vacuum thermal evaporation at a pressure of <8x10-7 Torr. All devices are capped with a 10-nm-thick exciton blocking layer (EBL) of bathocuproine (BCP) and a 100-nm-thick Al cathode. The active area of the obtained device is 0.785 mm2, defined by the cathode area. For this study, CuPc (99%), PbPc (99%), PtPc (99%) and rubrene (99%) were obtained from Lumtec Inc., C60 (99%) was obtained from MER Corporation, and BCP (98%) was obtained from Alfa Aesar. All materials were used as received without further purification.

Current density-voltage characteristics were measured in air with an Agilent 4155C parameter analyzer under AM1.5G (100 mW/cm2) solar simulated illumination from 150 W Oriel Xe lamp. All temperature-dependent experiments were carried out in a Janis cryogenic probe station with liquid nitrogen cooling under AM1.5G simulated solar illumination using a 300 W Oriel Xe solar simulator. Device temperature was monitored using a Si thermometer. External quantum efficiency measurements under bias were collected by measuring the photocurrent under monochromatic light illumination using a 300 W Oriel Xe lamp, a monochromator, an optical chopper wheel, and an SR810 lock-in

amplifier. The transient photovoltage (TPV) measurement was conducted using previously published methods (illumination area: 0.0176 cm2).[29-31] The devices for TPV measurements were fabricated on glass substrates pre-patterned with ITO for better electrical contact. The active area of the device is 0.25 cm2. Atomic force microscopy (AFM) measurements were performed on a Bruker Nanoscope V located in an argon glove box. AFM tips were aluminum-coated silicon nitride cantilevers with a nominal spring constant of 40 N m−1 and operated in AC mode, repulsive regime. All film thicknesses and optical constants were measured with a J. A. Woollam spectroscopic ellipsometer. Film thicknesses were fit using a Cauchy model.

7. Migration of Interfacial Charge-Transfer States

7.1 Background

In the last two chapters, CT states properties are engineered to suppress recombination losses in OPVs. In Chapter 5, crystalline D-A-A films facilitate the separation of CT states. In Chapter 6, the CT state size is increased by interlayer design, which reduces the binding energy of CT states and also the recombination losses. In this chapter, the transport of CT states, which has not been widely examined, is systematically investigated as it might lead to potential strategies to suppress geminate recombination losses in OPVs.

In a BHJ OPVs, CT states are generated in disordered D-A mixtures and possess different orientation upon exciton dissociation. The charge separation probability can be very different for these CT states depending on the local crystallinity, alignment with the electrical field, and energetic traps.[86] If CT states can migrate within the mixture, they might be able to reach other sites where charge separation is easier. Thus, a long-range CT migration can potentially facilitate free charge carrier generation and reduce geminate losses in OPVs. This leads to two key questions: whether CT states move and what the transport mechanism is if they do move.

While CT states were previously assumed to be immobile, recent studies have observed their diffusion.[179-180] Deotare et al. observed the motion of the emissive CT states formed in mixtures of m-MTDATA-3TPYMB and reported a diffusion length (L_D) of 5-10 nm for these states. However, whether CT states move in other organic system and the factors that impact their migration remain unclear.

7.2 Diffusion of CT States

Photoluminescence (PL) quenching has been used extensively to extract the diffusion length (L_D) of emissive Frenkel-type excitons, residing on just a single organic semiconductor molecule.[181-187] This technique has been adapted for the study of charge-transfer excitons, which are shared across the interface between donor and acceptor pairs, in this study with little modification.

A schematic of the photoluminescence (PL) quenching experiment for mobile CT states is shown in Figure 7.1. In this experiment, an emissive CT-forming D-A mixture would firstly absorb a photon and generate an exciton on either donor or acceptor component molecules. This local exciton rapidly undergoes exothermic charge transfer to form a CT state across the D-A interface. The newly formed CT then diffuse throughout the mixture. If the CT reaches the surface of an exciton quenching layer, it may undergo another exothermic charge transfer process dissociating the CT and quenching PL. Alternately, unquenched CTs may recombine providing PL.

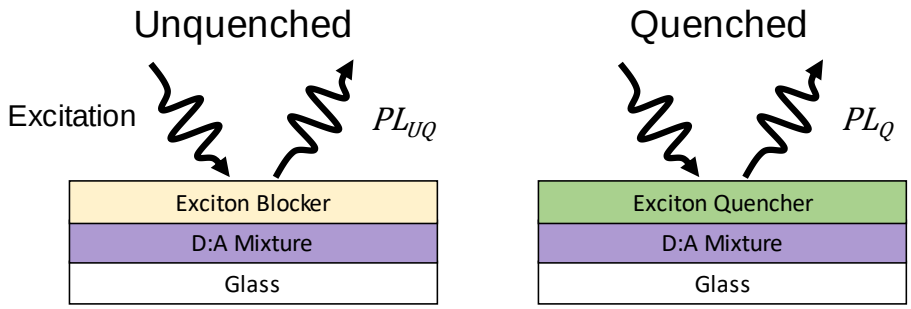

Figure 7.1 Schematic of photoluminescence (PL) quenching experiment.

In PL quenching, a pair of samples with differing neighboring interfaces are used to

probe CT emission in the presence and absence of quenching. An unquenched sample is fabricated by depositing a D-A mixture between exciton blocking layers, chosen to not dissociate or accept, through energy transfer, the mobile CT. A complementary sample with the top layer replaced with an exciton quencher is fabricated and the photoluminescence of each sample is compared. The ratio of total emission between quenched and unquenched samples defines a PL ratio which can be simulated using a standard one-dimensional diffusion with generation and recombination model.[48] Optical generation is treated using a transfer-matrix model for thin organic films described by Pettersson et al (discussed in Chapter 3). Iterative fitting for L_D between measured and modeled PL ratio characteristics across thickness allows for the extraction of CT L_D.

To verify PL quenching can be used for CT states, m-MTDATA-3TPYMB 1:1 mixed films with 10 nm 3TPYMB exciton blocking layers and 10 nm HATCN quenching layers are prepared. Their PL ratios are measured with optical excitation a wavelength of $\lambda = 370$ nm. Fitting yields a CT $L_D \sim 5$nm for the D-A mixture of 1:1 m-MTDATA-3TPYMB, consistent with earlier results of the same CT system.[179] This supports the application of PL quenching to the study of CT state diffusion and provides a simple technique to explore the motion of these states throughout D-A mixtures.

To understand the transport mechanism of CT states, m-MTDATA is also paired with other acceptor materials to determine the parameters that impact CT state diffusion. Figure 7.2a shows the molecular structures of acceptors tris(8-hydroxy-quinolinato)aluminum (Alq3), bathophenanthroline (BPhen) and bathocuproine (BCP) in addition to 3TPYMB. Figure 7.2b shows the emission spectra of 1:1 m-MTDATA-acceptor mixed films excited

at λ = 370 nm (m-MTDATA absorption). These mixed films all show broad emission with negligible m-MTDATA PL (peak at λ = 428 nm). This indicates optically excited m-MTDATA excitons are efficiently dissociated into CT states. Among these systems, m-MTDATA-BCP shows the bluest CT emission, reflecting the highest CT state energy.[102] Figure. 7.2c shows L_D of all four 1:1 m-MTDATA-acceptor systems as a function of CT emission peak energy. These results do not suggest a clear correlation between L_D and CT state energy. The m-MTDATA-BPhen system shows the longest L_D (= 6.5 nm) while it has lower CT state energy than both BCP and 3TPYMB cases. A similar donor sweep was also performed for the acceptor BCP to examine a larger range of CT state energy Besides m-MTDATA, BCP is paired with N,N'-bis(3-methylphenyl)-N,N'-diphenylbenzidine (TPD), 4,4'-cyclohexylidenebis[N,N-bis(4-methylphenyl)benzenamine] (TAPC) and tris(4-carbazoyl-9-ylphenyl)amine (TCTA). Figure 7.2d and e show the molecular structures of donor materials and emission spectra of the 1:1 donor-BCP mixed films. By replacing m-MTDATA with a deeper HOMO donor TCTA, the CT emission shows a significant blue shift by ~0.45 eV. Although the difference in CT state energy is relatively large for the donor-BCP systems, the measured CT state L_D has very similar values ~6 nm. This result further confirms that CT state energy is not a primary factor that determines the L_D of CT states.

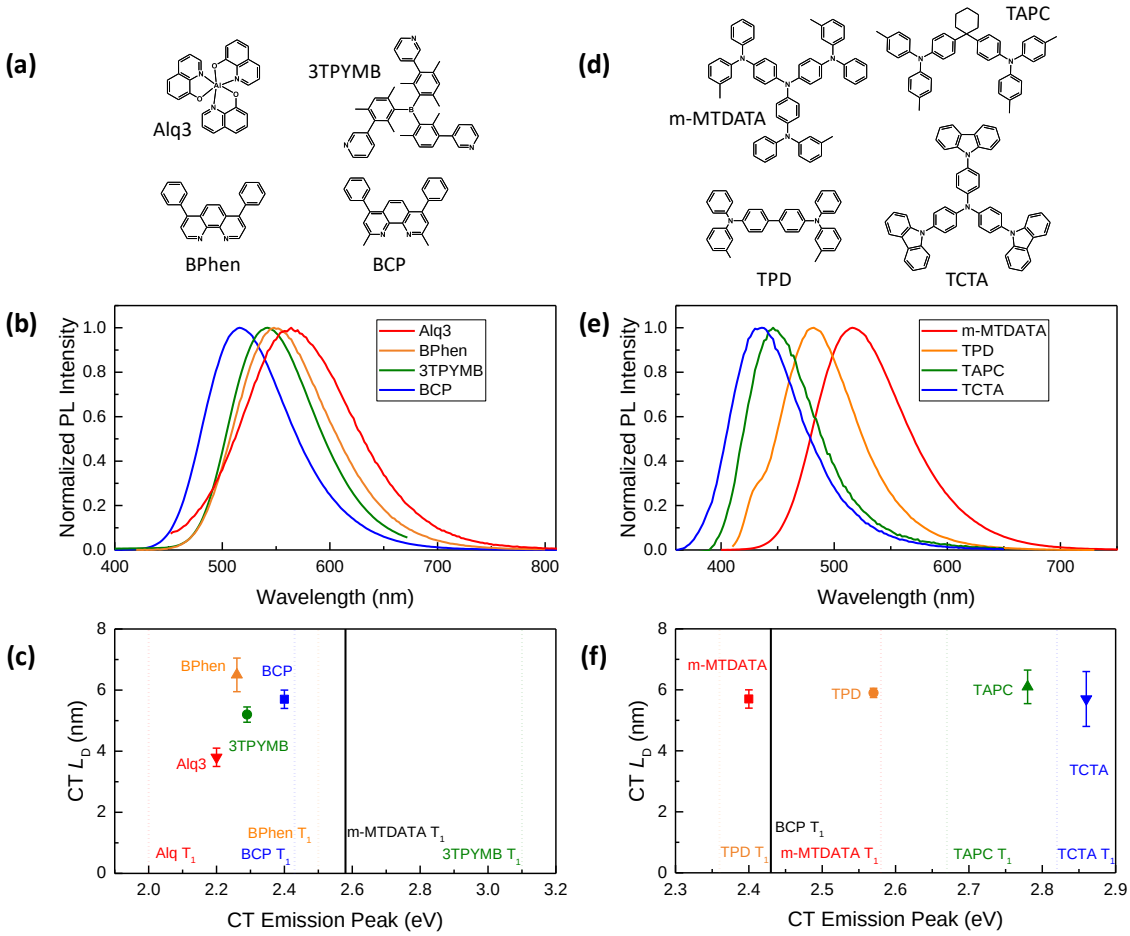

Figure 7.2 Acceptor sweep and donor sweep. (a) Molecular structures of acceptors, (b) Photoluminescence (PL) emission spectra, (c) CT state L_D measured by PL quenching as a function of CT emission peak energy for m-MTDATA-acceptor systems. (d) Molecular structures of donors, (e) PL emission spectra, (f) CT state L_D as a function of CT emission peak energy for donor-BCP systems. Triplet levels (T_1) of donor and acceptor materials are also plotted in (c) and (f). The L_D measurement for m-MTDATA-3TPBYB and m-MTDATA-Alq3 mixed films were performed and analyzed by Nolan Concannon.

For all the systems studied here, CT absorption is too weak to realize efficient CT to CT Förster energy transfer.[44] Also, the spectral overlap between CT emission and absorption of donor/acceptor materials is negligible so that CT state cannot Förster transfer to local singlet states and move as Frenkel excitons. As such, Förster energy transfer is

unlikely to be the transport mechanism for these CT states.[184] The CT state might undergo Dexter transfer directly to another CT state or to a local triplet state (as the singlet energy is too high) and move as Frenkel exciton.[86] For the latter case, accessibility to local triplet level is critical for CT state diffusion. For m-MTDATA-acceptor mixtures (Figure 7.2c), only the Alq3 system has a lower local triplet level than CT state energy.[188] However, its L_D is lower than all other three cases which have no local triplet state available.[179, 189-190] For the donor-BCP mixtures (Figure 7.2f), both the donor and acceptor triplet levels are lower than the corresponding CT states for the TPD, TAPC and TCTA systems. Yet these systems still show similar L_D to the m-MTDATA-BCP system with CT states as the lowest energy states. Based on these results, accessibility to local triplet states is also not a significant determinant of CT state diffusion. Direct Dexter transfer from a CT state to another CT state is, therefore, the remaining possible transport mechanism. This is consistent with previous work on m-MTDATA-3TPYMB system.[179] Deotare et al. observed a variation in electron-hole spacing during CT diffusion and suggested that the mechanism of CT motion is through asynchronous electron and hole transfer, whereby individual carrier transfer events lead to a net displacement of the bound interfacial exciton.[179]

If the CT state moves through an electron exchange mechanism at the D-A interface, motion of the slower component charge carrier can limit CT state diffusion as transport of both electron and hole is essential to complete each CT hopping process. This can explain the results of the donor sweep with the acceptor BCP. Based on previous reports, BCP has lower electron mobility than hole mobilities of donors shown in Figure 7.2d.[191-192] The

slow electron motion in BCP limits the CT diffusion and results in similar L_D regardless of the donors. Unlike the donor sweep, m-MTDATA-acceptor systems show more variation in CT state L_D and can be used to further exam the role of slow carriers.

To explore the relationship between CT diffusion and their component charge carrier transport properties, carrier mobilities of pure materials used in the acceptor sweep of this study were examined. Due to field enhancement of charge carrier mobility in organic semiconductors, the zero-field mobility is used to compare different material charge transport properties. Measurement of space-charge limited current (SCLC) has been used previously to extract carrier mobilities of a wide range of electron and hole transport materials for organic optoelectronics, including several materials used here.[51, 191-194]

Table 7.1 Equal m-MTDATA-Acceptor CT L_D and pure-component electron mobility for various acceptors.

Acceptor	L_D [nm]	Measured μ_0 [$cm^2\ V^{-1}\ s^{-1}$]	Literature μ_0 [$cm^2\ V^{-1}\ s^{-1}$]
BPhen	6.5	4.4×10^{-7}	[193] 5.5×10^{-7}
BCP	5.7	2.1×10^{-8}	[191] 2.3×10^{-8}
3TPYMB	5.0	1.3×10^{-9}	/
Alq_3	3.8	9.7×10^{-10}	[191] 4.7×10^{-9}

Space-charge limited current (SCLC) measurements for neat 3TPYMB films was performed by Nolan were performed and analyzed by Nolan Concannon

Table 7.1 lists the zero-field electron mobilities measured in this work and from literature for acceptor materials in Figure 7.2a. The values of the corresponding 1:1 D-A CT L_D are also listed for comparison. A correlation between acceptor electron mobility and CT L_D can be observed here. This serves as an initial observation comparing charge carrier

transport to CT transport, although other factors, such as CT lifetime may serve an outsized role in determining CT L_D. Due to the rich dynamics of CT excitons formed in D-A mixtures which are presently under detailed study and debate elsewhere,[179, 189] decoupling of diffusivity and lifetime for CT states cannot presently be accomplished. Thus, various D-A mixtures may only be compared at the level of diffusion length rather than more microscopic factors such as lifetime and diffusivity.

Zero-field hole mobility of m-MTDATA was also extracted from the measurement of SCLC, providing a value of ~$3 \cdot 10^{-6}$ cm^2/Vs against literature reports of ~$2 \cdot 10^{-6}$ cm^2/Vs, notably exceeding the electron mobilities seen above.[192] It is again suggested that for CT states formed in amorphous D-A mixtures of small molecules like those studied here that the low electron mobility of common acceptor materials is limiting to the effective transport of charge-transfer excitons.

7.3 Concentration Dependence

Besides the selection of active materials, changing composition of D-A mixtures can also tune charge transport properties and thus impact CT diffusion if the transport mechanism relies on charge carrier motion. Figure 7.3 shows the CT state L_D as a function of donor concentration for three different acceptors BPhen, BCP and 3TPYMB. The CT state L_D increases with decreasing donor concentration for all three systems. This agrees with our expectation for electron exchange CT transport mechanism since a lower concentration of donor materials can frustrate hole transport while facilitating electron

transport. When donor concentration is lower than 50%, electron and hole transport can be more balanced and therefore improve slowest carrier transport and CT state diffusion. For the donor rich regime where electron transport is slowed, L_D increases with neat acceptor electron mobilities listed in Table 7.1 and the difference in L_D values is larger than the acceptor rich case. This indicates that electron transport is a limiting factor for CT state diffusion in this region.

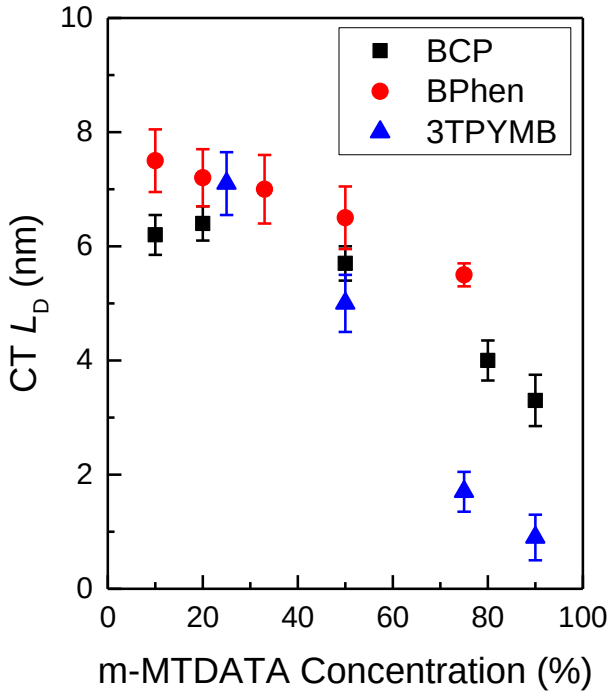

Figure 7.3 Impact of D-A composition. L_D of CT states as a function of donor m-MTDATA concentration for three acceptor materials BCP, BPhen, and 3TPYMB. The L_D measurements for m-MTDATA-3TPBYB mixed films with different donor concentration were performed and analyzed by Nolan Concannon.

To verify the relationship between carrier transport and CT state diffusion, carrier mobilities need to be measured for mixed films. In this study, the electron mobilities are

already very low for pure acceptor materials. It would be very challenging to measure electron mobilities accurately for donor rich mixed films. As such, m-MTDATA-BPhen system (highest mobility acceptor) is chosen as an example to investigate the impact of carrier mobility (diffusivity) on CT state diffusion.

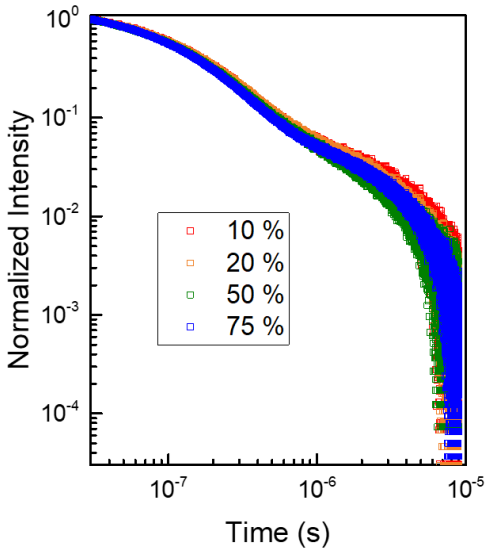

Figure 7.4. Transient PL decay as a function of donor concentration for m-MTDATA-BPhen heterojunction.

Figure 7.4 shows the transient PL decay of m-MTDATA-BPhen mixed films as a function of donor concentration. The PL represents the population of singlet CT states. Interestingly, the PL decay is almost the same with changing D-A composition. Although it is hard to extract lifetime for all the CT states (singlet and triplet),[189, 195] the same decay profiles suggest that CT lifetime does not vary with the composition of m-MTDATA-BPhen mixed films. The composition dependence of L_D is therefore only attributed to the changing CT state diffusivity.

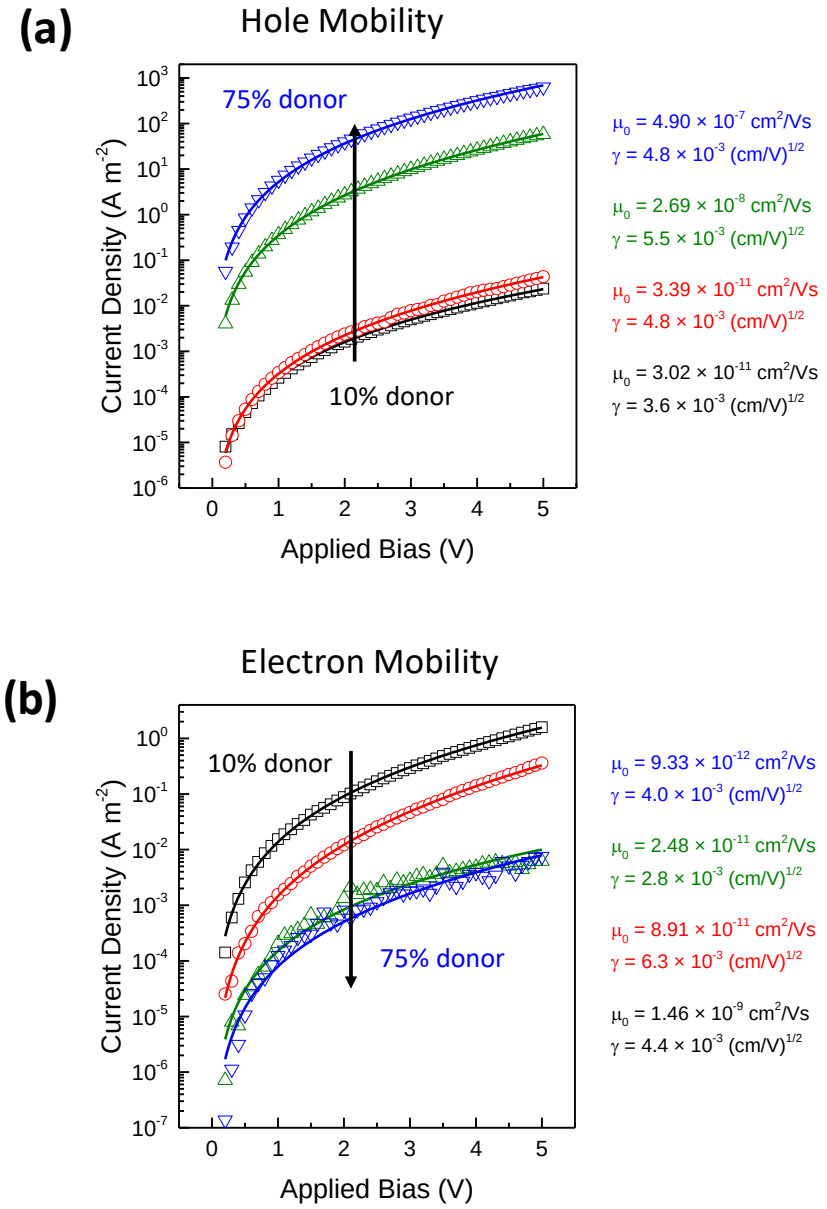

Figure 7.5 (a) Hole-only and (b) electron-only SCLC as a function of donor m-MTDATA concentration. The hole-only device has a structure: ITO/5 nm MoO_x/5 nm m-MTDATA/ 100 nm m-MTDATA-BPhen /5 nm m-MTDATA /5 nm MoO_x/100 nm Al. The electron-only device has a structure: ITO/30 nm Al/1 nm LiF/5 nm BPhen/100 nm m-MTDATA-BPhen/5 nm BPhen /1 nm LiF/100 nm Al.

Figure 7.5 shows the SCLC fitting for m-MTDATA-BPhen heterojunctions with

different donor concentration. The current density-voltage characteristics can be well fitted by to the model of SCLC with Poole-Frenkel enhancement:[196]

$$J = \frac{9}{8}\varepsilon_0\varepsilon_r\mu_0 \frac{E^2}{L} exp(0.89\gamma\sqrt{E}) \quad (7.1)$$

Here, E is the strength of the electric field within the mixed layer, and L is the thickness of the mixed layer, γ is the field activation parameter of mobility.

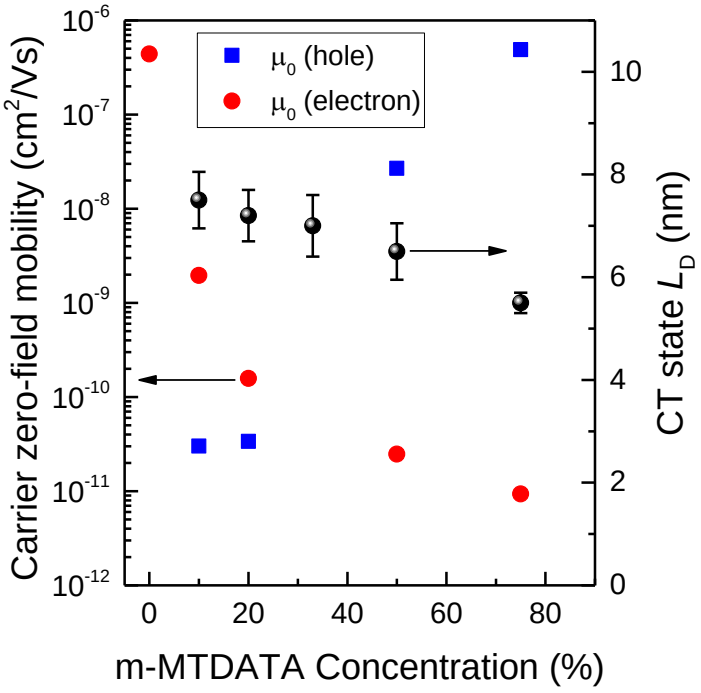

Figure 7.6 CT state L_D and zero-field charge carrier mobilities measured by SCLC as a function of m-MTDATA concentration for m-MTDATA-BPhen heterojunction.

Figure 7.6 shows the zero-field electron and hole mobilities extracted using Equation 7.1 as a function of donor concentration. The hole and electron mobilities drop rapidly upon dilution of donor and acceptor, respectively. Electron is identified as the slowest

carrier for 1:1 case and donor rich region while the hole becomes the slowest carrier in acceptor rich region. The mobilities of the slowest carrier increases and plateaus with decreasing donor concentration, consistent with the composition dependence of CT state L_D. This result further confirms that the transport of slower carrier determines diffusivity and thus L_D of CT states. To realize long-range transport of CT states, active materials with high charge carrier mobilities are essential

7.4 Conclusions

This chapter uses PL quenching to measure L_D of emissive CT states for various 1:1 D-A systems. By performing acceptor sweep experiment for donor material m-MTDATA, it is found that acceptor materials with better electron transport properties can result in a longer CT state L_D. Other factors like CT state energy, Förster energy transfer and accessibility to local triplet levels do not show a significant impact on CT state diffusion. Besides the selection of active materials, CT state L_D is also tunable by changing the composition of D-A systems. For three systems with relatively low electron mobility acceptor, CT L_D is found higher in acceptor rich films due to a better limiting carrier transport. In m-MTDATA-BPhen system, composition dependence of L_D is attributed to changing diffusivity of CT state as the CT lifetime is relatively stable across the composition. The SCLC measurements for this system reveal a correlation between CT L_D and mobility of the slowest carriers, suggesting that CT state motion is limited by its component carrier hopping along D-A interface.

7.5 Experimental Methods

4,4',4''-tris[(3-methylphenyl)phenylamino]triphenylamine (m-MTDATA >99%), 4,4'-cyclohexylidenebis[N,N-bis(4-methylphenyl)benzenamine] (TAPC >99.5%), bathocuproine (BCP >99%), bathophenanthroline (Bphen >99.5%), tri[3-(3-pyridyl)mesityl]borane (3TPYMB >99%), tris(8-hydroxyquinolinato)aluminum (Alq_3 >99.5%), and 1,4,5,8,9,11-hexaazatriphenylenehexacarbonitrile (HATCN >99%) were purchased from Luminescence Technology Corporation Inc. Molybdenum (VI) Oxide (MoO_3 99.5%) and Al pellets (99.999%) were purchased from Sigma-Aldrich Corporation. N,N'-Bis(3-methylphenyl)-N,N'-diphenylbenzidine (TPD 99%) and lithium fluoride (LiF 99.995%) were purchased from Alfa Aeser. 4,4',4"-tris(carbazol-9-yl)triphenylamine (TCTA 98%) was purchased from TCI Chemicals. All materials were used as received.

Samples for optical characterization were fabricated on glass substrates, while devices for electrical characterization were fabricated on glass substrates coated with a layer of indium-tin-oxide (ITO) from Xinyan Technology Ltd. with a sheet resistance of ~15 Ω per square. Substrates were cleaned sequentially in tergitol solution and organic solvents. Devices were exposed to UV-ozone for 15 min. All thin films were deposited by vacuum thermal evaporation at a base pressure below $8x10^{-7}$ Torr. Mixtures were deposited by co-deposition from multiple sources. All materials were deposited at rates of 0.1-2.5 Å/s. For electrical devices, a shadow mask was used to define a 1 mm diameter active area. To realize hole-only devices for space-charge limited current (SCLC) measurements, 5-nm-thick layers of MoO_x were deposited on either side of the organic active layer followed by

a 100-nm-thick Al top contact. For electron-only devices, 1-nm-thick layers of LiF were deposited on either side of the organic layer along with a 30-nm-thick Al bottom contact and a 100-nm-thick Al top contact.

Film thickness and optical constants were obtained using a J.A. Woollam variable-angle spectroscopic ellipsometer (VASE). Steady-state photoluminescence was measured using a Photon Technology International QuantaMaster 400 Fluorometer with excitation from a Xe lamp under illumination at 70º with respect to sample normal. Transient photoluminescence decays were measured using Thorlabs APD430A Avalanche Photodiode Detector recorded on a Tektronix TDS5104B Digital Phosphor Oscilloscope, with excitation from an Optical Building Blocks N_2 (λ=337.1 nm) laser operating at 3 Hz with attenuated 1.67 mJ pulses of ~1 ns in width. Current density-voltage characteristics were measured in the air using an Agilent 4155C parameter analyzer.

8. Probing Intrinsic Exciton Transport in Photovoltaic Cells

OPVs are particularly sensitive to exciton harvesting and are thus, a useful platform for the characterization of exciton diffusion. While device photocurrent spectroscopy can be used to extract the exciton diffusion length, this method is frequently limited by unknown interfacial recombination losses. With the understanding of CT states and recombination losses in OPVs, exciton transport and losses will be investigated in this chapter.

8.1 Background

Excitons are Coulombically-bound electron-hole pairs that serve as energetic intermediates in semiconductors. In many emerging semiconductor materials, the exciton and its properties feature prominently in determining device applications due to large binding energies that stabilize the exciton against thermally-driven dissociation[197-204]. Indeed, the high stability of the exciton has driven much research into the design of active materials and device architectures for organic light-emitting devices and organic photovoltaic cells (OPVs)[22, 205-210]. Recently, there has also been growing interest in manipulating exciton transport at semiconductor heterointerfaces for novel devices like excitonic transistors[179-180, 211]. For OPVs, in particular, excitons must migrate to a dissociating electron donor-acceptor interface, making exciton transport a critical step towards efficient photoconversion[31, 44, 149, 212-214]. Consequently, substantial previous work has been directed at both the measurement and engineering of the exciton diffusion length

(L_D). These efforts are essential as the scale of L_D dictates the optimal active layer thickness and domain size of D-A blends in planar (PHJ) and bulk heterojunction (BHJ) OPVs, respectively[215-219].

Probing exciton migration often relies on tracking the end-of-life products of excitons, including photons from exciton recombination and charge carriers from exciton dissociation[220-221]. For luminescent materials, L_D can be determined from a steady-state or time-resolved photoluminescence (PL)-based measurement[46, 184, 213]. Emitted photons reflect excitons that fail to reach the dissociating interface. While capable of yielding a materials-relevant value of L_D, this method is only sensitive to diffusive states that can decay radiatively and therefore cannot be applied to materials forming weakly emissive or dark excitons[222-224]. Since many high-performing active materials are weakly luminescent or dark[113, 136, 203, 207, 223], it is essential to develop more general means to accurately probe exciton transport in working devices.

A more general approach to extract L_D is by fitting the measured photocurrent (i.e. external quantum efficiency) spectrum of a bilayer OPV[30, 48, 225]. Device-based methods are typically preferred as they probe the L_D in a practical environment, as opposed to the often idealized structures utilized for PL measurements. This method is equally applicable to all excitons regardless of photoluminescence efficiency. Photoconversion can be considered in terms of four component processes, each with its own efficiency, namely light absorption (η_A), exciton diffusion and dissociation (η_D), charge transfer (CT) state separation (η_{CS}) and free carrier collection (η_{FC}). As such, with knowledge of η_{CS} and η_{FC}, coupled with an optical transfer matrix model for η_A, η_D and L_D can be extracted by fitting

with a diffusion equation. In practice, the values of η_{CS} and η_{FC} are not known, and frequently taken as unity or assumed to be fixed with changes in device architecture[30, 166, 226-228]. Thus, in general, the extracted value of L_D is thus a lower bound to the actual, materials-specific L_D. This limitation, coming from unknown geminate and non-geminate recombination losses, must be overcome in order to extract intrinsic, materials-specific values of L_D.

Recently, a technique based on transient photovoltage was reported to overcome the non-geminate recombination limitation on extracting L_D from OPVs[110, 116]. Photovoltage can be quantitatively translated into the number of free carriers stored within the device. For timescales much shorter than the carrier lifetime, the free carrier generation rate can be extracted from the initial photovoltage rise induced by illumination. The previously unknown η_{FC}, therefore, can be quantitively measured by comparing the results of photovoltage and photocurrent measurements. Interestingly, η_{FC} is found to be near-unity at short-circuit for many PHJ systems. Consequently, an inability to quantify geminate recombination loss is the primary factor frustrating accurate extraction of L_D in devices.

In this work, a device-based method is demonstrated. It can accurately measure the intrinsic value of L_D without the need to assume a value for η_{CS}. Previously, Vandewal et al. have shown that relaxed interfacial CT states (lowest energy) are the dominant source for free carrier generation in a wide range of D-A systems[106]. This conclusion is further confirmed by recent work by Kurpiers et al.[88]. The value of η_{CS} is thus independent of whether a carrier originates from the donor or acceptor exciton. As such, a ratio of the donor and acceptor internal quantum efficiencies (η_{IQE}) cancels this unknown quantity and

depends only on the exciton harvesting efficiencies (η_D) at short-circuit:

$$\frac{\eta_{IQE}^{D}}{\eta_{IQE}^{A}} = \frac{\eta_{D}^{D}\eta_{CS}}{\eta_{D}^{A}\eta_{CS}} = \frac{\eta_{D}^{D}}{\eta_{D}^{A}} \quad (8.1)$$

In order to model η_D, exciton diffusion is treated with a one-dimensional steady-state diffusion equation:

$$0 = D\frac{\partial^2 n(x)}{\partial x^2} - \frac{n(x)D}{{L_D}^2} + G(x) - n(x)k_F \quad with\ L_D = \sqrt{D\tau} \quad (8.2)$$

where n is the exciton density, D is the diffusion coefficient, τ is the exciton lifetime, and G is the optical exciton generation rate calculated by transfer matrix modeling. For systems with a spectral overlap of donor emission and acceptor absorption, the rate of donor-acceptor Förster energy transfer (rate constant: k_F) must be included. From the steady-state exciton density profile n(x), the η_D can be determined as:

$$\eta_D = 1 - \frac{\int n(x)/\tau\, dx}{\int G(x)dx} \quad (8.3)$$

By fitting the η_D ratio in Equation 8.1 as a function of active layer thickness, L_D values for the donor and acceptor materials can be extracted simultaneously.

Here, the photocurrent-ratio method is applied to extract L_D for a range of both luminescent and dark organic semiconductors, including both small molecule and polymer active materials. The broad utility of this approach is further demonstrated by also extracting L_D for thin films of colloidal, inorganic semiconductor quantum dots. In order to compare the results of the photocurrent-ratio method to well-established photoluminescence quenching methods, the archetypical donor-acceptor pairing of boron

subphthalocyanine chloride (SubPc) and C_{60} (Figure 8.1a) is first considered, where both active materials are luminescent. This system shows negligible non-geminate recombination loss at short-circuit[229-230], and prior work suggests that free carriers are likely generated from a single relaxed CT state[100], allowing Equation 8.1 to be applied. It is worth noting that in devices limited by non-geminate recombination, η_{FC} can be measured using transient photovoltage, leading to a modified, but equally useful form of Equation 8.1. For this luminescent pairing, it is demonstrated that the L_D values extracted using our device-based method are in excellent agreement with those extracted using conventional PL-based measurements. Importantly, it is further shown that the device-based method yields the intrinsic material L_D even for devices that suffer from very low efficiency.

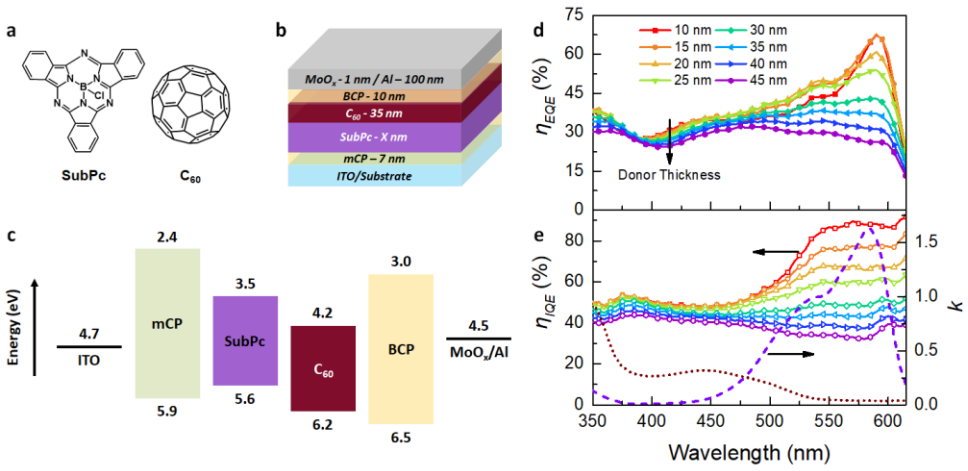

Figure 8.1 Device architectures and quantum efficiency spectra for SubPc-C_{60} planar OPVs. a, Molecular structure of SubPc and C_{60}. b, Device architecture for SubPc-C_{60} planar OPVs. The SubPc thickness X varies from 10 nm to 45 nm. c, Energy-level diagram for the devices in b. d, The η_{EQE} spectra measured at short-circuit as a function of SubPc layer thickness. e, The η_{IQE} spectra calculated by dividing the η_{EQE} spectra in d by the η_A calculated using a transfer matrix model. The extinction coefficients (k) of SubPc (purple dash line) and C_{60} (brown dot line) are also shown.

8.2 Extract L_D from a Ratio of Internal Quantum Efficiencies

To accurately measure L_D in bilayer OPVs, it is important to ensure that the only mechanism for exciton dissociation is at the donor-acceptor interface. Quenching at other interfaces or via bulk ionization will lead to errors in the extracted L_D. Figure 8.1b shows the SubPc-C_{60} PHJ OPV used for the measurement of L_D. The wide energy gap organic semiconductors 1,3-bis(carbazol-9-yl)benzene (mCP) and bathocuproine (BCP) are employed as exciton blocking layers (EBLs) to prevent exciton quenching at active layer-electrode interfaces. The exclusion of quenching at the electrodes is critical for accurate measurements of L_D as exciton loss is observed when SubPc is in direct contact with ITO or the commonly used buffer layer MoO_x.[137] A 1-nm-thick layer of MoO_x is used to increase the cathode work function and reduce the built-in electric field (E_{bi}) to exclude efficient exciton bulk ionization processes at short-circuit.[231] This is especially important for the SubPc-C_{60} system since both materials have been observed to show efficient free carrier generation in Schottky OPVs.[92, 232] While the application of a forward bias can also be used to reduce E_{bi}, the resulting carrier injection into the device could lead to exciton quenching, and an underestimate of L_D. It is worth noting that while a reduced E_{bi} could hinder the separation of relaxed CT states at the donor-acceptor interface, this work will demonstrate that this does not impact our measurement provided η_{CS} is identical for charges originating from both active materials.

Figure 8.1d shows external quantum efficiency (η_{EQE}) spectra for SubPc-C_{60} PHJ devices as a function of SubPc donor layer thickness with the acceptor and buffer layer

thicknesses held fixed. The η_A of the active materials calculated using a transfer matrix formalism allows the η_{EQE} spectra to be converted to η_{IQE} spectra (Figure 8.1e)[48]. To ensure the accuracy of the simulated η_A, the result from transfer matrix modeling is checked against experimentally determined device reflectivity (through the anode, reflecting off the cathode) measured at an incident angle of 15° to the substrate normal. The simulated 1-reflectivity (R) spectra (absorption of the device stack) agree well with experimental results as a function of donor thickness.[36] For the device with a donor thickness of 10 nm, the maximum η_{EQE} (at λ = 590 nm, SubPc absorption) exceeds 65% and the corresponding η_{IQE} is ~85%. This indicates that both exciton harvesting and charge collection are efficient in this device despite the reduced E_{bi}. From the extinction coefficients (k) of SubPc and C_{60}, spectral regions of dominant absorption for both donor and acceptor can be isolated. Accordingly, for the construction of the η_{IQE} ratio, the individual η_{IQE} of the donor and acceptor are extracted from λ = 575 nm (primarily SubPc absorption) and λ = 400 nm (primarily C_{60} absorption), respectively. Consistent with Equation 8.1, a η_D ratio (λ = 575 nm to λ = 400 nm) is calculated as a function of SubPc thickness (Figure 8.2a) which will be fit for L_D.

By fitting the η_D ratios in Figure 8.2a, L_D values for SubPc and C_{60} of L_D = (16.7 ± 1.7) nm and L_D = (18.5 ± 1.9) nm are simultaneously extracted. Due to the spectral overlap of SubPc PL emission and C_{60} absorption, donor-acceptor Förster energy transfer is included when using Equation 8.2. The SubPc-C_{60} Förster radius (R_0) have been previously measured to be 2.1 nm, consistent with the value of 2.1 nm calculated using Förster theory[46]. This R_0 is short compared to the intrinsic L_D of SubPc, thus it does not impact our L_D

measurement significantly since exciton diffusion is the dominant mechanism for harvesting in SubPc thin films.

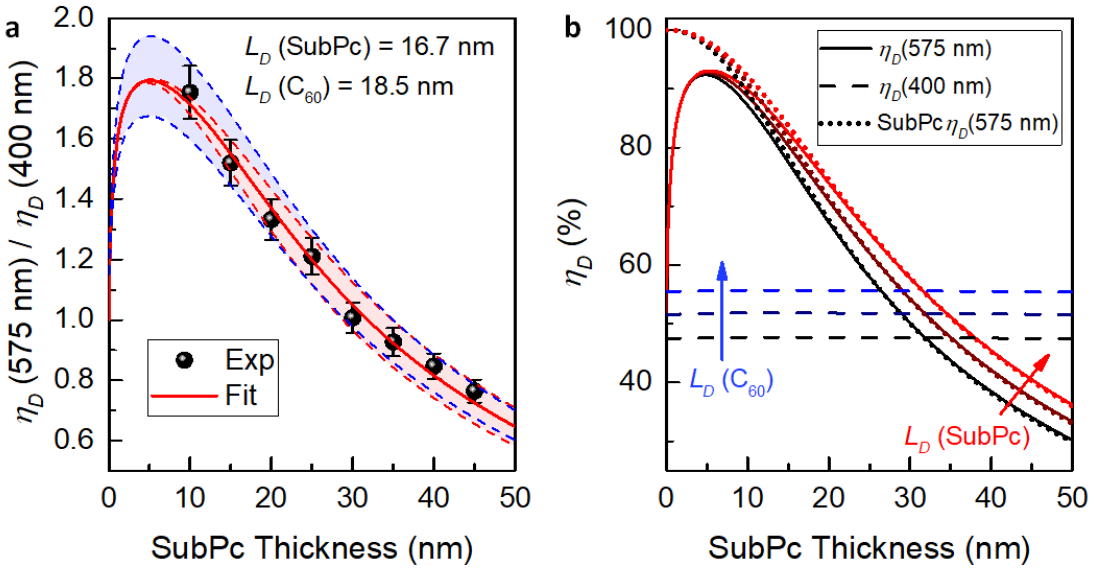

Figure 8.2 Extracting L_D from the thickness dependence of the diffusion efficiency ratio. a, Diffusion efficiency ratio ($\lambda = 575$ nm to $\lambda = 400$ nm) as a function of SubPc layer thickness with the corresponding exciton diffusion length (L_D) extracted from the fit (solid red line) to the data. Red (blue) dash lines are simulated diffusion efficiency ratio curves for a 10% change in extracted SubPc or C_{60} L_D while keeping the counterpart L_D fixed. b, Solid lines are the diffusion efficiency at λ = 575 nm as a function of SubPc layer thickness for different SubPc L_D (= 15.0/16.7/18.3 nm) and fixed C_{60} L_D = 18.5 nm. Similarly, the horizontal dash lines are the diffusion efficiency at λ = 400 nm for different C_{60} L_D (= 16.7/18.5/20.3 nm) and fixed SubPc L_D = 16.7 nm. The diffusion efficiencies of SubPc at $\lambda = 575$ nm are also plotted as dot lines.

As only the donor thickness is varied, the L_D of the donor and acceptor have different roles in determining the overall behavior of the η_D ratio as thickness changes (dash lines in Figure 8.2a). For example, if the SubPc L_D is varied by 10% (C_{60} L_D fixed), the resulting η_D ratios converge at small thickness while diverging at larger thickness, varying the shape of the dependence on thickness. Similar changes in the C_{60} L_D (10%, SubPc L_D fixed) lead

only to changes in the magnitude of the η_D ratio leaving the shape unchanged. To show this more explicitly, the values of η_D at λ = 575 nm and 400 nm are plotted as a function of donor thickness in Figure 8.2b.

The observation of a constant acceptor η_D with increasing donor thickness offers some inherent advantages. First, the L_D of the donor and acceptor can be fit independently, as the shape of the η_D ratio (or normalized η_D ratio) only depends on donor L_D. As such, any non-ideality in acceptor L_D measurement, such as exciton loss at the acceptor-cathode interface, would not reduce the accuracy of donor L_D provided free carriers are still only generated at the D-A interface. In addition, the relative change in η_{CS} with donor thickness is directly reflected by the acceptor η_{IQE}. Accordingly, the decrease in η_{IQE} (400 nm) with SubPc thickness (Figure 8.1e) indicates that a thicker donor layer leads to a lower η_{CS}. This is likely due to an increase in bulk resistance of the donor layer that consumes more built-in voltage and thus reduces the electric field strength at D-A interface[86].

8.3 PL-Based L_D Measurements

To determine whether the L_D extracted from the η_{IQE} ratio is intrinsic, conventional PL-based measurements are carried out for both SubPc and C_{60}. In many previous studies, η_{EQE}-based measurements of L_D have not been in agreement with those extracted from PL due to geminate recombination losses[110, 229], which are in general not negligible. If the recombination limitations are fully overcome in the method described here, these measurements should yield the same L_D.

For luminescent SubPc, the intrinsic L_D is extracted using thickness-dependent PL quenching and compared to the result obtained using the photocurrent-ratio method. In order to make a proper comparison, PL-quenching measurements are carried out on the identical device architecture used to measure L_D via η_{IQE} (Figure 8.3a). Light having a wavelength of λ = 500 nm is incident through the ITO anode at an angle θ of 70°. As the emitted photons represent the excitons that fail to reach D-A interface, the PL intensity can be expressed as:

$$PL = \eta_A(1-\eta_D)(I_{in}\eta_{PL}\eta_{det}) \quad (8.4)$$

where I_{in} is the incident photon flux, η_{PL} is the photoluminescence efficiency, η_{det} is the detection efficiency for all the emitted photons. Typically, L_D is extracted by fitting a ratio of the integrated PL of a quenched sample (Q) and an unquenched sample (UQ). This PL ratio reflects the number of recombining excitons (i.e. not collected at the quenching interface) under steady-state:

$$\frac{PL^Q}{PL^{UQ}} = \frac{\eta_A^Q(1-\eta_D^Q)(I_{in}\eta_{PL}\eta_{det})}{\eta_A^{UQ}(I_{in}\eta_{PL}\eta_{det})} = \frac{\eta_A^Q(1-\eta_D^Q)}{\eta_A^{UQ}} \quad (8.5)$$

The η_A and η_D can be simulated using a transfer matrix formalism and a diffusion model as previously described. Here, the SubPc-C_{60} PHJ devices in Figure 8.1b are used as quenched samples, with C_{60} acting as the quencher.

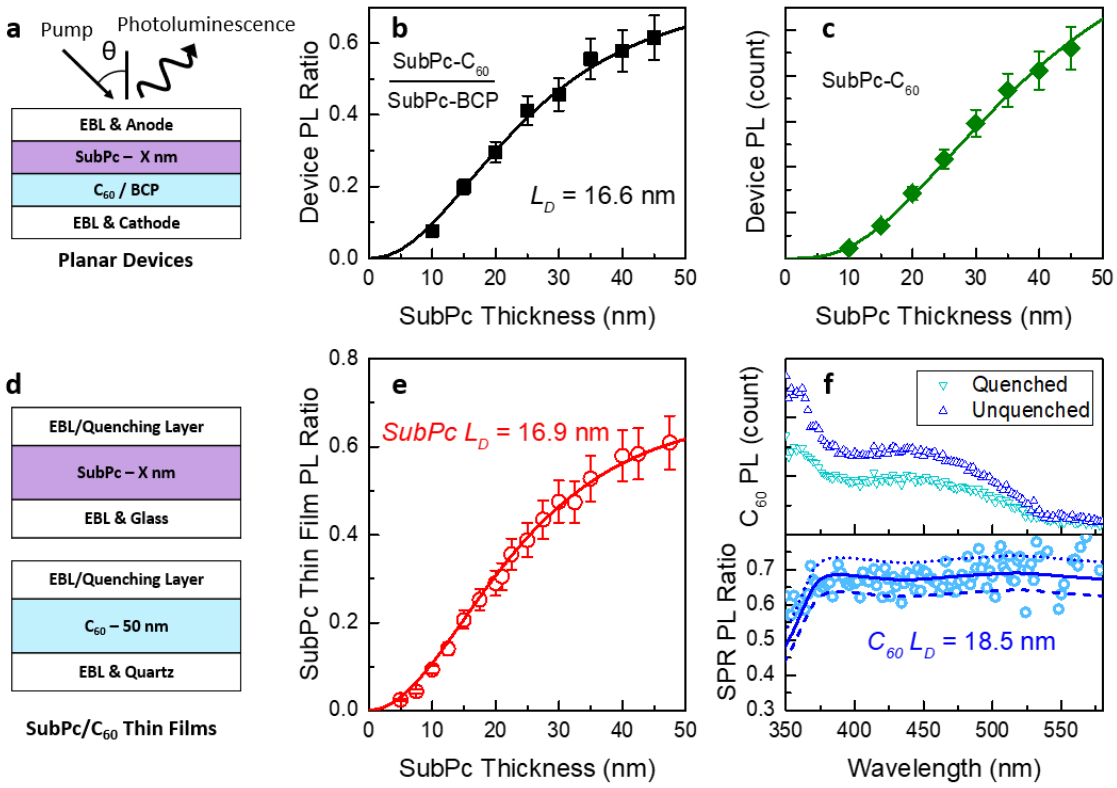

Figure 8.3 Photoluminescence-based measurements of exciton diffusion length. a, OPVs used for the extraction of L_D via photoluminescence (PL) quenching having the structure: ITO/7 nm mCP/X (=10-45) nm SubPc/35 nm C_{60} (quenched) or BCP (unquenched)/10 nm BCP/1 nm MoO_x/100 nm Al. The quenched samples are the same set of devices used for internal quantum efficiency measurements. b, PL ratio defined in Equation 8.5 versus SubPc thickness. c, SubPc PL intensity of the quenched samples versus SubPc thickness. The solid line is fit of the data using Equation 8.4. d, Architectures for conventional thin film PL ratio L_D measurements of SubPc and C_{60}. SubPc architectures have the structure: glass/10 nm mCP/X (=5.0-47.5) nm SubPc/10 nm HATCN (quenched) or mCP (unquenched) while C_{60} architectures have the structure: quartz/10 nm BCP/50 nm C_{60}/10 nm HATCN (quenched) or BCP (unquenched). e, The PL ratio of SubPc films as a function of SubPc thickness. f, Excitation spectra (upper panel) for the quenched and unquenched C_{60} films at an emission wavelength of 750 nm. The resulting spectrally resolved (SPR) PL ratio versus pump wavelength is shown in lower panel. SubPc films and devices are all pumped with λ = 500 nm light. The incident angle is 70° for all incident light.

A set of unquenched samples (η_D = 0) are fabricated by replacing acceptor C_{60} with the exciton blocking material BCP. The resulting PL ratio is plotted in Figure 8.3b and fit

as a function of SubPc thickness, yielding a SubPc L_D of (16.6 ± 2.0) nm. Clearly, the photocurrent-ratio and PL-based measurements conducted on the same set of devices show excellent agreement for the extracted L_D. This agreement suggests that the charge recombination present in the device-based measurement does not limit our ability to extract L_D. To further verify the extracted value of L_D, the L_D values determined by the PL ratio are used to simulate the PL of quenched devices with Equation 8.4. Figure 8.3c shows the integrated device PL of SubPc-C_{60} PHJ devices as a function of SubPc thickness. Taking the prefactor ($I_{in}\eta_{PL}\eta_{det}$) as independent of SubPc thickness, the experimental results are in good agreement with the simulation using L_D = 16.6 nm for SubPc.

In most reports of PL-based measurements of L_D, actual device architectures are not utilized, replaced instead with simple film stacks. In this configuration, exciton dissociation due to bulk-ionization is negligible due to the absence of electrodes. If bulk-ionization in SubPc is negligible for the devices in Figure 8.1b, L_D values for SubPc extracted from device and thin film PL should agree. As shown in Figure 8.3d, SubPc thin films are deposited on a 10-nm-thick mCP/glass substrate to ensure the SubPc film morphology is similar to the device-based measurement. The quenched films are capped with a 10-nm-thick layer of 1,4,5,8,9,11-hexaazatriphenylene hexacarbonitrile (HATCN) while the unquenched films are capped with a 10-nm-thick layer of mCP.[67] Based on the thickness dependent PL ratio of Figure 8.3e, an intrinsic L_D of (16.9 ± 2.0) nm is determined for SubPc. This value is larger than previous reports of the SubPc L_D, which is ~10 nm[46, 70, 187]. However, previous studies typically deposit SubPc directly on an inorganic substrate such as glass as opposed to a wide energy gap organic buffer layer. By removing the 10-nm-

thick mCP layer beneath the SubPc for unquenched samples, a reduction in η_{PL} is observed, suggesting a difference in the morphology of SubPc on different substrates.

For weakly luminescent C_{60}, a thin layer can result in a very low signal to noise ratio, which increases error for the extraction of L_D. As such, we employ a 50-nm-thick C_{60} layer and use spectrally resolved (SPR) PL quenching instead of thickness dependent PL quenching[187]. We also use quartz as the substrate to further reduce the background noise. Figure 8.3f shows PL excitation spectra for the quenched and unquenched C_{60} films at an emission wavelength of $\lambda = 750$ nm. The PL ratio is fit as a function of incident excitation wavelength, yielding an intrinsic L_D of (18.5 ± 3.0) nm for C_{60}. The excellent consistency of results between thin film and device-based measurements further confirm that an intrinsic L_D can be accurately measured using the η_{IQE}-based approach reported here. This agreement also suggests that there are no other diffusive dark states in SubPc and C_{60} that contribute to photocurrent since the photocurrent-ratio measurement probes both dark and emissive excitons while the PL-based measurement is only sensitive to emissive states.

8.4 Relaxation Losses from Bulk CT Excitons in C_{60}

With the L_D of SubPc and C_{60} extracted from device photocurrent spectra shown to be intrinsic, materials-relevant quantities, these values can be used to accurately simulate exciton diffusion and recombination losses in OPVs. The unknown geminate recombination loss (η_{CS}) that was circumvented in Equation 8.1 by taking a ratio of η_{IQE} values can now be calculated as the ratio of η_{IQE} to the calculated η_D. Figure 8.4a shows

the simulated η_{EQE} spectra for SubPc-C_{60} PHJ devices using the L_D extracted in Figure 8.1b, and the extracted η_{CS}. The simulated η_{EQE} spectra agree well with experimental results except for the wavelength range of λ = 410 - 550 nm. The observed η_{EQE} overestimation indicates the presence of a photocurrent loss pathway prior to exciton diffusion, or stated differently, the exciton relaxation yield is not unity. It also worth noting the clear reduction in η_{CS} with increasing donor layer thickness, likely reflecting a reduction in E_{bi}.

To identify whether the exciton relaxation loss is from SubPc or C_{60}, a second donor-acceptor system of SubPc-NPD is examined where SubPc serves as the electron acceptor (or hole donor)[203]. To ensure that the SubPc morphology is unchanged, an inverted device architecture is employed (ITO/7 nm mCP/X nm SubPc/35 nm NPD/10 nm mCP/3 nm MoO_x/100 nm Al) so that SubPc is still deposited on mCP. In these devices, the electron acceptor SubPc has low electron mobility, which can lead to significant recombination losses due to slow CT state separation[99]. The SubPc η_{IQE} (from λ = 525 nm) and NPD η_{IQE} (from λ = 385 nm) are both very low (< 8%). By fitting the η_D ratio as a function of SubPc thickness, an L_D of (15.2 ± 2.0) nm is obtained for SubPc, close to the value extracted from the SubPc-C_{60} system despite significantly increased recombination losses. This result illustrates the power of the photocurrent-ratio technique, even in a low-efficiency device with substantial recombination loss, the correct, intrinsic value of L_D is extracted. For the NPD dominant absorption region, an η_D (385 nm) = 47.1% is determined. Due to the large spectral overlap between NPD fluorescence and SubPc absorption, the dominant exciton harvesting mechanism within the NPD layer is Förster energy transfer to SubPc instead of exciton diffusion. In order to extract the L_D of NPD, a partner material should be chosen

with reduced spectral overlap. Figure 8.4b shows the simulated η_{EQE} spectra for SubPc-NPD PHJ devices based on the parameters extracted. Unlike the SubPc-C_{60} case, simulated and experimental η_{EQE} spectra show broadband agreement as a function of SubPc thickness. This suggests that the exciton relaxation losses in SubPc-C_{60} devices originate only from excited states in C_{60}.

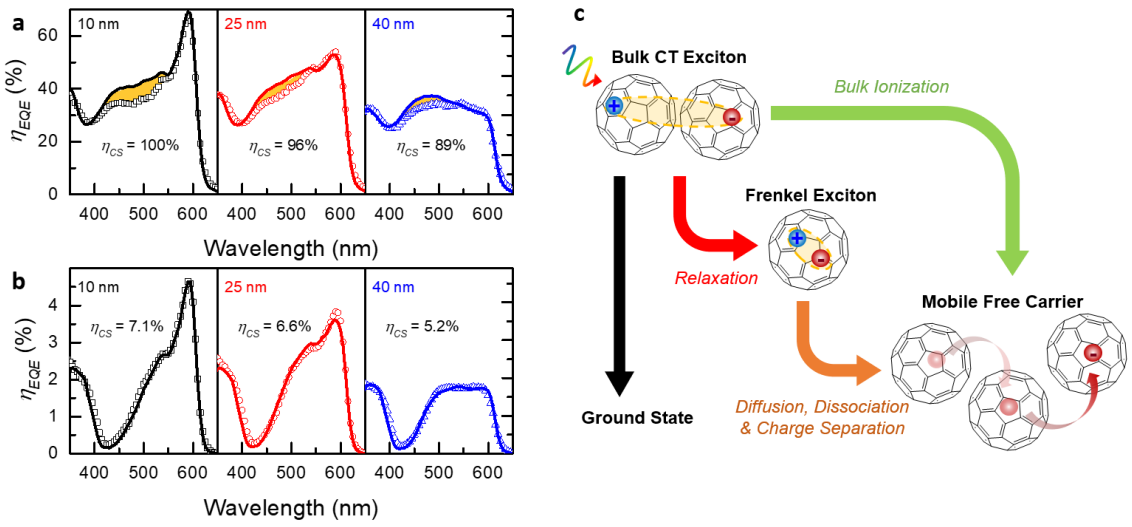

Figure 8.4 Simulation of external quantum efficiency for extraction of recombination loss. a, External quantum efficiency spectra for SubPc-C_{60} planar OPVs as a function of SubPc thickness (10, 25 and 40 nm). Experimental results are shown in symbols while solid lines are simulated spectra. b, The experimental (symbols) and simulated (solid lines) external quantum efficiency spectra of SubPc-NPD planar OPVs versus SubPc thickness. c, Schematic of free carrier generation in C_{60} from a photo-excited bulk CT exciton. The bulk CT excitons absorb over the wavelength range of $\lambda \sim$ 410-550 nm, while the low energy Frenkel excitons correspond to absorption at $\lambda >$550 nm.

Interestingly, the region (λ = 410 - 550 nm) where exciton relaxation losses are observed is consistent with the broad absorption peak of C_{60} bulk CT excitons[233]. These bulk CT excitons can be photoexcited directly and their absorption ($\lambda_{peak} \sim$ 450 nm) has been observed to decrease drastically when diluting C_{60} in thin film or solution[208, 234]. This

spectral agreement indicates that high energy bulk CT excitons do not uniformly relax to lowest energy Frenkel excitons in C_{60} despite their reasonably large energy difference (~0.5 eV). For the C_{60} bulk CT excitons that fail to relax, they may still contribute to photocurrent through bulk-ionization (Figure 8.4c), especially in devices with high built-in fields. As such, both relaxation loss and bulk-ionization of bulk CT excitons must be considered in order to accurately simulate broadband η_{EQE} spectra of C_{60}-based planar OPVs.

8.5 Dark Small Molecules, Polymers, Quantum Dots

With the photocurrent-ratio method thoroughly vetted against conventional PL approaches for SubPc-C_{60}, we investigate exciton transport in two dark small molecule materials, boron subnaphthalocyanine chloride (SubNc) and C_{70} (Figure 8.5a). While these materials have been frequently utilized in high-efficiency OPVs, their intrinsic L_D has not been directly measured as they are inaccessible by PL-based techniques[67, 203, 207, 235]. Similar to the SubPc-C_{60} system, we employ a SubNc-C_{70} PHJ device with varying donor thickness to extract the intrinsic L_D of both dark materials (structure: ITO/8.5 nm mCP/X (=9-40.5) nm SubNc/27 nm C_{70}/11 nm BCP/1 nm MoO_x/100 nm Al). Based on the extinction coefficients (k) of SubNc and C_{70} shown in Figure 8.5b, the individual η_{IQE} of the donor and acceptor can be extracted from λ = 685 nm (SubNc absorption peak) and λ = 430 nm (primarily C_{70} absorption), respectively. By fitting the donor-acceptor η_D ratio (determined as previously described) as a function of SubNc thickness (Figure 8.5c), we simultaneously extract an L_D of (21.2 ± 2.2) nm for SubNc and an L_D of (7.4 ± 0.8) nm for

C_{70}. The longer L_D of SubNc compared to SubPc (L_D = 16.7 nm) is consistent with previous observations based on the PL of dilute solid solutions[67]. The extracted L_D for C_{70} is significantly smaller than that of C_{60} (L_D = 18.5 nm). To better understand this difference, further work is needed to investigate differences in exciton lifetime and spin state between these fullerenes. Unlike the SubPc-C_{60} case, the simulated broadband η_{EQE} spectra of SubNc-C_{70} OPVs agree well with the experimental results, suggesting negligible exciton relaxation loss in C_{70}. This result may reflect a reduced CT state character for excitons in C_{70}.

To demonstrate the applicability of the photocurrent-ratio method in other excitonic systems, we also show two examples measuring exciton transport in solution processed PTB7 polymer films and inorganic CdSe quantum dot (QD) films. PTB7 is a high performing polymer electron donor in OPVs, with demonstrated power efficiencies as high as 9.2% when combined with the fullerene acceptor $PC_{71}BM$[236]. Here, we employ it as an electron donor material paired with fullerene acceptor C_{60}. Figure 8.5d shows the PTB7-C_{60} η_D ratio as a function of PTB7 thickness obtained from planar OPVs with a structure: ITO/2.5 nm HfO_2/X (=12-59) nm PTB7/37 nm C_{60}/10 nm BCP/1 nm MoO_x/100 nm Al. A thin layer of wide energy gap HfO_2 is utilized as an exciton blocking layer at ITO/donor interface (deposited via atomic layer deposition). The donor η_{IQE} is extracted from λ = 670 nm (PTB7 absorption peak) while the acceptor η_{IQE} is extracted from λ = 350 nm (C_{60} Frenkel exciton absorption peak).

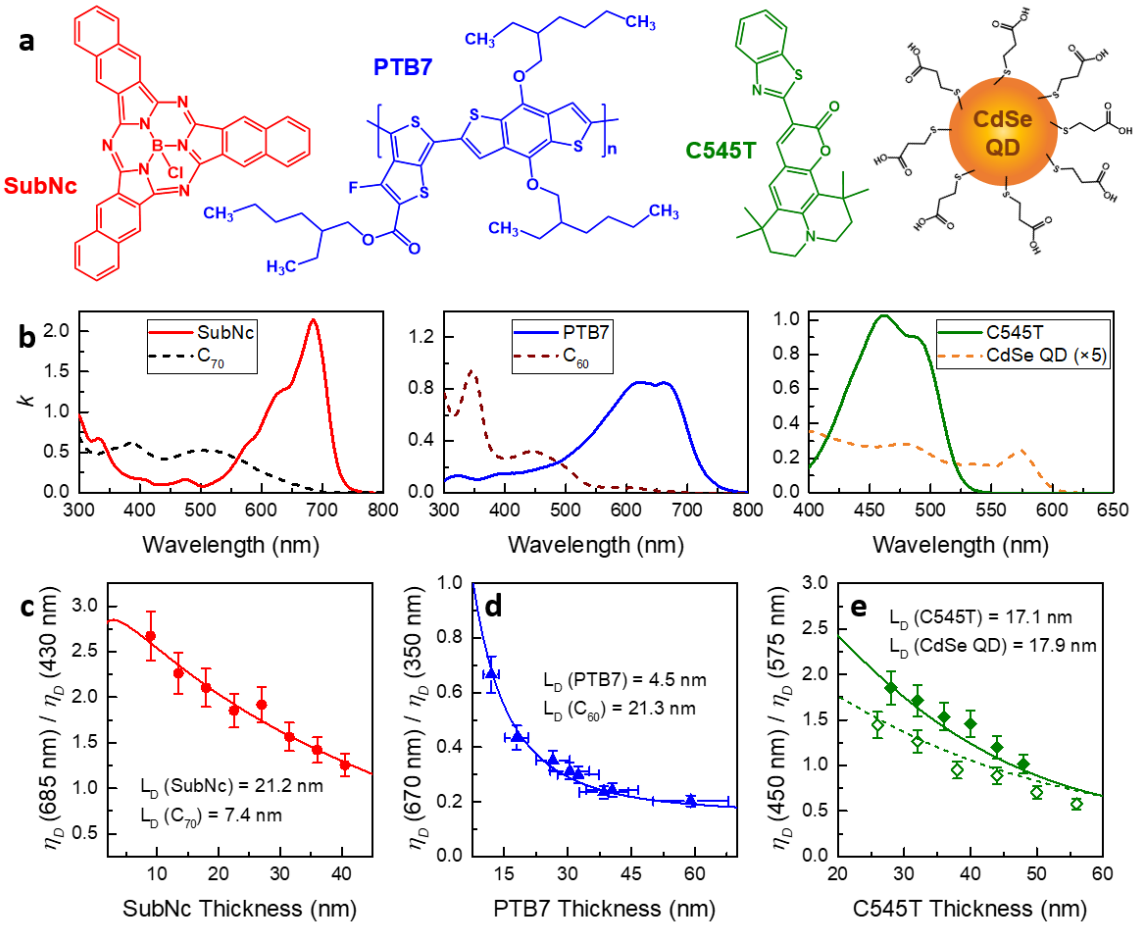

Figure 8.5 Measuring L_D of dark small molecules, polymers and quantum dots a, Molecular structure of SubNc, PTB7, C545T and schematic of a CdSe quantum dot (QD) with 3-MPA ligands on the surface. b, The extinction coefficients (k) of SubNc, C_{70}, PTB7, C_{60}, C545T, and CdSe QD thin films. The k of QDs is shown with a 5-fold magnification. c, Diffusion efficiency ratio (λ = 685 nm to λ = 430 nm) as a function of SubNc layer thickness with the corresponding exciton diffusion length (L_D) extracted from the fit (solid line) to the data. d, Diffusion efficiency ratio (λ = 670 nm to λ = 350 nm) as a function of PTB7 layer thickness. e, Diffusion efficiency ratio (λ = 450 nm to λ = 575 nm) as a function of C545T layer thickness and CdSe QD thickness (solid symbols: 66 nm QD layer; open symbols: 42 nm QD layer). The L_D values are extracted by fitting both sets of data simultaneously (solid line: fit for 66 nm QD devices; dash line: fit for 42 nm QD devices).

As negligible exciton relaxation loss is observed at λ = 350 nm in the previous SubPc-C_{60} case (Figure 8.4a), it is assumed that C_{60} has 100% exciton relaxation yield at this

wavelength. Fitting the η_D ratio in Figure 8.5d yields a short L_D of (4.5 ± 0.5) nm for PTB7 and an L_D of (21.3 ± 2.2) nm for C_{60}. The C_{60} L_D is similar to the value extracted from the SubPc-C_{60} system (18.5 nm).

For CdSe QD thin films, the QDs are zincblende nanocrystals (size ~4 nm) stabilized with 3-mercaptopropionic acid (3-MPA) after treatment via solid-state ligand exchange[237]. The resulting thin films have a very low extinction coefficient (k = 0.05 at excitonic peak, λ = 575 nm), and are therefore paired with a wider energy gap small molecule 2,3,6,7-tetrahydro-1,1,7,7,-tetramethyl-1H,5H,11H-10-(2-benzothiazolyl)quinolizino[9,9a,1gh]coumarin (C545T) which does not absorb at λ = 575 nm. Wide gap materials HfO_2 and di-[4-(N,N-di-p-tolyl-amino)-phenyl]cyclohexane (TAPC) are utilized as exciton blocking layers for CdSe QDs and C545T, respectively. The CdSe QD-C545T planar cell has an inverted device architecture: ITO/2.5 nm HfO_2/X (=42, 66) nm CdSe QD/Y (=26-56) nm C545T/11 nm TAPC/10 nm MoO_x/100 nm Al, where the CdSe QDs serves as the electron acceptor layer and photogenerated electrons are collected at ITO. It is again worth noting the ability of the photocurrent-ratio method in yielding intrinsic values of L_D even in devices with low efficiency. This allows active materials to be selected solely on the basis of realizing a minimal overlap in optical absorption. The QD film thickness is controlled by the number of cycles for the ligand exchange process[237]. Figure 8.5e shows the C545T-CdSe QD η_D ratio as a function of C545T thickness for two different QD film thicknesses. The donor η_{IQE} is extracted at λ = 450 nm (C545T absorption peak) while the acceptor η_{IQE} is extracted at λ = 575 nm (QD excitonic absorption peak). Results for devices with QD layer thickness of 42 nm and 66 nm are fitted simultaneously,

yielding an L_D of (17.9 ± 3.6) nm for the CdSe QDs and an L_D of (17.1 ± 3.4) nm for C545T. It is worth noting that the L_D of C545T extracted here is consistent with separate PL-based measurements we have carried out (16.7 nm). If instead the η_D ratio is fit for each QD thickness, the 42 nm (66 nm) QD-C545T devices yield an L_D of 18.7 nm (15.5 nm) and 19.8 nm (16.8 nm) for the QDs and C545T, respectively. The L_D of CdSe QDs extracted here is smaller than that previously reported for CdSe core-shell counterparts (20-40 nm)[238-239], likely reflecting that a wide gap shell is critical to frustrate exciton decay and enhance exciton transport for CdSe QDs.

8.6 Singlet Fission Materials

As the photocurrent-ratio method can probe dark exciton transport, it allows a better understanding of dark triplet exciton transport in singlet fission materials. Singlet fission is a process that converts a singlet exciton to two triplet excitons. It has been observed in a select number of organic semiconductors with their triplet exciton energy roughly half of the singlet exciton energy ($E(S_1) \approx 2E(T_1)$).[171, 173, 249-250] As briefly mentioned in Chapter 6, singlet fission materials are typically paired with narrow gap light absorbers to reduce thermalization energy loss in PVs (introduced in Chapter 3), a potential strategy to overcome the Shockley-Queisser limit.[172, 240] Pentacene (Pc) is one of the most common singlet fission materials. The fission process is exothermic for Pc ($E(S_1) > 2E(T_1)$, Figure 8.6a), leading to rapid fission in timescales ~80 fs and a high triplet quantum yield (η_T) ~200%.[223, 241] OPVs based on Pc has demonstrated >100% η_{EQE} when using optical

trapping design.[223] However, there is energy loss during the exothermic fission process in Pc ($E(S_1) - 2E(T_1) = 0.11$ eV, $E(S_1) = 1.86$ eV).[242-243] An ideal singlet fission material should achieve high η_T with negligible energy loss or even when the fission is slightly endothermic.

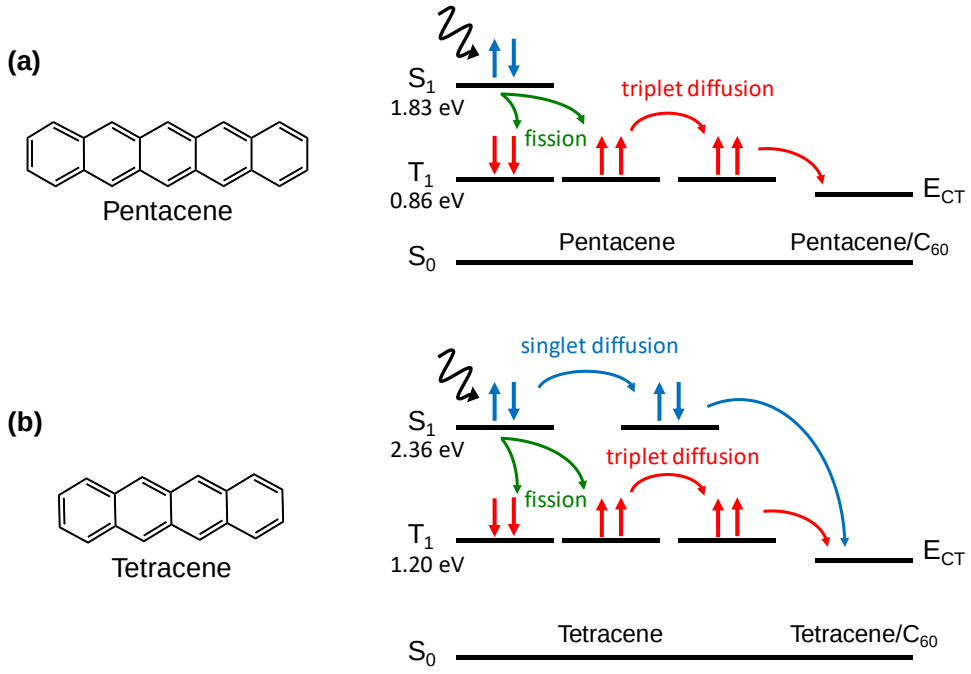

Figure 8.6 Singlet fission in pentacene and tetracene. (a) Exothermic fission process in pentacene leads to complete conversion from singlet to triplet states, only triplet excitons contribute to photocurrent when paired with C_{60} in OPVs. (b) Endothermic fission process in tetracene leads to incomplete singlet-triplet conversion. Both singlet and triplet can contribute to photocurrent in tetracene-C_{60} OPVs.

Singlet fission is a multi-step process. Firstly, a singlet state on one molecule interacts with a ground state neighboring molecule and form the triplet pair state. The triplet pair state then separates into two individual triplet excitons as they move away from each other.[171, 244] As such, the transport of triplet exciton plays an importance role in singlet fission and impact the η_T. However, it is challenging to probe triplet diffusion since triplet

states are dark.[245] There were attempts to probe triplet exciton diffusion from singlet emission since triplet states can convert back to singlet states when triplet exciton density is high enough to trigger triplet-triplet fusion process.[245-248] Singlet diffusion, triplet diffusion, singlet fission and triplet fusion are all taking place in these measurements, making the exciton dynamics complicated to model. As the photocurrent-ratio measurement can probe dark exciton transport directly, it allows accurate measurement of triplet exciton L_D for singlet fission materials in a simpler scenario (low triplet exciton population) without fission and fusion during the diffusion. Here, the triplet L_D of exothermic fission material Pc is measured directly with photocurrent-ratio method. For endothermic fission material tetracene (Tc), both singlet and triplet excitons can contribute to photocurrent when exciting Tc optically (Figure 8.6b).[174] In order to probe intrinsic triplet L_D directly, a triplet injection layer design is introduced to selectively excite the triplet states and isolate the role of triplet transport.

8.6.1 Photocurrent-Ratio Measurement for Pentacene

Similar to the previously photocurrent-ratio measurements, Pc (deposited at 0.2 nm/s) is used as the donor and paired with acceptor C_{60} (Figure 8.7a). As the triplet yield η_T can be non-unity in singlet fission materials, the D-A η_{IQE} ratio in Equation 8.1 is now expressed as:

$$\frac{\eta_{IQE}^{D}}{\eta_{IQE}^{A}} = \frac{\eta_T \eta_D^D \eta_{CS}}{\eta_D^A \eta_{CS}} = \frac{\eta_D^D}{\eta_D^A / \eta_T} \quad (8.6)$$

As discussed in Section 8.2, the acceptor diffusion efficiency is constant when only varying

donor thickness. In Equation 8.6, another constant η_T is also put into the denominator and the shape of η_{IQE} ratio curve is still only determined by donor η_D (numerator) and L_D. As such, the uncertainty in η_T would not impact donor L_D when only varying donor thickness. Instead of extracting acceptor L_D from the measurement, the ratio η_D^A/η_T would be extracted. For the efficient singlet fission material Pc, we use η_T = 200% and extract the corresponding acceptor L_D directly.

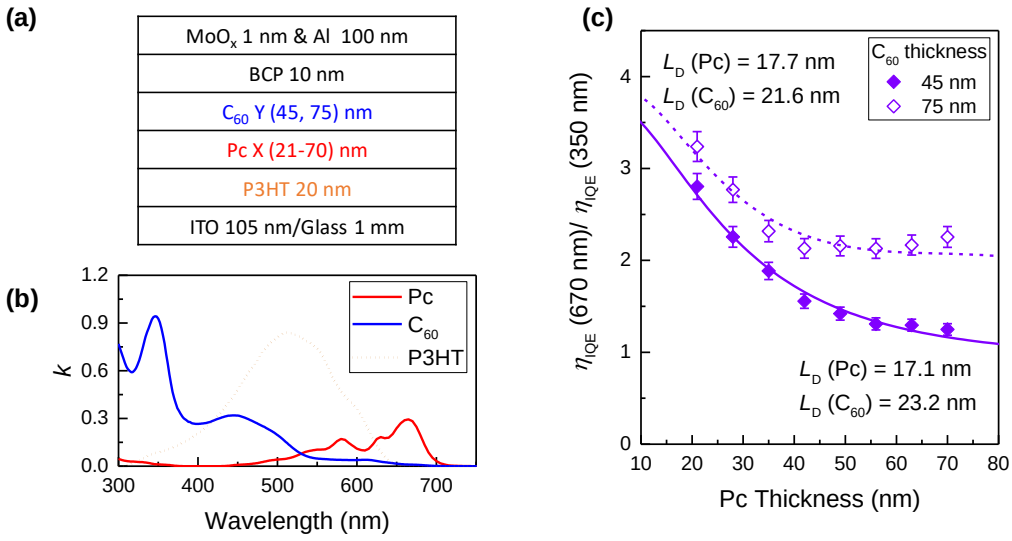

Figure 8.7 Measuring L_D of Pc (a) Device architecture for L_D measurement, a 20-nm-thick P3HT is used as an exciton blocking layer for donor Pc (b) The extinction coefficients (k) of Pc, C_{60}, and P3HT thin films. (c) Diffusion efficiency ratio (λ = 670 nm to λ = 350 nm) as a function of Pc layer thickness and C_{60} thickness (solid symbols: 45 nm C_{60} layer; open symbols: 75 nm C_{60} layer). The L_D values are extracted by fitting each set of data (one set for 45 nm C_{60}, another set for 75 nm C_{60}).

Figure 8.7b shows the extinction coefficients (k) of Pc, C_{60} and donor exciton blocking layer P3HT. The singlet excitons generated in P3HT can also contribute to photocurrent by Förster transfer to Pc singlet states.[249-250] To isolate the photoresponse of Pc and C_{60}, we chose λ = 670 nm (Pc absorption peak, no P3HT absorption) and λ = 350 nm (C_{60} Frenkel

exciton absorption peak, weak P3HT absorption, k(P3HT) = 0.08) to extract the donor and acceptor η_{IQE}, respectively. In Figure 8.7c, the η_{IQE} ratio is fitted for two sets of devices with different acceptor thickness. When fixing η_T = 200%, the set with 45 nm C_{60} yields a triplet L_D of 17.1 nm for Pc and an L_D of 23.2 nm for C_{60} while the other set with 75 nm C_{60} yields similar results: a triplet L_D of 17.7 nm for Pc and an L_D of 21.6 nm for C_{60}. The C_{60} L_D is consistent with the value (22.0 nm) extracted from spectrally resolved photoluminescence quenching measurements for C_{60} deposited on Pc.[249]

8.6.2 Direct Measurement of Triplet Diffusion in Singlet Fission Materials

For exothermic fission material Pc, the triplet L_D can be directly extracted with the photocurrent-ratio method since the triplet exciton is the only type of diffusive states that contributes to device photocurrent. For exothermic fission material Tc, however, both singlet and triplet exciton diffusion can contribute to photocurrent when Tc is optically excited. The photocurrent-ratio measurement for triplet L_D is therefore complicated by the existence of singlet diffusion. In order to isolate the role of triplet exciton diffusion, a triplet exciton injection layer is introduced to selectively excite the triplet state of Tc (Figure 8.8a). Instead of optically pumping Tc, a triplet forming material PtPc with higher energy T_1 is excited.[163-164] Since the $E(S_1)$ of PtPc is lower than Tc, the singlet state of Tc cannot be excited with singlet energy transfer.

As the donor triplet excitons are from injection layer, we need to measure the η_{IQE} of triplet injector instead of donor material. Equation 8.6 is now revised as:

$$\frac{\eta_{IQE}^{I}}{\eta_{IQE}^{A}} = \frac{\eta_T \eta_D^D \eta_{CS}}{\eta_D^A \eta_{CS}} = \frac{\eta_D^D}{\eta_D^A / \eta_T} \quad (8.7)$$

Where η_{IQE}^{I} is the η_{IQE} of triplet injection layer. The η_T is still the triplet exciton quantum yield but no longer representing singlet fission efficiency. It is the quantum yield of triplet excitons injected into the donor layer from excitons generated within the injection layer. Thus, the η_T is determined by exciton diffusion within the triplet injection layer and exciton transfer at injection layer/donor interface.

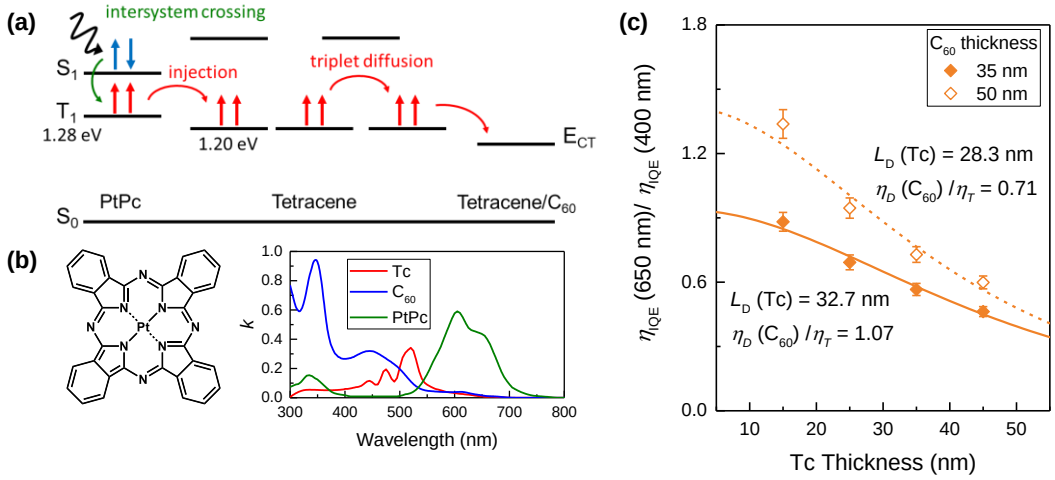

Figure 8.8 (a) Measuring triplet L_D of Tc with a triplet injection layer PtPc. (b) The extinction coefficients (k) of Tc, C_{60}, and PtPc thin films. (c) Diffusion efficiency ratio (λ = 650 nm to λ = 400 nm) as a function of Tc layer thickness and C_{60} thickness (solid symbols: 35 nm C_{60} layer; open symbols: 50 nm C_{60} layer). The Tc triplet L_D values and $\eta_D(C_{60})/\eta_T$ are extracted by fitting each set of data (one set for 35 nm C_{60}, another set for 50 nm C_{60}).

As triplet energy transfer is typically in a short range (Dexter type), the triplet exciton of the donor are assumed only generated within the first monolayer of donor molecules in the diffusion model. Here, we keep triplet injection layer thickness fixed and assume the η_T is insensitive to active layer thickness. When only varying donor thickness, the donor

triplet L_D and the ratio η_D^A/η_T can be extracted simultaneously. Figure 8.8b shows the extinction coefficients (k) of Tc, C_{60} and triplet injection layer PtPc. The injection layer η_{IQE} is extracted from λ = 650 nm (without absorption of Tc and C_{60}) while the acceptor η_{IQE} is extracted from λ = 400 nm (same as SubPc-C_{60} case) instead of λ = 350 nm (PtPc absorption peak). Figure 8.8c shows the PtPc-C_{60} η_{IQE} ratio as a function of Tc thickness obtained from planar OPVs with a structure: ITO/10 nm TAPC/10 nm PtPc/X (=15-45) nm Tc/Y (= 35, 50) nm C_{60}/10 nm BCP/1 nm MoO_x/100 nm Al. The triplet injector-acceptor η_{IQE} ratio as a function of Tc thickness is fitted for devices with 35-nm-thick C_{60}, yielding a triplet L_D of 32.7 nm for Tc and the efficiency ratio $\eta_D(C_{60})/\eta_T$ = 1.07. The devices with 50-nm-thick C_{60} yield a similar triplet L_D of 28.3 nm for Tc and a lower $\eta_D(C_{60})/\eta_T$ = 0.71 due to less efficient exciton harvesting in a thicker C_{60} layer. If assuming C_{60} L_D is same for two sets of devices, simultaneous fitting yields a triplet L_D of 32.1 nm for Tc, an L_D of 25.7 nm for C_{60}, and a η_T of 57%.

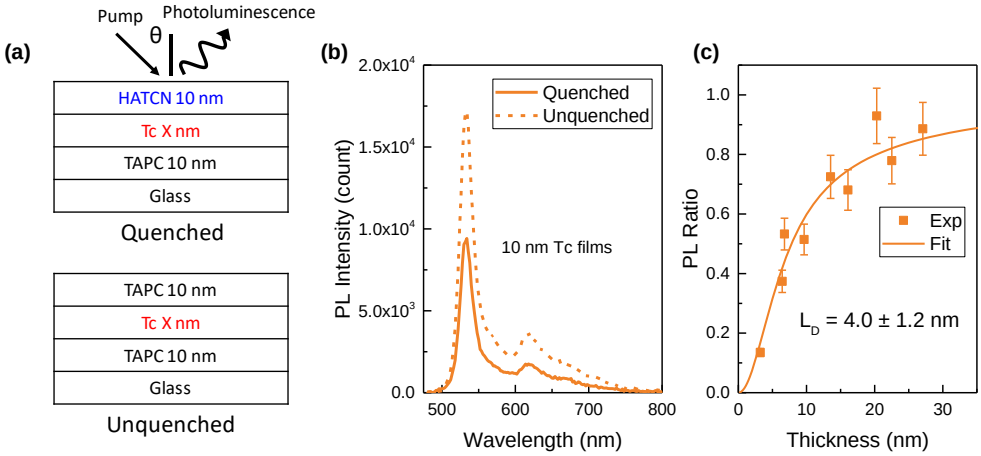

Figure 8.9 (a) Architectures for Tc singlet L_D measurements. Films are all pumped with λ = 450 nm light with an incident angle of 70°. (b) Representative PL spectra (10-nm-thick Tc) for the samples in (a). (c) The PL ratio of Tc films as a function of Tc thickness.

The singlet L_D is also measured with thickness-dependent PL quenching for Tc (Figure 8.9). The Tc films are optically excited with λ = 450 nm light with an incident angle of 70°. The result yields a singlet L_D of 4.0 nm, much shorter than the triplet L_D of Tc.

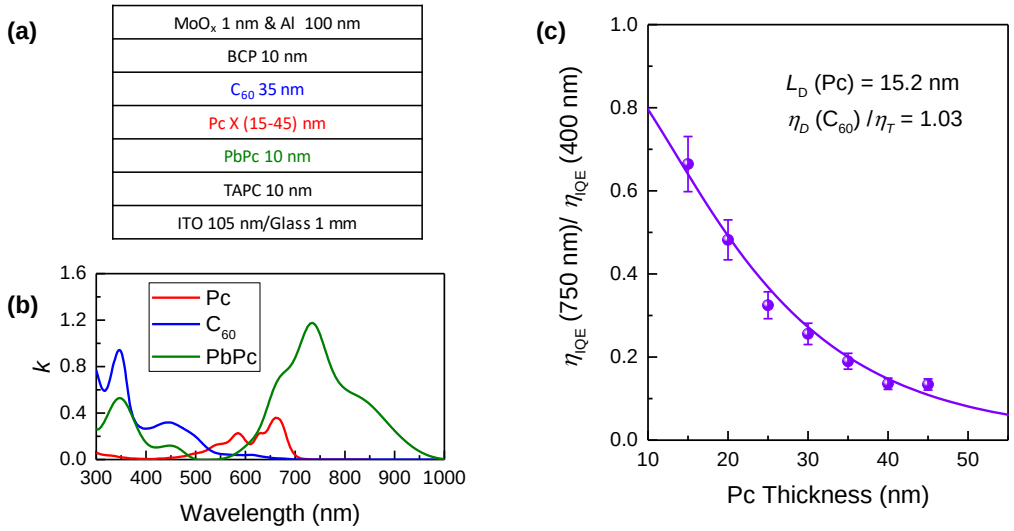

Figure 8.10 (a) Device architecture for Pc triplet L_D measurement, a 10-nm-thick PbPc is used as triplet exciton injection layer for donor Pc (b) The extinction coefficients (k) of Pc, C_{60}, and PbPc thin films. (c) Diffusion efficiency ratio (λ = 670 nm to λ = 400 nm) as a function of Pc layer thickness.

To show the general applicability of the triplet injection method for singlet fission materials, we also applied this method to Pc. A triplet injection layer PbPc (T_1 = 1.02) is used to selectively excite the triplet states in Pc (T_1 = 0.86). For this measurement, only donor thickness is varied (Figure 8.10a).[163-164] Figure 8.10b shows the extinction coefficients (k) of Pc, C_{60} and triplet injection layer PbPc. The injection layer η_{IQE} is extracted from λ = 750 nm while the acceptor η_{IQE} is extracted from λ = 400 nm. Similar to Tc case, fitting PtPc-C_{60} η_{IQE} ratio in Figure 8.10c as a function of Pc thickness yields $\eta_D(C_{60})/\eta_T$ = 1.03 and a triplet L_D =15.2 nm for Pc, similar to the result (17 nm) in Section

8.61. As such, photocurrent-ratio method with a triplet injection layer is a general method to directly measure triplet L_D for singlet fission materials.

8.7 Conclusions

We demonstrate a simple photocurrent-ratio method to measure the intrinsic L_D of excitonic semiconductors in bilayer photovoltaic cells. The impact of often unknown recombination losses is negated when taking a ratio of donor and acceptor η_{IQE}. For the luminescent organic pairing SubPc and C_{60}, their L_D values extracted using this method are in excellent agreement with those extracted from conventional PL quenching measurements, a direct result of the ability to remove the role of unknown geminate recombination losses. With knowledge of the intrinsic values of L_D, we are able to investigate the potential for relaxation losses which are typically overlooked in device-based studies of L_D. Indeed, bulk CT excitons generated in C_{60} have non-unity relaxation yield to Frenkel states and can generate free carriers directly through bulk-ionization. The generality of this photocurrent-ratio method is further demonstrated by extracting L_D for the dark small molecule SubNc, C_{70}, the high-performance polymer PTB7, CdSe quantum dot thin films, as well as for singlet fission materials Pc and Tc. Thus, we demonstrate a straightforward measurement for the extraction of L_D that is equally applicable to both luminescent and dark excitonic materials capable of being integrated into a bilayer photovoltaic cell.

8.8 Experimental Methods

Chemicals. For this study, SubPc (99%), mCP (99%), TPBi (99%), C545T (99%), TAPC (99%), pentacene (99%), PbPc (99%), PtPc (99%) and PTB7 (Mw > 50,000) were obtained from Lumtec Inc., C_{60} (99%) and C_{70} (99%) were obtained from MER Corporation, MoO_3 (99%) and BCP (98%) was obtained from Alfa Aesar, tetracene (97%) was obtained from TCI, chloroform (99%), 3-mercaptopropionic acid (99%), octane (98%), oleic acid (tech. grade 90%) acetonitrile (99.5%) and methyl acetate (anhydrous) were obtained from Sigma-Aldrich, selenium dioxide (99.8%) and 1-octadecene (90%) were obtained from Acros Organics. All materials above were used as received. The NPD (99%) was synthesized by the Dow Chemical Company and purified once by temperature-gradient sublimation[47]. Cadmium myristate was prepared on a multi-gram scale according to the method reported by Chen and co-workers[251].

Synthesis of zincblende CdSe QDs. Zincblende CdSe QDs with oleic acid capping ligands were synthesized as previously reported[237], based off the original synthesis by Chen and co-workers[251]. Briefly, 1-octadecene (63 mL), cadmium myristate (570 mg) and selenium dioxide (110 mg) were added to a 3-neck round bottom flask and degassed at 75 °C for 1 hour. After degassing, the reaction mixture was heated to 240 °C, at which point 1 mL of oleic acid was added dropwise to the solution once a red color was achieved. The reaction was allowed to proceed for 15 minutes and then cooled to room temperature for purification by centrifugation in methyl acetate. The resulting precipitate was dispersed

in octane and filtered using a 0.2 um PTFE syringe filter prior to film fabrication. Resulting solution concentration was approximately 25 g/L.

Thin-film and device preparation. Organic photovoltaic cells were fabricated using indium-tin-oxide (ITO)-coated glass substrates with a sheet resistance of ~8-12 Ω/□. Substrates were cleaned in tergitol solution and in organic solvents and treated in UV-Ozone ambient for 10 minutes prior to thin film deposition. All photoactive polymer and QD films were spin-coated onto an HfO_2-coated ITO substrate. The HfO_2 was deposited via atomic layer deposition at 200 °C. The polymer PTB7 was first dispersed in chloroform and then spin-coated at 3000 rpm for 45 s. The obtained samples were annealed in N_2 at 140 °C for 10 min. The polymer film thickness was controlled via the concentration of the PTB7 solution (2-10 g/L). Spin-coating and buildup of QD film thickness was realized using a solid-state ligand exchange procedure. CdSe QDs dispersed in octane were spin-coated at 1200 rpm for 30 s and then 6000 rpm for 60 s. The latter process is found to improve film uniformity and reproducibility. Next, 3-MPA (1% v/v) in acetonitrile was first deposited onto the film and allowed to sit for 10 s to facilitate the ligand exchange. The sample was then spun again at 1200 rpm for 30 s. Finally, the film was rinsed with pure acetonitrile by spinning at 6000 rpm for 60 s. This process was repeated 3-4 times until the desired QD film thickness was achieved. For P3HT exciton blocking layer, the polymer P3HT was first dispersed in chloroform and then spin-coated at 3000 rpm for 45 s. The obtained samples were annealed in N_2 at 140 °C for 10 min. All other layers were deposited at room temperature by high vacuum thermal evaporation at a pressure of $< 8x10^{-7}$ Torr. The active area of the obtained device is 0.785 mm^2, defined by the cathode area.

Optoelectronic characterization. Photoluminescence quenching data were recorded using a Photon Technology International QuantaMaster Fluorometer. All photoluminescence measurements were performed under N_2 purge. Photoluminescence quenching measurements were made at an incident angle of 70° to the substrate normal. External quantum efficiency measurements were collected by measuring the photocurrent under monochromatic light illumination using a 300 W Oriel Xe lamp, a monochromator, an optical chopper wheel, and an SR810 lock-in amplifier. Error bars for L_D represent a 95% confidence interval extracted from fitting parameters. All film thicknesses, reflectivity spectra were measured with a J. A. Woollam spectroscopic ellipsometer. The device reflectivity measurements were made at an incident angle of 15° to the substrate normal. Film thicknesses were fit using a Cauchy model. For simulations of device absorption efficiency optical constants of organic and QD thin films were extracted by fitting transmission (at normal incidence) and reflection (incident angle:15°) simultaneously with a transfer matrix formalism.

9. Conclusions

9.1 Summary and Conclusions

In Chapter 4, a novel characterization technique base on transient photovoltage signal is described. The technique allows quantitative elucidation of charge recombination losses due to different mechanisms, including geminate (CT states) and non-geminate (free charge carriers) recombination. Using this information, strategies are developed to suppress charge recombination losses in devices in Chapter 5 and 6. In chapter 5, the impact of thin-film crystallinity and molecular packing on geminate recombination loss is studied for OPVs using high dipole moment donor-acceptor-acceptor type small molecules. In Chapter 6, a new device architecture with an exciton permeable interlayer is demonstrated. This design reduces both geminate and non-geminate recombination losses in metal phthalocyanine-fullerene OPVs. In Chapter 7, the transport properties of CT states are also explored as a potential strategy to reduces geminate recombination losses in state-of-the-art OPVs.

With a deeper understanding of charge recombination and CT state properties, the focus of this thesis moves to the electrical characterization of energy (exciton) transport. This is a long-standing challenge for excitonic semiconductor studies as PV-based measurements are frequently limited by unknown charge recombination losses. In Chapter 8, a general, device-based photocurrent-ratio technique is demonstrated to measure intrinsic exciton diffusion length in OPVs. This broadly applicable method is capable of probing exciton transport for both luminescent and dark materials, as well as for small molecules, polymers,

and semiconductor quantum dots. As such, this general method would also be useful to study the diffusion of dark triplet excitons in the photoactive materials exhibiting singlet fission, a phenomenon can potentially overcome Schockley-Quessier limit for single-junction PVs.

9.2 Future Research Directions

9.2.1 Exploring Long-Range CT State Migration

As discussed in Chapter 7, long-range CT state migration can potentially help CT states to reach sites with higher separation probability and therefore reduce geminate recombination loss. Indeed, it can also be useful in other optoelectronic systems. For instance, OLEDs are frequently based on a composite emissive layer that combines a charge transporting host and a luminescent guest. An alternative approach has utilized a co-host design where an electrically generated CT state forms between the two host species before transferring energy to the guest.[252-254] This approach has permitted improvements in turn-on voltage and peak efficiency, as well as efficiency roll-off. Long-range transport of CT states would facilitate energy transfer from mixed host materials to local emitters and improve device efficiency. Besides, long-range CT state transport is promising for logic application. Excitonic transistors utilize delocalized CT excitons to carry information and have been demonstrated by High et al. for logic circuit.[211] However, most of the previous studies are based on inorganic semiconductors at low temperature for stabilization of CT excitons. Realizing long-range CT state transport in organics can potentially lead to room-

temperature excitonic transistors. From the results of Chapter 7, CT states are found mobile within organic D-A mixtures and their diffusion is limited by the component charge carrier hopping. The L_D values of these emissive CT states are all less than 10 nm, likely due to the poor electron and hole transport within the system studied. To realize a long-range CT migration, either diffusivity or lifetime of CT states need to be improved significantly.

To improve the diffusivity of CT states, active materials with better charge carrier transport are essential. Indeed, this aligns with the requirement for efficient CT state separation in OPVs. Thus, most of high-efficiency OPVs with high mobility D-A pairs are expected to have much higher CT diffusivity than the systems studied in Chapter 7. However, these systems often form CT states with very low PL efficiency, which makes the measurement of CT L_D challenging. A potential solution is to modify the photocurrent-ratio method introduced in Chapter 8. The D-A mixture of interest might be treated as a composite and serve as an electron donor for a quenching material. This allows the IQE ratio of the composite to the quenching material to be measured as a function of device configuration. However, the composite itself might generate free carriers directly, and thus it is challenging to measure the composite IQE contributed by CT state diffusion directly. This can be potentially addressed by inserting a thin wide-gap interlayer between the mixed layer and the quenching layer for isolating the photocurrent from direct dissociation of CT states. As the device-based CT state L_D measurement can be performed under different applied bias, it would provide more useful information than PL quenching method which operated without electrode and under weak electric field.

Besides using high charge mobility materials for higher CT diffusivity, stabilizing CT

state and increase its lifetime is another pathway to improve CT L_D. The D-A interlayer design introduced in Chapter 6 would be a promising strategy for this purpose. As discussed previously, an interlayer can increase the spatial extent of the CT state and slow the charge recombination. However, the interlayer can also reduce CT state binding energy, facilitating separation of CT states. This reduces CT state lifetime, not desired for excitonic transistor application. Wide-gap charge blocking materials can be employed to confine the electron and hole at D-A interface for keeping them bound. This forms a structure: wide-gap layer/thin donor/interlayer/thin acceptor/wide-gap layer. It is very similar to the coupled quantum well structure GaAs/thin $Al_{0.33}$ $Ga_{0.67}As$/GaAs/thin $Al_{0.33}$ $Ga_{0.67}As$/GaAs reported by High et al.[211] The electron and hole would be confined within their thin channels respectively and can hardly recombine due to the interlayer between them.

With a growing capability of tuning CT state diffusion, it would be necessary to also explore the impact of CT state diffusion on the performance of organic optoelectronic devices. For OPVs, understanding whether CT state diffusion helps or frustrates charge separation could have important implications in determining future device design.

9.2.2 Understanding Singlet-Fission Mechanisms

As introduced in Chapter 8, singlet fission is a process that generates two triplet excitons from one singlet exciton.[172, 174, 255-256] As all high energy excitons generated in an OPV will eventually lose their energy when relaxing to the low energy interfacial CT states, this phenomenon provides a pathway to reduce thermalization losses by creating additional excited states with above gap energy. When paired with a narrow gap material, singlet

fission material can minimize energy loss for photons above its optical energy gap while letting the narrow gap materials to harvest low energy photons. This is similar to the tandem cells which utilize wide gap and narrow gap sub-cells to harvest high energy and low energy photon respectively. Therefore, materials capable of singlet-fission could potentially boost device efficiency and circumvent the Shockley-Queisser limit for single junction OPVs.[171] Recent work also paired singlet fission material tetracene with conventional silicon PVs. A combined triplet quantum yield of 133% has been demonstrated for the fission in tetracene and the energy transfer to silicon.[240]

While the singlet-fission mechanism is still under intense study, it is widely agreed that an intermediate state called triplet pair is generated from singlet during the fission process.[171] This intermediate state may separate into two independent triplet excitons in an overall spin-allowed process.[257-259] An efficient triplet pair separation process is the key for high triplet exciton quantum yield and device efficiency. To date, the greatest challenge faced by singlet-fission based PVs is how to achieve efficient triplet pair dissociation, especially when the fission is not very exothermic.

As triplet pair separation require two triplet exciton moving away from each other, the transport of triplet exciton is likely playing a central role in this process. The triplet exciton transport is challenging to characterize as the triplet state is dark. The photocurrent-ratio method introduced in Chapter 8 allows non-emissive exciton diffusion to be accurately measured in a PV device. When the quantum yield of triplet excitons is relatively stable with active layer thickness, it is also extractable when fitting IQE-ratio as a function of both donor and acceptor thickness. Therefore, the photocurrent-ratio method would be very

useful to understand the triplet exciton diffusion and the triplet yield in various singlet-fission systems, such as singlet-fission thin films with different molecular structure, crystal structure, and grain size. By quantitatively studying the relationship between triplet L_D and triplet separation efficiency, the mechanisms of singlet fission process will be better understood, essential to future molecular design and process development for low energy loss singlet fission OPVs.

9.3 Afterword

During the last five years of my Ph.D. study, I have witnessed the OPV record efficiency growing from 12% to 17%. Currently, most of the high-efficiency systems are still show efficiency around 10%. A continuous collaborative effort from scientists and engineers is essential to raise this value to >15%. Despite the efficiency and lifetime is unlikely to exceed the inorganic counterpart such as Si and GaAs, OPV has advantages in light and flexible form factors, low-cost roll-to-roll fabrications, making it more likely to enter the market of portable and consumer products first. Whether OPV eventually realize its widespread commercial application or not, the answer should be clear in the next few years.

10. Bibliography

(1) Turner, J. A., A Realizable Renewable Energy Future. *Science* **1999,** *285* (5428), 687-689.

(2) Panwar, N.; Kaushik, S.; Kothari, S., Role of Renewable Energy Sources in Environmental Protection: A Review. *Renewable and Sustainable Energy Reviews* **2011,** *15* (3), 1513-1524.

(3) Chow, J.; Kopp, R. J.; Portney, P. R., Energy Resources and Global Development. *Science* **2003,** *302* (5650), 1528-31.

(4) Haegel, N. M.; Atwater, H.; Barnes, T.; Breyer, C.; Burrell, A.; Chiang, Y.-M.; De Wolf, S.; Dimmler, B.; Feldman, D.; Glunz, S., Terawatt-Scale Photovoltaics: Transform Global Energy. *Science* **2019,** *364* (6443), 836-838.

(5) Andreani, L. C.; Bozzola, A.; Kowalczewski, P.; Liscidini, M.; Redorici, L., Silicon Solar Cells: Toward the Efficiency Limits. *Advances in Physics: X* **2019,** *4* (1), 1548305.

(6) Bergmann, R., Crystalline Si Thin-Film Solar Cells: A Review. *Applied physics A* **1999,** *69* (2), 187-194.

(7) Shockley, W.; Queisser, H. J., Detailed Balance Limit of Efficiency of P-N Junction Solar Cells. *J. Appl. Phys.* **1961,** *32* (3), 510-519.

(8) Rühle, S., Tabulated Values of the Shockley–Queisser Limit for Single Junction Solar Cells. *Sol. Energy* **2016,** *130*, 139-147.

(9) Green, M. A.; Dunlop, E. D.; Levi, D. H.; Hohl-Ebinger, J.; Yoshita, M.; Ho-Baillie, A. W. Y., Solar Cell Efficiency Tables (Version 54). *Prog. Photovoltaics Res. Appl.* **2019,** *27* (7), 565-575.

(10) Research Cell Efficiency Records. *National Renewable Energy Laboratory* **2019**.

(11) Shaheen, S. E.; Ginley, D. S.; Jabbour, G. E., Organic-Based Photovoltaics: Toward Low-Cost Power Generation. *MRS bulletin* **2005,** *30* (01), 10-19.

(12) Shah, A.; Torres, P.; Tscharner, R.; Wyrsch, N.; Keppner, H., Photovoltaic Technology: The Case for Thin-Film Solar Cells. *science* **1999,** *285* (5428), 692-698.

(13) Green, M., Recent Developments in Photovoltaics. *Solar energy* **2004,** *76* (1), 3-8.

(14) Bosio, A.; Romeo, A.; Menossi, D.; Mazzamuto, S.; Romeo, N., The Second-Generation of Cdte and Cuingase2 Thin Film Pv Modules. *Crystal Research and Technology* **2011,** *46* (8), 857-864.

(15) Debbarma, M.; Sudhakar, K.; Baredar, P., Thermal Modeling, Exergy Analysis, Performance of Bipv and Bipvt: A Review. *Renewable and Sustainable Energy Reviews* **2017,** *73*, 1276-1288.

(16) Katagiri, H.; Jimbo, K.; Maw, W. S.; Oishi, K.; Yamazaki, M.; Araki, H.; Takeuchi, A., Development of Czts-Based Thin Film Solar Cells. *Thin Solid Films* **2009,** *517* (7), 2455-2460.

(17) Nozik, A., Quantum Dot Solar Cells. *Physica E: Low-dimensional Systems and Nanostructures* **2002,** *14* (1), 115-120.

(18) Jung, H. S.; Park, N. G., Perovskite Solar Cells: From Materials to Devices. *Small* **2015,** *11* (1), 10-25.

(19) Forrest, S. R., The Path to Ubiquitous and Low-Cost Organic Electronic Appliances on Plastic. *Nature* **2004,** *428* (6986), 911-918.

(20) Kearns, D.; Calvin, M., The Photovoltaic Effect and Photoconductivity in Laminated Organicsystems. *Journal of Chemical Physics* **1958,** *29* (UCRL--8441).

(21) Levin, I.; White, C. E., The Photovoltaic Behavior of Organic Substances in Solution. *The Journal of Chemical Physics* **1950,** *18* (4), 417-426.

(22) Zhang, S.; Qin, Y.; Zhu, J.; Hou, J., Over 14% Efficiency in Polymer Solar Cells Enabled by a Chlorinated Polymer Donor. *Adv. Mater.* **2018,** *30* (20), 1800868.

(23) Meng, L.; Zhang, Y.; Wan, X.; Li, C.; Zhang, X.; Wang, Y.; Ke, X.; Xiao, Z.; Ding, L.; Xia, R., Organic and Solution-Processed Tandem Solar Cells with 17.3% Efficiency. *Science* **2018,** *361* (6407), 1094-1098.

(24) Coropceanu, V.; Cornil, J.; da Silva Filho, D. A.; Olivier, Y.; Silbey, R.; Brédas, J.-L., Charge Transport in Organic Semiconductors. *Chem. Rev.* **2007,** *107* (4), 926-952.

(25) Baldo, M.; Thompson, M.; Forrest, S., High-Efficiency Fluorescent Organic Light-Emitting Devices Using a Phosphorescent Sensitizer. *Nature* **2000,** *403* (6771), 750-753.

(26) Freund, L. B.; Suresh, S., *Thin Film Materials: Stress, Defect Formation and Surface Evolution*. Cambridge University Press: 2004.

(27) Hopcroft, M. A.; Nix, W. D.; Kenny, T. W., What Is the Young's Modulus of Silicon? *Journal of microelectromechanical systems* **2010,** *19* (2), 229-238.

(28) Torres, J. M.; Bakken, N.; Stafford, C. M.; Li, J.; Vogt, B. D., Thickness Dependence of the Elastic Modulus of Tris (8-Hydroxyquinolinato) Aluminium. *Soft Matter* **2010,** *6* (22), 5783-5788.

(29) Djurovich, P. I.; Mayo, E. I.; Forrest, S. R.; Thompson, M. E., Measurement of the Lowest Unoccupied Molecular Orbital Energies of Molecular Organic Semiconductors. *Org. Electron.* **2009,** *10* (3), 515-520.

(30) Peumans, P.; Yakimov, A.; Forrest, S. R., Small Molecular Weight Organic Thin-Film Photodetectors and Solar Cells. *J. Appl. Phys.* **2003,** *93* (7), 3693.

(31) Mikhnenko, O. V.; Blom, P. W.; Nguyen, T.-Q., Exciton Diffusion in Organic Semiconductors. *Energy Environ. Sci.* **2015,** *8* (7), 1867-1888.

(32) Torabi, S.; Jahani, F.; Van Severen, I.; Kanimozhi, C.; Patil, S.; Havenith, R. W. A.; Chiechi, R. C.; Lutsen, L.; Vanderzande, D. J. M.; Cleij, T. J.; Hummelen, J. C.; Koster, L. J. A., Strategy for Enhancing the Dielectric Constant of Organic Semiconductors without Sacrificing Charge Carrier Mobility and Solubility. *Adv. Funct. Mater.* **2015,** *25* (1), 150-157.

(33) Cao, W.; Xue, J., Recent Progress in Organic Photovoltaics: Device Architecture and Optical Design. *Energy Environ. Sci.* **2014,** *7* (7), 2123.

(34) García-Valverde, R.; Cherni, J. A.; Urbina, A., Life Cycle Analysis of Organic Photovoltaic Technologies. *Progress in Photovoltaics: Research and Applications* **2010,** *18* (7), 535-558.

(35) Espinosa, N.; Hösel, M.; Angmo, D.; Krebs, F. C., Solar Cells with One-Day Energy Payback for the Factories of the Future. *Energy & Environmental Science* **2012,** *5* (1), 5117-5132.

(36) Zhang, T.; Dement, D. B.; Ferry, V. E.; Holmes, R. J., Intrinsic Measurements of Exciton Transport in Photovoltaic Cells. *Nat. Commun.* **2019,** *10* (1), 1156.

(37) Keiderling, C.; Dimitrov, S.; Durrant, J. R., Exciton and Charge Generation in Pc60bm Thin Films. *J. Phys. Chem. C* **2017,** *121* (27), 14470-14475.

(38) Marian, C. M., Spin–Orbit Coupling and Intersystem Crossing in Molecules. *Wiley Interdisciplinary Reviews: Computational Molecular Science* **2012,** *2* (2), 187-203.

(39) Turro, N. J.; Ramamurthy, V.; Scaiano, J. C., Book Review Modern Molecular Photochemistry of Organic Molecules. 2012.

(40) Baldo, M.; Thompson, M.; Forrest, S., High-Efficiency Fluorescent Organic Light-Emitting Devices Using a Phosphorescent Sensitizer. *Nature* **2000,** *403* (6771), 750.

(41) Segal, M.; Baldo, M.; Holmes, R.; Forrest, S.; Soos, Z., Excitonic Singlet-Triplet Ratios in Molecular and Polymeric Organic Materials. *Phys. Rev. B* **2003,** *68* (7), 075211.

(42) Pope, M.; Swenberg, C. E., *Electronic Processes in Organic Crystals and Polymers*. Oxford University Press: 1999.

(43) Turro, N. J., *Modern Molecular Photochemistry*. University Science Books: 1991.

(44) Menke, S. M.; Holmes, R. J., Exciton Diffusion in Organic Photovoltaic Cells. *Energy Environ. Sci.* **2014,** *7* (2), 499-512.

(45) Forster, T., 10th Spiers Memorial Lecture. Transfer Mechanisms of Electronic Excitation. *Discussions of the Faraday Society* **1959,** *27* (0), 7-17.

(46) Luhman, W. A.; Holmes, R. J., Investigation of Energy Transfer in Organic Photovoltaic Cells and Impact on Exciton Diffusion Length Measurements. *Adv. Funct. Mater.* **2011,** *21* (4), 764-771.

(47) Curtin, I. J.; Blaylock, D. W.; Holmes, R. J., Role of Impurities in Determining the Exciton Diffusion Length in Organic Semiconductors. *Appl. Phys. Lett.* **2016,** *108* (16), 163301.

(48) Pettersson, L. A. A.; Roman, L. S.; Inganas, O., Modeling Photocurrent Action Spectra of Photovoltaic Devices Based on Organic Thin Films. *J Appl Phys* **1999,** *86* (1), 487-496.

(49) Brédas, J.-L.; Calbert, J. P.; da Silva Filho, D.; Cornil, J., Organic Semiconductors: A Theoretical Characterization of the Basic Parameters Governing Charge Transport. *Proc. Natl. Acad. Sci.* **2002,** *99* (9), 5804-5809.

(50) Menard, E.; Podzorov, V.; Hur, S. H.; Gaur, A.; Gershenson, M. E.; Rogers, J. A., High-Performance N-and P-Type Single-Crystal Organic Transistors with Free-Space Gate Dielectrics. *Adv. Mater.* **2004,** *16* (23-24), 2097-2101.

(51) Wang, Z.; Helander, M. G.; Greiner, M. T.; Qiu, J.; Lu, Z.-H., Carrier Mobility of Organic Semiconductors Based on Current-Voltage Characteristics. *J. Appl. Phys.* **2010,** *107* (3), 034506.

(52) Mu, H.; Reddy, I.; Hunt, J.; Severs, P.; Patil, S., Electron Mobility Characterization in Oleds from Ac Small Signal Optical Modulation. *J. Phys. D: Appl. Phys.* **2010,** *43* (19), 195103.

(53) Noh, S.; Suman, C. K.; Hong, Y.; Lee, C., Carrier Conduction Mechanism for Phosphorescent Material Doped Organic Semiconductor. *J. Appl. Phys.* **2009,** *105* (3), 033709.

(54) McNeill, C. R., Morphology of All-Polymer Solar Cells. *Energy Environ. Sci.* **2012,** *5* (2), 5653.

(55) Mott, N. F.; Davis, E. A., *Electronic Processes in Non-Crystalline Materials*. Oxford university press: 2012.

(56) Miller, A.; Abrahams, E., Impurity Conduction at Low Concentrations. *Phys. Rev.* **1960,** *120* (3), 745.

(57) Gill, W., Drift Mobilities in Amorphous Charge-Transfer Complexes of Trinitrofluorenone and Poly-N-Vinylcarbazole. *J. Appl. Phys.* **1972,** *43* (12), 5033-5040.

(58) Fang, P., Analysis of Conversion Efficiency of Organic-Semiconductor Solar Cells. *Journal of Applied Physics* **1974,** *45* (10), 4672-4673.

(59) Bonham, J., Theory of Injection Photovoltages in Organic Insulators. *Australian Journal of Chemistry* **1976,** *29* (10), 2123-2136.

(60) Tang, C.; Albrecht, A., Photovoltaic Effects of Metal–Chlorophyll-a–Metal Sandwich Cells. *J. Chem. Phys* **1975,** *62* (6), 2139-2149.

(61) Morel, D.; Ghosh, A.; Feng, T.; Stogryn, E.; Purwin, P.; Shaw, R.; Fishman, C., High-Efficiency Organic Solar Cells. *Appl. Phys. Lett.* **1978,** *32* (8), 495-497.

(62) Kampas, F. J.; Gouterman, M., Porphyrin Films. 3. Photovoltaic Properties of Octaethylporphine and Tetraphenylporphine. *The Journal of Physical Chemistry* **1977,** *81* (8), 690-695.

(63) Tang, C. W., Two-Layer Organic Photovoltaic Cell. *Appl. Phys. Lett.* **1986,** *48* (2), 183-185.

(64) Barito, A.; Sykes, M. E.; Bilby, D.; Amonoo, J.; Jin, Y.; Morris, S. E.; Green, P. F.; Kim, J.; Shtein, M., Recovering Lost Excitons in Organic Photovoltaics Using a Transparent Dissociation Layer. *J. Appl. Phys.* **2013,** *113* (20), 203110.

(65) Barito, A.; Sykes, M. E.; Huang, B.; Bilby, D.; Frieberg, B.; Kim, J.; Green, P. F.; Shtein, M., Universal Design Principles for Cascade Heterojunction Solar Cells with High Fill Factors and Internal Quantum Efficiencies Approaching 100%. *Adv. Energy Mater.* **2014,** *4* (13), 1400216.

(66) Griffith, O. L.; Forrest, S. R., Exciton Management in Organic Photovoltaic Multidonor Energy Cascades. *Nano Lett.* **2014,** *14* (5), 2353-8.

(67) Menke, S. M.; Holmes, R. J., Energy-Cascade Organic Photovoltaic Devices Incorporating a Host-Guest Architecture. *ACS Appl. Mater. Interfaces* **2015,** *7* (4), 2912-8.

(68) Menke, S. M.; Mullenbach, T. K.; Holmes, R. J., Directing Energy Transport in Organic Photovoltaic Cells Using Interfacial Exciton Gates. *ACS Nano* **2015,** *9* (4), 4543-4552.

(69) Rai, D.; Holmes, R. J., Investigation of Excitonic Gates in Organic Semiconductor Thin Films. *Phys. Rev. Applied* **2019,** *11* (1), 014048.

(70) Menke, S. M.; Luhman, W. A.; Holmes, R. J., Tailored Exciton Diffusion in Organic Photovoltaic Cells for Enhanced Power Conversion Efficiency. *Nat. Mater.* **2013,** *12* (2), 152-7.

(71) Hiramoto, M.; Fujiwara, H.; Yokoyama, M., P-I-N Like Behavior in Three-Layered Organic Solar Cells Having a Co-Deposited Interlayer of Pigments. *Journal of applied physics* **1992,** *72* (8), 3781-3787.

(72) Peumans, P.; Uchida, S.; Forrest, S. R., Efficient Bulk Heterojunction Photovoltaic Cells Using Small-Molecular-Weight Organic Thin Films. *Nature* **2003,** *425* (6954), 158-162.

(73) Yu, G.; Gao, J.; Hummelen, J. C.; Wudl, F.; Heeger, A. J., Polymer Photovoltiac Cells: Enhanced Efficiencies Via a Network of Internal Donor-Acceptor Heterojunctions. *Science* **1995,** *270* (5243), 1789.

(74) Ameri, T.; Dennler, G.; Lungenschmied, C.; Brabec, C. J., Organic Tandem Solar Cells: A Review. *Energy Environ. Sci.* **2009,** *2* (4), 347.

(75) Zhao, W.; Qian, D.; Zhang, S.; Li, S.; Inganas, O.; Gao, F.; Hou, J., Fullerene-Free Polymer Solar Cells with over 11% Efficiency and Excellent Thermal Stability. *Adv. Mater.* **2016,** *28* (23), 4734-9.

(76) Cheng, P.; Wang, J.; Zhang, Q.; Huang, W.; Zhu, J.; Wang, R.; Chang, S. Y.; Sun, P.; Meng, L.; Zhao, H.; Cheng, H. W.; Huang, T.; Liu, Y.; Wang, C.; Zhu, C.; You, W.; Zhan,

X.; Yang, Y., Unique Energy Alignments of a Ternary Material System toward High-Performance Organic Photovoltaics. *Adv. Mater.* **2018,** *30* (28), e1801501.

(77) Di Carlo Rasi, D.; Hendriks, K. H.; Wienk, M. M.; Janssen, R. A. J., Quadruple Junction Polymer Solar Cells with Four Complementary Absorber Layers. *Adv. Mater.* **2018**, e1803836.

(78) Burke, T. M.; Sweetnam, S.; Vandewal, K.; McGehee, M. D., Beyond Langevin Recombination: How Equilibrium between Free Carriers and Charge Transfer States Determines the Open-Circuit Voltage of Organic Solar Cells. *Adv. Energy Mater.* **2015,** *5* (11), 1500123.

(79) Cowan, S. R.; Roy, A.; Heeger, A. J., Recombination in Polymer-Fullerene Bulk Heterojunction Solar Cells. *Phys. Rev. B* **2010,** *82* (24), 245207.

(80) Deibel, C.; Strobel, T.; Dyakonov, V., Role of the Charge Transfer State in Organic Donor–Acceptor Solar Cells. *Adv. Mater.* **2010,** *22* (37), 4097-4111.

(81) Shuttle, C. G.; O'Regan, B.; Ballantyne, A. M.; Nelson, J.; Bradley, D. D.; Durrant, J. R., Bimolecular Recombination Losses in Polythiophene: Fullerene Solar Cells. *Phys. Rev. B* **2008,** *78* (11), 113201.

(82) Credgington, D.; Hamilton, R.; Atienzar, P.; Nelson, J.; Durrant, J. R., Non-Geminate Recombination as the Primary Determinant of Open-Circuit Voltage in Polythiophene:Fullerene Blend Solar Cells: An Analysis of the Influence of Device Processing Conditions. *Adv. Funct. Mater.* **2011,** *21* (14), 2744-2753.

(83) Kniepert, J.; Schubert, M.; Blakesley, J. C.; Neher, D., Photogeneration and Recombination in P3ht/Pcbm Solar Cells Probed by Time-Delayed Collection Field Experiments. *J. Phys. Chem. Lett.* **2011,** *2* (7), 700-705.

(84) Koster, L.; Kemerink, M.; Wienk, M. M.; Maturová, K.; Janssen, R. A., Quantifying Bimolecular Recombination Losses in Organic Bulk Heterojunction Solar Cells. *Adv. Mater.* **2011,** *23* (14), 1670-1674.

(85) Credgington, D.; Jamieson, F. C.; Walker, B.; Nguyen, T. Q.; Durrant, J. R., Quantification of Geminate and Non-Geminate Recombination Losses within a Solution-Processed Small-Molecule Bulk Heterojunction Solar Cell. *Adv. Mater.* **2012,** *24* (16), 2135-41.

(86) Proctor, C. M.; Kuik, M.; Nguyen, T.-Q., Charge Carrier Recombination in Organic Solar Cells. *Prog. Polym. Sci.* **2013,** *38* (12), 1941-1960.

(87) Menke, S. M.; Ran, N. A.; Bazan, G. C.; Friend, R. H., Understanding Energy Loss in Organic Solar Cells: Toward a New Efficiency Regime. *Joule* **2017**.

(88) Kurpiers, J.; Ferron, T.; Roland, S.; Jakoby, M.; Thiede, T.; Jaiser, F.; Albrecht, S.; Janietz, S.; Collins, B. A.; Howard, I. A.; Neher, D., Probing the Pathways of Free Charge Generation in Organic Bulk Heterojunction Solar Cells. *Nat. Commun.* **2018,** *9* (1), 2038.

(89) Puttisong, Y.; Xia, Y.; Chen, X.; Gao, F.; Buyanova, I. A.; Inganäs, O.; Chen, W. M., Charge Generation Via Relaxed Charge-Transfer States in Organic Photovoltaics by an Energy-Disorder-Driven Entropy Gain. *J. Phys. Chem. C* **2018,** *122* (24), 12640-12646.

(90) Onsager, L., Initial Recombination of Ions. *Phys. Rev.* **1938,** *54* (8), 554.

(91) Braun, C. L., Electric Field Assisted Dissociation of Charge Transfer States as a Mechanism of Photocarrier Production. *J. Chem. Phys* **1984,** *80* (9), 4157-4161.

(92) Zou, Y.; Holmes, R. J., The Role of Exciton Ionization Processes in Bulk Heterojunction Organic Photovoltaic Cells. *Adv. Energy Mater.* **2015,** *5* (12), 1500019.

(93) Shockley, W.; Read Jr, W., Statistics of the Recombinations of Holes and Electrons. *Phys. Rev.* **1952,** *87* (5), 835.

(94) Hall, R. N., Electron-Hole Recombination in Germanium. *Phys. Rev.* **1952,** *87* (2), 387.

(95) Street, R.; Schoendorf, M.; Roy, A.; Lee, J., Interface State Recombination in Organic Solar Cells. *Phys. Rev. B* **2010,** *81* (20), 205307.

(96) Rauh, D.; Deibel, C.; Dyakonov, V., Charge Density Dependent Nongeminate Recombination in Organic Bulk Heterojunction Solar Cells. *Adv. Funct. Mater.* **2012,** *22* (16), 3371-3377.

(97) Kan, B.; Zhang, Q.; Li, M.; Wan, X.; Ni, W.; Long, G.; Wang, Y.; Yang, X.; Feng, H.; Chen, Y., Solution-Processed Organic Solar Cells Based on Dialkylthiol-Substituted Benzodithiophene Unit with Efficiency near 10%. *J. Am. Chem. Soc.* **2014,** *136* (44), 15529-15532.

(98) Mei, J.; Bao, Z., Side Chain Engineering in Solution-Processable Conjugated Polymers. *Chem. Mater.* **2013,** *26* (1), 604-615.

(99) Pandey, R.; Gunawan, A. A.; Mkhoyan, K. A.; Holmes, R. J., Efficient Organic Photovoltaic Cells Based on Nanocrystalline Mixtures of Boron Subphthalocyanine Chloride and C60. *Adv. Funct. Mater.* **2012,** *22* (3), 617-624.

(100) Pandey, R.; Holmes, R. J., Characterizing the Charge Collection Efficiency in Bulk Heterojunction Organic Photovoltaic Cells. *Appl. Phys. Lett.* **2012,** *100* (8), 083303.

(101) Bube, R. H.; Fahrenbruch, A. L., Photovoltaic Effect. *Adv. Electron. El. Phys.* **1981,** *56*, 163-217.

(102) Zou, Y.; Holmes, R. J., Correlation between the Open-Circuit Voltage and Charge Transfer State Energy in Organic Photovoltaic Cells. *ACS Appl. Mater. Interfaces* **2015,** *7* (33), 18306-11.

(103) Bartesaghi, D.; del Carmen Pérez, I.; Kniepert, J.; Roland, S.; Turbiez, M.; Neher, D.; Koster, L. J. A., Competition between Recombination and Extraction of Free Charges Determines the Fill Factor of Organic Solar Cells. *Nat. Commun.* **2015,** *6*, 7083.

(104) Burkhard, G. F.; Hoke, E. T.; McGehee, M. D., Accounting for Interference, Scattering, and Electrode Absorption to Make Accurate Internal Quantum Efficiency Measurements in Organic and Other Thin Solar Cells. *Adv. Mater.* **2010,** *22* (30), 3293-7.

(105) Albrecht, S.; Schindler, W.; Kurpiers, J.; Kniepert, J.; Blakesley, J. C.; Dumsch, I.; Allard, S.; Fostiropoulos, K.; Scherf, U.; Neher, D., On the Field Dependence of Free Charge Carrier Generation and Recombination in Blends of Pcpdtbt/Pc_{70}bm: Influence of Solvent Additives. *J. Phys. Chem. Lett.* **2012,** *3* (5), 640-5.

(106) Vandewal, K.; Albrecht, S.; Hoke, E. T.; Graham, K. R.; Widmer, J.; Douglas, J. D.; Schubert, M.; Mateker, W. R.; Bloking, J. T.; Burkhard, G. F., Efficient Charge Generation by Relaxed Charge-Transfer States at Organic Interfaces. *Nat. Mater.* **2014,** *13* (1), 63.

(107) Mihailetchi, V.; Wildeman, J.; Blom, P., Space-Charge Limited Photocurrent. *Phys. Rev. Lett.* **2005,** *94* (12), 126602.

(108) Shuttle, C.; Hamilton, R.; O'Regan, B.; Nelson, J. a.; Durrant, J., Charge-Density-Based Analysis of the Current–Voltage Response of Polythiophene/Fullerene Photovoltaic Devices. *Proc. Natl. Acad. Sci.* **2010,** *107* (38), 16448-16452.

(109) Marsh, R. A.; Hodgkiss, J. M.; Friend, R. H., Direct Measurement of Electric Field-Assisted Charge Separation in Polymer:Fullerene Photovoltaic Diodes. *Adv. Mater.* **2010,** *22* (33), 3672-6.

(110) Mullenbach, T. K.; Curtin, I. J.; Zhang, T.; Holmes, R. J., Probing Dark Exciton Diffusion Using Photovoltage. *Nat. Commun.* **2017,** *8*, 14215.

(111) Mullenbach, T. K.; Holmes, R. J., Relating Photocurrent, Photovoltage, and Charge Carrier Density to the Recombination Rate in Organic Photovoltaic Cells. *Appl. Phys. Lett.* **2015,** *107* (12), 123303.

(112) Chen, Y. H.; Lin, L. Y.; Lu, C. W.; Lin, F.; Huang, Z. Y.; Lin, H. W.; Wang, P. H.; Liu, Y. H.; Wong, K. T.; Wen, J.; Miller, D. J.; Darling, S. B., Vacuum-Deposited Small-Molecule Organic Solar Cells with High Power Conversion Efficiencies by Judicious Molecular Design and Device Optimization. *J. Am. Chem. Soc.* **2012,** *134* (33), 13616-23.

(113) Zou, Y.; Holst, J.; Zhang, Y.; Holmes, R. J., 7.9% Efficient Vapor-Deposited Organic Photovoltaic Cells Based on a Simple Bulk Heterojunction. *J. Mater. Chem. A* **2014,** *2* (31), 12397.

(114) Griffith, O. L.; Liu, X.; Amonoo, J. A.; Djurovich, P. I.; Thompson, M. E.; Green, P. F.; Forrest, S. R., Charge Transport and Exciton Dissociation in Organic Solar Cells Consisting of Dipolar Donors Mixed with C70. *Phys. Rev. B* **2015,** *92* (8), 085404.

(115) Carr, J.; Chaudhary, S., On Accurate Capacitance Characterization of Organic Photovoltaic Cells. *Appl. Phys. Lett.* **2012,** *100* (21), 213902.

(116) Zhang, T.; Holmes, R. J., Photovoltage as a Quantitative Probe of Carrier Generation and Recombination in Organic Photovoltaic Cells. *J. Mater. Chem. C* **2017,** *5* (45), 11885-11891.

(117) Zou, Y.; Holmes, R. J., The Role of Exciton Ionization Processes in Bulk Heterojunction Organic Photovoltaic Cells. *Adv. Energy Mater.* **2015,** *5* (12).

(118) Heidel, T. D.; Hochbaum, D.; Sussman, J. M.; Singh, V.; Bahlke, M. E.; Hiromi, I.; Lee, J.; Baldo, M. A., Reducing Recombination Losses in Planar Organic Photovoltaic Cells Using Multiple Step Charge Separation. *J. Appl. Phys.* **2011,** *109* (10), 104502.

(119) Bilby, D.; Amonoo, J.; Sykes, M. E.; Frieberg, B.; Huang, B.; Hungerford, J.; Shtein, M.; Green, P.; Kim, J., Reduction of Open Circuit Voltage Loss in a Polymer Photovoltaic Cell Via Interfacial Molecular Design: Insertion of a Molecular Spacer. *Appl. Phys. Lett.* **2013,** *103* (20), 203902.

(120) Zhong, Y.; Tada, A.; Izawa, S.; Hashimoto, K.; Tajima, K., Enhancement of Voc without Loss of Jsc in Organic Solar Cells by Modification of Donor/Acceptor Interfaces. *Adv. Energy Mater.* **2014,** *4* (5), 1301332.

(121) Qi, B.; Wang, J., Fill Factor in Organic Solar Cells. *Phys. Chem. Chem. Phys.* **2013,** *15* (23), 8972-82.

(122) Chiu, S. W.; Lin, L. Y.; Lin, H. W.; Chen, Y. H.; Huang, Z. Y.; Lin, Y. T.; Lin, F.; Liu, Y. H.; Wong, K. T., A Donor-Acceptor-Acceptor Molecule for Vacuum-Processed Organic Solar Cells with a Power Conversion Efficiency of 6.4%. *Chem. Commun.* **2012,** *48* (13), 1857-9.

(123) Zhang, X.-H.; Cui, Y.; Katoh, R.; Koumura, N.; Hara, K., Organic Dyes Containing Thieno [3, 2-B] Indole Donor for Efficient Dye-Sensitized Solar Cells. *J. Phys. Chem. C* **2010,** *114* (42), 18283-18290.

(124) Irgashev, R. A.; Karmatsky, A. A.; Kozyukhin, S. A.; Ivanov, V. K.; Sadovnikov, A.; Kozik, V. V.; Grinberg, V. A.; Emets, V. V.; Rusinov, G. L.; Charushin, V. N., A Facile and Convenient Synthesis and Photovoltaic Characterization of Novel Thieno [2, 3-B] Indole Dyes for Dye-Sensitized Solar Cells. *Synth. Met.* **2015,** *199*, 152-158.

(125) Mitsumoto, R.; Araki, T.; Ito, E.; Ouchi, Y.; Seki, K.; Kikuchi, K.; Achiba, Y.; Kurosaki, H.; Sonoda, T.; Kobayashi, H., Electronic Structures and Chemical Bonding of Fluorinated Fullerenes Studied by Nexafs, Ups, and Vacuum-Uv Absorption Spectroscopies. *J. Phys. Chem. A* **1998,** *102* (3), 552-560.

(126) Xie, Q.; Arias, F.; Echegoyen, L., Electrochemically-Reversible, Single-Electron Oxidation of C60 and C70. *J. Am. Chem. Soc.* **1993,** *115* (21), 9818-9819.

(127) Bürckstümmer, H.; Tulyakova, E. V.; Deppisch, M.; Lenze, M. R.; Kronenberg, N. M.; Gsänger, M.; Stolte, M.; Meerholz, K.; Würthner, F., Efficient Solution-Processed Bulk Heterojunction Solar Cells by Antiparallel Supramolecular Arrangement of Dipolar Donor–Acceptor Dyes. *Angew. Chem. Int. Ed.* **2011,** *123* (49), 11832-11836.

(128) Bürckstümmer, H.; Kronenberg, N. M.; Gsänger, M.; Stolte, M.; Meerholz, K.; Würthner, F., Tailored Merocyanine Dyes for Solution-Processed Bhj Solar Cells. *J. Mater. Chem.* **2010,** *20* (2), 240-243.

(129) Würthner, F.; Yao, S.; Debaerdemaeker, T.; Wortmann, R., Dimerization of Merocyanine Dyes. Structural and Energetic Characterization of Dipolar Dye Aggregates and Implications for Nonlinear Optical Materials. *J. Am. Chem. Soc.* **2002,** *124* (32), 9431-9447.

(130) Würthner, F.; Meerholz, K., Systems Chemistry Approach in Organic Photovoltaics. *Chem. Eur. J.* **2010,** *16* (31), 9366-9373.

(131) Tress, W.; Petrich, A.; Hummert, M.; Hein, M.; Leo, K.; Riede, M., Imbalanced Mobilities Causing S-Shaped Iv Curves in Planar Heterojunction Organic Solar Cells. *Appl. Phys. Lett.* **2011,** *98* (6), 063301.

(132) Kim, Y.; Choulis, S. A.; Nelson, J.; Bradley, D. D. C.; Cook, S.; Durrant, J. R., Device Annealing Effect in Organic Solar Cells with Blends of Regioregular Poly(3-Hexylthiophene) and Soluble Fullerene. *Appl. Phys. Lett.* **2005,** *86* (6), 063502.

(133) Li, G.; Shrotriya, V.; Huang, J.; Yao, Y.; Moriarty, T.; Emery, K.; Yang, Y., High-Efficiency Solution Processable Polymer Photovoltaic Cells by Self-Organization of Polymer Blends. *Nat. Mater.* **2005,** *4* (11), 864-868.

(134) Sakai, J.; Taima, T.; Yamanari, T.; Saito, K., Annealing Effect in the Sexithiophene:C70 Small Molecule Bulk Heterojunction Organic Photovoltaic Cells. *Sol. Energy Mater. Sol. Cells* **2009,** *93* (6-7), 1149-1153.

(135) Zhang, T.; Han, H.; Zou, Y.; Lee, Y.-C.; Oshima, H.; Wong, K.-T.; Holmes, R. J., Impact of Thermal Annealing on Organic Photovoltaic Cells Using Regioisomeric Donor–Acceptor–Acceptor Molecules. *ACS Appl. Mater. Interfaces* **2017,** *9* (30), 25418-25425.

(136) Bergemann, K. J.; Liu, X.; Panda, A.; Forrest, S. R., Singlets Lead to Photogeneration in C60-Based Organic Heterojunctions. *Phys. Rev. B* **2015,** *92* (3).

(137) Zou, Y.; Holmes, R. J., Influence of a Moox Interlayer on the Open-Circuit Voltage in Organic Photovoltaic Cells. *Appl. Phys. Lett.* **2013,** *103* (5), 053302.

(138) Schlenker, C. W.; Thompson, M. E., The Molecular Nature of Photovoltage Losses in Organic Solar Cells. *Chem. Commun.* **2011,** *47* (13), 3702-16.

(139) Perez, M. D.; Borek, C.; Forrest, S. R.; Thompson, M. E., Molecular and Morphological Influences on the Open Circuit Voltages of Organic Photovoltaic Devices. *J. Am. Chem. Soc.* **2009,** *131* (26), 9281-9286.

(140) Vandewal, K.; Tvingstedt, K.; Gadisa, A.; Inganas, O.; Manca, J. V., On the Origin of the Open-Circuit Voltage of Polymer-Fullerene Solar Cells. *Nat. Mater.* **2009,** *8* (11), 904-9.

(141) Rand, B. P.; Burk, D. P.; Forrest, S. R., Offset Energies at Organic Semiconductor Heterojunctions and Their Influence on the Open-Circuit Voltage of Thin-Film Solar Cells. *Phys. Rev. B* **2007,** *75* (11), 115327.

(142) Maurano, A.; Hamilton, R.; Shuttle, C. G.; Ballantyne, A. M.; Nelson, J.; O'Regan, B.; Zhang, W.; McCulloch, I.; Azimi, H.; Morana, M.; Brabec, C. J.; Durrant, J. R., Recombination Dynamics as a Key Determinant of Open Circuit Voltage in Organic Bulk Heterojunction Solar Cells: A Comparison of Four Different Donor Polymers. *Adv. Mater.* **2010,** *22* (44), 4987-92.

(143) Mutolo, K. L.; Mayo, E. I.; Rand, B. P.; Forrest, S. R.; Thompson, M. E., Enhanced Open-Circuit Voltage in Subphthalocyanine/C60 Organic Photovoltaic Cells. *J. Am. Chem. Soc.* **2006,** *128* (25), 8108-8109.

(144) He, Y.; Chen, H.-Y.; Hou, J.; Li, Y., Indene-C_{60} Bisadduct: A New Acceptor for High-Performance Polymer Solar Cells. *J. Am. Chem. Soc.* **2010,** *132* (4), 1377-1382.

(145) Tada, A.; Geng, Y.; Wei, Q.; Hashimoto, K.; Tajima, K., Tailoring Organic Heterojunction Interfaces in Bilayer Polymer Photovoltaic Devices. *Nat. Mater.* **2011,** *10* (6), 450-5.

(146) Campbell, I. H.; Crone, B. K., Improving an Organic Photodiode by Incorporating a Tunnel Barrier between the Donor and Acceptor Layers. *Appl. Phys. Lett.* **2012,** *101* (2), 023301.

(147) Kumar, A.; Pace, G.; Bakulin, A. A.; Fang, J.; Ho, P. K. H.; Huck, W. T. S.; Friend, R. H.; Greenham, N. C., Donor–Acceptor Interface Modification by Zwitterionic Conjugated Polyelectrolytes in Polymer Photovoltaics. *Energy Environ. Sci.* **2013,** *6* (5), 1589.

(148) Chen, S.; Tsang, S. W.; Lai, T. H.; Reynolds, J. R.; So, F., Dielectric Effect on the Photovoltage Loss in Organic Photovoltaic Cells. *Adv. Mater.* **2014,** *26* (35), 6125-31.

(149) Kippelen, B.; Brédas, J.-L., Organic Photovoltaics. *Energy Environ. Sci.* **2009,** *2* (3), 251-261.

(150) Lam, S. L.; Liu, X.; Zhao, F.; Lee, C.-L. K.; Kwan, W. L., Manipulating Open-Circuit Voltage in an Organic Photovoltaic Device Via a Phenylalkyl Side Chain. *Chem. Commun.* **2013,** *49* (40), 4543-4545.

(151) Nakanotani, H.; Furukawa, T.; Morimoto, K.; Adachi, C., Long-Range Coupling of Electron-Hole Pairs in Spatially Separated Organic Donor-Acceptor Layers. *Sci. Adv.* **2016,** *2* (2), e1501470.

(152) Caplins, B. W.; Mullenbach, T. K.; Holmes, R. J.; Blank, D. A., Femtosecond to Nanosecond Excited State Dynamics of Vapor Deposited Copper Phthalocyanine Thin Films. *Phys. Chem. Chem. Phys.* **2016,** *18* (16), 11454-11459.

(153) Pandey, A. K., Highly Efficient Spin-Conversion Effect Leading to Energy up-Converted Electroluminescence in Singlet Fission Photovoltaics. *Sci. Rep.* **2015,** *5*, 7787.

(154) Vincett, P. S., Phosphorescence and Fluorescence of Phthalocyanines. *J. Chem. Phys* **1971,** *55* (8), 4131.

(155) Fahrenbruch, A.; Aranovich, J., Heterojunction Phenomena and Interfacial Defects in Photovoltaic Converters. In *Solar Energy Conversion*, Springer: 1979; pp 257-326.

(156) Elumalai, N. K.; Uddin, A., Open Circuit Voltage of Organic Solar Cells: An in-Depth Review. *Energy Environ. Sci.* **2016,** *9* (2), 391-410.

(157) Proctor, C. M.; Nguyen, T.-Q., Effect of Leakage Current and Shunt Resistance on the Light Intensity Dependence of Organic Solar Cells. *Appl. Phys. Lett.* **2015,** *106* (8), 23_1.

(158) Widmer, J.; Tietze, M.; Leo, K.; Riede, M., Open-Circuit Voltage and Effective Gap of Organic Solar Cells. *Adv. Funct. Mater.* **2013,** *23* (46), 5814-5821.

(159) Bisquert, J.; Garcia-Belmonte, G., On Voltage, Photovoltage, and Photocurrent in Bulk Heterojunction Organic Solar Cells. *J. Phys. Chem. Lett.* **2011,** *2* (15), 1950-1964.

(160) Koster, L. J. A.; Mihailetchi, V. D.; Ramaker, R.; Blom, P. W. M., Light Intensity Dependence of Open-Circuit Voltage of Polymer:Fullerene Solar Cells. *Appl. Phys. Lett.* **2005,** *86* (12), 123509.

(161) Vandewal, K.; Tvingstedt, K.; Gadisa, A.; Inganäs, O.; Manca, J. V., Relating the Open-Circuit Voltage to Interface Molecular Properties of Donor:Acceptor Bulk Heterojunction Solar Cells. *Phys. Rev. B* **2010,** *81* (12).

(162) Zhang, T.; Holmes, R. J., Overcoming the Trade-Off between Exciton Dissociation and Charge Recombination in Organic Photovoltaic Cells. *Appl. Phys. Lett.* **2018,** *113* (14), 143302.

(163) Cho, S.; Piper, L.; DeMasi, A.; Preston, A.; Smith, K.; Chauhan, K.; Sullivan, P.; Hatton, R.; Jones, T. S., Electronic Structure of C60/Phthalocyanine/Ito Interfaces Studied Using Soft X-Ray Spectroscopies. *J. Phys. Chem. C* **2010,** *114* (4), 1928-1933.

(164) Kaneto, K.; Yoshino, K.; Inuishi, Y., Phosphorescence in Platinum Phthalocyanine Single Crystals Excited by Ruby Laser. *J. Phys. Soc. Jpn.* **1974,** *37* (5), 1297-1300.

(165) Minami, N., Photocurrent Spectra of Phthalocyanine Thin-Film Electrodes in the Visible to near-Infrared. *J. Chem. Soc., Faraday Trans. 2* **1982,** *78* (11), 1871-1880.

(166) Kim, I.; Haverinen, H. M.; Wang, Z.; Madakuni, S.; Kim, Y.; Li, J.; Jabbour, G. E., Efficient Organic Solar Cells Based on Planar Metallophthalocyanines. *Chem. Mater.* **2009,** *21* (18), 4256-4260.

(167) Hiramoto, M.; Kubo, M.; Shinmura, Y.; Ishiyama, N.; Kaji, T.; Sakai, K.; Ohno, T.; Izaki, M., Bandgap Science for Organic Solar Cells. *Electronics* **2014,** *3* (2), 351-380.

(168) Tegeler, E.; Iwan, M.; Koch, E.-E., Electronic Structure of the Valence Bands of H2-, Mg-and Pt-Phthalocyanine Derived from Soft X-Ray Emission and Photoelectron Emission Spectra. *J. Electron. Spectrosc.* **1981,** *22* (3), 297-307.

(169) Qin, D.; Gu, P.; Dhar, R. S.; Razavipour, S. G.; Ban, D., Measuring the Exciton Diffusion Length of C60 in Organic Planar Heterojunction Solar Cells. *Phys. Status Solidi A* **2011,** *208* (8), 1967-1971.

(170) Groves, C., Suppression of Geminate Charge Recombination in Organic Photovoltaic Devices with a Cascaded Energy Heterojunction. *Energy Environ. Sci.* **2013,** *6* (5), 1546.

(171) Xia, J.; Sanders, S. N.; Cheng, W.; Low, J. Z.; Liu, J.; Campos, L. M.; Sun, T., Singlet Fission: Progress and Prospects in Solar Cells. *Adv. Mater.* **2017,** *29* (20).

(172) Ehrler, B.; Wilson, M. W.; Rao, A.; Friend, R. H.; Greenham, N. C., Singlet Exciton Fission-Sensitized Infrared Quantum Dot Solar Cells. *Nano Lett.* **2012,** *12* (2), 1053-1057.

(173) Lee, J.; Jadhav, P.; Reusswig, P. D.; Yost, S. R.; Thompson, N. J.; Congreve, D. N.; Hontz, E.; Van Voorhis, T.; Baldo, M. A., Singlet Exciton Fission Photovoltaics. *Acc. Chem. Res.* **2013,** *46* (6), 1300-1311.

(174) Jadhav, P. J.; Mohanty, A.; Sussman, J.; Lee, J.; Baldo, M. A., Singlet Exciton Fission in Nanostructured Organic Solar Cells. *Nano Lett.* **2011,** *11* (4), 1495-8.

(175) An, Q.; Zhang, F.; Zhang, J.; Tang, W.; Deng, Z.; Hu, B., Versatile Ternary Organic Solar Cells: A Critical Review. *Energy Environ. Sci.* **2016**.

(176) Huang, J.-S.; Goh, T.; Li, X.; Sfeir, M. Y.; Bielinski, E. A.; Tomasulo, S.; Lee, M. L.; Hazari, N.; Taylor, A. D., Polymer Bulk Heterojunction Solar Cells Employing Förster Resonance Energy Transfer. *Nat. Photonics* **2013,** *7* (6), 479-485.

(177) Honda, S.; Yokoya, S.; Ohkita, H.; Benten, H.; Ito, S., Light-Harvesting Mechanism in Polymer/Fullerene/Dye Ternary Blends Studied by Transient Absorption Spectroscopy. *J. Phys. Chem. C* **2011,** *115* (22), 11306-11317.

(178) Honda, S.; Ohkita, H.; Benten, H.; Ito, S., Selective Dye Loading at the Heterojunction in Polymer/Fullerene Solar Cells. *Adv. Energy Mater.* **2011,** *1* (4), 588-598.

(179) Deotare, P. B.; Chang, W.; Hontz, E.; Congreve, D. N.; Shi, L.; Reusswig, P. D.; Modtland, B.; Bahlke, M. E.; Lee, C. K.; Willard, A. P.; Bulovic, V.; Van Voorhis, T.; Baldo, M. A., Nanoscale Transport of Charge-Transfer States in Organic Donor-Acceptor Blends. *Nat. Mater.* **2015,** *14* (11), 1130-4.

(180) Unuchek, D.; Ciarrocchi, A.; Avsar, A.; Watanabe, K.; Taniguchi, T.; Kis, A., Room-Temperature Electrical Control of Exciton Flux in a Van Der Waals Heterostructure. *Nature* **2018,** *560* (7718), 340-344.

(181) Mullenbach, T. K.; McGarry, K. A.; Luhman, W. A.; Douglas, C. J.; Holmes, R. J., Connecting Molecular Structure and Exciton Diffusion Length in Rubrene Derivatives. *Adv. Mater.* **2013,** *25* (27), 3689-93.

(182) Matthew Menke, S.; Holmes, R. J., Evaluating the Role of Energetic Disorder and Thermal Activation in Exciton Transport. *J. Mater. Chem. C* **2016**.

(183) Menke, S. M.; Holmes, R. J., Exciton Transport in an Organic Semiconductor Exhibiting Thermally Activated Delayed Fluorescence. *J. Phys. Chem. C* **2016,** *120* (16), 8502-8508.

(184) Mikhnenko, O. V.; Azimi, H.; Scharber, M.; Morana, M.; Blom, P. W.; Loi, M. A., Exciton Diffusion Length in Narrow Bandgap Polymers. *Energy Environ. Sci.* **2012,** *5* (5), 6960-6965.

(185) Scully, S. R.; McGehee, M. D., Effects of Optical Interference and Energy Transfer on Exciton Diffusion Length Measurements in Organic Semiconductors. *J. Appl. Phys.* **2006,** *100* (3), 034907.

(186) Shaw, P. E.; Ruseckas, A.; Samuel, I. D., Exciton Diffusion Measurements in Poly (3-Hexylthiophene). *Adv. Mater.* **2008,** *20* (18), 3516-3520.

(187) Lunt, R. R.; Giebink, N. C.; Belak, A. A.; Benziger, J. B.; Forrest, S. R., Exciton Diffusion Lengths of Organic Semiconductor Thin Films Measured by Spectrally Resolved Photoluminescence Quenching. *J. Appl. Phys.* **2009,** *105* (5), 053711.

(188) Rai, D.; Holmes, R. J., Measurement of the Triplet Exciton Diffusion Length in Organic Semiconductors. *J. Mater. Chem. C* **2019,** *7* (19), 5695-5701.

(189) Goushi, K.; Yoshida, K.; Sato, K.; Adachi, C., Organic Light-Emitting Diodes Employing Efficient Reverse Intersystem Crossing for Triplet-to-Singlet State Conversion. *Nat. Photonics* **2012,** *6* (4), 253-258.

(190) dos Santos, P. L.; Dias, F. B.; Monkman, A. P., Investigation of the Mechanisms Giving Rise to Tadf in Exciplex States. *J. Phys. Chem. C* **2016,** *120* (32), 18259-18267.

(191) Yasuda, T.; Yamaguchi, Y.; Zou, D.-C.; Tsutsui, T., Carrier Mobilities in Organic Electron Transport Materials Determined from Space Charge Limited Current. *Jpn. J. Appl. Phys.* **2002,** *41* (9R), 5626.

(192) Matsushima, T.; Jin, G.-H.; Kanai, Y.; Yokota, T.; Kitada, S.; Kishi, T.; Murata, H., Interfacial Charge Transfer and Charge Generation in Organic Electronic Devices. *Org. Electron.* **2011,** *12* (3), 520-528.

(193) Xu, W.; Bai, Y.; Jiang, X.; Zhang, Z., The Estimation of Electron Mobility of 4, 7-Diphyenyl-1, 10-Phenanthroline Using Space-Charge-Limited Currents. *Solid State Communications* **2008,** *146* (7-8), 311-314.

(194) Khan, M.; Xu, W.; Khizar-ul-Haq; Bai, Y.; Jiang, X.; Zhang, Z.; Zhu, W.; Zhang, Z.; Zhu, W., Electron Mobility of 4, 7-Diphyenyl-1, 10-Phenanthroline Estimated by Using Space-Charge-Limited Currents. *J. Appl. Phys.* **2008,** *103* (1), 014509.

(195) Al Attar, H. A.; Monkman, A. P., Electric Field Induce Blue Shift and Intensity Enhancement in 2d Exciplex Organic Light Emitting Diodes; Controlling Electron-Hole Separation. *Adv. Mater.* **2016,** *28* (36), 8014-8020.

(196) Murgatroyd, P., Theory of Space-Charge-Limited Current Enhanced by Frenkel Effect. *J. Phys. D: Appl. Phys.* **1970,** *3* (2), 151.

(197) Ye, Z.; Cao, T.; O'Brien, K.; Zhu, H.; Yin, X.; Wang, Y.; Louie, S. G.; Zhang, X., Probing Excitonic Dark States in Single-Layer Tungsten Disulphide. *Nature* **2014,** *513* (7517), 214.

(198) Ye, Y.; Wong, Z. J.; Lu, X.; Ni, X.; Zhu, H.; Chen, X.; Wang, Y.; Zhang, X., Monolayer Excitonic Laser. *Nat. Photonics* **2015,** *9* (11), 733.

(199) Blancon, J.-C.; Tsai, H.; Nie, W.; Stoumpos, C. C.; Pedesseau, L.; Katan, C.; Kepenekian, M.; Soe, C. M. M.; Appavoo, K.; Sfeir, M. Y., Extremely Efficient Internal Exciton Dissociation through Edge States in Layered 2d Perovskites. *Science* **2017,** *355* (6331), 1288-1292.

(200) Zhang, Q.; Chu, L.; Zhou, F.; Ji, W.; Eda, G., Excitonic Properties of Chemically Synthesized 2d Organic–Inorganic Hybrid Perovskite Nanosheets. *Adv. Mater.* **2018,** *30*, 1704055.

(201) Milichko, V. A.; Makarov, S. V.; Yulin, A. V.; Vinogradov, A. V.; Krasilin, A. A.; Ushakova, E.; Dzyuba, V. P.; Hey-Hawkins, E.; Pidko, E. A.; Belov, P. A., Van Der Waals Metal-Organic Framework as an Excitonic Material for Advanced Photonics. *Adv. Mater.* **2017,** *29* (12), 1606034.

(202) Najafov, H.; Lee, B.; Zhou, Q.; Feldman, L. C.; Podzorov, V., Observation of Long-Range Exciton Diffusion in Highly Ordered Organic Semiconductors. *Nat. Mater.* **2010,** *9* (11), 938.

(203) Cnops, K.; Rand, B. P.; Cheyns, D.; Verreet, B.; Empl, M. A.; Heremans, P., 8.4% Efficient Fullerene-Free Organic Solar Cells Exploiting Long-Range Exciton Energy Transfer. *Nat. Commun.* **2014,** *5*, 3406.

(204) Shirasaki, Y.; Supran, G. J.; Bawendi, M. G.; Bulović, V., Emergence of Colloidal Quantum-Dot Light-Emitting Technologies. *Nat. Photonics* **2013,** *7* (1), 13.

(205) Sun, Y.; Giebink, N. C.; Kanno, H.; Ma, B.; Thompson, M. E.; Forrest, S. R., Management of Singlet and Triplet Excitons for Efficient White Organic Light-Emitting Devices. *Nature* **2006,** *440* (7086), 908-12.

(206) Coburn, C.; Lee, J.; Forrest, S. R., Charge Balance and Exciton Confinement in Phosphorescent Organic Light Emitting Diodes. *Adv. Opt. Mater.* **2016,** *4* (6), 889-895.

(207) Che, X.; Li, Y.; Qu, Y.; Forrest, S. R., High Fabrication Yield Organic Tandem Photovoltaics Combining Vacuum- and Solution-Processed Subcells with 15% Efficiency. *Nat. Energy* **2018,** *3* (5), 422-427.

(208) Che, X.; Xiao, X.; Zimmerman, J. D.; Fan, D.; Forrest, S. R., High-Efficiency, Vacuum-Deposited, Small-Molecule Organic Tandem and Triple-Junction Photovoltaic Cells. *Adv. Energy Mater.* **2014,** *4* (18), 1400568.

(209) Zhao, W.; Li, S.; Yao, H.; Zhang, S.; Zhang, Y.; Yang, B.; Hou, J., Molecular Optimization Enables over 13% Efficiency in Organic Solar Cells. *J. Am. Chem. Soc.* **2017,** *139* (21), 7148-7151.

(210) Lin, Y.; Zhao, F.; Wu, Y.; Chen, K.; Xia, Y.; Li, G.; Prasad, S. K.; Zhu, J.; Huo, L.; Bin, H., Mapping Polymer Donors toward High-Efficiency Fullerene Free Organic Solar Cells. *Adv. Mater.* **2017,** *29* (3), 1604155.

(211) High, A. A.; Novitskaya, E. E.; Butov, L. V.; Hanson, M.; Gossard, A. C., Control of Exciton Fluxes in an Excitonic Integrated Circuit. *Science* **2008,** *321* (5886), 229-231.

(212) Lin, J. D.; Mikhnenko, O. V.; Chen, J.; Masri, Z.; Ruseckas, A.; Mikhailovsky, A.; Raab, R. P.; Liu, J.; Blom, P. W.; Loi, M. A., Systematic Study of Exciton Diffusion Length in Organic Semiconductors by Six Experimental Methods. *Mater Horiz.* **2014,** *1* (2), 280-285.

(213) Hedley, G. J.; Ruseckas, A.; Samuel, I. D., Light Harvesting for Organic Photovoltaics. *Chem. Rev.* **2016,** *117* (2), 796-837.

(214) Scharber, M. C.; Mühlbacher, D.; Koppe, M.; Denk, P.; Waldauf, C.; Heeger, A. J.; Brabec, C. J., Design Rules for Donors in Bulk-Heterojunction Solar Cells—Towards 10% Energy-Conversion Efficiency. *Adv. Mater.* **2006,** *18* (6), 789-794.

(215) Park, S. H.; Roy, A.; Beaupré, S.; Cho, S.; Coates, N.; Moon, J. S.; Moses, D.; Leclerc, M.; Lee, K.; Heeger, A. J., Bulk Heterojunction Solar Cells with Internal Quantum Efficiency Approaching 100%. *Nat. Photonics* **2009,** *3* (5), 297.

(216) Mayer, A. C.; Scully, S. R.; Hardin, B. E.; Rowell, M. W.; McGehee, M. D., Polymer-Based Solar Cells. *Mater. Today* **2007,** *10* (11), 28-33.

(217) Halls, J. J.; Pichler, K.; Friend, R. H.; Moratti, S.; Holmes, A., Exciton Diffusion and Dissociation in a Poly (P-Phenylenevinylene)/C60 Heterojunction Photovoltaic Cell. *Appl. Phys. Lett.* **1996,** *68* (22), 3120-3122.

(218) Tamai, Y.; Ohkita, H.; Benten, H.; Ito, S., Exciton Diffusion in Conjugated Polymers: From Fundamental Understanding to Improvement in Photovoltaic Conversion Efficiency. *J. Phys. Chem. Lett.* **2015,** *6* (17), 3417-28.

(219) Westenhoff, S.; Howard, I. A.; Friend, R. H., Probing the Morphology and Energy Landscape of Blends of Conjugated Polymers with Sub-10 Nm Resolution. *Phys. Rev. Lett.* **2008,** *101* (1), 016102.

(220) Penwell, S. B.; Ginsberg, L. D. S.; Noriega, R.; Ginsberg, N. S., Resolving Ultrafast Exciton Migration in Organic Solids at the Nanoscale. *Nat. Mater.* **2017,** *16* (11), 1136-1141.

(221) Kose, M. E.; Graf, P.; Kopidakis, N.; Shaheen, S. E.; Kim, K.; Rumbles, G., Exciton Migration in Conjugated Dendrimers: A Joint Experimental and Theoretical Study. *ChemPhysChem* **2009,** *10* (18), 3285-94.

(222) Thompson, N. J.; Wilson, M. W.; Congreve, D. N.; Brown, P. R.; Scherer, J. M.; Bischof, T. S.; Wu, M.; Geva, N.; Welborn, M.; Van Voorhis, T., Energy Harvesting of Non-Emissive Triplet Excitons in Tetracene by Emissive Pbs Nanocrystals. *Nat. Mater.* **2014,** *13* (11), 1039.

(223) Congreve, D. N.; Lee, J.; Thompson, N. J.; Hontz, E.; Yost, S. R.; Reusswig, P. D.; Bahlke, M. E.; Reineke, S.; Van Voorhis, T.; Baldo, M. A., External Quantum Efficiency above 100% in a Singlet-Exciton-Fission–Based Organic Photovoltaic Cell. *Science* **2013,** *340* (6130), 334-337.

(224) Efros, A. L.; Rosen, M.; Kuno, M.; Nirmal, M.; Norris, D. J.; Bawendi, M., Band-Edge Exciton in Quantum Dots of Semiconductors with a Degenerate Valence Band: Dark and Bright Exciton States. *Phys. Rev. B* **1996,** *54* (7), 4843.

(225) Luhman, W. A.; Holmes, R. J., Enhanced Exciton Diffusion in an Organic Photovoltaic Cell by Energy Transfer Using a Phosphorescent Sensitizer. *Appl. Phys. Lett.* **2009,** *94* (15), 153304.

(226) Terao, Y.; Sasabe, H.; Adachi, C., Correlation of Hole Mobility, Exciton Diffusion Length, and Solar Cell Characteristics in Phthalocyanine/Fullerene Organic Solar Cells. *Appl. Phys. Lett.* **2007,** *90* (10), 103515.

(227) Guide, M.; Lin, J. D.; Proctor, C. M.; Chen, J.; García-Cervera, C.; Nguyen, T.-Q., Effect of Copper Metalation of Tetrabenzoporphyrin Donor Material on Organic Solar Cell Performance. *J. Mater. Chem. A* **2014,** *2* (21), 7890-7896.

(228) Siegmund, B.; Sajjad, M. T.; Widmer, J.; Ray, D.; Koerner, C.; Riede, M.; Leo, K.; Samuel, I. D.; Vandewal, K., Exciton Diffusion Length and Charge Extraction Yield in Organic Bilayer Solar Cells. *Adv. Mater.* **2017,** *29* (12), 1604424.

(229) Curtin, I. J.; Holmes, R. J., Decoupling Photocurrent Loss Mechanisms in Photovoltaic Cells Using Complementary Measurements of Exciton Diffusion. *Adv. Energy Mater.* **2018**, 1702339.

(230) Credgington, D.; Liu, S.-W.; Nelson, J.; Durrant, J. R., In Situ Measurement of Energy Level Shifts and Recombination Rates in Subphthalocyanine/C60 Bilayer Solar Cells. *J. Phys. Chem. C* **2014,** *118* (40), 22858-22864.

(231) Yi, Y.; Jeon, P. E.; Lee, H.; Han, K.; Kim, H. S.; Jeong, K.; Cho, S. W., The Interface State Assisted Charge Transport at the Moo(3)/Metal Interface. *J. Chem. Phys* **2009,** *130* (9), 094704.

(232) Chandran, H. T.; Ng, T. W.; Foo, Y.; Li, H. W.; Qing, J.; Liu, X. K.; Chan, C. Y.; Wong, F. L.; Zapien, J. A.; Tsang, S. W.; Lo, M. F.; Lee, C. S., Direct Free Carrier Photogeneration in Single Layer and Stacked Organic Photovoltaic Devices. *Adv. Mater.* **2017,** *29* (22), 1606909.

(233) Hahn, T.; Tscheuschner, S.; Saller, C.; Strohriegl, P.; Boregowda, P.; Mukhopadhyay, T.; Patil, S.; Neher, D.; Bässler, H.; Köhler, A., Role of Intrinsic Photogeneration in Single Layer and Bilayer Solar Cells with C60 and Pcbm. *J. Phys. Chem. C* **2016,** *120* (43), 25083-25091.

(234) Ishibashi, Y.; Arinishi, M.; Katayama, T.; Miyasaka, H.; Asahi, T., Femtosecond Excited-State Dynamics of Fullerene-C60 Nanoparticles in Water. *Phys. Chem. Chem. Phys.* **2018,** *20* (2), 958-966.

(235) Li, Y.; Lin, J. D.; Liu, X.; Qu, Y.; Wu, F. P.; Liu, F.; Jiang, Z. Q.; Forrest, S. R., Near-Infrared Ternary Tandem Solar Cells. *Adv. Mater.* **2018,** *30* (45), 1804416.

(236) He, Z.; Zhong, C.; Su, S.; Xu, M.; Wu, H.; Cao, Y., Enhanced Power-Conversion Efficiency in Polymer Solar Cells Using an Inverted Device Structure. *Nat. Photonics* **2012,** *6* (9), 591-595.

(237) Dement, D. B.; Puri, M.; Ferry, V. E., Determining the Complex Refractive Index of Neat Cdse/Cds Quantum Dot Films. *J. Phys. Chem. C* **2018,** *122* (37), 21557-21568.

(238) Akselrod, G. M.; Prins, F.; Poulikakos, L. V.; Lee, E. M.; Weidman, M. C.; Mork, A. J.; Willard, A. P.; Bulovic, V.; Tisdale, W. A., Subdiffusive Exciton Transport in Quantum Dot Solids. *Nano Lett.* **2014,** *14* (6), 3556-62.

(239) Lee, E. M. Y.; Tisdale, W. A., Determination of Exciton Diffusion Length by Transient Photoluminescence Quenching and Its Application to Quantum Dot Films. *J. Phys. Chem. C* **2015,** *119* (17), 9005-9015.

(240) Einzinger, M.; Wu, T.; Kompalla, J. F.; Smith, H. L.; Perkinson, C. F.; Nienhaus, L.; Wieghold, S.; Congreve, D. N.; Kahn, A.; Bawendi, M. G., Sensitization of Silicon by Singlet Exciton Fission in Tetracene. *Nature* **2019,** *571* (7763), 90.

(241) Wilson, M. W.; Rao, A.; Clark, J.; Kumar, R. S. S.; Brida, D.; Cerullo, G.; Friend, R. H., Ultrafast Dynamics of Exciton Fission in Polycrystalline Pentacene. *J. Am. Chem. Soc.* **2011,** *133* (31), 11830-11833.

(242) Jundt, C.; Klein, G.; Sipp, B.; Le Moigne, J.; Joucla, M.; Villaeys, A., Exciton Dynamics in Pentacene Thin Films Studied by Pump-Probe Spectroscopy. *Chemical physics letters* **1995,** *241* (1-2), 84-88.

(243) Burgos, J.; Pope, M.; Swenberg, C. E.; Alfano, R., Heterofission in Pentacene-Doped Tetracene Single Crystals. *physica status solidi (b)* **1977,** *83* (1), 249-256.

(244) Miyata, K.; Conrad-Burton, F. S.; Geyer, F. L.; Zhu, X. Y., Triplet Pair States in Singlet Fission. *Chem Rev* **2019,** *119* (6), 4261-4292.

(245) Akselrod, G. M.; Deotare, P. B.; Thompson, N. J.; Lee, J.; Tisdale, W. A.; Baldo, M. A.; Menon, V. M.; Bulovic, V., Visualization of Exciton Transport in Ordered and Disordered Molecular Solids. *Nat. Commun.* **2014,** *5*, 3646.

(246) Tayebjee, M. J.; Clady, R. G.; Schmidt, T. W., The Exciton Dynamics in Tetracene Thin Films. *Phys Chem Chem Phys* **2013,** *15* (35), 14797-805.

(247) Wan, Y.; Guo, Z.; Zhu, T.; Yan, S.; Johnson, J.; Huang, L., Cooperative Singlet and Triplet Exciton Transport in Tetracene Crystals Visualized by Ultrafast Microscopy. *Nat. Chem.* **2015,** *7* (10), 785-92.

(248) Zhu, T.; Huang, L., Exciton Transport in Singlet Fission Materials: A New Hare and Tortoise Story. *J. Phys. Chem. Lett.* **2018,** *9* (22), 6502-6510.

(249) Curtin, I. J., Measuring Nanoscale Exciton Transport and Carrier Recombination in Organic Solar Cells. *UMN Thesis* **2018**.

(250) Tabachnyk, M.; Ehrler, B.; Bayliss, S.; Friend, R. H.; Greenham, N. C., Triplet Diffusion in Singlet Exciton Fission Sensitized Pentacene Solar Cells. *Appl. Phys. Lett.* **2013,** *103* (15), 153302.

(251) Chen, O.; Chen, X.; Yang, Y.; Lynch, J.; Wu, H.; Zhuang, J.; Cao, Y. C., Synthesis of Metal–Selenide Nanocrystals Using Selenium Dioxide as the Selenium Precursor. *Angew. Chem. Int. Ed.* **2008,** *120* (45), 8766-8769.

(252) Park, Y. S.; Lee, S.; Kim, K. H.; Kim, S. Y.; Lee, J. H.; Kim, J. J., Exciplex-Forming Co-Host for Organic Light-Emitting Diodes with Ultimate Efficiency. *Adv. Funct. Mater.* **2013,** *23* (39), 4914-4920.

(253) Moon, C. K.; Suzuki, K.; Shizu, K.; Adachi, C.; Kaji, H.; Kim, J. J., Combined Inter- and Intramolecular Charge-Transfer Processes for Highly Efficient Fluorescent Organic Light-Emitting Diodes with Reduced Triplet Exciton Quenching. *Adv. Mater.* **2017,** *29* (17), 1606448.

(254) Zhang, D.; Cai, M.; Zhang, Y.; Bin, Z.; Zhang, D.; Duan, L., Simultaneous Enhancement of Efficiency and Stability of Phosphorescent Oleds Based on Efficient Forster Energy Transfer from Interface Exciplex. *ACS Appl. Mater. Interfaces* **2016,** *8* (6), 3825-3832.

(255) Chu, C.-W.; Shao, Y.; Shrotriya, V.; Yang, Y., Efficient Photovoltaic Energy Conversion in Tetracene-C60 Based Heterojunctions. *Appl. Phys. Lett.* **2005,** *86* (24), 243506.

(256) Ehrler, B.; Walker, B. J.; Bohm, M. L.; Wilson, M. W.; Vaynzof, Y.; Friend, R. H.; Greenham, N. C., In Situ Measurement of Exciton Energy in Hybrid Singlet-Fission Solar Cells. *Nat. Commun.* **2012,** *3*, 1019.

(257) Monahan, N.; Zhu, X.-Y., Charge Transfer–Mediated Singlet Fission. *Annu. Rev. Phys. Chem.* **2015,** *66*, 601-618.

(258) Chan, W.-L.; Ligges, M.; Zhu, X., The Energy Barrier in Singlet Fission Can Be Overcome through Coherent Coupling and Entropic Gain. *Nat. Chem.* **2012,** *4* (10), 840.

(259) Musser, A. J.; Liebel, M.; Schnedermann, C.; Wende, T.; Kehoe, T. B.; Rao, A.; Kukura, P., Evidence for Conical Intersection Dynamics Mediating Ultrafast Singlet Exciton Fission. *Nat. Phys.* **2015,** *11* (4), 352.

Appendix

A: List of Publications and Presentations

PUBLICATIONS

1. **Zhang, T.**; Rai, D.; Holmes, R. J., *Probing triplet exciton transport in singlet-fission materials*. (2019), in preparation.

2. **Zhang, T.**; Concannon, N. M.; Holmes, R. J., *Migration of charge-transfer states at organic semiconductor heterojunctions*. (2019), in preparation.

3. Shi, K.; Curtin, I. J.; Healy, A. T.; **Zhang, T.**; Rai, D.; Blank, D. A.; Holmes, R. J., *Probing enhanced exciton diffusion in a triplet-sensitized organic photovoltaic cell*. (2019), in preparation.

4. **Zhang, T.**; Dement, D. B.; Ferry, V. E.; Holmes, R. J., *Intrinsic measurements of exciton transport in photovoltaic cells*. Nat. Commun. (2019), 10, 1156.

5. **Zhang, T.**; Holmes, R. J., *Overcoming the trade-off between exciton dissociation and charge recombination in organic photovoltaic cells*. Appl. Phys. Lett. (2018), 113, 143302.

6. **Zhang, T.**; Han, H.; Zou, Y.; Lee, Y.-C.; Oshima, H.; Wong, K.-T.; Holmes, R. J., *Impact of thermal annealing on organic photovoltaic cells using regioisomeric donor–acceptor–acceptor molecules*. ACS Appl. Mater. Interfaces (2017), 9, 25418-25425.

7. **Zhang, T.**; Holmes, R. J., *Photovoltage as a quantitative probe of carrier generation and recombination in organic photovoltaic cells*. J. Mater. Chem. C (2017), 5, 11885-11891.

8. Mullenbach, T. K.; Curtin, I. J.; **Zhang, T.**; Holmes, R. J., *Probing dark exciton diffusion using photovoltage*. Nat. Commun. (2017), 8, 14215.

PRESENTATIONS

1. **Zhang, T.**; Holmes, R. J., *Engineering donor-acceptor interface for suppression of recombination in organic photovoltaic cells*, 2018 Industrial Partnership for Research in Interfacial & Materials Engineering Annual Meeting, 05/30/2018, Minneapolis (Oral).

2. **Zhang, T.**; Holmes, R. J., *Characterizing and suppressing recombination losses in organic photovoltaic cells*, 2018 Industrial Partnership for Research in Interfacial & Materials Engineering Annual Meeting, 05/30/2018, Minneapolis (Poster).

3. **Zhang, T.**; Holmes, R. J, *Overcoming recombination limitations in device-based measurements of exciton diffusion in organic semiconductors*, 2018 MRS Spring Meeting, 04/04/2018, Phoenix (Oral).

4. **Zhang, T.**; Holmes, R. J., *Suppressing charge recombination in organic photovoltaic cells using an exciton permeable interlayer*, 2017 MRS Fall Meeting, 11/27/2017, Boston (Poster).

5. **Zhang, T.**; Holmes, R. J., *Characterizing carrier recombination losses using photovoltage in organic photovoltaic cells*, 2017 Industrial Partnership for Research in Interfacial & Materials Engineering Annual Meeting, 05/31/2017, Minneapolis (Oral).

6. **Zhang, T.**; Holmes, R. J., *Facilitating carrier harvesting in organic photovoltaic cells through an exciton permeable charge spacer*, 2017 Industrial Partnership for Research in Interfacial & Materials Engineering Annual Meeting, 05/31/2017, Minneapolis (Poster).

7. **Zhang, T.**; Han, H.; Lee, Y.-C.; Oshima, H.; Zou, Y.; Wong, K.-T.; Holmes, R. J., *Impact of thermal annealing on organic photovoltaic cells using tunable donor-acceptor-acceptor molecules*, 2016 MRS Fall Meeting, 11/28/2016, Boston (Poster).

B. Matlab Codes

Code for transfer matrix and exciton diffusion

This code is a combination of two programs to extract the device absorption efficiency, exciton diffusion efficiency, external quantum efficiency as a function incident light wavelength, angle and polarization.

```
%%%%%%%%%%&&&&&&&&&& Transfer Matrix &&&&&&&&&&%%%%%%%%%%

%*** Load Optical Constants ***%
OCraw = importdata('Index_of_Refraction_Library.xlsx');
OC = OCraw.data.data;% optical constants data
OCname = OCraw.colheaders.data;% name of the mats
OCwavelength = OC(:,strmatch('Wavelength',OCname));% file wavelength

%*** INPUT PARAMETERS ***%
lambda =300:5:850;        % wavelength, nm
pol = 0; % polarization (0:s, 1:p)
plotwl = 420;                  % plot wavelength, nm
stepsize = 0.01;                  % for position in device, nm
CCE =1;phi =00; % Collection efficiency and incident angle
layers = {'SiO2' 'ITO' 'P3HT' 'Pentacene' 'C60' 'BCP' 'MoO3' 'Al' 'Air'}; % name of layers in order
thickness = [1E6 105 20 49 45 10 1 100 1];% thickness of each layer, nm;
LD = [0 0 0 17.1 23.2];      % exciton diffusion length, nm
CT =    [0 0 0 2 3]; %charge transfer side% (0:none; 1:bothside; 2:right; 3:left)
tau =CT*0+0.5; % exciton lifetime, ns
DR0= 0 ;DDen= 1.5; % Förster radius, acceptor density [nm] [nm^-3];
AR0= 0 ;ADen= 2.1;% Förster radius, donor density [nm] [nm^-3];
Detar = 0;Aetar = 0; %Prefactor of interfacial recombination efficiency (0:perfect quencher,10000:perfect
blocker);

%%%%%%%%%%
```

```
%*** Absorption Coefficient ***%
alpha = zeros(m,length(lambda));
for j = 1:m
      alpha(j,:) = 4*pi*imag(q(j,:))./(lambda);%nm^-1
end

% Calculate Incoherent power transmission through air-glass interface
% See Griffiths "Intro to Electrodynamics 3rd Ed. Eq. 9.86 & 9.87
if pol == 0
T_glass = abs(2*(cos(phi*pi/180))./((cos(phi*pi/180))+q(1,:))).^2.*real(q(1,:))/(cos(phi*pi/180));
R_glass = abs(((cos(phi*pi/180))-q(1,:))./((cos(phi*pi/180))+q(1,:))).^2;
else
T_glass =
abs(2.*(1.*nc(1,:)).*(cos(phi*pi/180))./(((nc(1,:).^2).*cos(phi*pi/180))+(1^2).*q(1,:))).^2.*real(q(1,:))/(cos
(phi*pi/180));
R_glass = abs(((nc(1,:).^2).*(cos(phi*pi/180))-
(1^2).*q(1,:))./((nc(1,:).^2).*(cos(phi*pi/180))+(1^2).*q(1,:))).^2;
end
% Calculate power reach glass/ITO interface after absorption of glass
P_glass = T_glass.*exp(-alpha(1,:).*thickness(1));
A_glass = T_glass-P_glass; % absorption of glass

% Calculate E-field at each wavelength and position
t = thickness; t(1) = 0;% set glass end 0
t_cumsum=cumsum(t);% position of each interface
x_pos=0:stepsize:sum(t);x_pos(1)=0.000001; %positions to evaluate field
x_mat=sum(repmat(x_pos,length(t),1)>repmat(t_cumsum',1,length(x_pos)),1)+1;
% find out which material certain x_pos belongs to
E=zeros(length(x_pos),length(lambda));
R=lambda*0;T=lambda*0;

for l = 1:length(lambda)
% Calculate total Scattering Matrix 'S '
      S=F_I_mat(q(1,l),q(2,l),nc(1,l),nc(2,l),pol); % First interface
      for j = 2:(m-1)
            S=S*F_L_mat(q(j,l),t(j),lambda(l))*F_I_mat(q(j,l),q(j+1,l),nc(j,l),nc(j+1,l),pol);
      end
      R(l)=(abs(S(2,1)/S(1,1)))^2; % Power Reflection from layers (not glass)
      T(l)=(real(q(end,l))./real(q(1,l)))*(abs(1/S(1,1)))^2; % Power Pass the layers (not glass)

% Calculate all other transfer matrices
      for j = 2:(m-1)
            ej=2*pi*q(j,l)/lambda(l);
            dj=t(j);
            x_indices=find(x_mat == j); % indices of points which are in the material layer considered
            x=x_pos(x_indices)-t_cumsum(j-1); % distance from j(j-1) interface
            % Calculate S'
            S_prime=F_I_mat(q(1,l),q(2,l),nc(1,l),nc(2,l),pol);
            for i=3:j
```

```
                S_prime=S_prime*F_L_mat(q(i-1,l),t(i-1),lambda(l))*F_I_mat(q(i-1,l),q(i,l),nc(i-
1,l),nc(i,l),pol);
            end
            % Calculate S''
            S_doubleprime=eye(2); % no reflection in cathode
            for i=j:(m-2)

S_doubleprime=S_doubleprime*F_I_mat(q(i,l),q(i+1,l),nc(i,l),nc(i+1,l),pol)*F_L_mat(q(i+1,l),t(i+1),lamb
da(l));
            end
            S_doubleprime=S_doubleprime*F_I_mat(q(m-1,l),q(m,l),nc(m-1,l),nc(m,l),pol);
            % Normalized Field profile
            E(x_indices,l)=(S_doubleprime(1,1)*exp(-1i*ej*(dj-x))+S_doubleprime(2,1)*exp(1i*ej*(dj-
x))) ./(S_prime(1,1)*S_doubleprime(1,1)*exp(-
1i*ej*dj)+S_prime(1,2)*S_doubleprime(2,1)*exp(1i*ej*dj));
        end
end

AbsTOT = P_glass.*(1-R-T);% total absorption beside glass
Reflection=R.*P_glass+R_glass;% overall reflection
Absorption=zeros((m-1),length(lambda));

for j=2:(m-1)
        Dposition=find(x_mat == j);
        Energy_Absrate=repmat(alpha(j,:).*(real(q(j,:))),length(Dposition),1).*(abs(E(Dposition,:)).^2);%
Energy absorbed position vs. wavelength (not include 0.5*c*e0)
        Absorption(j,:) = trapz(Dposition.*stepsize, Energy_Absrate,1);
        Absorption(j,:) = Absorption(j,:)./(real(q(1,:))*1^2);
        % absolute absorption for E0+ in glass = 1, I=n*E(=1)^2;
        Absorption=abs(Absorption);
end

% Ratio = AbsTOT./Abstot;% Actual total absorption over absorption for incident E0 =1 in glass
Absorption = Absorption.*repmat(P_glass,m-1,1);% Absorption Efficiency(%)
E = E.*repmat(sqrt(P_glass./real(q(1,:))),size(E,1),1);% Electrical Field (E0+ =1 in air)
Abstot = sum(Absorption,1);Abstot = (Abstot')*100;
Absorption(1,:) = lambda/100;

%*** Electrical Field ***%

%Electric field intensity |E|^2 as a function of position (incident |E0|^2 =1)
plotwlnumber = find(lambda == plotwl);% number of wavelength to plot
A_Esq(:,1)=x_pos; A_Esq(:,2)=abs(E(:,plotwlnumber)).^2; A_Esq(1,1)=0;

figure(1)
plot(A_Esq(:,1),A_Esq(:,2),'Linewidth',2);
% Draws vertical lines at each material boundary in the stack and labels
% each layer
axislimit1=axis;
for i=2:m-1
        line([sum(t(1:i)) sum(t(1:i))],[0 axislimit1(4)]);
```

```
    text((t_cumsum(i)+t_cumsum(i-
1))/2,0,layers{i},'HorizontalAlignment','center','VerticalAlignment','bottom')
end
xlabel('Position from glass (nm)');
ylabel('Normalized |E|^2');


%*** Absorption & Reflection ***%
figure(2)

Absorption=abs(Absorption)*100;%unit(%)
Reflection=Reflection'*100;%unit(%)
Transmission = (T.*P_glass*100)';%unit(%)
A_glass=A_glass'*100;%unit(%)
IReflection=100-Reflection;
AEC=Absorption(end,:);AEC=AEC';%Cathode Absorption(%)

donor=find(CT == 2);
acceptor=find(CT == 3);

% Absorption(donor,:)=Absorption(donor,:)*2;

plot(lambda,Absorption(donor,:),'r',lambda,Absorption(acceptor,:),'b','Linewidth',2);
hold on
plot(lambda, Reflection,'k-.')
xlabel('Lambda (nm)');
ylabel('Absorption Efficiency (%)');


%*** Standard Diffusion Equation ***%
% Donor
DD=D(donor);DLD = LD(donor);
Dposition=find(x_mat == donor);
DGeneration =repmat(alpha(donor,:).*real(q(donor,:)),length(Dposition),1).*(abs(E(Dposition,:)).^2);
DExcitonTOT=((sum(DGeneration,1)-
((DGeneration(1,:)+DGeneration(size(DGeneration,1),:))/2))*stepsize);
[Dx_pos,Dnex,DJout] = F_Diffusion(DGeneration,DLD,Dposition,stepsize,DR0,DDen,DD,0,DetaR);
%Ddiffusion = DJout./DExcitonTOT;% Diffusion Efficiency
Ddiffusion = 1-(trapz(Dx_pos,Dnex)/tau(donor))./DExcitonTOT;% Diffusion Efficiency

% Ddiffusion = Ddiffusion+DJout./DExcitonTOT;% Diffusion Efficiency
% Ddiffusion = -DJout./DExcitonTOT;
Ddiffusion(isnan(Ddiffusion)==1) = 0;DEQE = 2*Absorption(donor,:).* Ddiffusion;

% Acceptor
AD=D(acceptor);ALD = LD(acceptor);
Aposition=find(x_mat == acceptor);
AGeneration =repmat(alpha(acceptor,:).*real(q(acceptor,:)),length(Aposition),1).*(abs(E(Aposition,:)).^2);
AExcitonTOT=((sum(AGeneration,1)-
((AGeneration(1,:)+AGeneration(size(AGeneration,1),:))/2))*stepsize);
[Ax_pos,Anex,AJout] = F_Diffusion(AGeneration,ALD,Aposition,stepsize,AR0,ADen,AD,1,AetaR);
```

```
%Adiffusion = AJout./AExcitonTOT;% Diffusion Efficiency
Adiffusion = 1+(trapz(Ax_pos,Anex)/tau(acceptor))./AExcitonTOT;% Diffusion Efficiency
Adiffusion(isnan(Adiffusion)==1) = 0;AEQE = Absorption(acceptor,:).* Adiffusion;

figure(3)
plot(Dx_pos,Dnex(:,plotwlnumber),'r','Linewidth',2);
hold on
plot(Ax_pos+Dx_pos(end),Anex(:,plotwlnumber),'b','Linewidth',2);
xlabel('Position (nm)');ylabel('Exciton Density (/nm)');

AEd = (Absorption(donor,:))';AEa = (Absorption(acceptor,:))';AEtot = AEd+AEa;
AErest = IReflection-AEtot-A_glass-AEC;% buffer layer absorbsion
DEd = Ddiffusion'*100;DEa = Adiffusion'*100;
EQE = DEQE+AEQE;EQE = EQE';
DEQE=DEQE';AEQE=AEQE';
EQECCE = (EQE)*CCE;
DEtot = EQE./AEtot;

figure(4)
plot(lambda,DEQE*CCE,'r',lambda,AEQE*CCE,'b',lambda,EQE*CCE,'k','Linewidth',2);
xlabel('Lambda (nm)');
ylabel('External Quantum Efficiency (%)');

% Interface Matrix Function
function I = F_I_mat(q1,q2,nc1,nc2,pol)
if pol == 0
r=(q1-q2)/(q1+q2);
t=2*q1/(q1+q2);
else
r=((nc1^2)*q2-(nc2^2)*q1)/((nc2^2)*q1+(nc1^2)*q2);
t=2*(nc1*nc2)*q1/((nc2^2)*q1+(nc1^2)*q2);
end
I=[1 r; r 1]/t;
end

% Layer Matrix Function
function L = F_L_mat(n,d,lambda)
ei=2*pi*n/lambda;
L=[exp(-1i*ei*d) 0; 0 exp(1i*ei*d)];
end

% Diffusion Function
function [x_pos,nex,Jout] = F_Diffusion(Generation,LD,position,stepsize,R0,Den,D,DA,etaR)
% Numerical Solution through Matrix For Diffusion PDE
% Input Generation, LD, positon, stepsize, diffusivity, donor or acceptor (1)
ni = size(Generation,1)-2;% number of interior position
x_posit = position * stepsize;x_posit=x_posit';x_posit=x_posit-x_posit(1);% nm from interface
nex = Generation*0;Jout = zeros(1,size(Generation,2));
% Donor or Acceptor
if DA == 1
    Graw = flipud(Generation);% inverse order
```

```
    x_pos = flipud(x_posit);
else
    Graw = Generation;
    x_pos = x_posit;
end
Graw(1,:)=0;Graw(size(Graw,1),:)=0;
% M matrix
PreF = 1+(Den*pi*(R0^6))./(6*((x_posit(end)+stepsize-x_posit).^3));% prefactor for Förster transfer
M_diag = (-2) * ones(ni+2,1)-PreF*(stepsize^2)/(LD^2);% diagonal
M_sub = 1 * ones(ni+1,1);% two sides of diagonal
M = spdiags([[M_sub;0],M_diag,[0;M_sub]],[-1 0 1],ni+2,ni+2);% build matrix
M(1,1) = -1;M(1,2) = 1;% reflective n2-n1=0

M(ni+2,ni+1) = etaR;M(ni+2,ni+2) = -etaR-(0.5^2)/(LD^2);% kr/(kQ+kr+kFörster) = etaR

for l=1:size(Graw,2)
G = Graw(:,l);
% C matrix
C=-((G*(stepsize^2))/D);% right hand side of equation
% Solve Exciton density M*nexciton = C;
nexciton = M\C;
nex(:,l)=nexciton;
% Exciton Flux
Ji = zeros(ni+1,1);
for i=1:ni+1
Ji(i) = ((nexciton(i+1)-nexciton(i))/stepsize)*D;
end
J = -[Ji;2*Ji(ni+1)-Ji(ni)];    % linear interpolation to boundary
%Jout(l) = J(ni+2); % flux get out;
Jout(l) = J(1); % flux get out;
end
```

Code for photocurrent ratio L_D fitting

This code is for extract the intrinsic exciton diffusion length for both donor and acceptor materials from device internal quantum efficiency ratio (= diffusion efficiency ratio). The F_RD function is the function file of transfer matrix code listed above, with diffusion efficiency ratio RD = DEtot(nd)/DEtot(na).

```
%%%%%%%%%%&&&&&&&&&& RD Fitting &&&&&&&&&&%%%%%%%%%%%%%%%%
FitType = 0; % Absolute Value:0 Shape:1
lambda = [400 650];
nd=find(lambda==650);
na=find(lambda==400);
DonorLD = 15:1:17;
AcceptorLD = 15:2:30;
ITO = 105;
Dth =[15 20 25 30 35 40 45]; Ath =[35 35 35 35 35 35 35];
RDexp = [0.753189624    0.524963087    0.364124916    0.268342245    0.200803568    0.134768595
    0.141698272];
%%%%%%%%%%%%%%%%%%%%%%%%%%&&&&&&&&&& Code
&&&&&&&&&&%%%%%%%%%%%%%%%%%%%%%%%%%%%%%%
OCraw = importdata('Index_of_Refraction_Library.xlsx');
F_RDfit = RDexp*0;RDfit = F_RDfit;
D = 1E50;
DDeltaLD = DonorLD*0;
ADeltaLD = AcceptorLD*0;
if FitType == 0

for DLD = DonorLD
for ALD = AcceptorLD
for Dthick = 1:length(Dth)
[RD]=F_RD(DLD,ALD,OCraw,Ath(Dthick),Dth(Dthick),ITO,lambda,nd,na);
RDfit(Dthick)=RD*TIE;
end
Delta = sum(((RDfit-RDexp)./RDexp).^2);
% Scale = RDexp./RDfit;
% Delta = std(Scale);

DDeltaLD (find(DonorLD == DLD)) = Delta;
ADeltaLD (find(AcceptorLD == ALD)) = Delta;

if Delta < D
    D = Delta;
    F_DLD = DLD;F_ALD = ALD;F_TIE = TIE;
    F_RDfit = RDfit;
%       F_Scale = mean(Scale);F_RDfit = RDfit*F_Scale;
    figure(1)
    plot(Dth, RDexp,'ko',Dth, F_RDfit,'r')
end
end
end
```

```
else
RDexp = RDexp./max(RDexp);
AcceptorLD = 1;
for DLD = DonorLD
for ALD = AcceptorLD
for Dthick = 1:length(Dth)
[RD]=F_RD(DLD,ALD,OCraw,Ath,Dth(Dthick),ITO,lambda,nd,na);
RDfit(Dthick)=RD;
end
Scale = RDexp./RDfit;
Delta = std(Scale);
if Delta < D
      D = Delta;
      F_DLD = DLD;F_ALD = ALD;
      F_Scale = mean(Scale);F_RDfit = RDfit*F_Scale;
      figure(1)
      plot(Dth, RDexp,'ko',Dth, F_RDfit,'r')
end
end
end
end
Summary(:,1)=Dth;
Summary(:,2)= F_RDfit;
Summary(:,3)=RDexp;
```

Code for charge carrier mobility fitting

This code is for extract the space-charge-limited-current carrier mobility, field activation parameter and build-in voltage of single carrier devices.

```
%%%%%%%%%%%%%%%%%&&&&&&&&&&SCLC&&&&&&&&&&%%%%%%%%%%%%%%%%%

% Input %
d =100; % thickness [nm]
n = 1.71; % NIR refractive index []

% Fitting Range %
Vfit_range = [0.2 5]; % voltage range for fitting
Vbi_range =0:0.1:0; % built-in voltage [V]
logu0_range = -10:0.01:-5; % log10(mobility [cm2/Vs])
logy_range = -5:0.01:-1; % log10(gamma [cm/V]^0.5)

%%%%%%%%%%%%%%%%%%%%%%%%%%%%%%%%%%%%%%%%%%%%%%%%%%%%%%%%%%%%%

er = n^2; % dielectric constant []
e0 = 8.85E-12; % vacuum permittivity [F/m = C/Vm]
L = d*1E-9; % thickness [m]
D = 1E50;

A = (1E-3)^2/4*pi;% Device area [m^2]
% A = (1E-3)^2;
[filename,pathname] = uigetfile('*.*');
IVraw = importdata([pathname,filename]);IVraw = IVraw.data;
if IVraw(1,1)>IVraw(2,1)
    IVraw = flipud(IVraw);
end
Vapp = IVraw(:,1); % applied voltage [V]
Jexp = IVraw(:,2)/A; % measured current density [A/m2]

n1 = find(abs(Vapp-Vfit_range(1))==min(abs(Vapp-Vfit_range(1))));
n2 = find(abs(Vapp-Vfit_range(2))==min(abs(Vapp-Vfit_range(2))));
Vapp = Vapp (n1:n2);Jexp = abs (Jexp (n1:n2));log_Jexp = log10(Jexp);

for Vbi = Vbi_range % [V]
for u0 = 10.^(logu0_range-4) % [m2/Vs]
for y =   10.^(logy_range-1) % [(m/V)^0.5]

E = (Vapp - Vbi)./L; % electric field strength [V/m]
Jsim = (9/8*er*e0*u0).*((E.^2)./L).*exp(0.89*y.*((E).^0.5));
log_Jsim = log10(abs(Jsim));

Delta = sum(((log_Jsim-log_Jexp)./1).^2);

if Delta < D
    D = Delta;
```

```
    F_Vbi = Vbi;F_u0 = u0;F_y = y;
    F_log_Jsim = log_Jsim;

    figure(1)
    plot(Vapp,log_Jexp,'ko',Vapp,log_Jsim,'r')
end

end
end
end
```

C. Supporting Information for Chapter 4

Comparison between charge extraction decay and open-circuit voltage decay

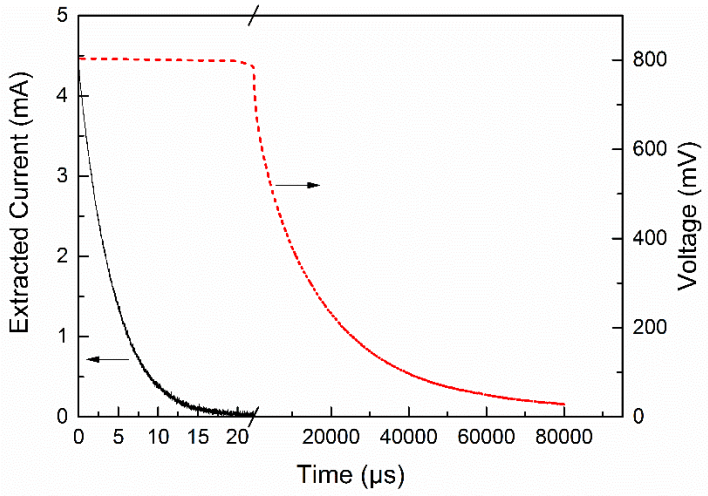

Figure C.1 (Solid black line) Decay of extracted current obtained by switching the DTDCPB-C_{60} BHJ in Figure 4.1d from open-circuit (V_{OC} = 797 mV) to short-circuit. (Broken red line) Voltage decay (V_{OC} = 803 mV at t = 0 μs) of the DTDCPB-C_{60} BHJ device at open-circuit. The illumination to provide initial V_{OC} is turned off at t = 0 μs.

Lifetime of free charge carriers

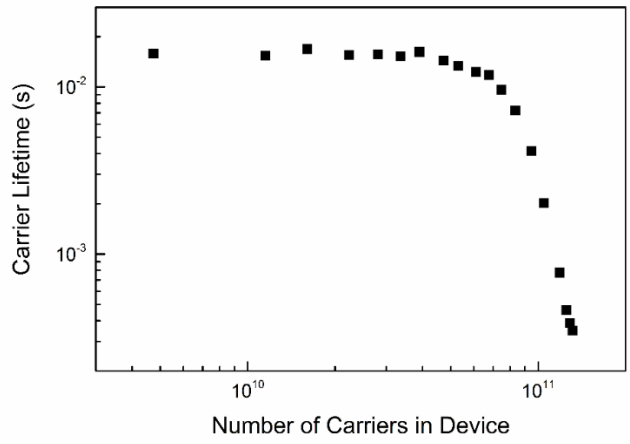

Figure C.2 Carrier lifetime as a function of carrier number in DTDCPB-C_{60} BHJ. The lifetime here is derived as the ratio of carrier number to carrier recombination rate measured in Figure 4.3b.

Additional plots of carrier rise and decay

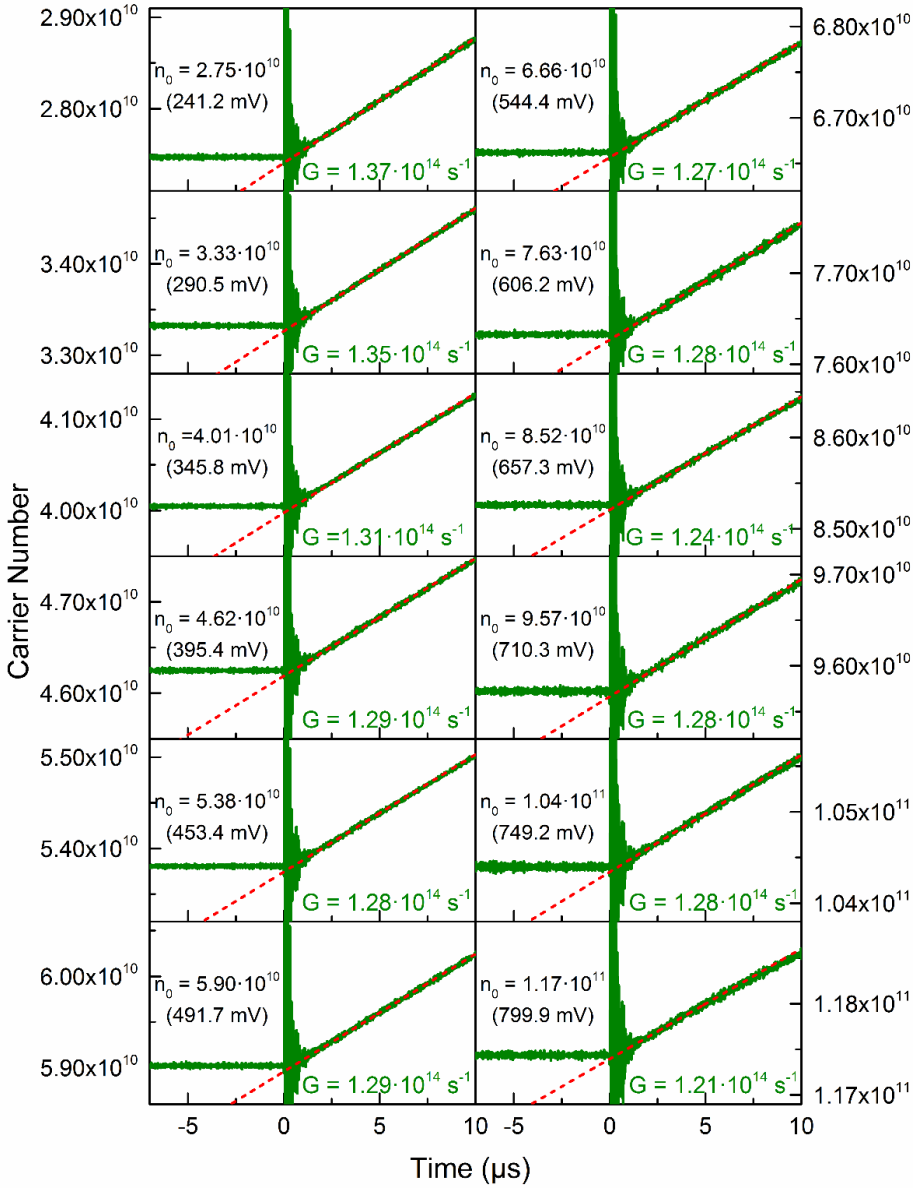

Figure C.3 Plots of charge carriers rise within the device in Figure 4.3 versus time for measurement of carrier generation rate (G). The rates are approximated as the slope of linear rise region (first 5 us). The operating voltages (V_{OP} = 241.2 - 799.9 mV) corresponding to n_0 are shown in brackets. The device is held at steady state before t = 0 μs using constant background illumination (blue LED). A second green LED is turned on at t = 0 μs and leads to increase in carrier number stored within the device.

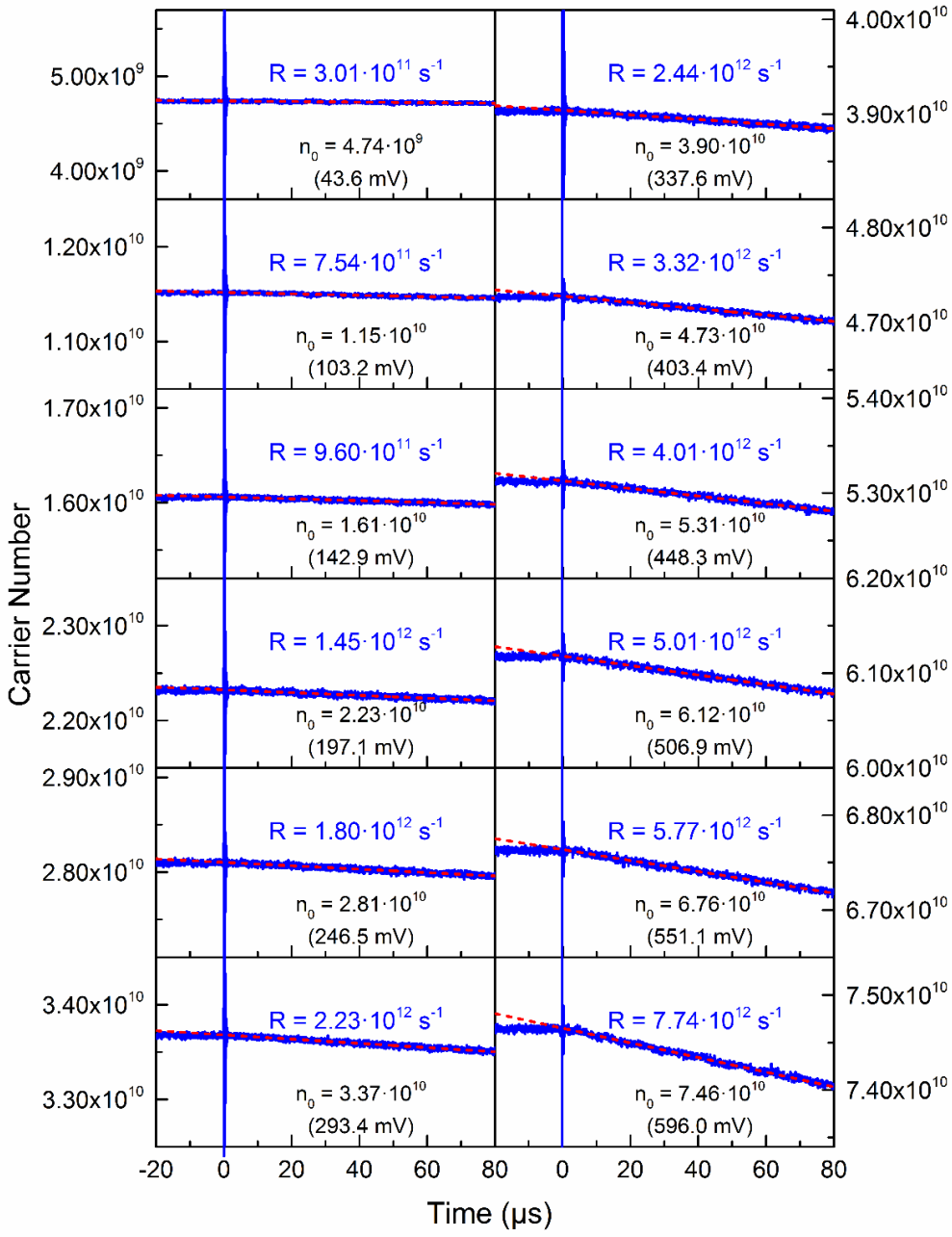

Figure C.4 Plots of carrier decay within the device in Figure 4.3 (V_{OP} = 43.6 - 596.0 mV) for measurement of carrier recombination rate (R). The rates are approximated as the slope of linear decay region (first 20 us). The operating voltages correspond n_0 are shown in brackets. The device is held at steady state before t = 0 μs using constant background illumination (blue LED). Background illumination is turned off at t = 0 μs and leads to decrease in carrier number stored within the device.

Intensity dependent short-circuit current

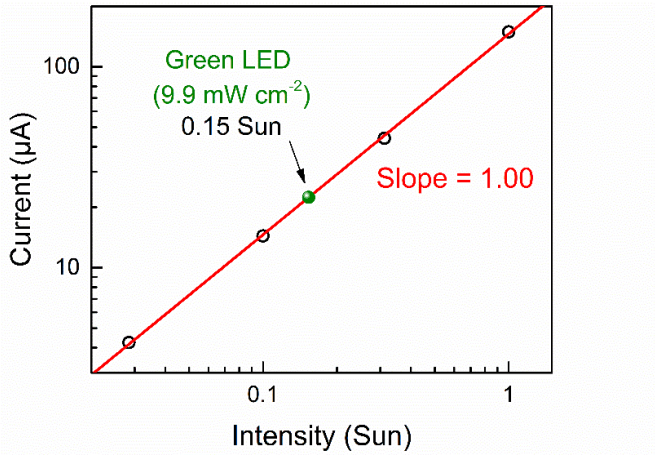

Figure C.5 Short-circuit current (I_{SC}) of the DTDCPB-C_{60} BHJ in Figure 4.1d as a function of simulated AM1.5G light intensity (open circle) in logarithmic scale. A linear fit (solid red line) with a slope of 1.00 to the data is also shown. The I_{SC} in Figure 4.4 (illuminated by a green LED) is corresponding to a short-circuit current generated by 0.15 Sun simulated AM1.5G illumination.

Charge collection efficiency determined by reverse bias external quantum efficiencies

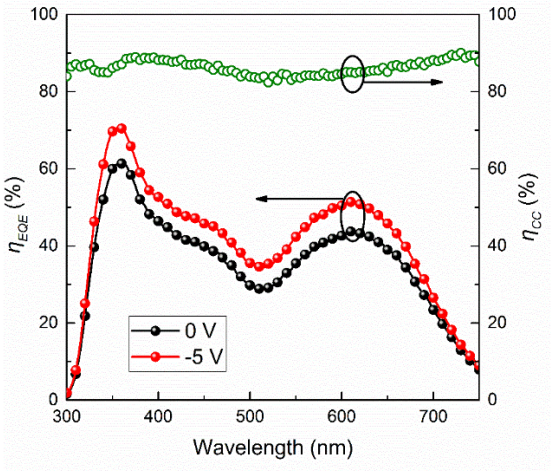

Figure C.6 External quantum efficiency (η_{EQE}) of the DTDCPB-C_{60} BHJ in Figure 4.1d at short-circuit (black closed symbols) and -5 V (red closed symbols). The absorption efficiency (η_A) is approximated as the reverse bias η_{EQE} at -5 V. The charge collection efficiency (η_{CC}) is determined as the ratio of short-circuit η_{EQE} to η_A

Intensity dependence of extracted carriers and generation current

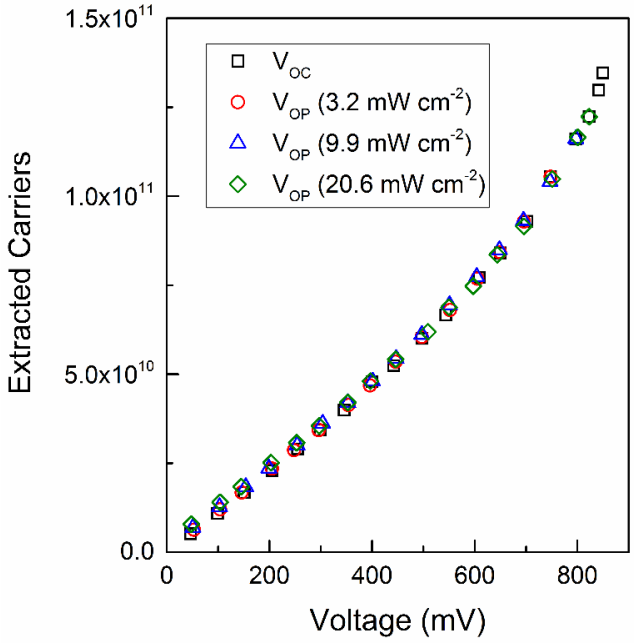

Figure C.7 The number of extracted carriers as a function of open-circuit voltage (V_{OC}) and operating voltage (V_{OP}) derived by integrating current transients with respect to time.

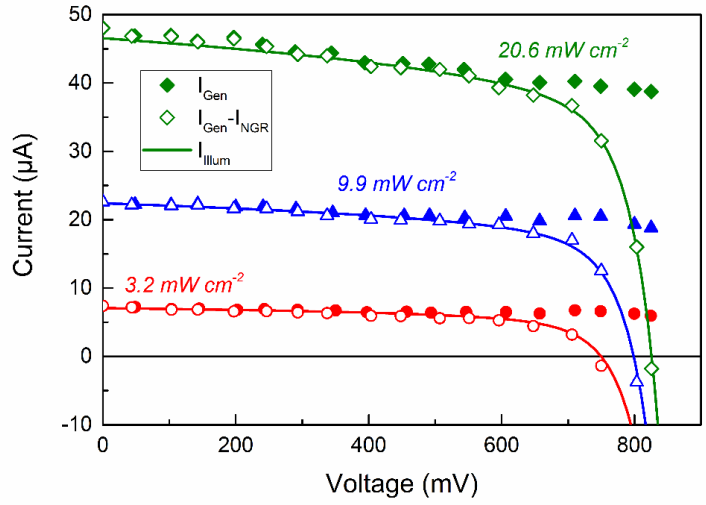

Figure C.8 Generation current, illumination current and recreated illumination current using I_{NGR} from TPV measurement as a function of voltage in DTDCPB-C_{60} BHJ under green LED illumination (3.2/9.9/20.6 mW cm^{-2}).

Comparison between I_{Gen} and I_{Illum}-I_{Dark} difference

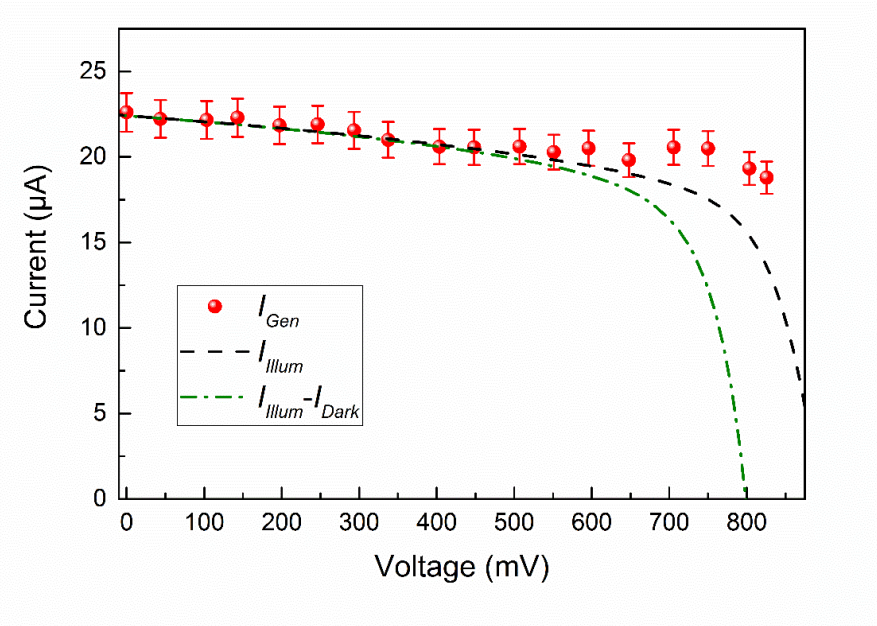

Figure C.9 Carrier generation current (I_{Gen}) extracted from photovoltage measurements compared to the difference between the measured illuminated current (I_{Illum}) and dark current (I_{Dark}) of the DTDCPB-C_{60} BHJ in Figure 4.1d as a function of applied voltage.

To understand whether the difference between I_{Illum} and I_{Dark} is a good approximation for the I_{Gen} for the DTDCPB-C_{60} BHJ in Figure 4.4, both I_{Gen} (from photovoltage) and the approximate I_{Gen} (I_{Illum}-I_{Dark}) are plotted as a function of voltage in Figure C.9. The I_{Illum}-I_{Dark} difference is in good agreement with the photovoltage-extracted I_{Gen} up to 600 mV, where the I_{NGR} is much lower than I_{Gen}. When the I_{NGR} increases with voltage (> 600 mV), the I_{Illum}-I_{Dark} difference is smaller than I_{Gen}. This is likely due to the increased carrier density in the active layer under illumination compared to in the dark, especially under high forward bias, which leads to a larger I_{NGR}.

Impact of neat DTDCPB layer on Charge Separation

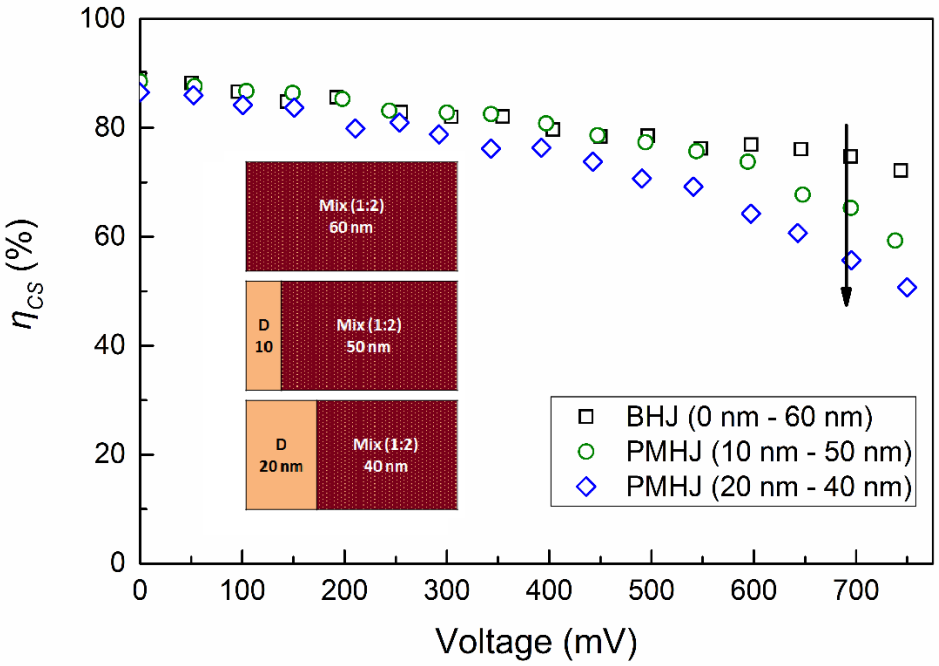

Figure C.10 Charge separation efficiency (η_{CS}) of OPVs with the following structure: 10 nm MoO_x/x nm DTDCPB/ (60-x) nm DTDCPB-C_{60} (1:2) mixture/10 nm BCP/100 nm Al. The η_{CS} as a function of voltage is measured as described in main text using a blue LED (455 nm) with intensity of 14.7 mW cm^{-2}.

To understand the origin of severe geminate recombination loss in DTDCPB-C_{60} PHJ, the role of neat DTDCPB in CT state separation is examined. Figure C.10 shows the charge separation efficiency (η_{CS}) of DTDCPB-C_{60} OPVs with 60-nm-thick active layer as a function of neat DTDCPB layer thickness. Blue LED illumination (mostly absorbed by C_{60}) is employed to only populate CT states in mixture. As built-in voltage (V_{bi}) is mainly determined by work function difference between electrodes, we assume change in V_{bi} is not significant as a function with neat layer thickness. The result shows that the η_{CS}

decreases with DTDCPB thickness for a given applied voltage (V), especially for high forward bias, when the driving voltage (V_{bi}-V) is small. As the physical environment of CT states in mixture are the same (charge carrier mobility, lifetime of CT states and dielectric constant), η_{CS} is only depends on strength of electric field. Therefore, the decreased η_{CS} with DTDCPB thickness suggests that neat DTDCPB consume more built-in field than mixture. A thicker neat layer leads to weaker electric field at donor-acceptor interface and lower η_{CS} for the same driving voltage.

LED spectra

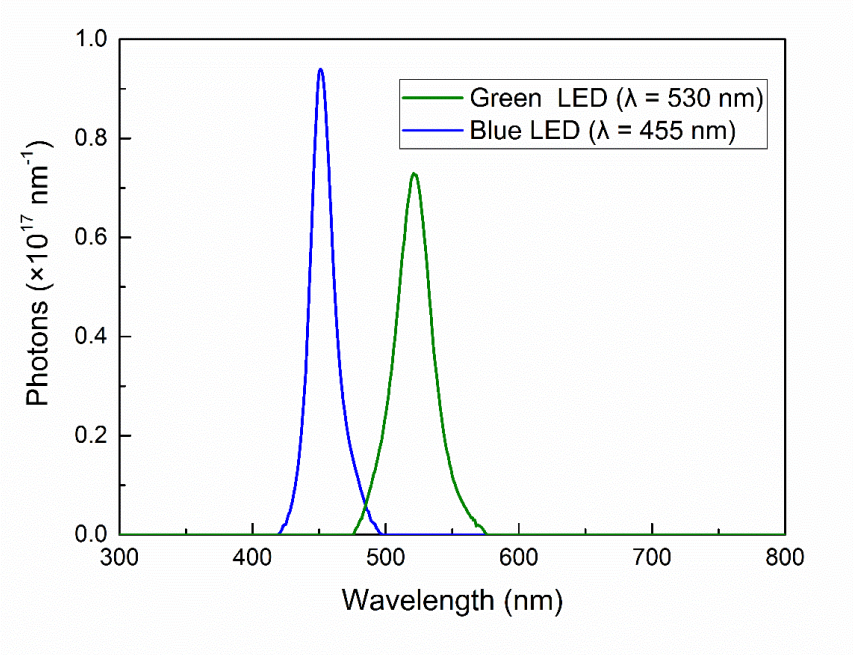

Figure C.11 Pump spectra for LEDs peaked at wavelengths of λ = 455 nm (blue) and λ = 530 nm (green). The spectra are normalized to 1 W illumination through an aperture with an area of 0.0176 cm^2.

Device performance under 1 sun illumination

Table C.1 Performance of devices in Figure 4.1d under simulated AM1.5G 1 Sun illumination. All devices were illuminated through an aperture with an area of 0.0176 cm^2.

1 Sun Parameters	V_{OC} (V)	J_{SC} (mA cm^{-2})	FF	η_P (%)
DTDCPB-C_{60} BHJ	0.86	8.46	0.67	4.86
DTDCPB-C_{60} PHJ	0.80	0.82	0.22	0.15
CuPc-C_{60} PHJ	0.24	3.55	0.52	0.44

The performance of devices studied in this work (AM1.5G 1 Sun) are shown in Table C.1. The DTDCPB-based BHJ has been used to demonstrate high η_P (8~10%) when using C_{70} as the electron acceptor material.

D. Supporting Information for Chapter 5

X-ray diffraction patterns of NTU-1 thin films

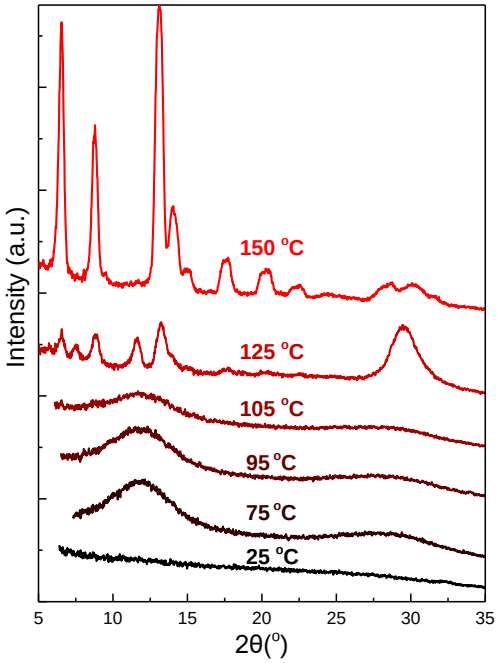

Figure D.1 X-ray diffraction pattern for a ~300-nm-thick film of NTU-1 on a silicon wafer as a function of annealing temperature. A Co Kα source with λ = 1.78899 Å is used this measurement.

Without annealing, NTU-1 films show no obvious diffraction peak. For films annealed at 75°C-105°C, a broad peak can be observed at 2θ~14°. When the annealing temperature is increased to 125°C, more sharp peaks show up, indicating an increased crystallinity. Films annealed at 150°C show additional peaks and higher peak intensity than the 125°C film. This trend is similar to observations of NTU-2 thin film XRD patterns versus annealing temperature.

Exciton harvesting in NTU-2

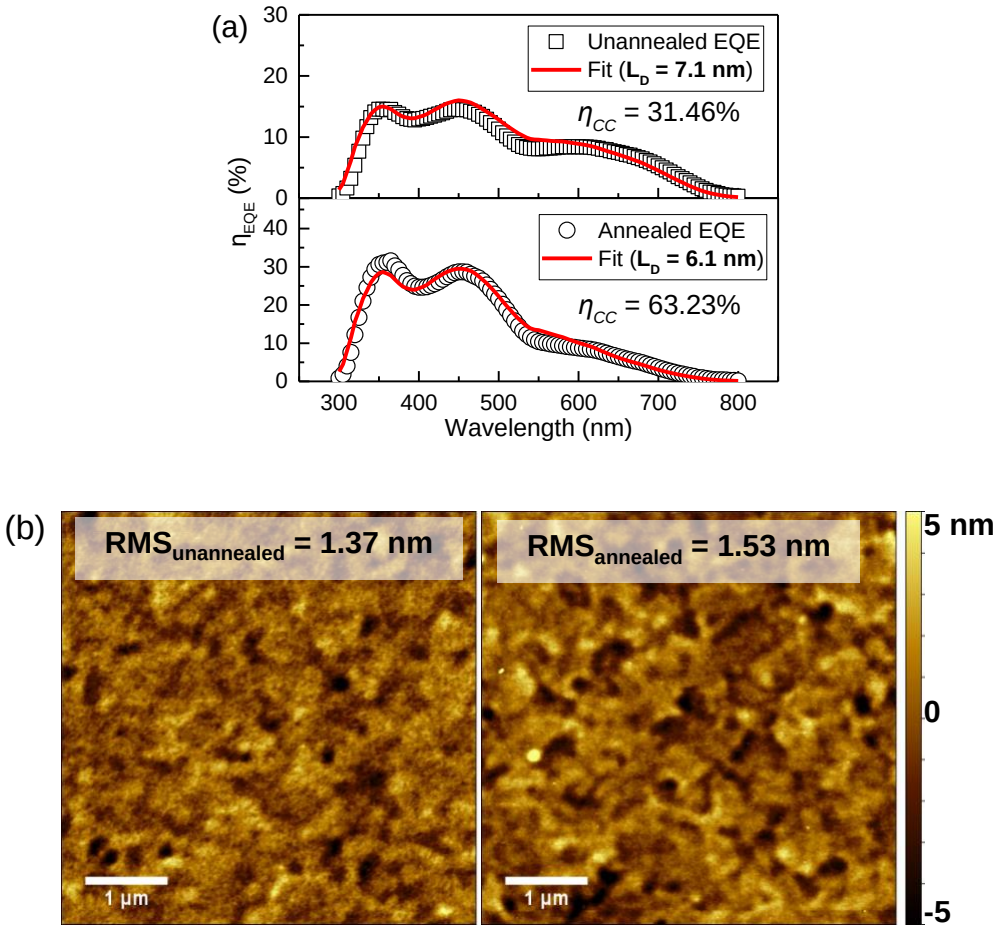

Figure D.2 (a) External quantum efficiency (η_{EQE}) for the devices in Figure 5.5a (structure: 10 nm MoO_x/20 nm NTU-x/35 nm C_{60}/10 nm BCP/100 nm Al). The solid lines are fits to the η_{EQE} data with the NTU-2 donor exciton diffusion length (L_D) and wavelength-independent charge collection efficiency (η_{CC}) as fit parameters.[48] (b) Atomic force micrographs of 20-nm-thick NTU-2 films on MoO_x (10 nm) covered ITO substrates.

Dark Current Characteristics as a Function of Thermal Annealing

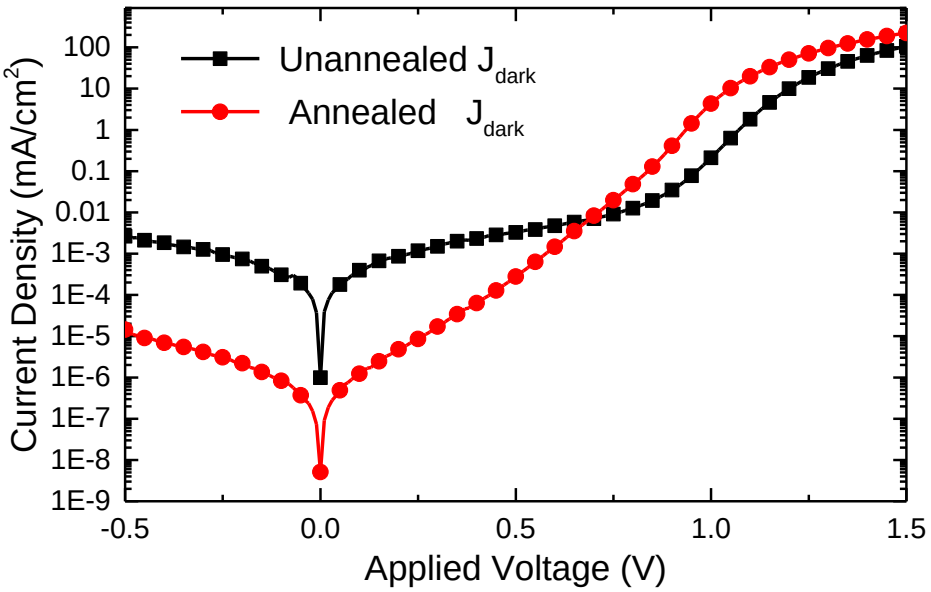

Figure D.3 Current density-voltage characteristics for the unannealed and annealed devices in Figure 5.3a (structure: 10 nm MoO_x/20 nm NTU-x/35 nm C_{60}/10 nm BCP/100 nm Al) in the dark, presented on a semilog plot and using the absolute value of current density.

NTU-2 Crystal Structure and Molecular Orientation

The crystal structure of NTU-2 was derived from a solution-grown single crystal using X-ray diffraction. The structure of NTU-2 is triclinic (space group: P-1) with a = 6.97 Å, b = 16.15 Å, c = 18.45 Å and α = 113.24°, β = 98.19°, γ = 96.67°. Figure D.4a shows the calculated power XRD pattern based on the above triclinic structure, and it agrees well with the pattern obtained from raw source powder prior to vacuum deposition measured in Bragg-Brentano (θ-2θ) geometry. However, the patterns of 125 °C (optimal) and 150 °C thin films from Figure 5.4a do not perfectly match the calculated pattern. The 150 °C

pattern shows additional peaks for $2\theta < 8°$, which cannot be attributed to lattice strain and systematic absence. Consequently, a different crystal structure is likely to present in films annealed at 150 °C. The emergence of a different polymorph of NTU-2 may reflect differences in preparation method (thermal annealing on vacuum-deposited thin film vs. solution growth).[4-5] For scattering patterns collected from films annealed at 125 °C, the peak at $2\theta = 9.8°$ (peak I) matches the peak position for the $(0\ 1\ \bar{2})$ plane in the calculated pattern while the peak at $2\theta = 11.3°$ (peak II) does not match any peaks of the calculated pattern. The 150 °C pattern that likely consists of a different polymorph also show a peak at $2\theta = 11.3°$, suggesting that the 125 °C pattern might reflect both polymorphs.

Figure D.4b shows the 2D XRD of 125 °C annealed NTU-2 film on glass. The incident angle ω was set as θ of peak I and peak II respectively to form the θ-2θ geometry for the target peaks. When ω is set as θ of peak I, a higher intensity is observed at the middle of the peak I ring, indicating the film is textured and the planes corresponding to peak I tend to sit parallel to substrate. Therefore, other planes of the oriented crystals should also show a textured ring (lower intensity at middle and peak intensity on two shoulders) in θ-2θ geometry. However, when ω is set as θ of peak II, a relatively uniform intensity distribution with slightly higher intensity at the middle is observed for the peak II ring. It suggests that two peaks are likely from different polymorphs and the polymorph causing peak I is more textured within the film.

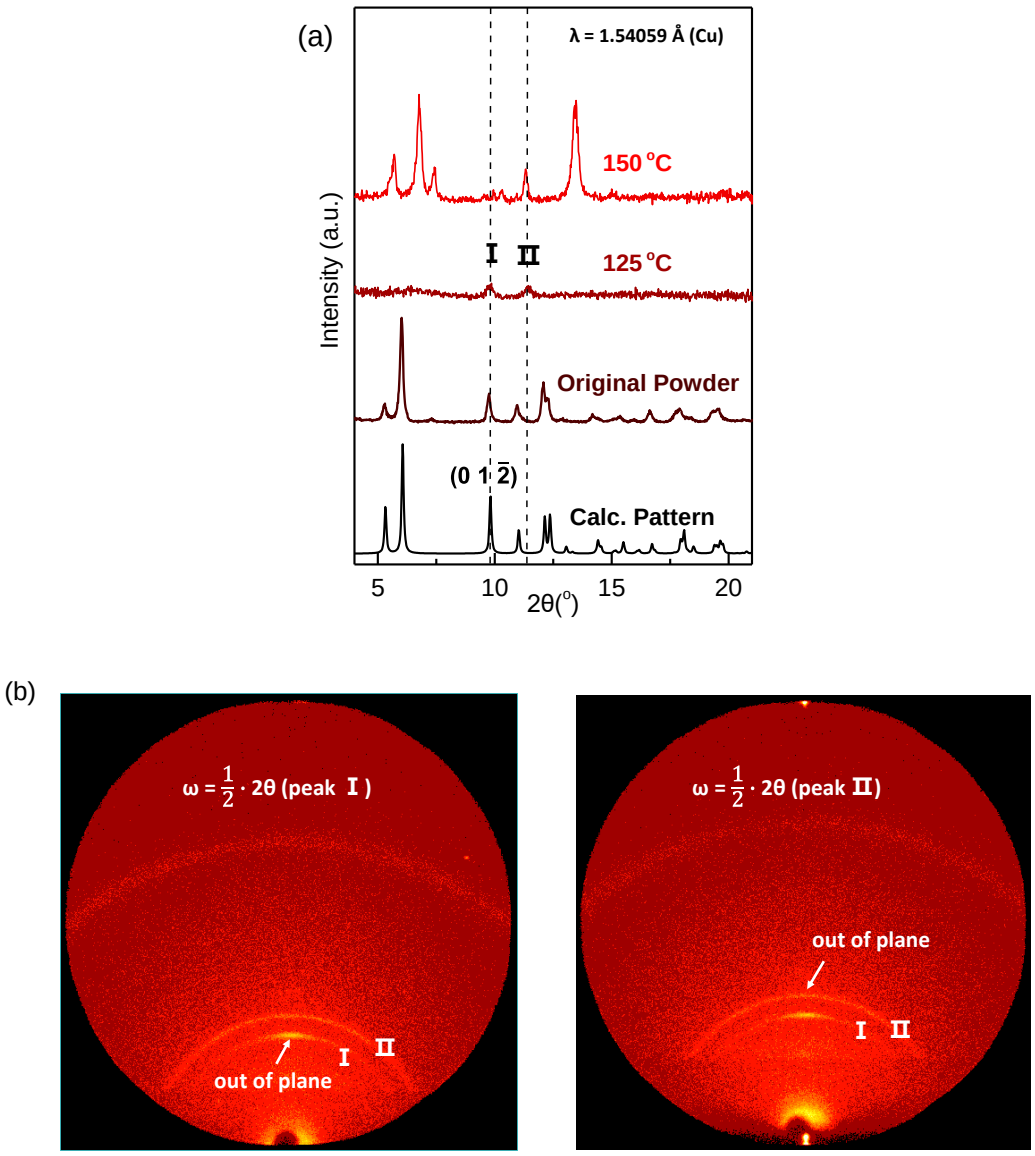

Figure D.4 (a) X-ray diffraction patterns for NTU-2 triclinic structure (calculated), raw source powder prior to vacuum deposition and ~300-nm-thick films of NTU-2 (125 °C and 150 °C) on glass. (b) 2D X-ray diffraction plots for ~300-nm-thick films of NTU-2 (125 °C annealed) on glass with an incident angle (ω) set to be θ of peak I and peak II in 125 °C thin film pattern.

Figure D.5 shows the molecular packing of NTU-2 with the $(0\ 1\ \bar{2})$ triclinic plane, presumably corresponding to the textured peak I, parallel to the substrate. NTU-2 molecules adopt an edge on configuration with respect to the substrate. This molecular configuration is likely to cause a decrease in light absorption, consistent with the observed reduction in thin film extinction coefficients in Figure 5.4b.

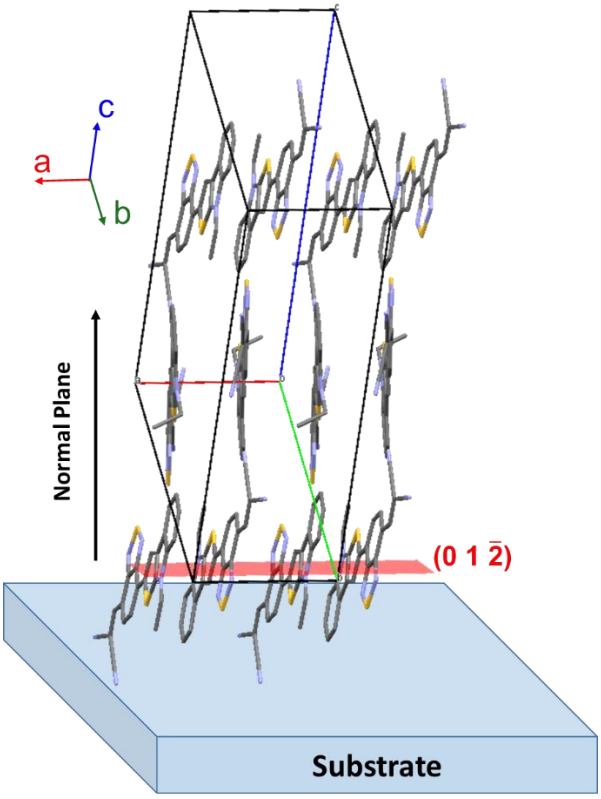

Figure D.5 Molecular packing of NTU-2 with the $(0\ 1\ \bar{2})$ triclinic plane parallel to the substrate.

The improved charge transport within 125 °C annealed NTU-2 is likely from enhanced π-stacking within textured crystalline films, which can lead to improved charge carrier mobility. The rapid decrease in device performance with annealing temperature above

150 °C might relate to transitions from the predominant growth of one polymorph (triclinic) to another and a reduction in charge carrier mobility, which has been observed in polymorphic organic small molecules.[5-6] In order to completely confirm the molecular orientation and origin of unmatched peaks in powder and thin film, the other crystal structures of NTU-2 must be quantitatively solved.

E. Supporting Information for Chapter 6

Charge extraction and transient photovoltage decay

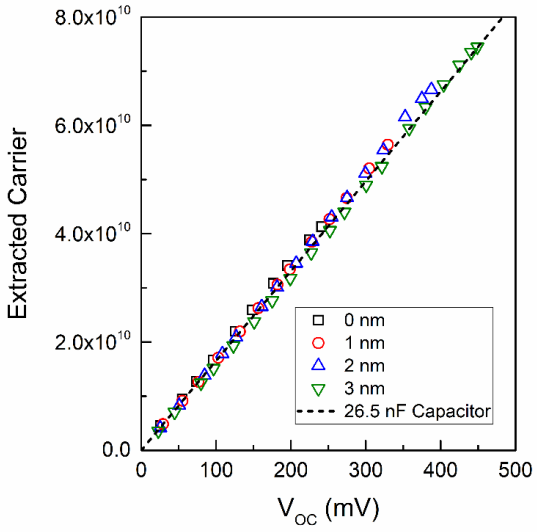

Figure E.1 The number of extracted carriers as a function of open-circuit voltage (V_{OC}) for CuPc-rubrene (0-3 nm)-C_{60} planar cells. Carrier number increases linearly rather than exponentially with V_{OC}, suggesting geometric capacitance is dominant for these devices. A calculated voltage dependent carrier number for 26.5 nF capacitor is also plotted as dash line.

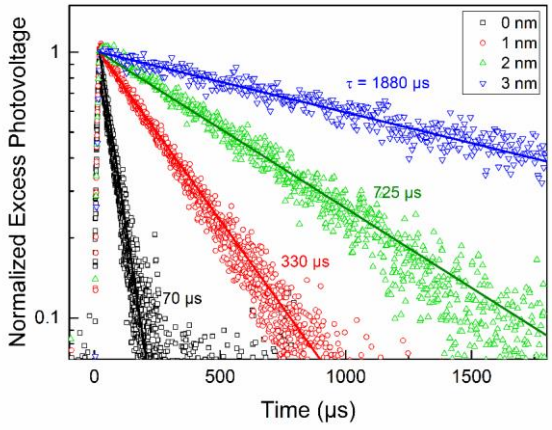

Figure E.2 Representative plots of small perturbation photovoltage decay for CuPc-rubrene (0-3 nm)-C_{60} planar cells. The devices are held at open-circuit with a V_{OC} of 200 mV before excited with a short light pulse (20 µs, start at t = 0 µs, green LED, λ_{peak} = 530 nm, intensity: 16.5 mW cm^{-2}) to induce excess charge carriers and voltage.

Interlayer Coverage

As the interlayer used in this work is very thin, how effectively rubrene covers CuPc must be determined. Figure E.3a shows a donor-interlayer-acceptor device with an interlayer coverage of x. The total measured dark current density (J_{Dark}) shown in Figure 6.2b can be thought of in terms of J_{Dark} for a bilayer device (J_{DA}) and a device with full-coverage interlayer (J_{DIA}). The coverage can be expressed as: $x = (J_{DA} - J_{Dark}) / (J_{DA} - J_{DIA})$. When assuming $J_{DIA} = 0$, the minimal coverage can be extracted as $(1 - J_{Dark}/J_{DA})$

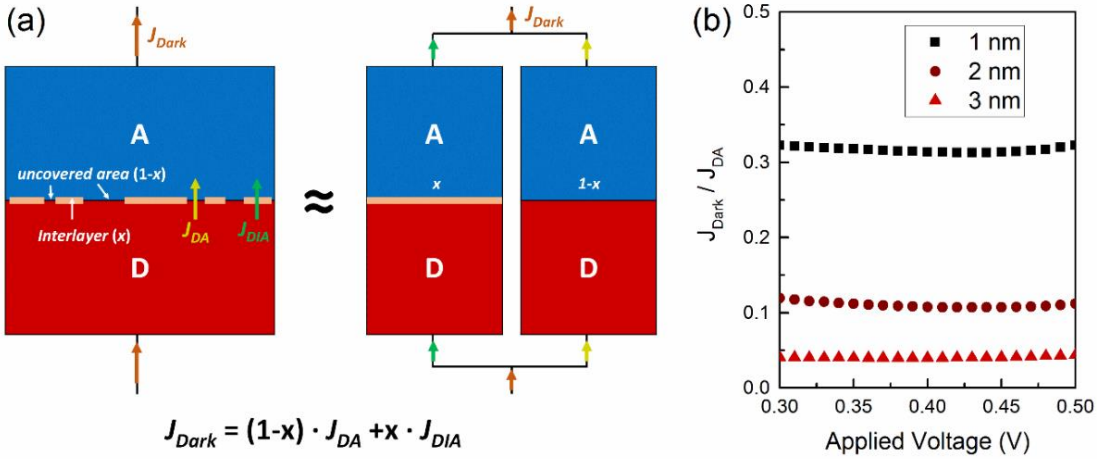

Figure E.3 A planar OPV with a donor-acceptor interface partially separated by an incomplete interlayer (left). The interlayer coverage is *x*. This device can be treated as parallel combination of a bilayer device and one with a full interlayer (right). (b) The dark current density (J_{Dark}) normalized to bilayer case as a function of applied voltage ('diode' dominant region).

Figure E.3b shows J_{Dark}/J_{DA} as a function of applied voltage in 'diode' dominant region, showing the least device-to-device variation. The J_{Dark} drops to ~30% of J_{DA} when inserting 1-nm-thick rubrene at CuPc-C_{60} interface. For 1 nm case, at least 70% of the interface is covered with rubrene. With increasing rubrene thickness, the minimal rubrene

coverage also increases to 89% (2 nm) and 96% (nm).

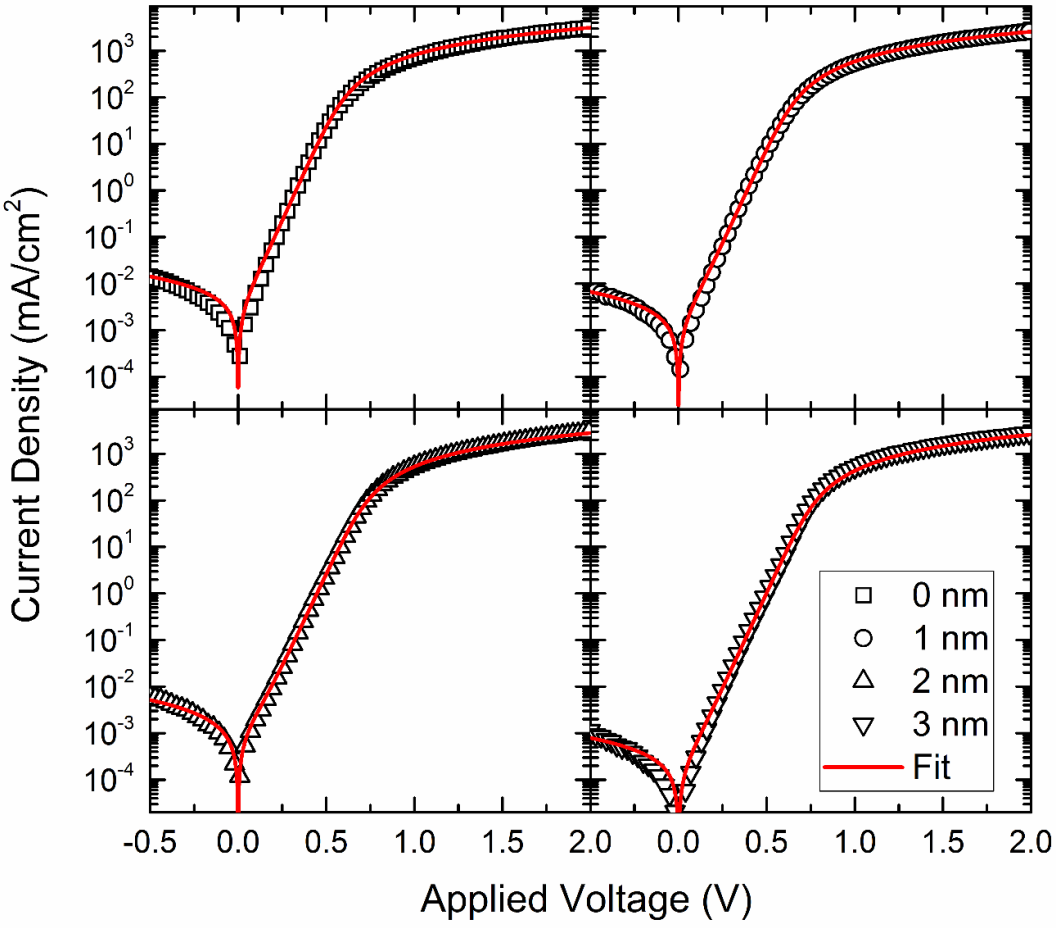

Figure E.4 Dark current density in Figure 6.2b fit by Equation 6.1 in the main text (structure: 15 nm CuPc/ 0-3 nm rubrene/35 nm C_{60}/10 nm BCP/100 nm Al).

Rubrene-C_{60} CT state energy

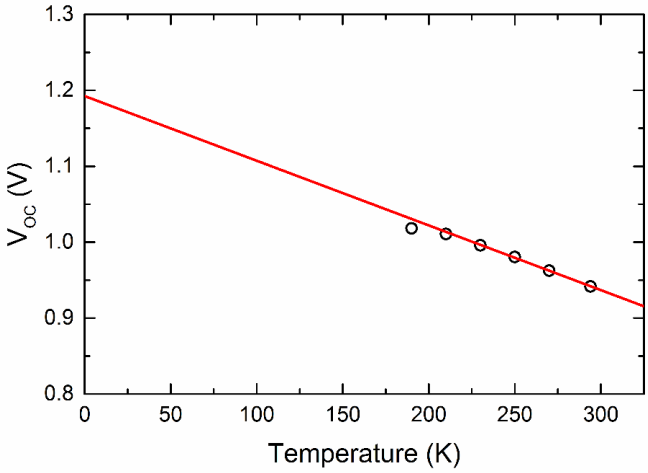

Figure E.5 Temperature dependence of V_{OC} for a rubrene-C_{60} bilayer device (structure: 15 nm rubrene/35 nm C_{60}/10 nm BCP/100 nm Al). (a) Temperature dependence of V_{OC} for the devices in Figure 6.1d as a function of rubrene interlayer thickness. Linear extrapolations of V_{OC} to 0 K are based on data in the temperature range of 190−294 K.

Metal Phthalocyanine-C_{60} OPVs

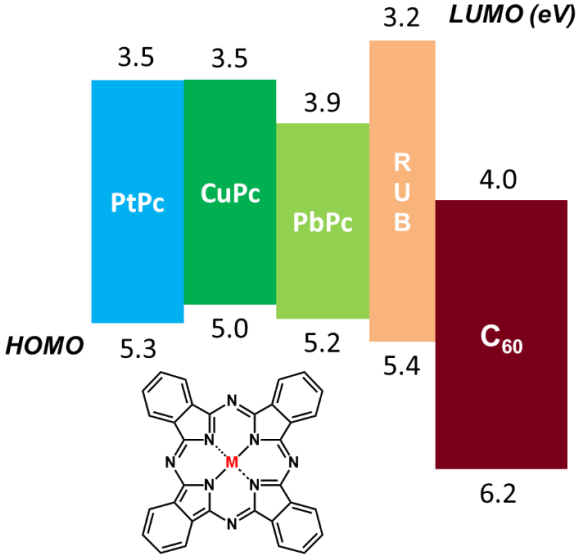

Figure E.6 Energy levels for the materials used in this study and molecular structure of metal phthalocyanine (MPc, M = Pt, Cu, Pb). [132, 143-144]

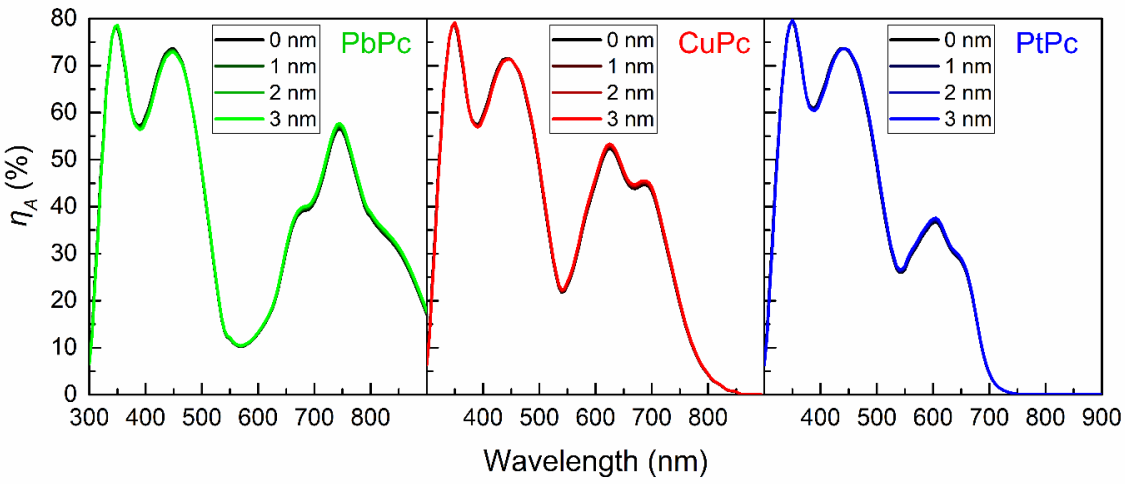

Figure E.7 Simulated absorption efficiencies (η_A) of MPc-C_{60} planar OPVs as a function of rubrene interlayer thickness.

Absorption-diffusion product of C_{60} and optical constants

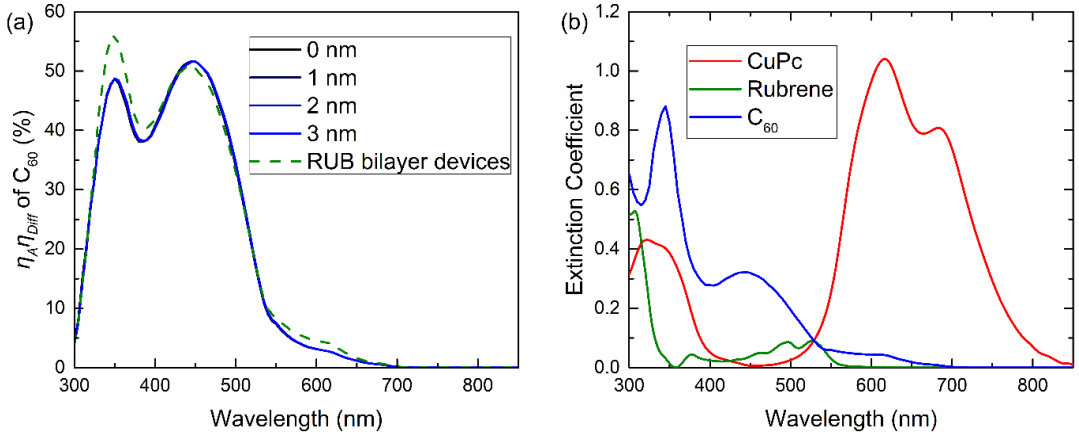

Figure E.8 (a) C_{60} contributed absorption-diffusion product ($\eta_A\eta_{Diff}$) of a CuPc-C_{60} planar device as a function of interlayer thickness (structure: 15 nm CuPc/ 0-3 nm rubrene/35 nm C_{60}/10 nm BCP/100 nm Al). The C_{60} contributed $\eta_A\,\eta_{Diff}$ of a rubrene-C_{60} bilayer device is also shown as green dash line (structure: 15 nm rubrene/35 nm C_{60}/10 nm BCP/100 nm Al). (b) Optical constants of CuPc, rubrene and C_{60} thin film on glass measured by ellipsometer.

Intensity dependence of short-circuit current density

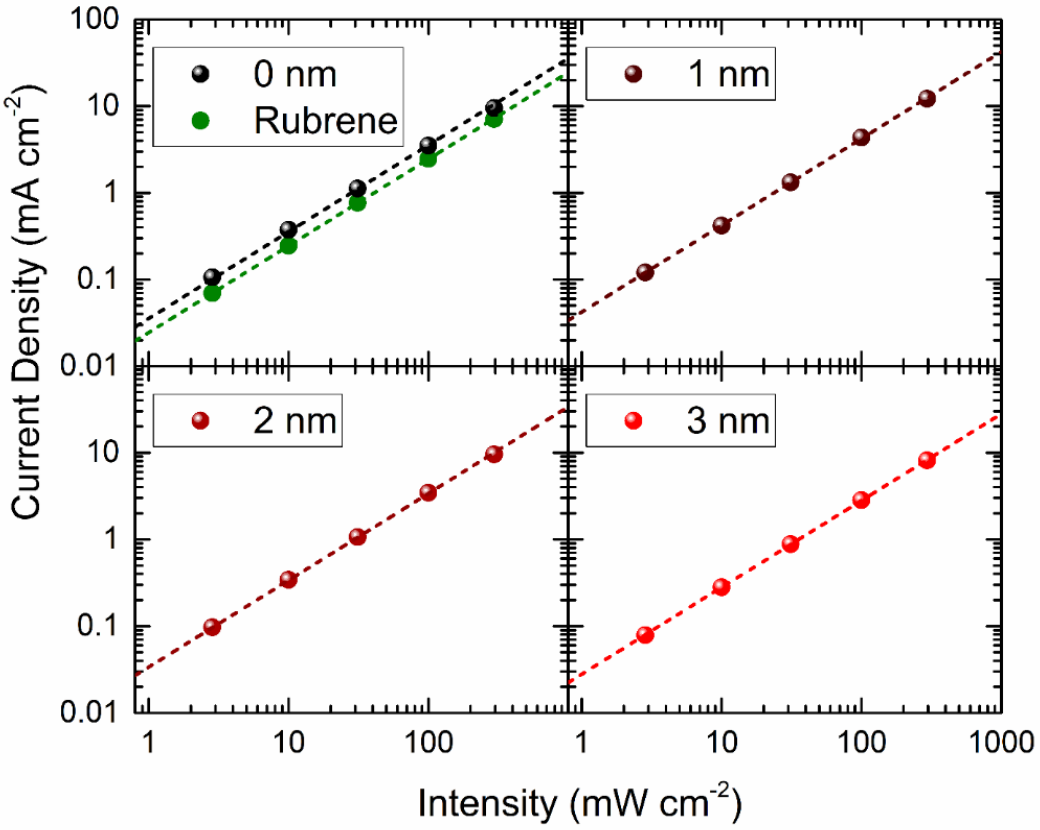

Figure E.9 Short-circuit current density (simulated AM 1.5G) of rubrene-C_{60} bilayer device and CuPc-C_{60} planar device as a function of interlayer thickness. The linear fits with slope = 1.0 are shown as dash lines.

F. Supporting Information for Chapter 7

PL Ratio fitting for m-MTDATA acceptor sweep

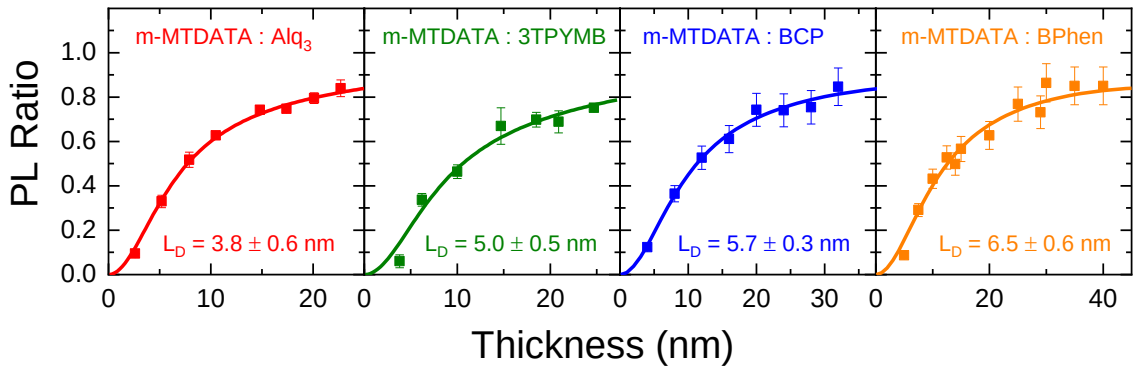

Figure F.1 Thickness dependent PL quenching measurements and fitting results for even mixtures of m-MTDATA-Alq$_3$, m-MTDATA-3TPYMB, m-MTDATA-BCP, and m-MTDATA-BPhen. A 10-nm-thick exciton blocking layer of TAPC are used for measurements with the acceptor Alq$_3$, while a 10-nm-thick layer of the acceptor is used in this capacity for all other acceptors. The results of m-MTDATA-3TPBYB and m-MTDATA-Alq3 mixed films were measured by Nolan Concannon.

PL Ratio fitting for BCP donor sweep

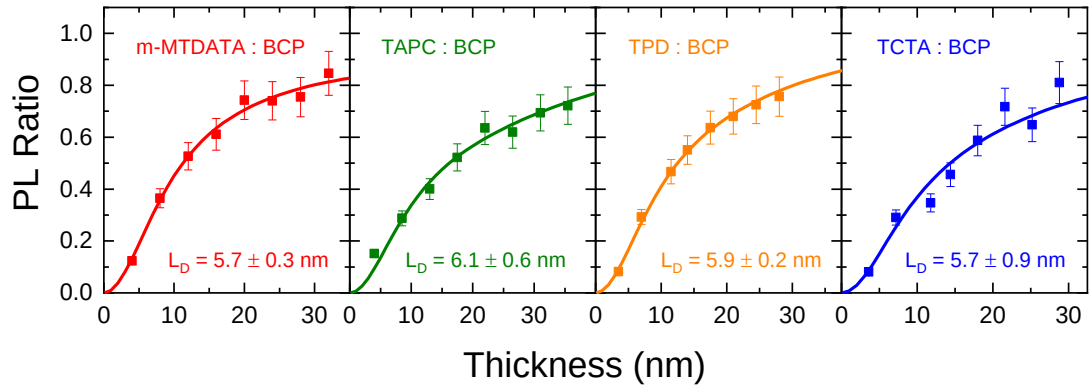

Figure F.2 Thickness dependent PL quenching measurements and fitting results for even mixtures of m-MTDATA-BCP, TAPC-BCP, TPD-BCP, and TCTA-BCP. A 10-nm-thick exciton blocking layer of the acceptor BCP are used for all measurements. Additionally, a 7-10-nm-thick quenching layer of HATCN is used.

Space-charge-limited-current (SCLC) measurements

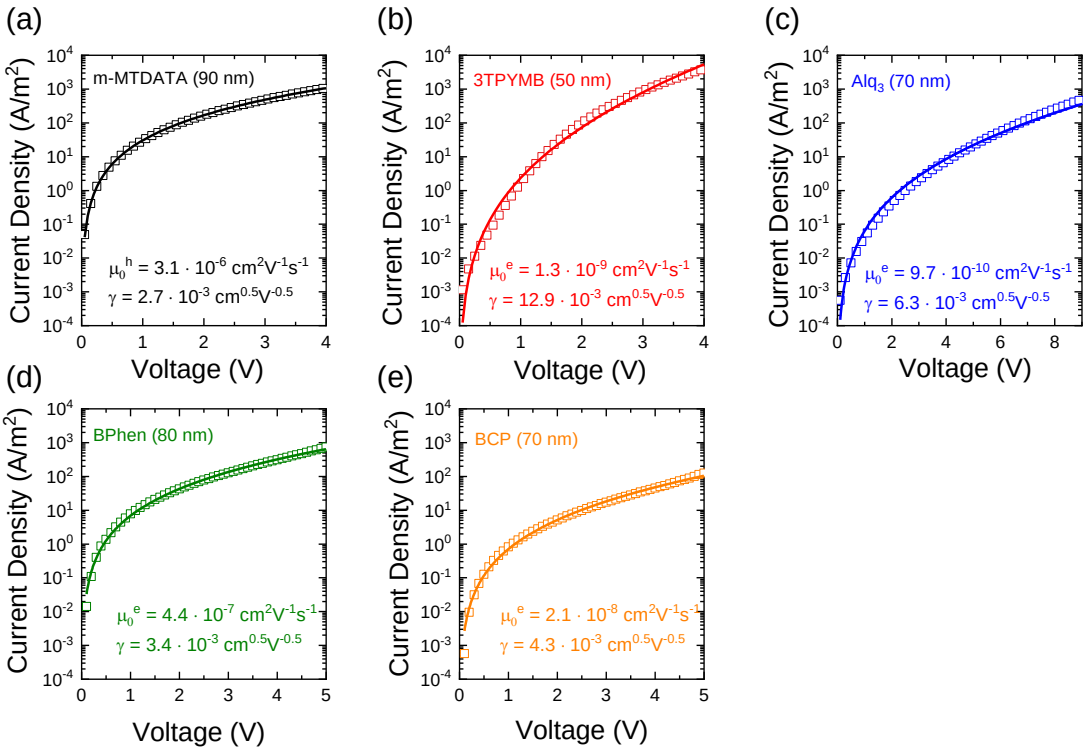

Figure F.3 SCLC of neat m-MTDATA and acceptors. J-V characteristic and SCLC fit for neat films of: (a) m-MTDATA (90 nm, hole-only) (b) 3TPYMB (50 nm, electron-only) (c) Alq_3 (70 nm, electron-only) (d) BPhen (80 nm, electron-only) (e) BCP (70 nm, electron-only). The m-MTDATA and 3TPYMB results are measured by Nolan Concannon.

Composition dependence of CT L_D for m-MTDATA-BPhen/BCP/3TPYMB heterojunctions

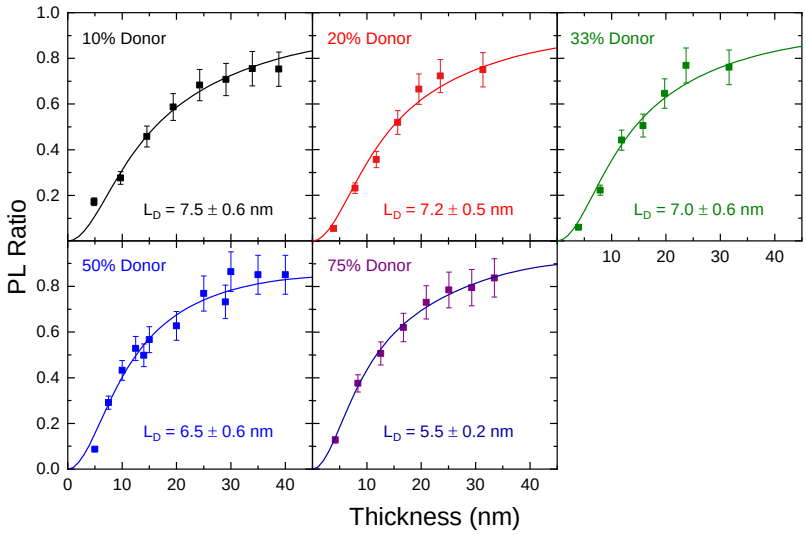

Figure F.4 Thickness dependent PL quenching measurements and fits are shown for mixtures of 10, 20, 33, 50, and 75% donor m-MTDATA with BPhen. All measurements employed 10-nm-thick exciton blocking layers of the acceptor and 7-10-nm-thick exciton quenching layers of HATCN.

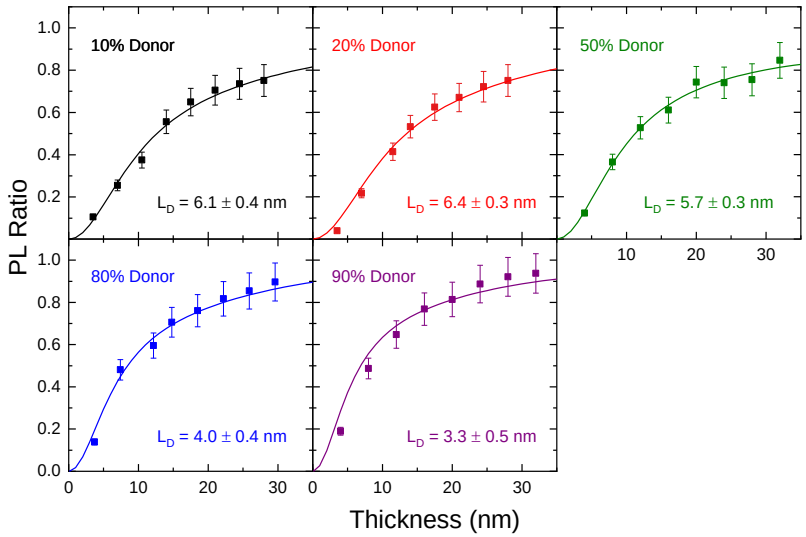

Figure F.5 Thickness dependent PL quenching measurements and fits are shown for mixtures of 10, 20, 50, 80, and 90% donor m-MTDATA with BCP.

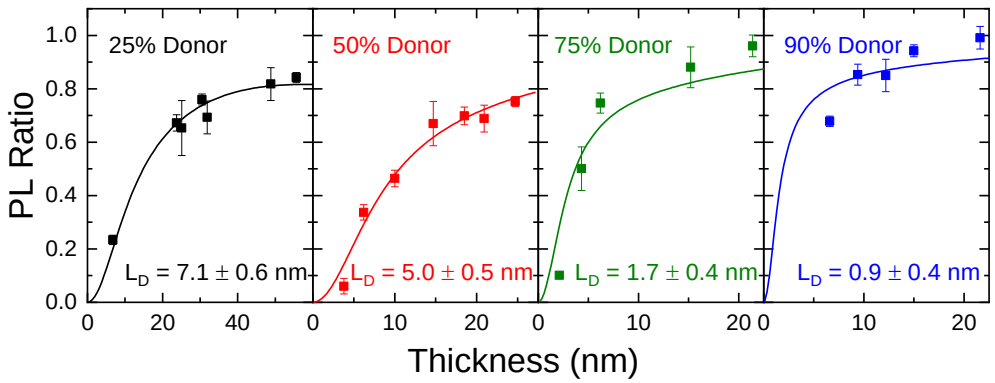

Figure F.6 Thickness dependent PL quenching measurements and fits are shown for mixtures of 25, 50, 75, and 90% donor m-MTDATA with 3TYPMB. This measurement were performed by Nolan Concannon.

G. Supporting Information for Chapter 8

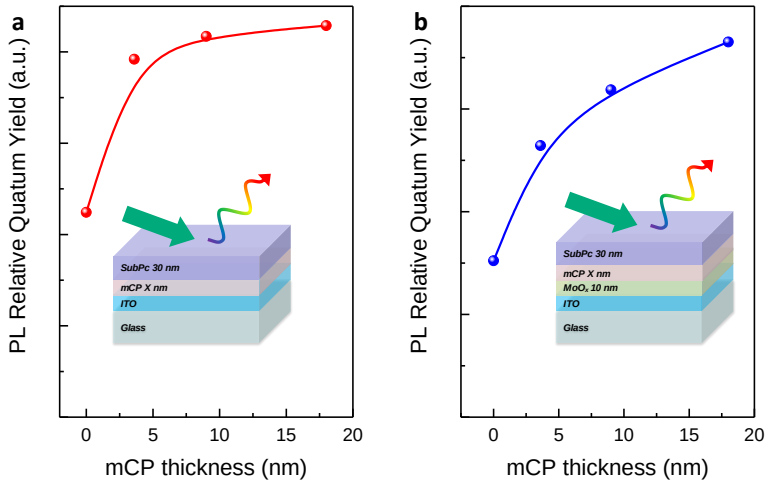

Figure G.1 Preventing exciton loss at SubPc-ITO and SubPc-MoO_x interface. Photoluminescence (PL) relative quantum yield of SubPc films as a function of mCP thickness between SubPc and ITO/MoO_x. The PL relative quantum yield calculated as the ratio of integrated PL to the number of generated excitons. Exciton generation is simulated by a transfer matrix model[48]. SubPc films are all pumped with λ = 500 nm light. The incident angle is 70° for all incident light. An increase in PL relative quantum yield with mCP (exciton blocking) thickness suggests exciton loss at SubPc-ITO and SubPc-MoO_x interfaces.

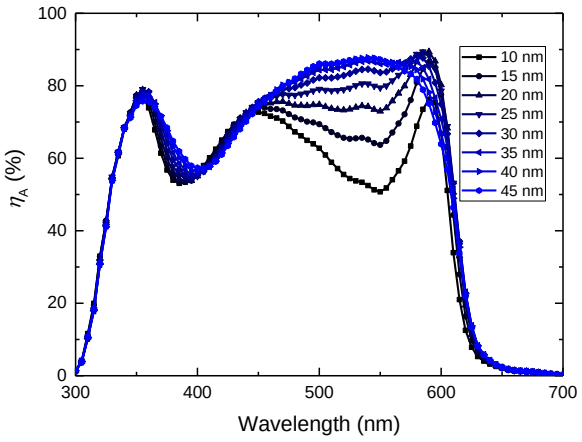

Figure G.2 Absorption efficiency spectra of SubPc-C_{60} planar OPVs. The absorption efficiency (η_A) spectra of devices in Figure 8.1b are calculated using transfer matrix model. The plotted η_A is the total active layer absorption efficiency, including the absorption of

both SubPc and C_{60}.

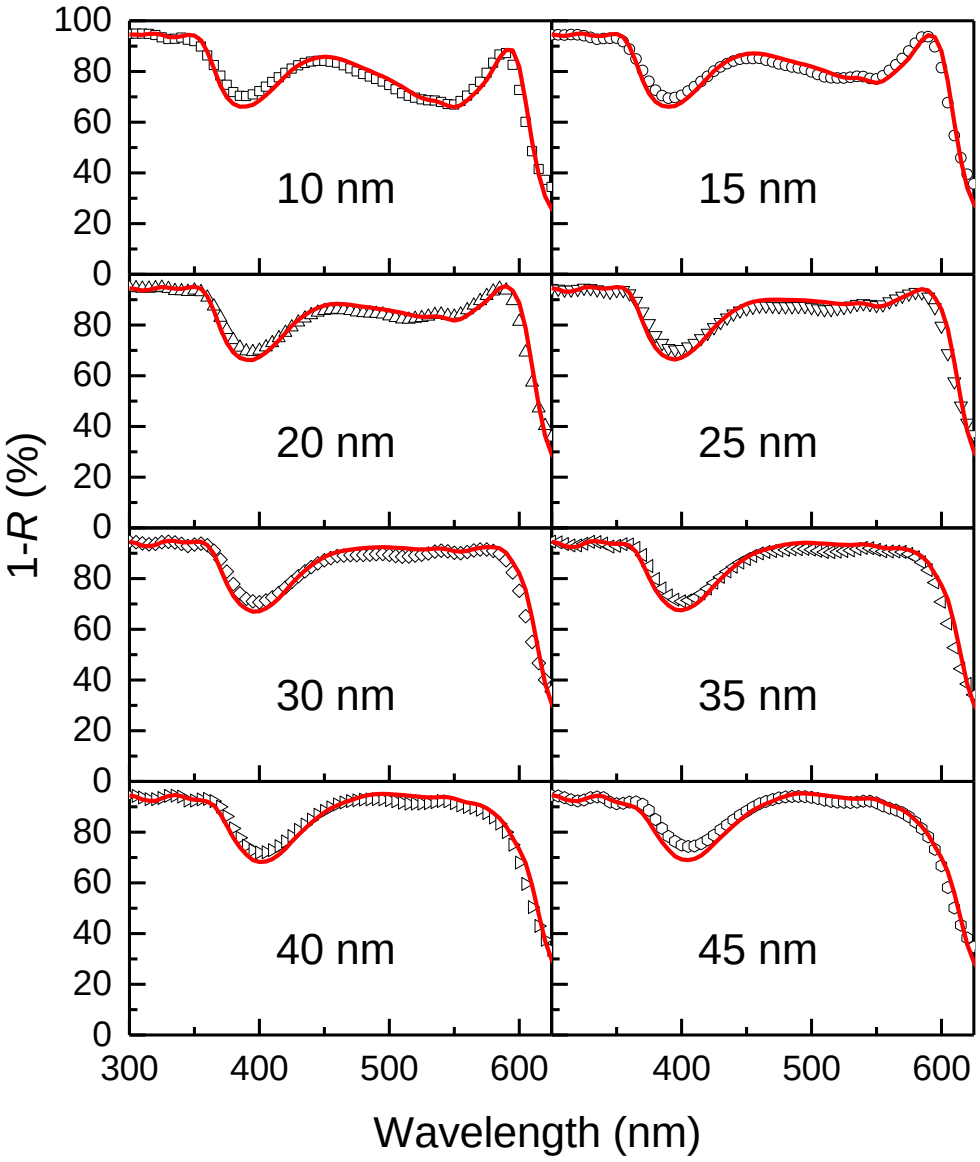

Figure G.3 Experimental and simulated reflectivity of SubPc-C_{60} planar OPVs. The reflectivity (R) of devices in Figure 8.1b is measured off the Al cathode through the ITO/organic layers. The reflectivity measurements were made at an incident angle of 15° to the substrate normal. The experimental results are shown in symbols and the simulation is shown as a red solid line.

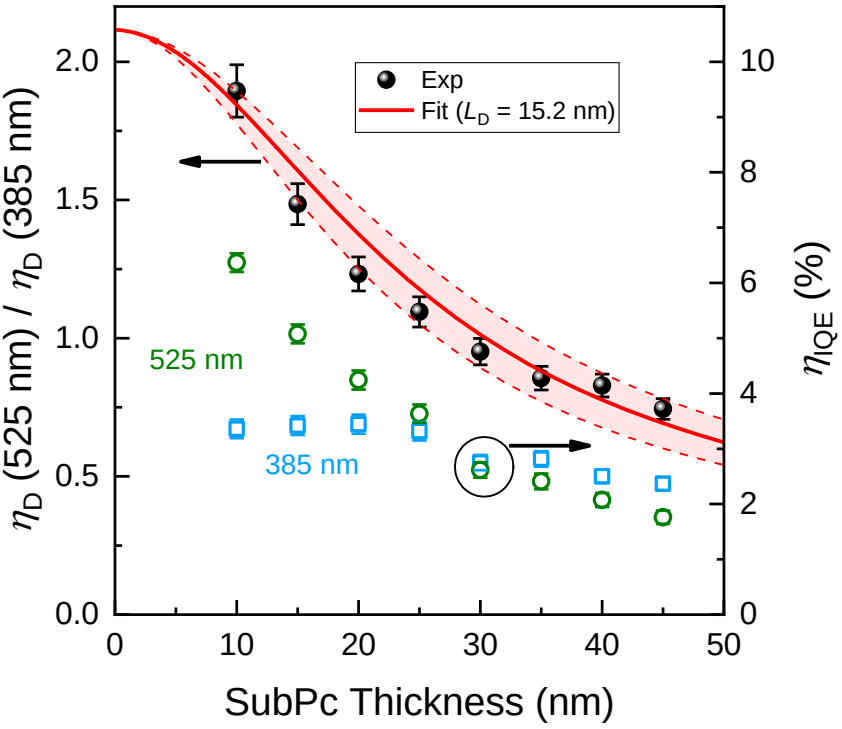

Figure G.4 Extracting exciton diffusion length from of SubPc-NPD planar OPVs. Diffusion efficiency ratios (λ = 525 nm to λ = 385 nm) as a function of SubPc thickness for SubPc-NPD planar OPVs. The red solid line is the best fit of the data, corresponding to a SubPc L_D of 15.2 nm. The internal quantum efficiency at wavelengths of λ = 385 nm and λ = 575 nm is shown on the right axis. Error bars represent the standard deviation of measured devices.

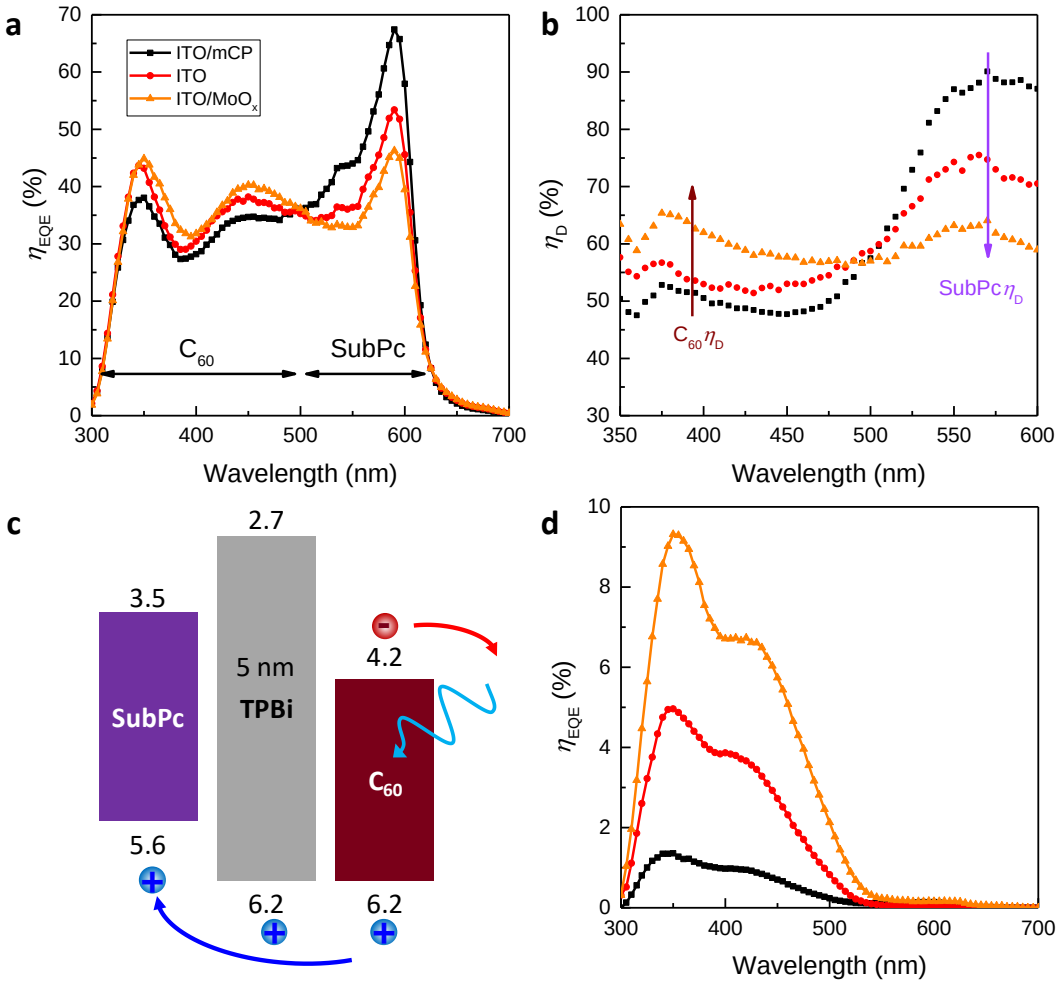

Figure G.5 Impact of anode buffer layer on exciton harvesting. (a) External quantum efficiency spectra for SubPc-C_{60} OPVs with structure: ITO/7 nm mCP or no buffer layer or 10 nm MoO_x/10 nm SubPc/35 nm C_{60}/10 nm BCP/1 nm MoOx/ 100 nm Al. Horizontal arrows denote the spectral regions of dominant absorption for SubPc and C_{60}. (b) Diffusion efficiency spectra determined from the external quantum efficiency in (a) by assuming unity charge separation efficiency. The purple and brown arrows show the impact of anode buffer layers on exciton harvesting in SubPc and C_{60}, respectively. (c) Schematic of photocurrent generation in a SubPc-TPBi-C_{60} planar device made by inserting 5-nm-thick TPBi interlayer at D-A interface of devices in (a). (d) The external quantum efficiency spectra of SubPc-TPBi-C_{60} planar devices.

In many OPV designs, an exciton blocking layer (EBL) is not included on the ITO

anode as it increases the bulk resistance and reduces device built-in field (E_{bi}). Many previous studies deposit the donor material directly on ITO or on deep work function buffer layers such as MoO_x [65, 70, 141, 231]. Here, we compare three different anode contacts: ITO/mCP/donor, ITO/donor and ITO/MoO_x/donor for a SubPc-C_{60} PHJ. The E_{bi} within the device is expected to be highest for deep work function MoO_x and lowest for a more resistive EBL of mCP.

For the SubPc-C_{60} PHJ device with 10-nm-thick donor, the η_{CS} is found to be ~100% at short-circuit (Figure 8.4a) even when a 7-nm-thick anode EBL of mCP is incorporated. As such, increasing E_{bi} will not further improve η_{CS} for this device. The impact of anode buffer layers and E_{bi} on exciton harvesting can be directly determined from changes in η_{IQE}. Figure G.5a and b show the η_{EQE} and η_D ($\approx\eta_{IQE}$) of SubPc-C_{60} PHJ devices with different anode contacts. Compared to a device with an mCP EBL, the devices with bare ITO and MoO_x show lower η_{EQE} and η_D for the SubPc absorption dominant region. This suggests that the ITO and MoO_x surfaces can quench SubPc excitons and reduce photocurrent, consistent with the observation in Figure G.1. A lower L_D will be extracted assuming these interfaces are exciton reflecting when using previous charge carrier-based measurements. For the C_{60} absorption dominant region, the devices with bare ITO and MoO_x show an increase in η_{EQE} and η_D compared to the device with an mCP EBL. As we only varied the anode-donor interface, donor-acceptor and acceptor-cathode interfaces remain the same. Exciton diffusion is not expected to change within C_{60} layer based on the simulation[48]. As such, the mechanism for more efficient exciton harvesting is likely to be enhanced exciton bulk-ionization.

To isolate the role of bulk-ionization in exciton harvesting, a 5-nm-thick 2,2',2"-(1,3,5-benzinetriyl)-tris(1-phenyl-1-H-benzimidazole) TPBi interlayer is inserted between SubPc and C_{60}, to frustrate charge transfer (Figure G.5c). As no exciton dissociating interface is available, the only carrier generation pathway is bulk ionization by E_{bi}. Figure G.5d shows the η_{EQE} of SubPc-TPBi-C_{60} PHJ devices with different anode contacts. These devices show increased η_{EQE} with E_{bi} and negligible photoresponse for $\lambda > 550$ nm, similar to the photoresponse of C_{60} Schottky OPVs[233]. This suggests that the free carriers are directly generated from high energy bulk CT excitons in C_{60} and the contribution from the lowest energy Frenkel excitons are negligible for both SubPc and C_{60}. The interlayer device with an mCP EBL shows very low η_{EQE} (~1% at $\lambda = 400$ nm), which verifies the assumption for η_{IQE}-based L_D measurement: excitons are only dissociated at D-A interface. However, the interlayer device with deep work function MoO_x has much higher η_{EQE} (~10 % for the maximum), close to 20% of the bilayer device η_{EQE} in the C_{60} dominant absorption region. In this case, the recombination losses and η_{CS} of this device are no longer identical for donor and acceptor materials due to the multiple sources for free carrier generation.

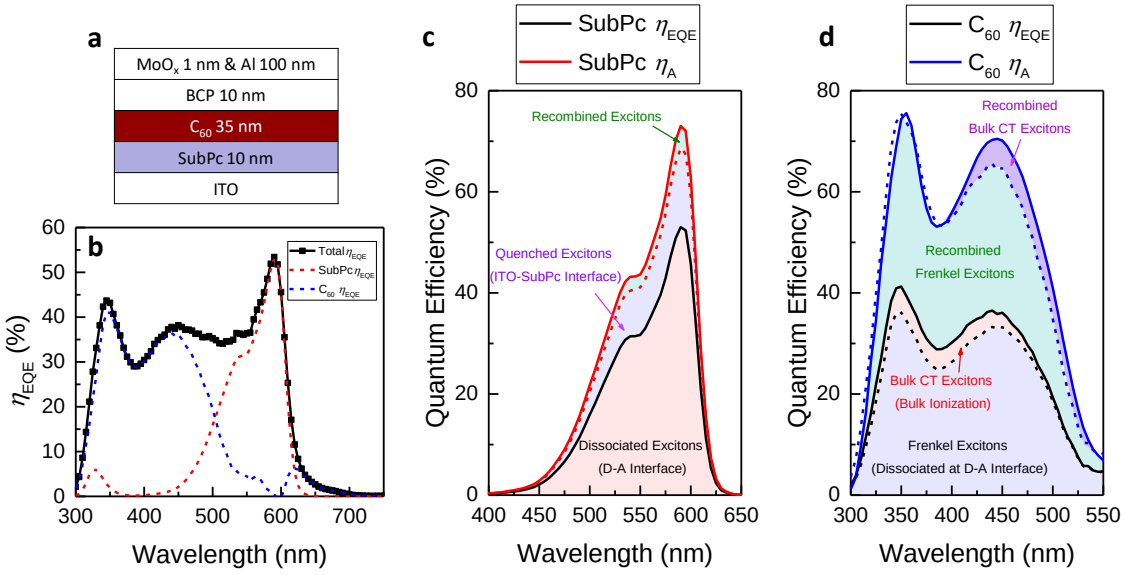

Figure G.6 Decoupling exciton quenching and dissociation in an OPV. a, Device architecture of SubPc-C_{60} planar OPV used to assess losses related to quenching at the ITO electrode. b, External quantum efficiency spectra for the SubPc-C_{60} OPV in (a). The donor and acceptor contributions are shown as dashed lines. c, Decoupling for photogeneration in SubPc. Red solid line is the SubPc absorption efficiency spectrum simulated by transfer matrix model. Shaded regions indicate the magnitude of each exciton relaxation pathway. d, Decoupling exciton quenching and dissociation for photogeneration in C_{60}. Blue solid line is the C_{60} absorption efficiency simulated using an optical transfer matrix model.

As the devices described in the main text for the measurement of L_D are designed to avoid exciton dissociation everywhere but at the D-A interface, a comparison between these and conventional devices permits a quantitative probe of all quenching and dissociation pathways. Here, we fully decouple the various exciton relaxation pathways in a conventional device without an mCP anode buffer layer (Figure G.6a), which is the same device used in Figure G.5a.

The shaded areas in Figure G.6c and d denote the relative importance of each pathway.

To realize this decoupling, we first determine the ITO-SubPc boundary condition for exciton quenching using the donor η_{EQE} at λ = 590 nm (~54%) in Figure G.6b (solid black line) and the intrinsic L_D of SubPc extracted using the methods described in the main text. This boundary condition allows us to simulate the theoretical donor η_{EQE} in the absence of exciton loss at the ITO-SubPc interface (dashed red line). Comparing the solid black and dashed red lines offers a measure of excitons lost at ITO-SubPc interface. The difference between the dashed red line and the solid red line (calculated η_A) is the fraction of donor excitons lost to natural decay.

The same analysis may also be performed for the acceptor, using the extracted acceptor η_{EQE} in Figure G.6b. As with Figure G.5, the photocurrent contribution from the bulk-ionization of C_{60} CT excitons can be determined from interlayer devices (Figure G.5c). Indeed, subtraction of the interlayer device η_{EQE} (red line, Figure G.5d) from the overall acceptor η_{EQE} (black line, Figure G.6d) yields the contribution of Frenkel excitons to the photoresponse (dashed black line, Figure G.6d). With this curve and the η_D of Frenkel excitons determined using the C_{60} L_D, the theoretical η_{EQE} of C_{60} can be derived (dashed blue line, Figure G.6d), assuming all Frenkel excitons are dissociated at the D-A interface. The difference between this curve and the calculated acceptor absorption efficiency (η_A, blue line, Figure G.6d) yields the exciton loss from CT exciton recombination.

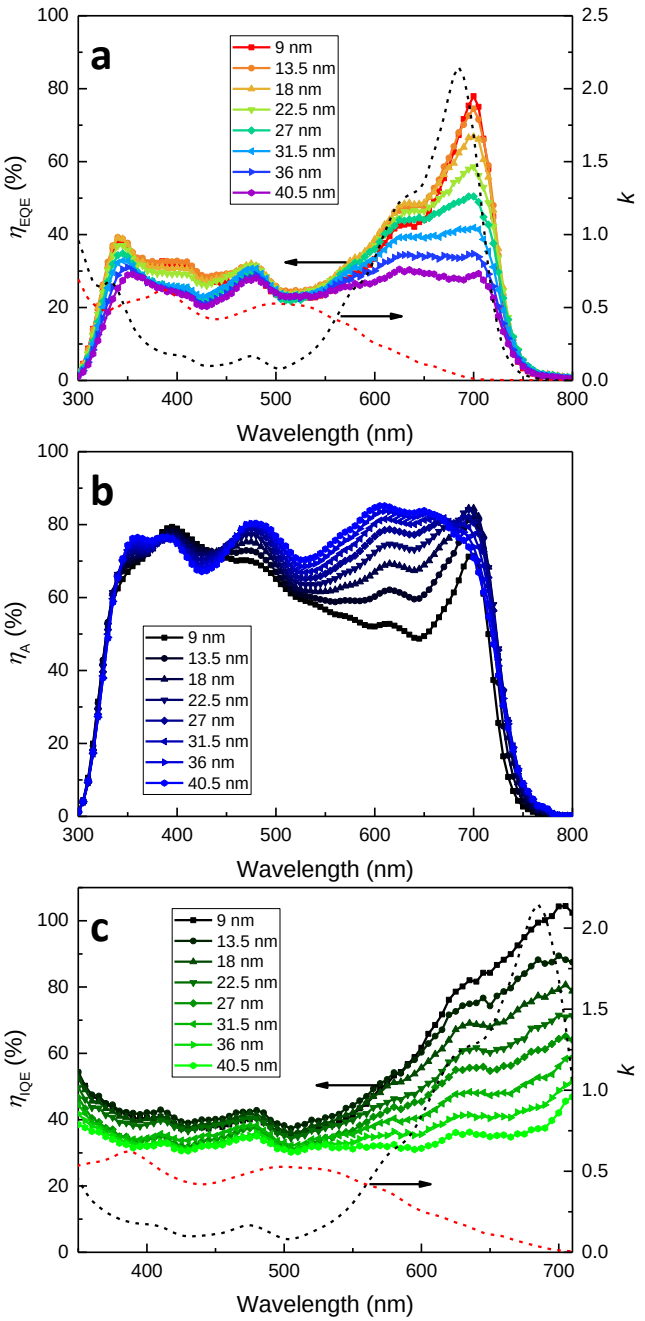

Figure G.7 Quantum efficiency spectra for SubNc-C_{70} planar OPVs. (a) The η_{EQE} spectra measured at short-circuit as a function of SubNc layer thickness. The devices have the structure: ITO/8.5 nm mCP/X (=9-40.5) nm SubNc/27 nm C_{70}/11 nm BCP/1 nm MoO_x/100 nm Al. (b) The η_A spectra calculated using a transfer matrix model. (c) The η_{IQE} spectra calculated by dividing the η_{EQE} spectra in a by the η_A spectra in b. The extinction coefficients (k) of SubNc (black dash line) and C_{70} (red dash line) are also shown.

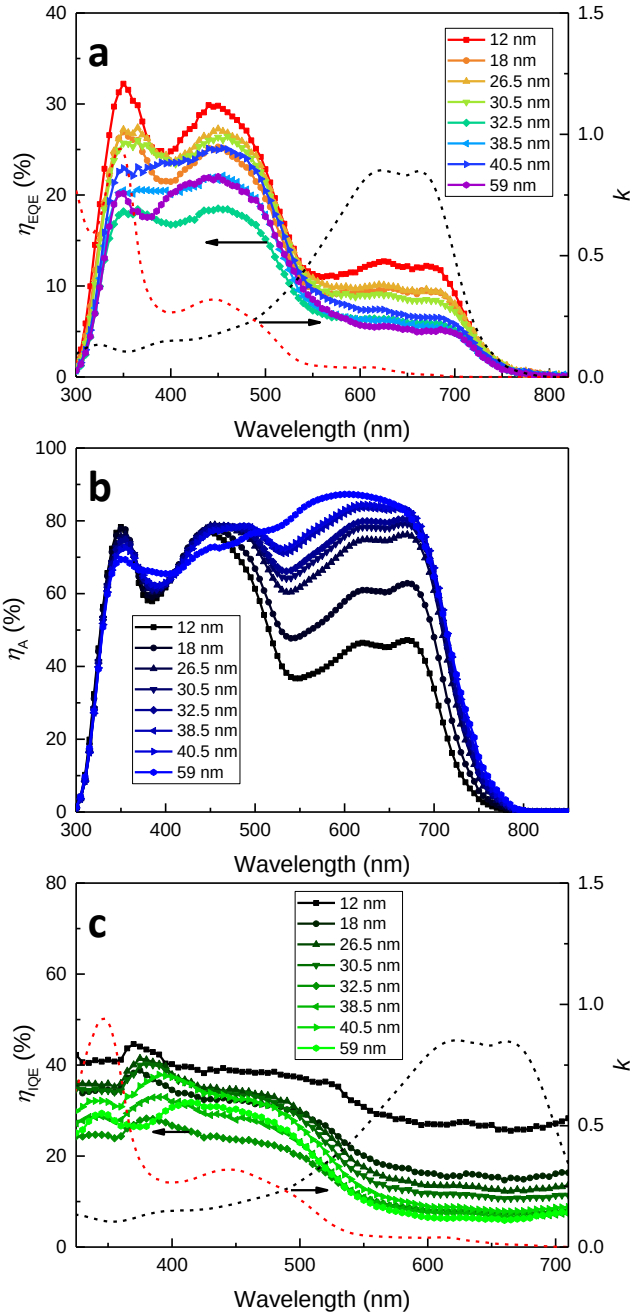

Figure G.8 Quantum efficiency spectra for PTB7-C_{60} planar OPVs. (a) The η_{EQE} spectra measured at short-circuit as a function of PTB7 polymer layer thickness. The devices have the structure: ITO/2.5 nm HfO_2/X (=12-59) nm PTB7/37 nm C_{60}/10 nm BCP/1 nm MoO_x/100 nm Al. (b) The η_A spectra calculated using a transfer matrix model. (c) The η_{IQE} spectra calculated by dividing the η_{EQE} spectra in a by the η_A spectra in b. The extinction coefficients (k) of PTB7 (black dash line) and C_{60} (red dash line) are also shown.

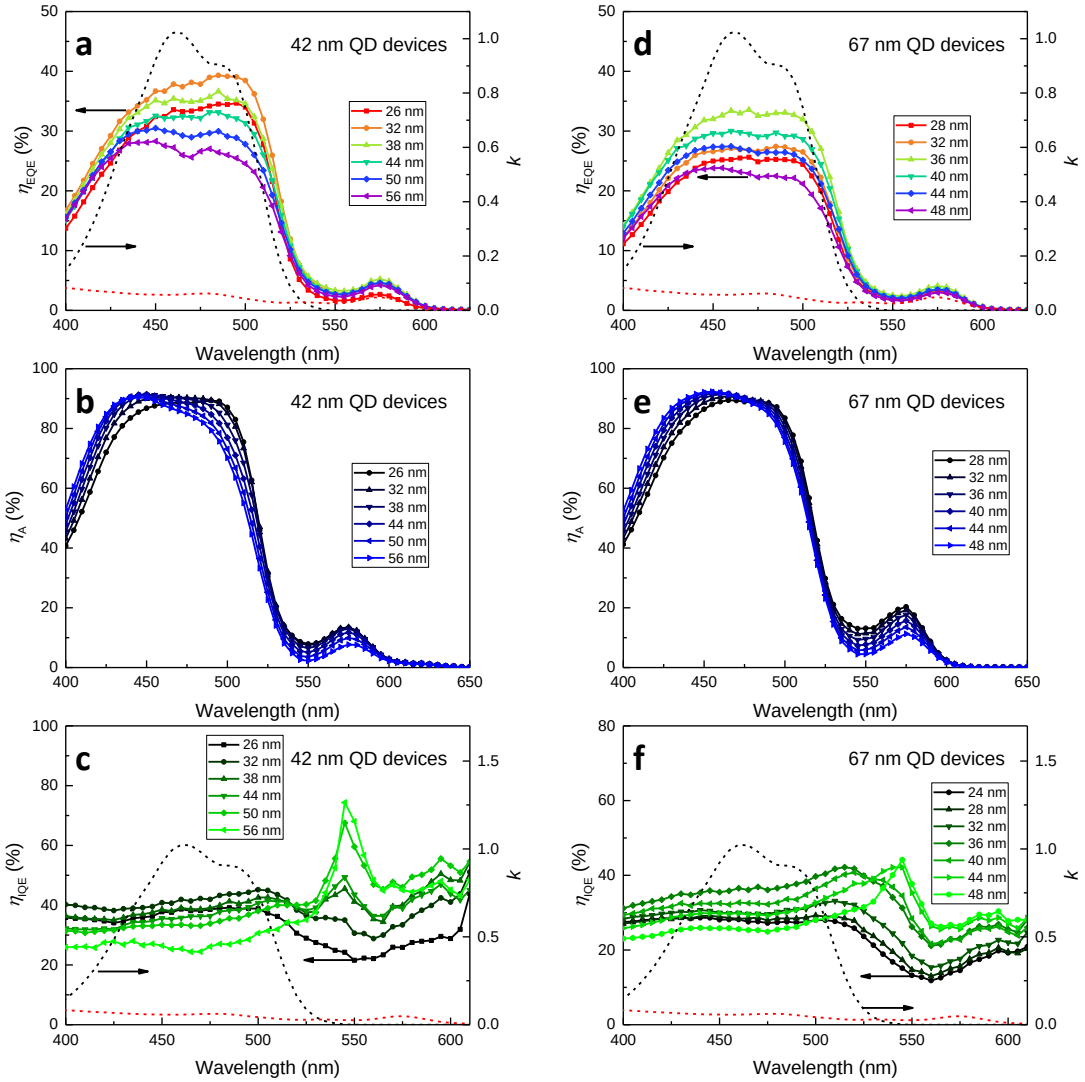

Figure G.9 Quantum efficiency spectra for CdSe QD-C545T planar photovoltaic cells. (a) The η_{EQE} spectra measured at short-circuit as a function of C545T layer thickness. The devices have the structure: ITO/2.5 nm HfO_2/42 nm CdSe QD/Y (=26-56) nm C545T/11 nm TAPC/10 nm MoO_x/100 nm Al. (b) The η_A spectra of devices in a calculated using a transfer matrix model. (c) The η_{IQE} spectra calculated by dividing the η_{EQE} spectra in a by the η_A spectra in (b). (d) The η_{EQE} spectra of devices as a function of C545T layer thickness. Device structure: ITO/2.5 nm HfO_2/67 nm CdSe QD/Y (=24-48) nm C545T/11 nm TAPC/10 nm MoO_x/100 nm Al. (e) The η_A spectra of devices in (d). (f) The η_{IQE} spectra calculated by dividing the η_{EQE} spectra in d by the η_A spectra in e. The extinction coefficients (k) of C545T (black dash line) and CdSe QD (red dash line) are also shown.

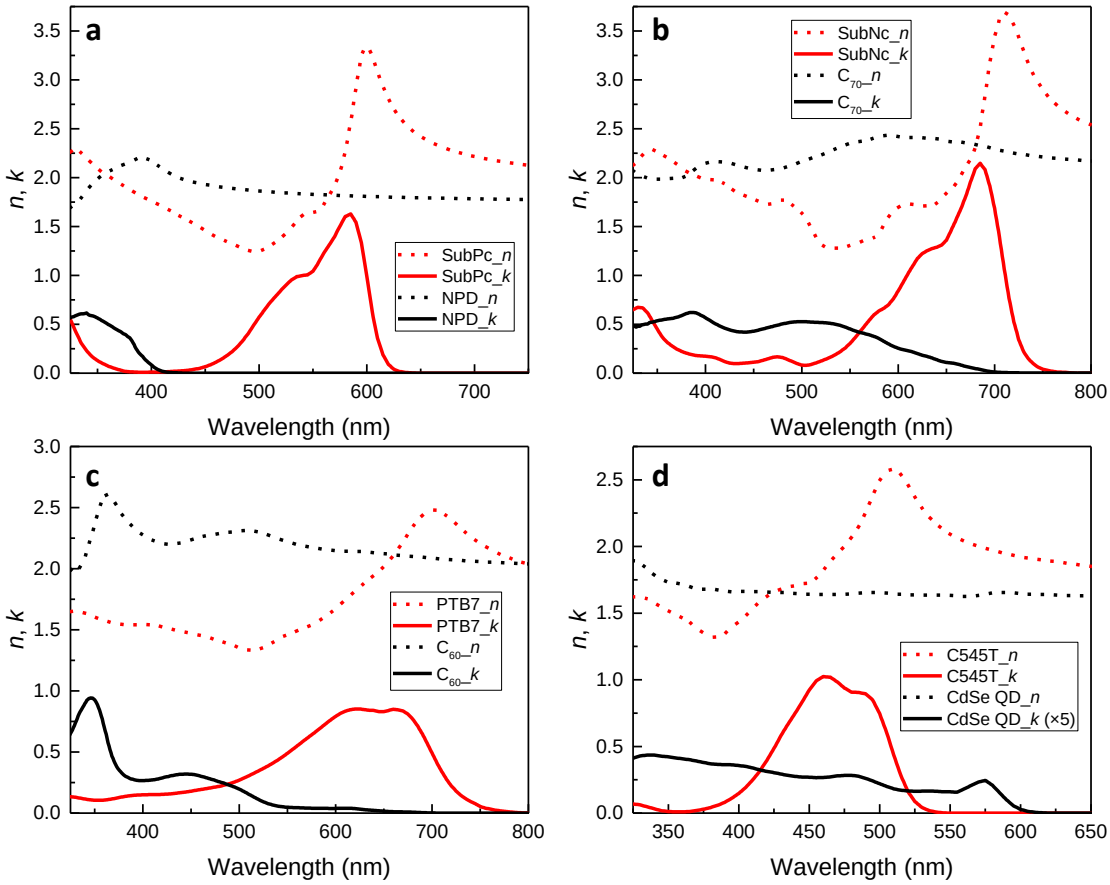

Figure G.10 Optical constants of photoactive materials for L_D measurements. The refractive index n (dash line) and the extinction coefficient k (solid line) of (a) SubPc, NPD (b) SubNc, C_{70} (a) PTB7, C_{60} (d) C545T, CdSe quantum dots (QDs). The k of CdSe QDs is shown with a 5-fold magnification.

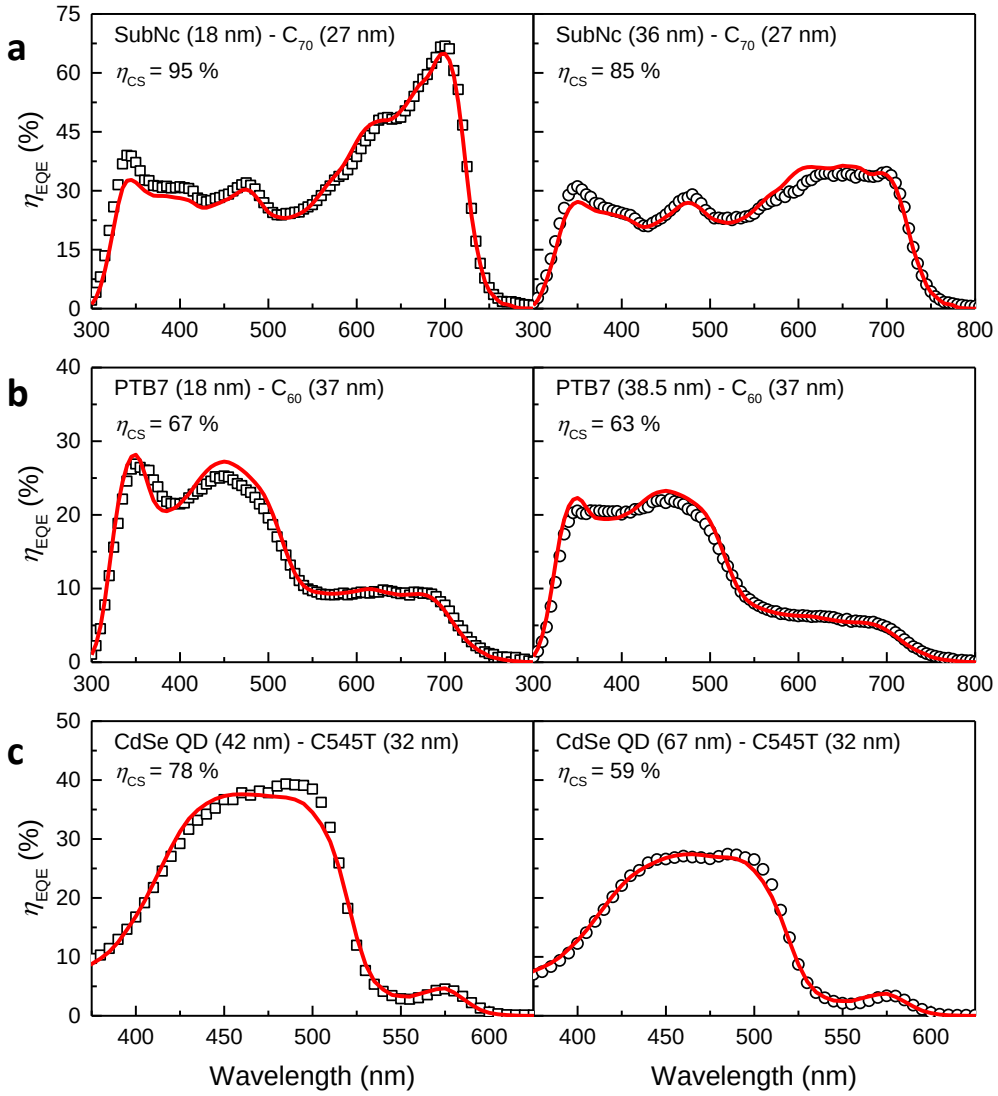

Figure G.11 Simulation of external quantum efficiency for extraction of charge separation efficiency. (a) The η_{EQE} spectra for SubNc-C_{70} planar OPVs in Figure G.7 as a function of SubNc thickness (18 and 36 nm). Experimental results are shown in symbols while solid lines are simulated spectra (simulated using L_D values shown in Figure 8.5). (b) The η_{EQE} spectra for PTB7-C_{60} planar OPVs in Figure G.8 versus PTB7 thickness (18 and 38.5 nm). The simulated η_{EQE} spectra show slight overestimation compared to experimental results for wavelength ~450 nm, similar to the SubPc-C_{60} case with non-unity exciton relaxation yield for C_{60} bulk CT excitons. (c) The η_{EQE} spectra for CdSe quantum dot (QD)-C545T planar photovoltaic devices in Figure G.9 versus QD thickness (42 and 67 nm).

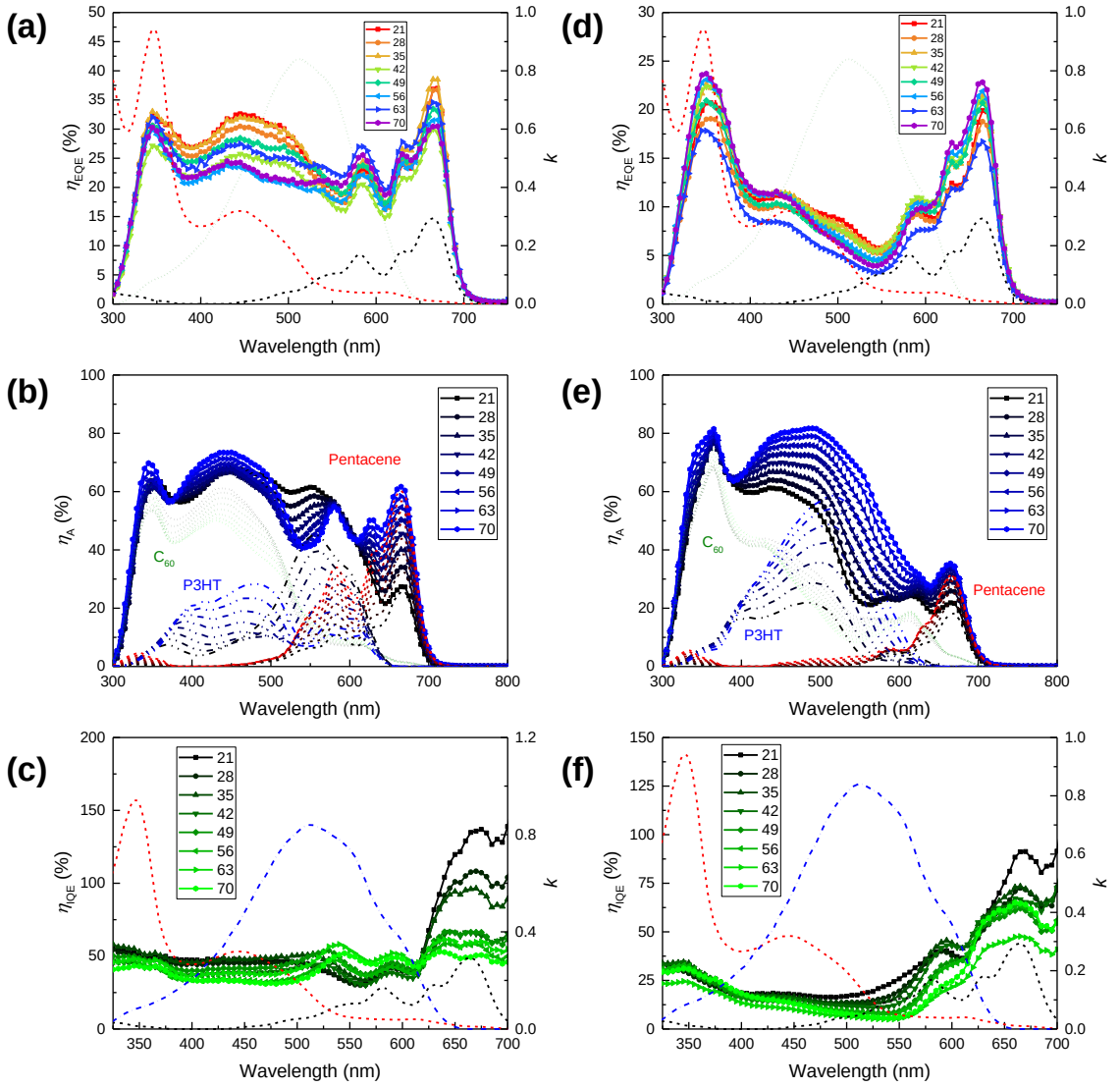

Figure G.12 Quantum efficiency spectra for Pc-C_{60} planar photovoltaic cells. (a) The η_{EQE} spectra measured at short-circuit as a function of Pc layer thickness. The devices have the structure: ITO/20 nm P3HT/X (=21-70) nm Pc/45 nm C_{60}/10 nm BCP/1 nm MoO_x/100 nm Al. (b) The η_A spectra of devices in a calculated using a transfer matrix model. (c) The η_{IQE} spectra calculated by dividing the η_{EQE} spectra in a by the η_A spectra in (b). (d) The η_{EQE} spectra of devices as a function of Pc layer thickness. Device structure: ITO/20 nm P3HT/X (=21-70) nm Pc/75 nm C_{60}/10 nm BCP/1 nm MoO_x/100 nm Al. (e) The η_A spectra of devices in (d). (f) The η_{IQE} spectra calculated by dividing the η_{EQE} spectra in d by the η_A spectra in e. The extinction coefficients (k) of Pc (black dash line), C_{60} (red dash line), and P3HT (blue dash dot line) are also shown.

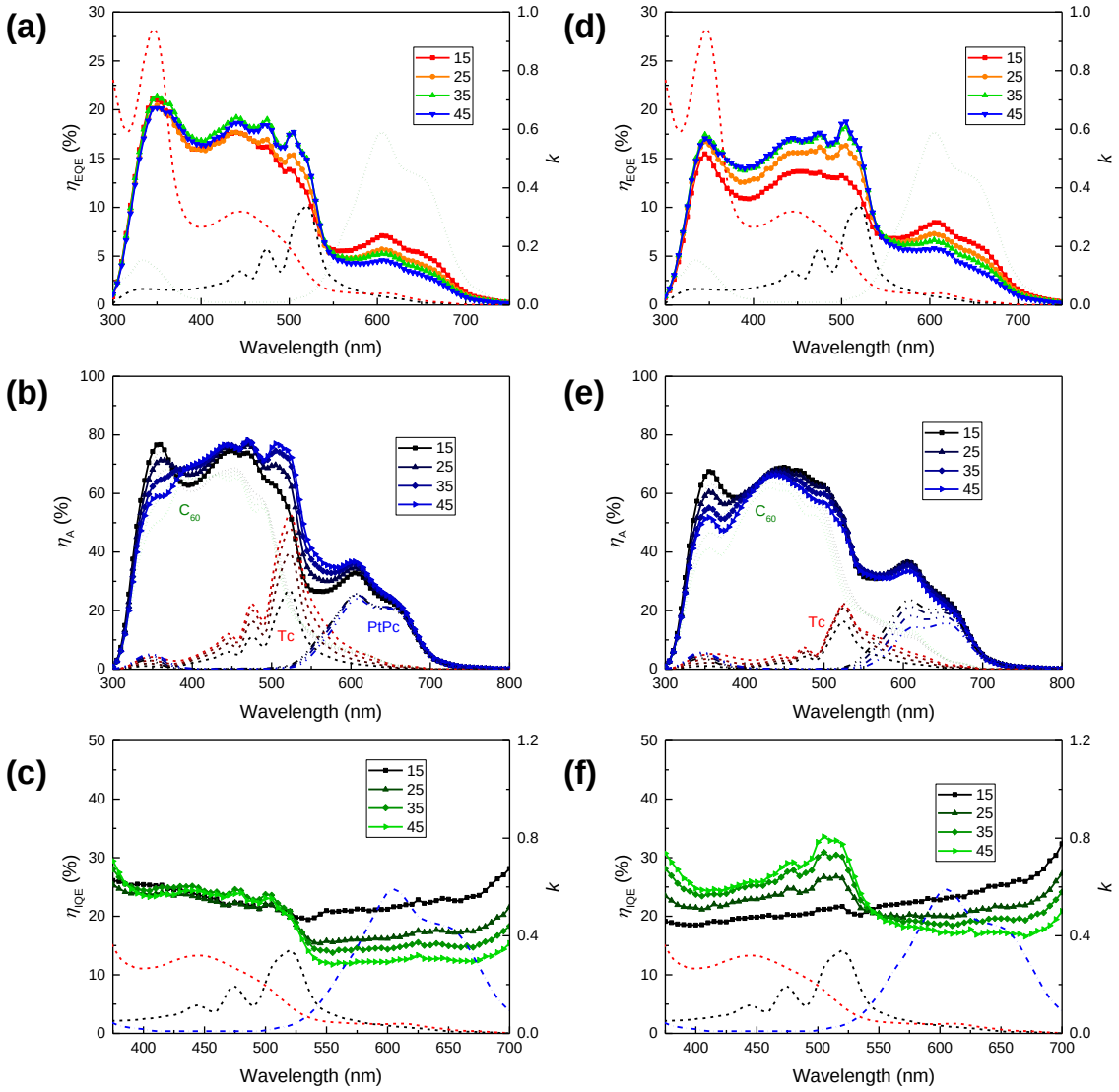

Figure G.13 Quantum efficiency spectra for PtPc-Tc-C_{60} planar photovoltaic cells. (a) The η_{EQE} spectra measured at short-circuit as a function of Tc layer thickness. The devices have the structure: ITO/10 nm TAPC/10 nm PtPc/X (=15-45) nm Tc/35 nm C_{60}/10 nm BCP/1 nm MoO_x/100 nm Al. (b) The η_A spectra of devices in a calculated using a transfer matrix model. (c) The η_{IQE} spectra calculated by dividing the η_{EQE} spectra in a by the η_A spectra in (b). (d) The η_{EQE} spectra of devices as a function of Tc layer thickness. Device structure: ITO/10 nm TAPC/10 nm PtPc/X (=15-45) nm Tc/50 nm C_{60}/10 nm BCP/1 nm MoO_x/100 nm Al. (e) The η_A spectra of devices in (d). (f) The η_{IQE} spectra calculated by dividing the η_{EQE} spectra in d by the η_A spectra in e. The extinction coefficients (k) of Tc (black dash line), C_{60} (red dash line), and PtPc (blue dash dot line) are also shown.

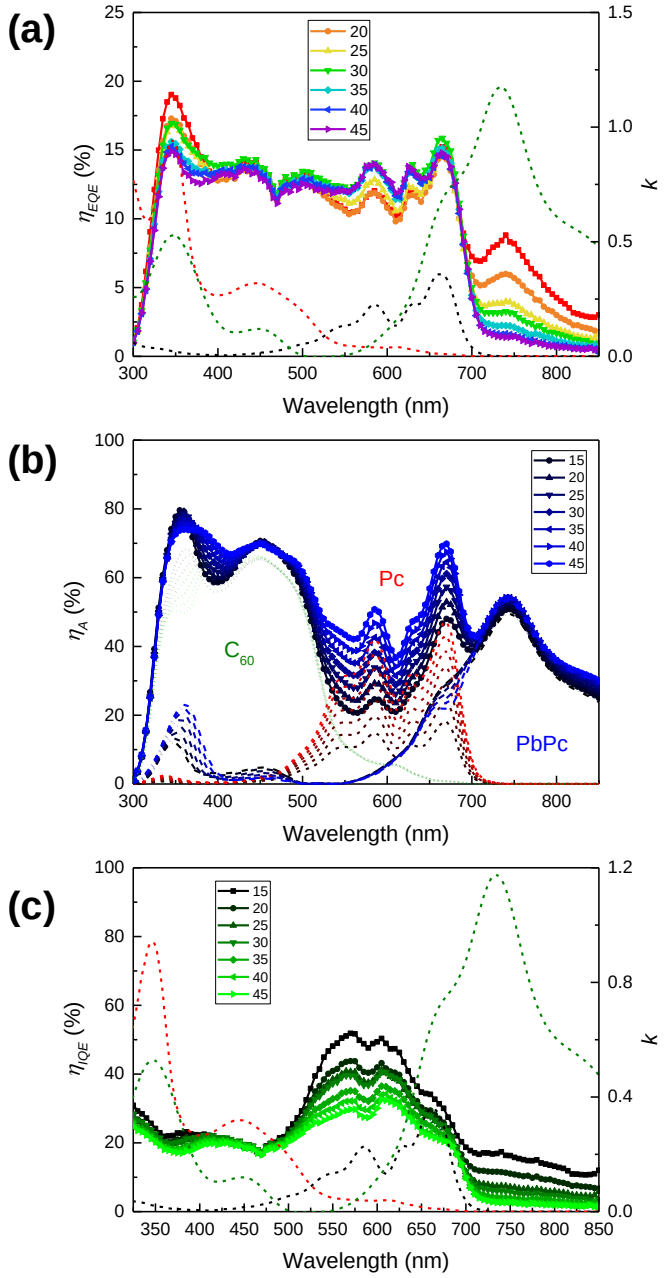

Figure G.14 Quantum efficiency spectra for PbPc-Pc-C_{60} planar photovoltaic cells. (a) The η_{EQE} spectra measured at short-circuit as a function of Pc layer thickness. The devices have the structure: ITO/10 nm TAPC/10 nm PbPc/X (=15-45) nm Pc/35 nm C_{60}/10 nm BCP/1 nm MoO_x/100 nm Al. (b) The η_A spectra of devices in a calculated using a transfer matrix model. (c) The η_{IQE} spectra calculated by dividing the η_{EQE} spectra in a by the η_A spectra in (b). The extinction coefficients (k) of Pc (black dash line), C_{60} (red dash line), and PbPc (green dash line) are also shown.